-PET- Vol. 57

ISSN : 1737-9934

Advanced techniques on control & signal processing

Proceedings of
Engineering & Technology
-PET-

Editor :

Dr. Ahmed Rhif (Tunisia)

International Centre for Innovation & Development
-ICID-

ISSN: 1737-9334
-PET- Vol. 57

ICID

International Centre for Innovation & Development

Proceedings of Engineering & Technology
-PET-

Advanced techniques on control & signal processing

Editor:

Dr. Ahmed Rhif (Tunisia)

International Centre for Innovation & Development
–ICID–

Editor in Chief:

Dr. Ahmed Rhif (**Tunisia**)
Ahmed.rhif@gmail.com
Dean of International Centre for Innovation & Development (**ICID**)

Editorial board:

Janset Kuvulmaz Dasdemir, **Turkey**

Mohsen Guizani, **USA**

Quanmin Zhu, **UK**

Muhammad Sarfraz, **Kuwait**

Minyar Sassi, **Tunisia**

Seref Naci Engin, **Turkey**

Victoria Lopez, **Spain**

Yue Ma, **China**

Zhengjie Wang, **China**

Amer Zerek, **Libya**

Abdulrahman A. A. Emhemed, **Libya**

Abdelouahid Lyhyaoui, **Morocco**

Ali Haddi, **Morocco**

Hedi Dhouibi, **Tunisia**

Jalel Chebil, **Tunisia**

Tahar Bahi, **Algeria**

Youcef Soufi, **Algeria**

Ahmad Tahar Azar, **Egypt**

Sundarapandian Vaidyanathan, **India**

Ahmed El Oualkadi, **Morocco**

Chalee Vorakulpipat, **Thailand**

Faisal A. Mohamed Elabdli, **Libya**

Feng Qiao, **UK**

Lijie Jiang, **China**

Mohammed Sidki, **Morocco**

Natheer K.Gharaibeh, **Jordan**

O. Begovich Mendoza, Mexico

Özlem Senvar, **Turkey**

Qing Zhu, **USA**

Ved Ram Singh, **India**

Beisenbia Mamirbek, **Kazakhstan**

Claudia Fernanda Yasar, **Turkey**

Habib Hamdi, **Tunisia**

Laura Giarré, **Italy**

Lamamra Kheireddine, **Algeria**

Maria Letizia Corradini, **Italy**

Ozlem Defterli, **Turkey**

Abdel Aziz Zaidi, **Tunisia**

Brahim Berbaoui, **Algeria**

Jalel Ghabi, **Tunisia**

Yar M. Mughal, **Estonia**

Syedah Sadaf Zehra, **Pakistan**

Ali Mohammad-Djafari, **France**

Greg Ditzler, **USA**

Fatma Sbiaa, **Tunisia**

Kenz A.Bozed, **Libya**

Lucia Nacinovic Prskalo, **Croatia**

Mostafa Ezziyyani, **Morocco**

Nilay Papila, **Turkey**

Rahmita Wirza, **Malaysia**

Summary

Comparative of Data Acquisition Using Wired and Wireless Communication System Based on Arduino and nRF24L01

Hafed Efheij #1,Ataher Abdulaziz Akrima #2,Walid Shanab#3, Abdulgader M A Elfasi#4

#1 *lecture assistant at College of Electronic Technology-Tripoli, Libya*
1 Hafedrs@gmail.com
#2 *lecture assistant at College of Electronic Technology-Tripoli, Libya*
2 taher_krima@yahoo.com
#3 *lecture at higher institute of Engineering Technology- Tripoli, Libya*
3 walid.t.shanab72@gmail.com
#4 *lecture assistant at College of Electronic Technology-Tripoli, Libya*
4 Abdul_arife@hotmail.com

***Abstract*- The topic of this paper is divided into two parts where the first part presents high-speed data transmission on flexible cables and the second part presents a wireless remote monitoring and controlling system with wireless data transmission The paper is focusing generally on data acquisition system and particularly on the performance of data transmission using wired and wireless communication channels. Also, a comparison between wired and wireless communication channels regarding to several characteristics. The data acquisition system in both of wired & wireless models has been designed practically based on Arduino uno. The data were extracted through different sensors such as temperature sensor, gas sensor and light intensity sensor. All the collected data was simulated by LabVIEW software which is helping to monitoring, recording and tracking the collected data.**

The simulated data proved that the wireless model achieved mobility & semi-accurate results, while the wired model gave a large bandwidth and more security.

.

***Index terms* — RF, LabVIEW, Arduino, wired, wireless MQ7, termstate , Results, LDR,nRF24l01 Conclusion, Reference.**

I. INTRODUCTION

Many utility industry operators are looking for new ways to maximize their investment in communication networks while ensuring reliable, secure data transmission. There is a variety of communications solutions available, the two most common being wireless technology and wired options-such as copper and fiber-optic cable. While both have a place in utility market applications, there are many factors contributing to this increase- , including cost savings, flexibility and power consumption. When looking at the big picture, a utility operator will discover each technology has its own advantages and disadvantages [1].

Data transfer is the process of using computing techniques and technologies to transmit or transfer electronic or analog data from one computer node to another. Data is transferred in the form of bits and bytes over a digital or analog medium, and the process enables digital or analog communications and their movement between devices. Data transfer is also known as data transmission [2].

Wired communications is a broad term that is used to describe any type of communication process that relies on the direct use of cables and wiring to transmit or transfer audio and visual information or data. A classic example of wired communications is the traditional home telephone that is connected to the local telephone switch via wires that are ran from the home to the switch. The use of wired services remains common and is not likely to disappear in the near future. Local telephone networks often form the basis for wired communications that are used by both residential and business customers in the area. Most of the networks today rely on the use of fiber-optic communication technology as a means of providing clear signaling for both inbound and outbound transmissions. Fiber optics are capable of accommodating far more signals than the older copper wiring used in generations past, while still maintaining the integrity of the signal over longer distances [3].

Wireless communications is a fast-growing technology to provide the flexibility and mobility in our today's environment. Observably, reducing the cable restriction is one of the benefits of wireless with respect to cabled devices. Other benefits include the low cost and easy deployment [3].

Wireless technologies are designed to reduce the time and different type of obstacles created by the cables. Therefore, wireless networks have more convenient working as compared to other type of wired networking. Wireless technology is the type of the computer networking in which computer is connected with the different telecommunication devices wirelessly. It is used for the sake of different purposes such as communication or data transmission. These all types

ISSN 1737-9334

of transmission that is related to the wireless networks are carried out with help of different types of waves which have micro wavelength in nature Wireless communication can be possible via radio frequency (RF), microwave and infrared to provide high speed network connections. Technologies such as Bluetooth, Wi-Fi, GPS and GPRS uses radio frequencies to communicate between two points whereas Infrared uses Infrared waves for communication. Using wireless technology, information can be exchange in long range, fastly and securely [3].

Therefore, this paper will design a transmission and receiving circuits and simulate the collected data that acquired from the sensors by software. This data will send to the receiver through separate wired and wireless communication channels. The data will be displayed and controlled through the front panel of the (LabVIEW) program that will be connected to the receiver. Moreover, the simulated data will be compared, and evaluates the usage of wireless technologies to be used in control applications after compared with wired technologies.

II. BLOCK DIAGRAM OF A TYPICAL DIGITAL COMMUNICATION SYSTEM

In figure 1 the block diagram applicable to either an analog or digital communication system is shown.

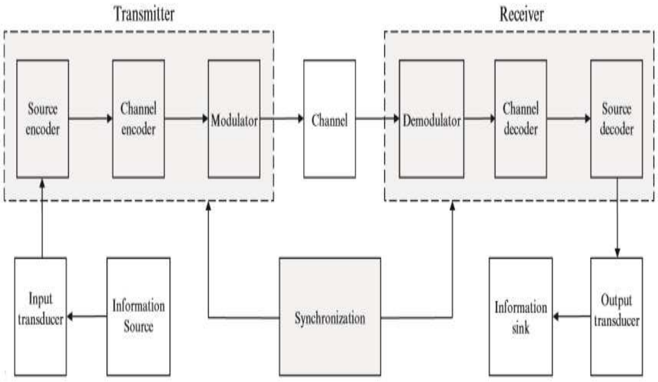

Figure 1: Block diagram of digital communication system

source is typically first passed through a source encoder, which prepares the source messages. For a voice or video source it The would consist of an analog-to-digital converter.

Next, the channel encoder adds a number of bits (redundancy) for error detection or correction purposes. To transmit this symbol sequence across a physical channel requires energy; this is the function of the modulator stage. It takes the symbol occurring in each Ts (symbol interval) and maps it onto a continuous-time waveform which is then sent across the channel [4].

At the receiver, one simply passes the received signal through the inverse of the operations at the transmitter, although it is not that straightforward due to the influence of the channel. If the channel did not filter or distort the signal, did not add noise to it, and if there was no interference from other users, then it would be simple. However, some or all of these degradations are present in physical channels [4].

The channel model depends on the media over which the transmission of modulated signals takes place. For guided media, such as twisted-pair wire, coaxial cable, and optical fiber, the background noise is mainly Gaussian. However, also in wireless channel such as satellite communications, only Gaussian noise is typically added to the received signal. The terrestrial microwave channel is similar but the transmitted signal may also be subjected to reflection, diffraction, and refraction, which leads to fading. Fading is a frequent degradation in mobile communications where the signal path from the transmitter to the receiver changes rapidly [4].

III. INTRODUCTION TO LabVIEW

Programmers develop software applications every day in order to increase efficiency and productivity in various situations. LABVIEW, as a programming language, is a powerful tool that can be used to help achieve these goals. LabVIEW (Laboratory Virtual Instrument Engineering Workbench) is a graphically-based programming language developed by National Instruments. LabVIEW, it is a system design platform and environment for a visual programming language from National instruments. It is commonly used for the data acquisition, instrument control and industrial automation on variety of platforms. The Dataflow programming is used as the programming language in Lab VIEW. The execution is determined by the structure of graphical block diagram (LabVIEW) source code on which the programmer connects the different function codes by drawing wires, these wires propagate variables and any node can execute as soon as all its input data become available. Since there might be the case of multiple nodes simultaneously, hence it is capable of parallel execution. LabVIEW ties the creation of user interface (front panels) into the development cycle. LabVIEW programs or routines are called virtual instruments (VI). Each of it is having three components: a block diagram, a front panel and a connector panel. The front panel is built with controls and indicators. Controls are the inputs and they allow a user to supply information to the VI. Indicators are the output, they display the results based on the inputs given to the VI. The connector panel is used to represent the VI in the block diagrams of the other calling VI. The back panel i.e. the block diagram contains the graphical source code. All the objects which are placed on the front panel will appear as the terminals on back panel. The back panel also contains the structures and the functions which performs operation on controls and supply the data. Nodes are also connected to one another using wires. Thus VI can either run as a program with front panel as user interface. The graphical approach also allows non-programmers to build programs by dragging and dropping virtual representations of lab equipment with which they are already familiar. Interfacing to devices: Lab VIEW gives the support to the interfacing of devices, instruments, cameras etc. users interface to hardware either by writing the direct bus command or using high level, device specific drivers that provides native Lab VIEW function nodes for controlling the device [5].

IV. SYSTEM DESIGN

The following charts show the project structure as shown in figure 2 and figure 3

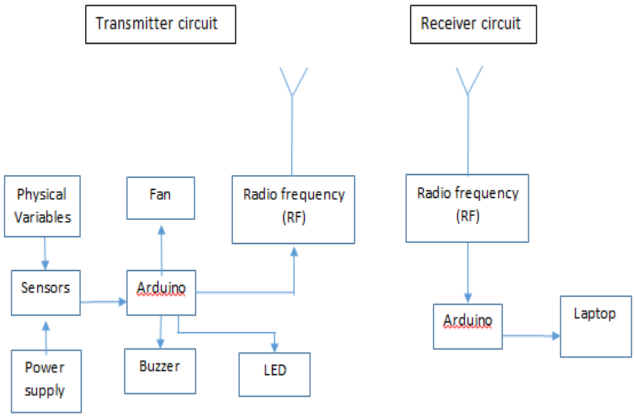

Figure 2: Circuit of data acquisition via wireless communication

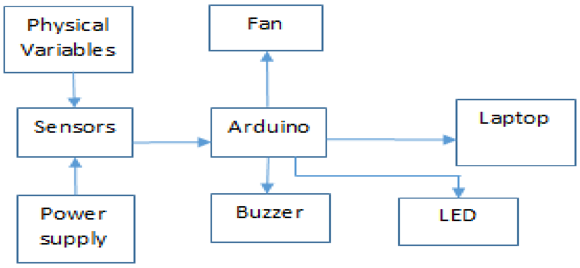

Figure 3: Circuit of data acquisition via wired communication

The block diagram illustrates the physical entity of the project, which depends primarily on the use of the Arduino board to handle and control all operations. The electronic components that used in the project will be identified along with details of how they will be connected to the Arduino board. The aim of the physical entity is to study the real design of the project and the tools of the project and how to connect them so that connection gives the best possible design and avoid the occurrence of errors resulted from the connection. This entity is very simple and accurate, so that it can be referenced and used at any time without any complexity in the structure of the physical entity by explaining the entrances and exits of the Arduino control panel.

- Arduino

Arduino is an open-source platform used for building electronics projects. Arduino consists of both a physical programmable circuit board often referred to as a microcontroller and a piece of software, or IDE (Integrated Development Environment) that runs on the computer, used to write and upload computer code to the physical board. The Arduino platform has become quite popular with electronics, the Arduino does not need a separate piece of hardware (called a programmer) in order to load new code onto the board, simply uses an USB cable. Additionally, the Arduino IDE uses a simplified version of C++. The Arduino Uno is a microcontroller board based on the ATmega328. It has 14 digitalinput/output pins (of which 6 can be used as PWM outputs), 6 analog inputs, [33] Fig 5 shows an Arduino uno board.

Fig 5 Arduino Uno

- NRF24L01 Transceiver Module

NRF24L01 is a single chip radio transceiver for the worldwide 2.4 - 2.5 GHz ISM band and which can operate with baud rates from 250 kbps up to 2 Mbps. If used in open space and with lower baud rate its range can reach up to 800 meters (line of site). Figure 6 shows the NRF24L01 Transceiver Module [18].

Figure 6: NRF24L01 Module

This chip will be connected with the Arduino Uno board used in the project to send and receive the data wireless.
The chip has eight pins. Three of these pins are for the SPI communication and they need to be connected to the SPI pins of the Arduino, however each Arduino board has different SPI pins. The pins CSN and CE can be connected to any digital pin of the Arduino board and are used for setting the module in standby or active mode, as well as for switching between transmit or command mode. The last pin is an interrupt pin which does not have to be used. Table 1 shows pin function and how to connect the pins to the Arduino Uno board.

Table 1: NR24L01 Pin

Pin	Name	Pin Function	Description	Wiring to Arduino Uno
1	GND	power	Ground	GND
2	VCC	Power	Power Supply	3.3V
3	CE	Digital Input	Chip Enable Activates RX or TX mode.	9
4	CSN	Digital Input	SPI Chip Select	10
5	SCK	Digital Input	SPI Clock	13
6	MOSI	Digital Input	SPI Slave Data Input	11
7	MISO	Digital Output	SPI Slave Data Output	12
8	IRQ	Digital Output	Maskable interrupt pin	-

- Sensors

In this study, three sensors are used for home automation: a Light dependent resistor (LDR) sensor, DS18B20 temperature Sensor, and MQ2 for gases. DS18B20 temperature Sensor is sealed digital temperature probe can precisely measure temperatures in wet environments with a simple 1-Wire interface as shown in figure 7. The DS18B20 provides 9 to 12-bit (configurable) temperature readings over a 1-Wire interface, so that only one wire (and ground) needs to be connected from a central microprocessor [6].

Figure 7: Temperature Sensor

The MQ2 Gas sensor can detect or measure gasses such as LPG, Alcohol, Propane, Hydrogen, Butane, CO and even methane. The module version of this sensor as shown in figure 8 comes with a Digital Pin which makes this sensor to operate even without a microcontroller. When measuring the gas in ppm the analog pin has to be used. The analog pin is also TTL driven and works on 5V and, hence, can be used with most common microcontrollers. [7].

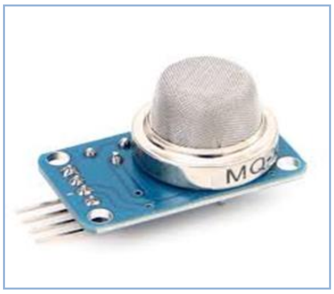

Figure 8: MQ-2 sensor

An LDR is a component that has a (variable) resistance which changes with the light intensity that falls upon it. This allows them to be used in light sensing circuits, as show in figure 9. It can be used with microcontroller development platforms such as Arduino but should have to use a voltage

Figure 9: LDR sensor

- Receivers

A buzzer is a device which makes a buzzing or beeping noise figure 10 shows the electronic.

The LED is a semiconductor light source that emits light when current flows through it.
Fan / Relay use fan & relay to control the temperature. Figure (4.11) shows the relay and fan.

Figure 10: Relay & Fan

V. THE FRONT PANEL

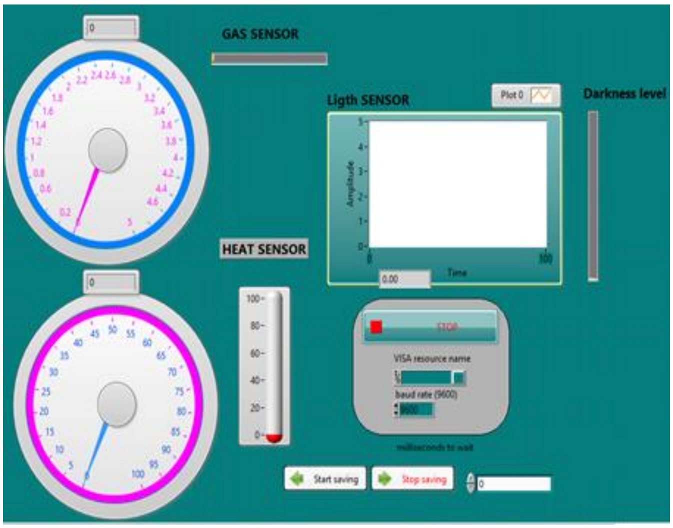

Figure 11: Front panel design

The front panel contains two gauges one of them representing the obtained data from gas sensor, the other representing the obtained data from temperature sensor. In addition, it contains the horizontal progress bar to representing the data obtained from the gas sensor and a thermometer to representing the temperature obtained from the temperature sensor. Also contains a chart representing the (light intensity) that obtained from the LDR sensor and the vertical progress bar representing (the intensity of darkness).
In addition, buttons related to the NI-VISA and buttons related to the database designed, including a button to specify the data recording time in milliseconds and a button to record data and another to stop data recording.

VI. Final form of the project

Implement data acquisition system using wired and wireless communication.

- **Send and Receive data via wireless**

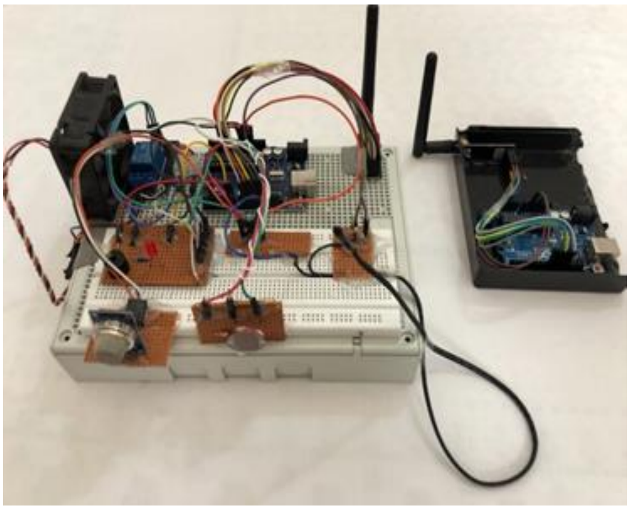

Figure 12: Final form circuit to Send and receive data via wireless

- **Send and Receive data via wired**

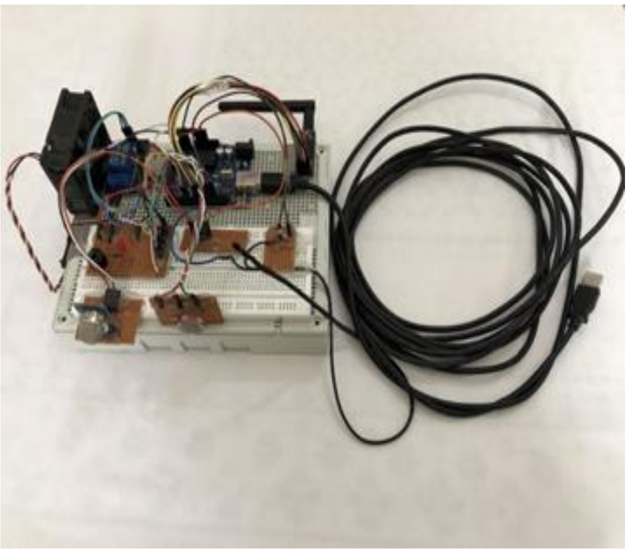

Figure 13: Final form circuit to send and receive data via wired

VII. RESULTS

In this section, results will be illustrated by using LabVIEW program to simulate the data acquired from three sensors (temperature, light intensity, gas) and represent them in a graphical interface which is easier for the user to read and deal with. The performance of wireless and wired communications can be clarified and a detailed comparison has made between them.

- **Comparison of data acquired using wired and wireless communications based on reference measurements**

In this comparison, there was the possibility of measuring different temperatures at the same conditions by using a laboratory thermometer, recording them as reference temperatures and comparing the temperatures readings obtained through the wireless and wired transmission based on the reference temperatures.

The following table 2 shows absolute results of the temperatures obtained from the laboratory thermometer and temperature sensor obtained through wired and wireless transmission at distance 4.5meters.

The average difference between the temperature of the laboratory thermometer and the temperature sensor in the wireless transmission is 3.32°C, while the average difference between the temperature of the laboratory thermometer and the temperature sensor in the wire transmission is 4oC.

It is possible to reduce the difference by 3.32°C through the LabVIEW program for the reliability of the accuracy of the result

The average difference of data obtained by wired and wireless transmission is 0.7°C. It turns out that recorded temperature in wired transmission is less than the recorded temperature in the wireless transmission, due to the loss of cable. In this comparison, it was not possible to measure the intensity of light and gas because laboratory measurement devices were not available.\

Table 2: The practical measurements

Data Acquired	Reference measurement device	Reference measurements	wireless measurements	wired measurements
Temperature	Laboratory thermometer	25.8°C	22.7°C	21.7°C
		22.5°C	20.0 °C	19.4°C
		25.1°C	21.4°C	20.9°C
		28.3°C	24.7°C	24.0°C
		30.3°C	26.6°C	26.0°C
Gas	-	-	0.05v	0.06v
Light intensity	-	-	4.5v	4.8v

.

- **Comparison of data acquired using wired and wireless communications based on database designed**

The data storage time was determined in each second. Initially, a change was made in the gas ratio, where the change could be noticed directly from the front panel. Another change was made in the intensity of the light, and finally, the change was made in the temperature.The data obtained and collected from three sensors were stored in the designed database; these changes are made twice, through wired and wireless connections, then the results between them are compared. Figure 14 and Figure 15 show the data obtained during wireless and wired communication respectively. 10 results are displayed for each sensor taken in 10 seconds. It can't be relied upon because the changes that occurred to the physical variables to be measured were not under the same conditions.

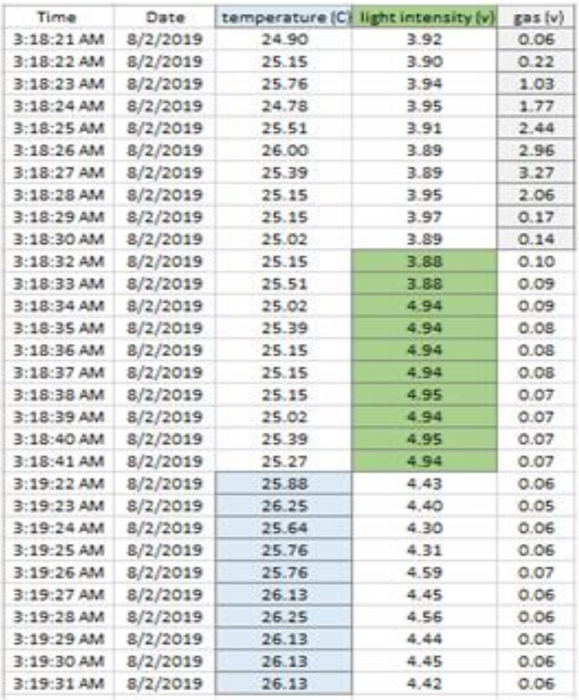

Time	Date	temperature (C)	light intensity (v)	gas (v)
3:18:21 AM	8/2/2019	24.90	3.92	0.06
3:18:22 AM	8/2/2019	25.15	3.90	0.22
3:18:23 AM	8/2/2019	25.76	3.94	1.03
3:18:24 AM	8/2/2019	24.78	3.95	1.77
3:18:25 AM	8/2/2019	25.51	3.91	2.44
3:18:26 AM	8/2/2019	26.00	3.89	2.96
3:18:27 AM	8/2/2019	25.39	3.89	3.27
3:18:28 AM	8/2/2019	25.15	3.95	2.06
3:18:29 AM	8/2/2019	25.15	3.97	0.17
3:18:30 AM	8/2/2019	25.02	3.89	0.14
3:18:32 AM	8/2/2019	25.15	3.88	0.10
3:18:33 AM	8/2/2019	25.51	3.88	0.09
3:18:34 AM	8/2/2019	25.02	4.94	0.09
3:18:35 AM	8/2/2019	25.39	4.94	0.08
3:18:36 AM	8/2/2019	25.15	4.94	0.08
3:18:37 AM	8/2/2019	25.15	4.94	0.08
3:18:38 AM	8/2/2019	25.15	4.95	0.07
3:18:39 AM	8/2/2019	25.02	4.94	0.07
3:18:40 AM	8/2/2019	25.39	4.95	0.07
3:18:41 AM	8/2/2019	25.27	4.94	0.07
3:19:22 AM	8/2/2019	25.88	4.43	0.06
3:19:23 AM	8/2/2019	26.25	4.40	0.05
3:19:24 AM	8/2/2019	25.64	4.30	0.06
3:19:25 AM	8/2/2019	25.76	4.31	0.06
3:19:26 AM	8/2/2019	25.76	4.59	0.07
3:19:27 AM	8/2/2019	26.13	4.45	0.06
3:19:28 AM	8/2/2019	26.25	4.56	0.06
3:19:29 AM	8/2/2019	26.13	4.44	0.06
3:19:30 AM	8/2/2019	26.13	4.45	0.06
3:19:31 AM	8/2/2019	26.13	4.42	0.06

Figure 14: Database for wireless communication

Time	Date	temperature (C)	light intensity (v)	gas (v)
3:22:54 AM	8/2/2019	24.54	3.95	0.84
3:22:55 AM	8/2/2019	24.41	3.99	1.40
3:22:56 AM	8/2/2019	24.66	4.00	1.75
3:22:57 AM	8/2/2019	24.66	3.95	1.71
3:22:58 AM	8/2/2019	24.66	3.98	1.66
3:22:59 AM	8/2/2019	24.53	4.00	1.96
3:23:00 AM	8/2/2019	24.53	3.98	1.68
3:23:01 AM	8/2/2019	24.78	3.97	2.03
3:23:02 AM	8/2/2019	24.66	3.99	2.41
3:23:03 AM	8/2/2019	24.66	4.00	2.73
3:23:34 AM	8/2/2019	24.29	3.86	0.07
3:23:35 AM	8/2/2019	24.17	4.95	0.07
3:23:36 AM	8/2/2019	24.54	4.95	0.06
3:23:37 AM	8/2/2019	24.29	4.95	0.06
3:23:38 AM	8/2/2019	24.29	4.95	0.06
3:23:39 AM	8/2/2019	24.29	4.95	0.05
3:23:40 AM	8/2/2019	24.66	4.96	0.05
3:23:41 AM	8/2/2019	24.54	4.96	0.05
3:23:42 AM	8/2/2019	24.17	4.95	0.05
3:23:43 AM	8/2/2019	24.41	4.95	0.05
3:24:17 AM	8/2/2019	24.90	4.53	0.05
3:24:18 AM	8/2/2019	25.39	4.57	0.05
3:24:19 AM	8/2/2019	25.39	4.32	0.04
3:24:20 AM	8/2/2019	25.88	4.59	0.04
3:24:21 AM	8/2/2019	26.86	4.48	0.05
3:24:22 AM	8/2/2019	28.08	4.55	0.04
3:24:23 AM	8/2/2019	28.69	4.62	0.04
3:24:24 AM	8/2/2019	28.57	4.53	0.04
3:24:25 AM	8/2/2019	28.44	4.64	0.05
3:24:26 AM	8/2/2019	28.32	4.45	0.04

Figure 15: Database for wired communication

Next, the same conditions were maintained to compare the data obtained from the sensors at a distance of 4.5 meters. It was found that the results of the wired transmission were less accurate than the results of the wireless transmission .This is due to the loss of the signal in the cable.

In this case, the reliability of the accuracy of results in the wireless transmitter is better as shown in figures 16 and figures 16. However, this does not mean that the wireless connection is better than the wired connection; both of their characteristics will be compared and verified.

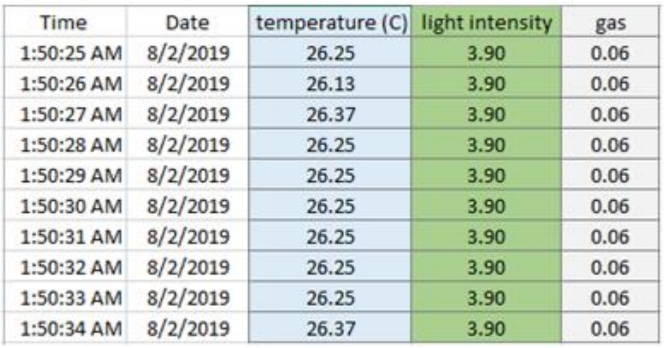

Time	Date	temperature (C)	light intensity	gas
1:50:25 AM	8/2/2019	26.25	3.90	0.06
1:50:26 AM	8/2/2019	26.13	3.90	0.06
1:50:27 AM	8/2/2019	26.37	3.90	0.06
1:50:28 AM	8/2/2019	26.25	3.90	0.06
1:50:29 AM	8/2/2019	26.25	3.90	0.06
1:50:30 AM	8/2/2019	26.25	3.90	0.06
1:50:31 AM	8/2/2019	26.25	3.90	0.06
1:50:32 AM	8/2/2019	26.25	3.90	0.06
1:50:33 AM	8/2/2019	26.25	3.90	0.06
1:50:34 AM	8/2/2019	26.37	3.90	0.06

Figure 16: Data base for wireless communication

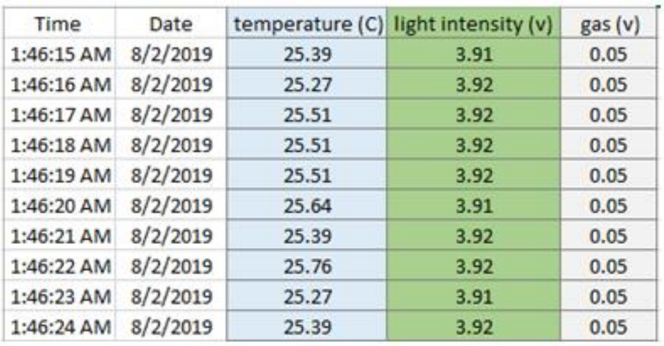

Time	Date	temperature (C)	light intensity (v)	gas (v)
1:46:15 AM	8/2/2019	25.39	3.91	0.05
1:46:16 AM	8/2/2019	25.27	3.92	0.05
1:46:17 AM	8/2/2019	25.51	3.92	0.05
1:46:18 AM	8/2/2019	25.51	3.92	0.05
1:46:19 AM	8/2/2019	25.51	3.92	0.05
1:46:20 AM	8/2/2019	25.64	3.91	0.05
1:46:21 AM	8/2/2019	25.39	3.92	0.05
1:46:22 AM	8/2/2019	25.76	3.92	0.05
1:46:23 AM	8/2/2019	25.27	3.91	0.05
1:46:24 AM	8/2/2019	25.39	3.92	0.05

Figure 17: Data base for wired communication

- **Comparisons between wired and wireless communications based on the data acquired**

There are many characteristics for both wired and wireless communication, table 3 illustrates the most important of these . Some characteristics has been tested and confirmed.

Table 3: a comparisons between wired and wireless communication

Sr.No	Characteristics	Wired Networks	Wireless Networks
1.	User connectivity	Connectivity is possible only to or from those physical locations where the network cabling extends.	Connectivity is possible beyond the bounds of physical network cabling.
2.	Mobility	Limited (because it operates only on connected computers linked with the network).	Outstanding (enable wireless user to connect to network and communicate to other users any time.
3.	Security	Good	Weak
4.	Reliability	High	Reasonably high (because if a major section such as the router, breaks down the whole network will be affected.
5.	Speed and Bandwidth	High Up to 100mbps	Low Up to 54mbps
6.	Connection setup time	Less	More
7.	Cables	Ethernet, copper and optical fibers.	Works on radio waves and microwave
8.	Quality of service	Better	Poor (Delays and longer connection set up times)

Conclusion

This project focuses on the performance of wired and wireless communication systems and a comparison between them. Therefore, both Physical and wireless transmission media have been studied. In this paper, Arduino appeared to be a flexible and efficient environment to implement the data acquisition system. Therefore, the transfer data have been studied and using wired and wireless communications, have been transmitted and dealt with by the LabVIEW program. The results confirm that the performance of a wireless communication system is better in terms of accuracy of the results and mobility, but the performance of wired communication system is better in terms of bandwidth, security and reliability. As a reference, the results of data acquired based on wired and wireless transmissions were included in the examination.

REFERENCES

[1] Wired vs. Wireless Technologies for Communication Networks in Utility Markets, (accessed on the 18 June 2019 available at: https://www.utilityproducts.com/testmeasurement/article/16002788/wired-vswireless- technologies-for-communication-networks-in-utility-markets

[2] What does Data Transfer mean? , (accessed on the 20 June 2019, available at: https://www.techopedia.com/definition/18715/data-transfer).

[3] Jafaru ibrahim, tonga agadi danladi and musefiu aderinola. "comparative analysis between wired and wireless technologies in communications: a review." int. c (2017).

[4] Arduino Uno, (accessed on the 12 May 2019, available at: https://store.arduino.cc/arduino-uno-rev3)

[5] NRF24L01 Data sheet, (accessed on the 12 may 2019 available at: https://pdf1.alldatasheet.com/datashepdf/view/90046/ETC/NRF2401.html).

[6] S.Kumari, G.Rathi, P.Attri, M.Kumar.”Types of Sensors and Their Applications .”International Journal of Engineering Research and Development (2014):72-85.

[7] Temperature sensor datasheet, (accessed on the 16 May 2019, available at: http://www.hobbytronics.co.uk/ds18b20-waterproof-temperature- sensor).

[8] MQ-2 gas sensor datasheet, (accessed on the 16 May 2019, available at: https://shop.edwinrobotics.com/sensors/1422-mq2-gas-sensor-module.html).

[9] LDR datasheet, (accessed on the 16 May 2019, available at: https://components101.com/ldr-datasheet).

[10] Maxim Integrated. Application Notes. Available online: http://www.maximintegrated.com/en/ app-notes/index.mvp/id (accessed on 16 September 2014).

[11] ATMEL. Available online: http://www.atmel.com/images/avr_3_04.pdf (accessed on 16 September 2014).

New design of Flyback micro inverter for PV Applications

Elyes Mbarek[#1], Hamed Balloumi[*2], Ferid Kourda[#3]

[#]Universite de Tunis El Manar, ENIT-L.S.E, BP 37, 1002 Tunis Ie Belvedere, Tunis, Tunisia

[1]`Mbarek.Elyes@gmail.com`
[3]`hamed.balloumi@enit.rnu.tn`
Ferid.kourda@enit.utm.tn

***Abstract*— this paper, New design of micro inverter for PV Applications. The proposed micro inverter system is used to connect the PV panel to the grid with achieving maximum Power Point Tracking (MPPT) control. Flyback micro inverter operates in DCM and injects a sinusoidal current into the grid with unity power factor. A complete system has been simulated using PSIM program**

***Keywords*— Single-Stage, Grid-Connected, Micro inverter, Flyback, DCM, MPPT**

I. INTRODUCTION

Solar energy presents a promising source for electricity generation. Inverter presents the central element of the solar photovoltaic conversion chain. Different solutions are currently in the exploitation or development phase. Micro inverters present an interesting solution to develop for small powers PV systems, low cost and extensible solution that can increase the installed photovoltaic power system

II. PROPOSED MICRO INVERTER

Fig.1 presents how the proposed Flyback micro inverter performs energy from DC side to the AC grid site. Micro inverter includes different parts:

-High frequency transformer with three windings: one primary and two secondary

- A primary controlled switch S1 is modulated in high frequency, S1 duty cycle should be made to vary throughout the AC voltage line cycle.
- The two secondary controlled switches placed in each secondary winding SV2 and SV3 are modulated with grid frequency. Each of them is able to transfer energy to the AC side during a utility grid half cycle and they ensure an AC output wave form synchronized with the grid.
- LC filter is used to filter the output produced by the rest of the converter; so that the appropriate final output current is produced and fed to the grid.

The control bloc of Flyback micro inverter includes:

- Phase locked loop PLL bloc that generates signal, control each controlled switch SV2 and SV3
- A maximum power point extractor MPPT bloc that calculates the duty cycle Dmax in order to extract the maximum power from photovoltaique panel

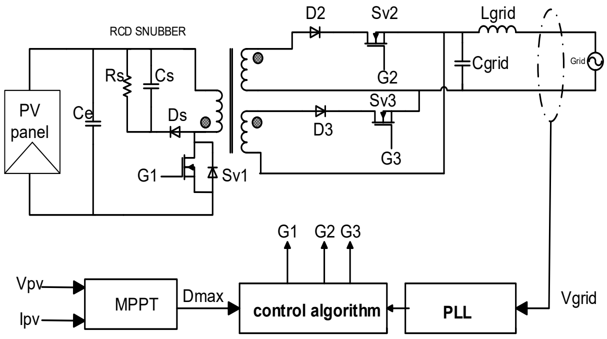

Fig. 1 Proposed Flyback micro inverter

The switching sequence of each semiconductor can be observed in Fig.2.

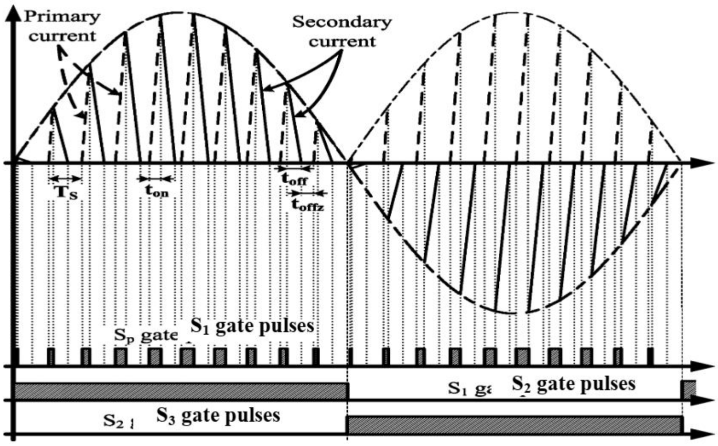

Fig.2 switching sequence of SV1, SV2 and SV3

ISSN 1737-9334

III. OPERATION MODE OF FLYBACK MICRO INVERTER IN DCM MODE

When the primary switch SV1 is on; the primary current I1 in the primary winding of transformer increases, the energy coming from the solar panel is stored in the magnetizing inductance Lm of the HF transformer.

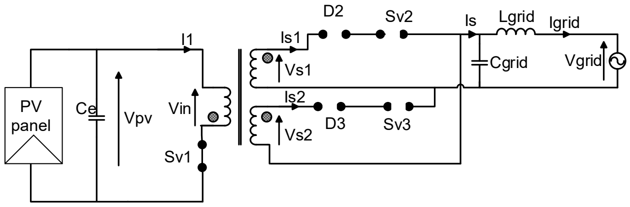

Fig4. Micro inverter when primary switch Sv1 is on

The voltage at the primary winding of transformer is:

$$Vin = NVg(t) = Lm\frac{dI1(t)}{dt} \qquad (1)$$

When N is the turns ratio (N=Np/Ns), Lm magnetizing inductance.
The pic value of primary current I1max can be expressed

$$I1max = \frac{Vin.dmax}{Lm.fs} \qquad (2)$$

The ton_max can be expressed as:

$$ton_{max} = dmax.Ts = \frac{dmax}{fs} \qquad (3)$$

When dmax is the maximum duty cycle and fs the switching frequency of primary switch SV1, The AC grid voltage can be expressed as:

$$Vg(t) = Vgmax.sin(wg.t) \qquad (4)$$

WHEN VGMAX=325V AND WG=314RAD/S

When SV1 is off, the stored energy in the HF transformer will transfer to the grid through the output rectifier D2 and the controlled switch SV2 if the grid voltage Vgrid is positive.

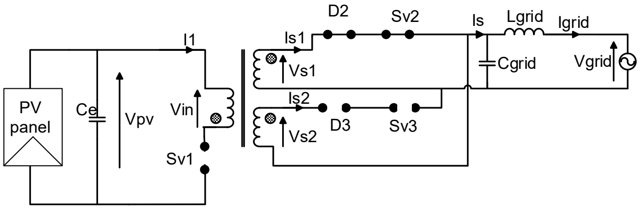

Fig5. Micro inverter when primary switch Sv1 is off

The stored energy in the HF will transfer to the grid, through the output rectifier D3 and control switch SV3 when grid voltage Vgrid is negative.

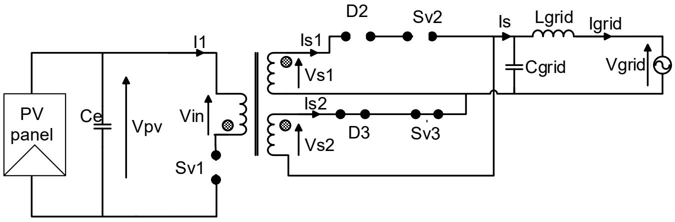

Fig.6 Micro inverter when primary switch Sv1 is off

The proposed flyback micro inverter operates in discontinuous conduction mode (DCM) due to its simplicity of control
The maximum duty cycle can be expressed:

$$dmax \leq \frac{1}{\frac{Vin}{NVgmax}+1} \qquad (5)$$

The magnetique inductance Lm can be expressed

$$Lm = \frac{1}{2}(\frac{Vin}{Vgmax})^2\frac{dmax^2 Vgmax^2}{fs*Lm} \qquad (6)$$

IV. SIMULATION RESULTS

The proposed converter was simulated using PSIM software. The converter was implemented with following specifications:

Parameters	**value**
Rated output power Ps	150W
Switching frequency fs	60Khz
Magnetizing inductance Lm	6.65µH
PV input voltage Vpv	30V
Grid frequency fgrid	50Hz

Input capacitor Ce	10µf
Turn ratio of transformer N	0.11
Output filter capacitor	300nf
Output filter inductance	2mH

Fig.7 shows voltage value across SV1 switch. The voltage is zero for the conduction phase of the transistor. The overvoltage reaches 120V caused by leakage inductance of the transformer

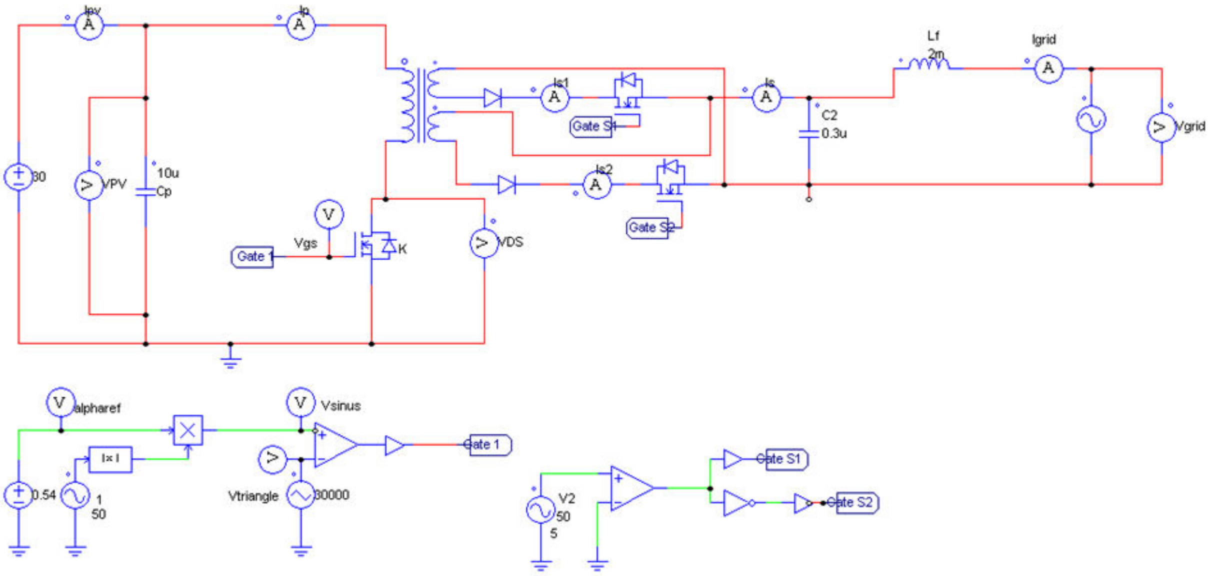

Fig.7 inverter simulating using PSIM software

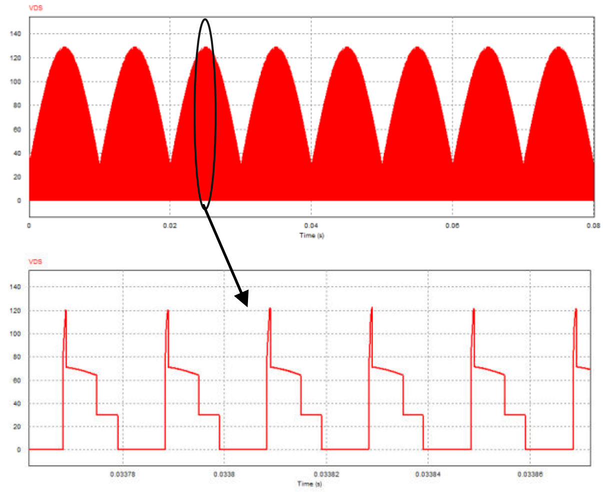

Fig.8 voltage value across SV1 switch

Fig.9 show the primary transformer current Ip. The current reaches 40A ,when the primary switch SV1 is on

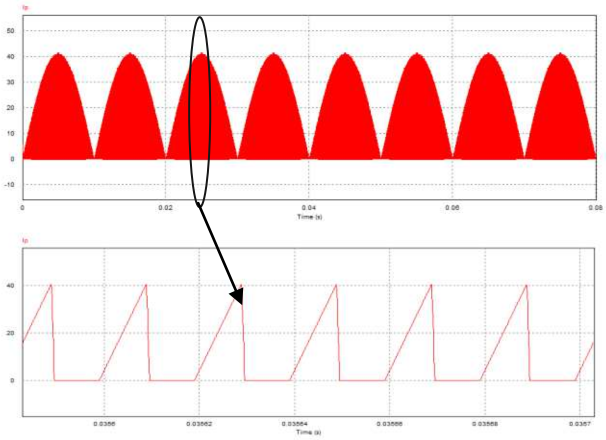

Fig.9 primary transformer current Ip

Fig.9 Shows the secondary currents IS and IS2 before filtering for the case of 150W constant active power transfer. Fig.10 and Fig.11 show grid injected current and grid voltage for the case of 150W

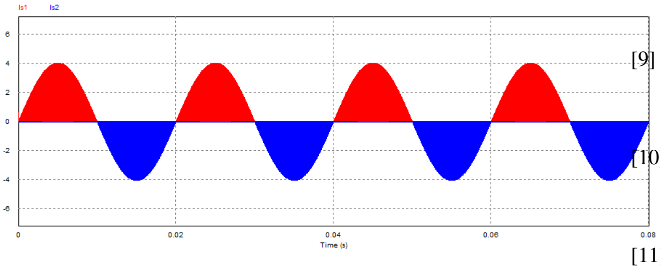

Fig.9 secondary current IS1 and IS2

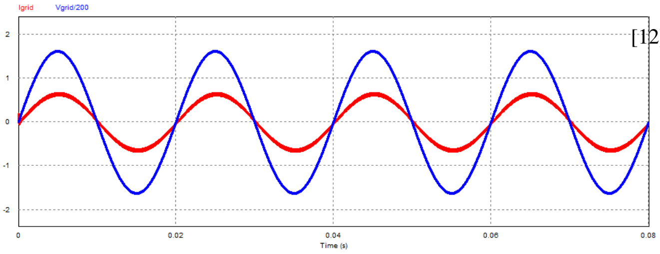

Fig.10 output voltage and current

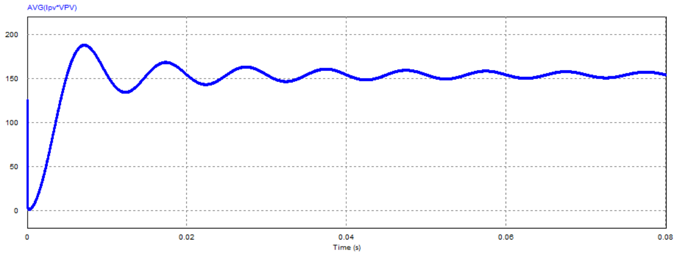

Fig.11 injected power

A. *References*

[1] D. Meneses, F. Blaabjerg, O. Garcia and J. Cobos, “Review and comparison of step-up transformer less topologies for photovoltaic ac-module application,” IEEE Trans. Power Electron., vol. 28, no. 6, pp. 2649 -2662, Jun. 2013.

[2] T. Freddy, N. A. Rahim, W. P. Hew and H. S. Che, “Comparison and Analysis of Single-Phase Transformerless Grid-Connected PV Inverters,” IEEE Trans. Power Electron., vol. 29, no. 10, pp. 5358 - 5369, Oct. 2014.

[3] A. Ch. Kyritsis, E. C. Tatakis and N. P. Papanikolaou, “Optimum design of the current-source Flyback inverter for decentralized grid-connected photovoltaic systems,” IEEE Trans. Energy Conv., vol.23, no.1, pp. 281-293, Mar. 2008.

[4] Z. Zhang, X.-F. He and Y.-F. Liu, “An optimal control method for photovoltaic grid-tied-interleaved Flyback micro inverters to achieve high efficiency in wide load range,” IEEE Trans. Power Electron., vol. 28, no. 11, pp. 5074–5087, Nov. 2013.

[5] A. C. Nanakos, E. C. Tatakis and N. P. Papanikolaou, “A weighted-efficiency-oriented design methodology of flyback inverter for ac photovoltaic modules,” IEEE Trans. Power Electron., vol. 27, no. 7, pp. 3221- 3233, Jul. 2012.

[6] H. Hu, S. Harb, N. H. Kutkut, Z. J. Shen and I. Batarseh, “A single-stage micro inverter without using eletrolytic capacitors,” IEEE Trans. Power Electron., vol. 28, no. 6, pp. 2677–2687, Jun. 2013.

[7] Y. Li and R. Oruganti, “A Low Cost Flyback CCM Inverter for AC Module Application,” IEEE Trans. Power Electron., vol. 27, no. 3, pp. 1295–1303, Mar. 2012.

[8] T. V. Thang, N. M. Thao, J.-H. Jang and J.-H. Park, “Analysis and design of grid-connected photovoltaic systems with multiple-integrated converters and a pseudo-dc-link inverter,” IEEE Trans. Ind. Electron., vol.61, no. 7, pp. 3377–3386, Jul. 2014.

[9] F. F. Edwin, W. Xiao and V. Khadikar, “Dynamic modeling and control of interleaved flyback module integrated converter for PV power applications,” IEEE Trans. Ind. Electron., vol. 61, no. 3, pp. 1377–1388,Mar. 2014.

[10] G. C. Christidis, A. C. Nanakos and E. C. Tatakis, “Hybrid Discontinuous/Boundary Conduction Mode of Flyback Microinverter for AC-PV Modules,” IEEE Trans. Power Electron., vol. 31, no. 6, Jun. 2016.

[11] G. S. Dimitrakakis, E. C. Tatakis and E. J. Rikos, “A semiempirical model to determine HF copper losses in magnetic components with nonlayered coils,” IEEE Trans. Power Electron., vol. 23, no. 6, pp. 2719-2728, Nov. 2008.

[12] K. Venkatachalam, C. R. Sullivan, T. Abdallah and H. Tacca, “Accurate prediction of ferrite core loss with non-sinusoidal waveforms using only Steinmetz parameters,” Proc. IEEE Comput. Power Electron. Conf., 2002, pp. 36-41.

Smart Secure Door Lock Based on Machine Learning

Abdelmadjid Recioui
Laboratory of Signals and Systems, Institute of Electrical and Electronic Engineering, University M'hamed Bougara of Boumerdes, Boumerdes, Algeria.
Boumerdes, Algeria.
a_recioui@univ-boumerdes.dz

Abstract_ In this work, a smart secure door lock for home automation is proposed. A smart door lock is a piece of equipment that uses digital information in the form of a secret code or a personalized smart phone application to authenticate users allowed to open a door instead of the conventional key system. In the system, a microcontroller embedded into the lock acts as the main control unit of the door. This smart lock operates on Bluetooth technology to communicate with a smart phone Bluetooth personal application. The two devices share encrypted data to control the door wirelessly and neural networks are used to match the codes. In addition, the application uses a machine learning algorithm to customize the way the door locks and unlocks for maximum security. Users allowed to access a given area can be added or removed within the application. Only one person can perform this task (the master) so as to avoid adding anyone without permission. This work find its applicability in critical places with a limited access such as banks and data centers. Furthermore, for people who might not be able to use a smart phone, a keypad has been integrated to the system for secret code control with an LCD display.

Keywords: Home Security, Machine learning, smart applications, neural networks.

1. INTRODUCTION

How can door hardware make every one life easier? What if you never had to worry if your kids remember to unlock the door on their way out? What if you are not obliged to handle a metal key in your pocket and take wherever you go? And let not talk about when you lose it or when you want to pass it to someone else (key copy), everyday life gets easier with the technology developed (smart door lock).

The system was designed to lock and unlock the door using smartphone; it is easy to install. While providing a high security rating, once installed the system pairs easily with your smartphone to provide a comfortable access using a secure connection.

The android app is easy to setup, manage and use every day, it uses a new developed machine learning technology, which provide high security and performance. It is based on a pass-sketch to control the lock. An additional advantage is that different users can control the door lock using different sketches and change it easily. The first one uses the system is "the master" device it can add up to 10 user with the possibility of removing any device from the devices list.

Now your smart phone is your key, you can pass your new key to others just bay charring it using different chare options on the app or just download it directly from AppStore.

The system is based on Bluetooth communication from the mobile device to microcontroller, which is the brain of the device it manages and sends all commend signals to control the hardware part.

The project includes another alternative and efficient way to control the door lock. A keypad system is used to enter the door password, which is made of 4 digits to open the dooronce the device is turned on by the main switch.In addition, you can set the auto-close mode after you enter, or you can just turn the system off, the door will be locked after 5seconds automatically. An LCD display is interfaced to enable the user communication to the system; it will display the information only if the main switch powers it, and so it is always off. The most important reason for this decision is saving power. A buzzer and a couple of LEDs are used for indication purposes.

2. SYSTEM STRUCTURE

As shown in figure 1, the system consists of several parts. The mobile device can be any device; smartphone, tablet… etc. – in general, any device able to Communicate via Bluetooth protocol, of course with a preinstalled android app that can manage the system easily. A Bluetooth module is used to wirelessly pass the data to the system. It uses UART protocol in order to send data to the embedded system. Once the data reaches the MCU it is received, decoded executed and new control signals are generated to determine the state of the outputs, the servo is used to control the opening and the closing of the door according to the coming signals from the MCU; The LCD display is used to see whether the entered password from the keypad is correct or not.

ISSN 1737-9334

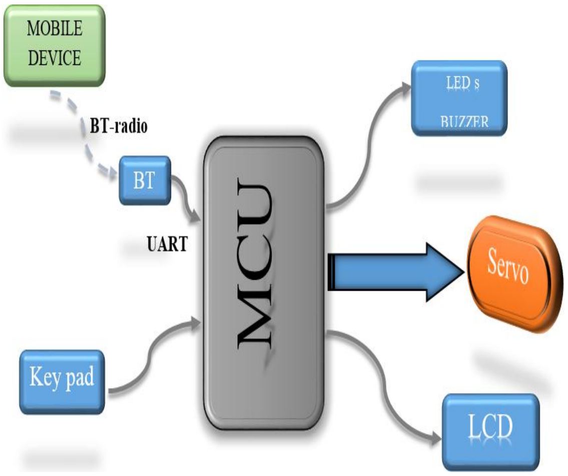

Figure 1: Smart Lock System block diagram

It is also used to interface with the project to show lock status and different options and choices the system offers. The keypad, which is one of the most important input devices used in electronics engineering is the easiest and the cheapest way to give commands or instructions to an electronic system. Whenever a key is pressed in the keypad module, the MCU detects it and shoes the corresponding effects on the LCD.A buzzer and some LEDs are used for indication purposes.

3. IMPLEMENTATION & DESIGN

3.1 Hardware design

In order to setup the project hardware ,the following equipment are needed:

- Arduino Uno board with the ATmega328p microcontroller.
- HC-05 BT module.
- 4x4 KP matrix.
- 16x2 LCD.
- SM (reference).
- Ordinary lock.
- Smart phone (MD) with preinstalled android app.
- Breadboard.
- Buzzer, few Resistors & LEDs.
- Power supply.

Understanding the above equipment connection is divided into four main part as follows:

- **LCD, I^{2}C module & MCU**

To ease the LCD to MCU connection an I^{2}C module has been developed in order to replace the direct wiring, which is made with at least 12 wires, with a 4 wire connection as shown in figure 3.1.

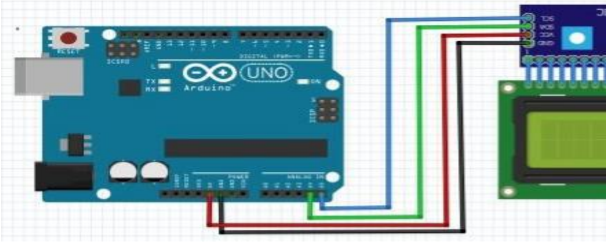

Figure 2 LCD & MCU connection.

The I^{2}C module has four pins: V_{CC}, GND, and the SDA and SCL signals. As described in the theoretical part. The Arduino provides the A4 and A5 pins that are connected to SDA and SCL signals respectively, for I^{2}C connection protocol. Each pin in the module is connected to the pin shares the same name in LCD.

- **MCU & keypad**

The 4×4 keypad is connected with the Arduino as given in the bellow wiring-diagram. The pins are directly connected to any digital/Analogue in/out pins of the Arduino; this keypad has a pin no. written on its connector.

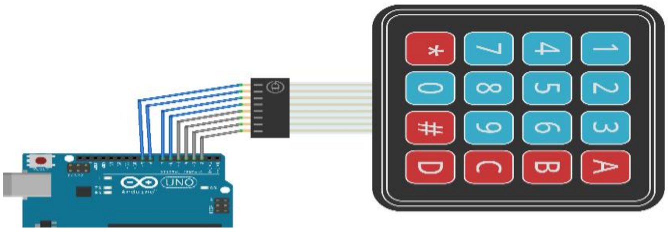

Figure 3 keypad & MCU connection.

In this circuit,multiplexing techniqueis required to interface keypad to enter the password in the system. However, in this Arduino projectwe have used keypad library so we do not need to make any multiplexing code for this system. We only need to use keypad library for providing input.

- **MCU & HC-05**

To control the SM using the smart phone, key signals are sent to the microcontroller via the Bluetooth module HC- 05, so that it is well connected to both devices in order to guarantee a secure and good communication between the system parts; however, it is connected wirelessly with the MD and physically with the UNO as shown in figure 3.3.

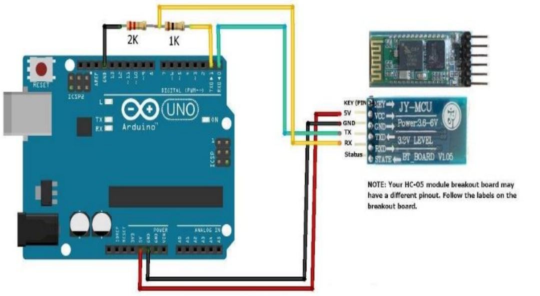

Figure 4 HC-05 & MCU connection.

The Bluetooth module uses the SPP (i.e. serial port protocol) to communicate with Arduino board,the particular module that we are using (HC 05) can be powered from 3.6 to 6 volts, because it comes on breakout board, which contains a voltage regulator. However, the logic voltage level of the data pins is 3.3V. Therefore, the line between the Arduino TX (Transmit Pin, which has 5V output) and the Bluetooth module RX (Receive Pin, which supports only 3.3V) needs to be connected through a voltage divider in order not to burn the module. On the other hand, the line between the Bluetooth module

TX pin and the Arduino RX pin can be connected directly because the 3.3V signal from the Bluetooth module is enough to be accepted as a high logic at the Arduino Board.

- **MCU & Servomotor**

The servomotor can be connected to the Arduino via its three pins: V_{CC}, GND and PWM pin. The PWM pin can be connected to any digital pin on the Arduino. An example of a connection is shown in figure 3.4.

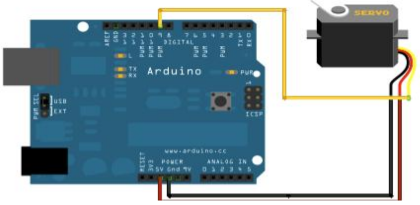

Figure 5 MCU and Servomotor connection.

After summing the previous parts and by selecting the appropriate pins connection the overall system sketch is shown in figure 3.5.

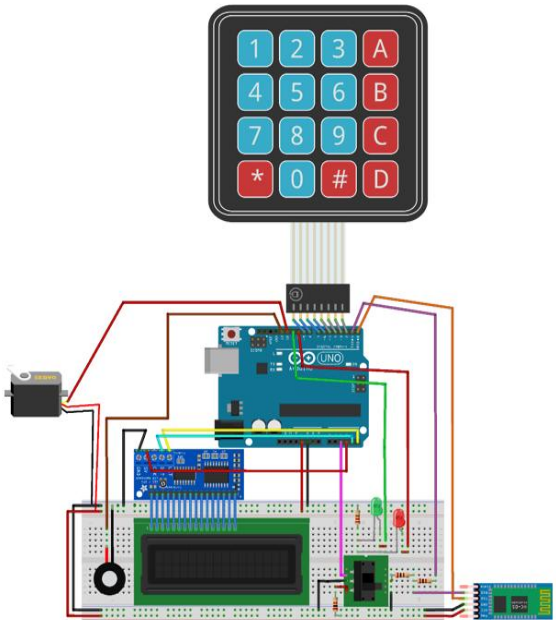

Figure 6The overall system connection.

Once the system circuit connections are completed, we are ready to design the second part of the project allows and determines the relationship between the MD & the MCU and that between the MCU and the other components.

3.2 Software design

3.2.1 MCU program implementation:

MCU application plays a significant role in the thesis work. It controls the two main parts of the project hardware by managing and processing the data coming from the **KP** and that from the **MD** via the **BT module;** depending on that control signals are generated to determine the display of **LCD** and the state of the lock by turning the **SM** either CW/CCW, also other control commends are sent to the LEDs and the Buzzer for indication purposes.

According to the description above the MCU has to executes a huge number of code lines and functions

- Receiving, decoding and executing data, and generating control signals
- Data processing (fetch & store).
- It possesses an intuitive graphical interface, which allows good utility of the device
- It manages the servo position, which is a good performance closed loop system.
- Controlling the indication parts (buzzer &LEDs).

→ ***Unlocking the door using the smartphone:***

- This part also is written in the loop function. Once the BT and smartphone are connected, we can send date to MCU to enable the control. Different data are sent and managed according to the following algorithm.

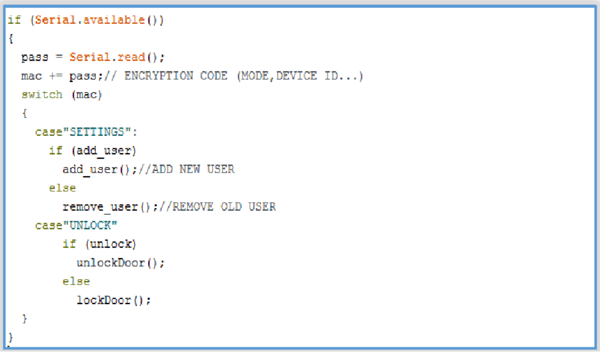

```
if (Serial.available())
{
  pass = Serial.read();
  mac += pass;// ENCRYPTION CODE (MODE,DEVICE ID...)
  switch (mac)
  {
    case"SETTINGS":
      if (add_user)
        add_user();//ADD NEW USER
      else
        remove_user();//REMOVE OLD USER
    case"UNLOCK"
        if (unlock)
          unlockDoor();
        else
          lockDoor();
  }
}
```

Figure 7 BT algorithm

- Each function has its own steps to do such as storing and removing data from the memory to add or remove users and the corresponding check for the existence of the device when locking or unlocking the door and so on.
- The password in both cases is saved in the EEPROM memory, which is a non-volatile i.e. the data is saved one ever the power is off so that we guarantee the same settings for the user in such rare cases.
- Now the program is ready, so when we will click the upload button, the program will automatically activate the Bluetooth communication. The HC-05 Bluetooth module will start to flash every two seconds, which indicates that the module is connect and we will be able to control the lock using our pre-installed android app in our smartphone.

3.2.2 Android application:

The app consists of only one and unique activity. It has been designed under the principles of Google's material. It uses a "RelativeLayout" [16] as a main layout. RelativeLayout displays its views in relative position to each other and itself.

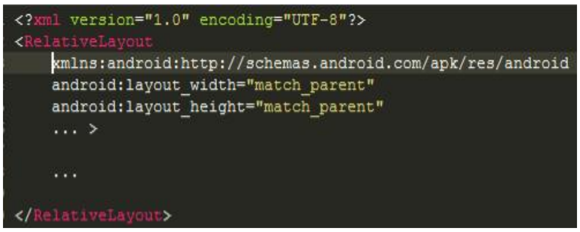

```
<?xml version="1.0" encoding="UTF-8"?>
<RelativeLayout
    xmlns:android:http://schemas.android.com/apk/res/android
    android:layout_width="match_parent"
    android:layout_height="match_parent"
    ... >

    ...

</RelativeLayout>
```

Figure 8 Example of declaring a RelativeLayout.

The activity itself is used to keep the Bluetooth connection with the HC-05. In fact, using different activities was extremely difficult and this because an android activity gets destroyed when another one in opened. When an activity is destroyed, the related variable to it gets destroyed too, and hence the Bluetooth connection is lost.

In order to overcome this problem, fragments has been used instead. Fragments are like reusable components or sub-activities. Afragment is used to control part of a screen, and can be reusedbetween screens.

As shown in the figure 3.18, three fragments has been created grouped in ViewPager [17]. Each fragment have its own layout, and hence UI. Each UI is responsible of triggering a GUI event (button clicks …).

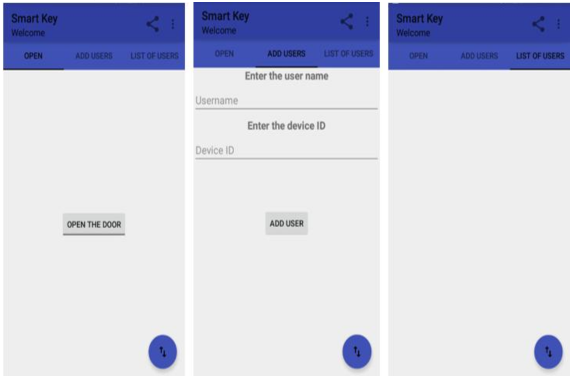

Figure 9 Android app and its different fragments.

The Bluetooth connection is handled by the main activity and therefore is never lost. Data can be sent or received within the context of the activity.

In order to communicate with HC-05, a Java class called "BluetoothConnectionService" has been implemented according to the android API documentation.

To start a connection, the Bluetooth of the smartphone should be paired first with the HC-05, and by clicking on the floating action button [18](the button in the bottom left corner) a connection is established. In order to do so, the paired Bluetooth device is retrieved. Passing this device variable to the "BluetoothConnectionService.java" the connection starts. The used code is shown in figure 3.19.

The next problem we faced is how to communicate between the fragments and the main activity? Indeed, even though the fragments are a part of their parent, they cannot access its variables and vice-versa. The behaviour has been adopted by the android developers in order not to violate the "Encapsulation Principle". But, why do we need to communicate between the activity and its children? In fact, the Bluetooth connection is hold by the activity, and the UI is hold by the fragments. In order to react to GUI events, the fragments must have access to the "BluetoothConnectionService.java" object class for sending and receiving data.

To get around this problem, a Java programming technique has been adopted: the Observer Pattern.

The **Observer pattern** is a software design pattern in which an object, called the **subject**, maintains a list of its dependents, called **observers**, and notifies them automatically of any state changes, usually by calling one of their methods. It is mainly used to implement distributed event handling systems, in "event driven" software. Most modern languages such as C# have built in "event" constructs which implement the observer pattern components, for easy programming and short code.

In the below UML diagram, the *subject* class doesn't update the state of dependent objects directly. Instead, *subject* refers to the *Observer* interface (*update()*) for updating state, which makes the *subject* independent of how the state of dependent objects is updated. The *Observer1* and*Observer2*classes implement the *Observer*interface by synchronizing their state with subject's state [19].

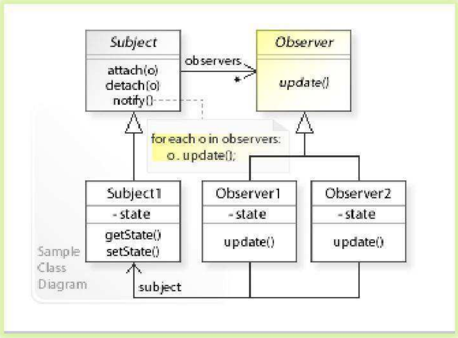

Figure 10UML diagram showing the workflow of the observer pattern.

The UML sequence diagram shows the run-time interactions:

The *Observer1* and*Observer2*objects call *attach (this)* on *Subject1* to register themselves. Assuming that the state of *Subject1* changes, *Subject1*calls *notify* () on itself.

notify () calls *update()*on the registered *Observer1* and *Observer2* objects, which request the changed data (*getState* ()) from *Subject1* to update (synchronize) their state [19].

Using this highly efficient technique, the fragments now can communicate with the activity, and update its state, whenever a GUI event occurs.

Accordingly, the activity reacts by sending or receiving data from the HC-05.

- **Fragments description:**

→ ***Fragment "Connect":***

This part of application is responsible for opening and closing the door. It consists only of one Button, called a Toggle button, meaning that it can toggle between an on and off state.

When clicking on the button, the device Bluetooth ID is sent to the HC-05. If ever this user is registered in to the device a message is sent back to confirm its membership. The code for sending is shown in figure (the code of receiving can be found in the appendix). Accordingly, the door opens or closes. The first person who uses the device is the "master", because there is no users before him/her.

.

→ ***Fragment "Add Users":***

Here, users can be added by the master by entering in the fields devoted, the name and the device Bluetooth address of the new user. When clicking on the "add" button, the current device ID is sent first to the UNO in order to check if the adder is the master. Indeed, only the master can add or remove users. If we get a positive answer the user's ID is sent back to the UNO, which retains it. The name field is used to display the list of users in the next fragment.

→ ***Fragment "List of user":***

This is the last fragment in which devices list get displayed. Here a similar problem to the activity has been met in the way of communicating the added user to the list. Effectively, the fragments cannot communicate with each other directly for programming principles. A similar solution has been adopted to solve the issue.

Users can be removed from the list on a long click on it. At the end of the click the position of that user is sent to the Uno which deletes it in turn.

Activity and fragment variables gets lost whenever the app process is killed. In reality even the list of users gets lost when the app is closed. In order to keep the list of the users permanently, it is saved in a hidden file to prevent it from being deleted by the user.

The application is also provided with a share button in its toolbar to share the app with other persons instead of being downloaded each time.

3.2.3 Machine learning:

This part will be really brief. It describes the way a convolutional neural networks can be used to classify a dataset of pictures.

Since implementing a CNN is very hard, we will be using the "Keras" library for deep learningwritten in Python.

The CNN test has been driven on the MNIST well-known dataset[] (a dataset of hand written digits as shown in figure 3.23), and since training a machine learning algorithm is an extremely computational task, a laptop has been used. Figure 3.24 shows a well commented code snippet that demonstrates "How the CNN is built".

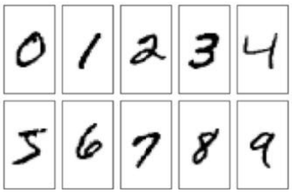

Figure 11 MNIST dataset sample.

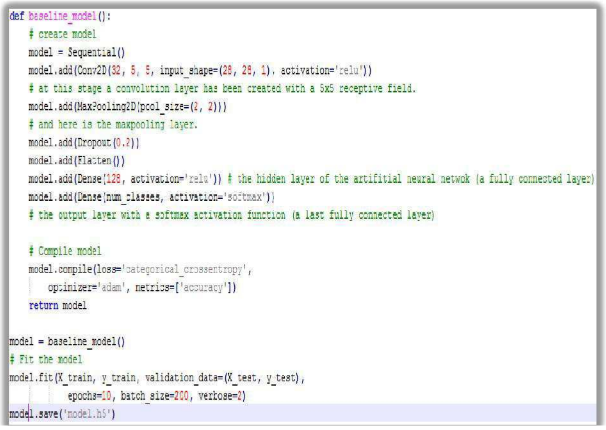

```
def baseline_model():
    # create model
    model = Sequential()
    model.add(Conv2D(32, 5, 5, input_shape=(28, 28, 1), activation='relu'))
    # at this stage a convolution layer has been created with a 5x5 receptive field.
    model.add(MaxPooling2D(pool_size=(2, 2)))
    # and here is the maxpooling layer.
    model.add(Dropout(0.2))
    model.add(Flatten())
    model.add(Dense(128, activation='relu')) # the hidden layer of the artifitial neural netwok (a fully connected layer)
    model.add(Dense(num_classes, activation='softmax'))
    # the output layer with a softmax activation function (a last fully connected layer)

    # Compile model
    model.compile(loss='categorical_crossentropy',
        optimizer='adam', metrics=['accuracy'])
    return model

model = baseline_model()
# Fit the model
model.fit(X_train, y_train, validation_data=(X_test, y_test),
          epochs=10, batch_size=200, verbose=2)
model.save('model.h5')
```

Figure 12 Python CNN.

The last code outputs a file containing the weights of the trained CNN model that will be used in our small Desktop application written in Python. See figure 3.25. The training process took approximately 8.8 minutes with a final accuracy of 99% which is pretty good. Results are shown in figure 3.28.

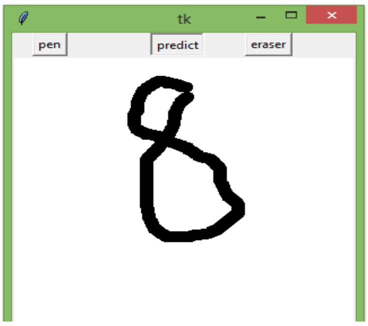

Figure 13 a Sketch sample.

When clicking on the "predict" button as shown in figure 3.25 a shot of the canvas where the "8" has been drawn will be taken. This last one is passed through the pre-trained CNN model that outputs a prediction as in figure 3.26.

Figure 3.27 shows the code snippet used to get such results.

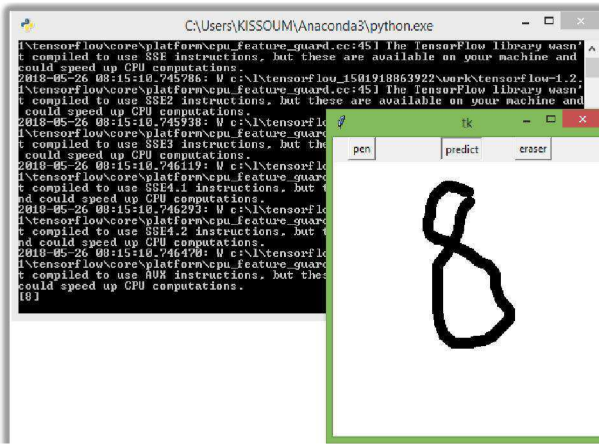

```
1\tensorflow\core\platform\cpu_feature_guard.cc:45] The TensorFlow library wasn'
t compiled to use SSE instructions, but these are available on your machine and
could speed up CPU computations.
2018-05-26 08:15:10.745786: W c:\l\tensorflow_1501918863922\work\tensorflow-1.2.
1\tensorflow\core\platform\cpu_feature_guard.cc:45] The TensorFlow library wasn'
t compiled to use SSE2 instructions, but these are available on your machine and
 could speed up CPU computations.
2018-05-26 08:15:10.745938: W c:\l\tensorflo
1\tensorflow\core\platform\cpu_feature_guard
t compiled to use SSE3 instructions, but the
 could speed up CPU computations.
2018-05-26 08:15:10.746119: W c:\l\tensorflo
1\tensorflow\core\platform\cpu_feature_guard
t compiled to use SSE4.1 instructions, but t
nd could speed up CPU computations.
2018-05-26 08:15:10.746293: W c:\l\tensorflo
1\tensorflow\core\platform\cpu_feature_guard
t compiled to use SSE4.2 instructions, but t
nd could speed up CPU computations.
2018-05-26 08:15:10.746470: W c:\l\tensorflo
1\tensorflow\core\platform\cpu_feature_guard
t compiled to use AVX instructions, but thes
could speed up CPU computations.
[8]
```

Figure14 Prediction results

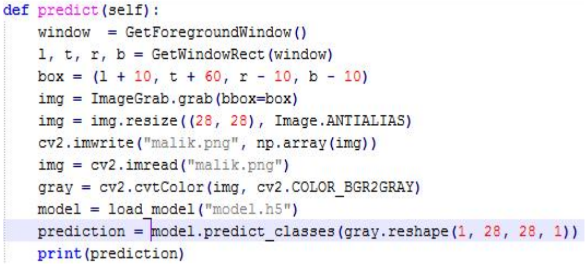

```
def predict(self):
    window  = GetForegroundWindow()
    l, t, r, b = GetWindowRect(window)
    box = (l + 10, t + 60, r - 10, b - 10)
    img = ImageGrab.grab(bbox=box)
    img = img.resize((28, 28), Image.ANTIALIAS)
    cv2.imwrite("malik.png", np.array(img))
    img = cv2.imread("malik.png")
    gray = cv2.cvtColor(img, cv2.COLOR_BGR2GRAY)
    model = load_model("model.h5")
    prediction = model.predict_classes(gray.reshape(1, 28, 28, 1))
    print(prediction)
```

Figure 28 Typical code used in the window

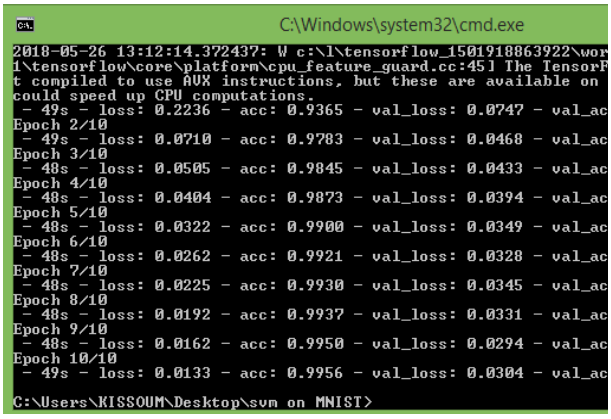

```
2018-05-26 13:12:14.372437: W c:\l\tensorflow_1501918863922\wor
1\tensorflow\core\platform\cpu_feature_guard.cc:45] The TensorF
t compiled to use AVX instructions, but these are available on
could speed up CPU computations.
 - 49s - loss: 0.2236 - acc: 0.9365 - val_loss: 0.0747 - val_ac
Epoch 2/10
 - 49s - loss: 0.0710 - acc: 0.9783 - val_loss: 0.0468 - val_ac
Epoch 3/10
 - 48s - loss: 0.0505 - acc: 0.9845 - val_loss: 0.0433 - val_ac
Epoch 4/10
 - 48s - loss: 0.0404 - acc: 0.9873 - val_loss: 0.0394 - val_ac
Epoch 5/10
 - 48s - loss: 0.0322 - acc: 0.9900 - val_loss: 0.0349 - val_ac
Epoch 6/10
 - 48s - loss: 0.0262 - acc: 0.9921 - val_loss: 0.0328 - val_ac
Epoch 7/10
 - 48s - loss: 0.0225 - acc: 0.9930 - val_loss: 0.0345 - val_ac
Epoch 8/10
 - 48s - loss: 0.0192 - acc: 0.9937 - val_loss: 0.0331 - val_ac
Epoch 9/10
 - 48s - loss: 0.0162 - acc: 0.9950 - val_loss: 0.0294 - val_ac
Epoch 10/10
 - 49s - loss: 0.0133 - acc: 0.9956 - val_loss: 0.0304 - val_ac

C:\Users\KISSOUM\Desktop\svm on MNIST>
```

Figure 15Training results.

4. CONCLUSION

The goal of the work is to propose a more secure door lock system that can be controlled wirelessly using an Android application. The range and security aspects were considered through the Bluetooth technology and a passcode-based security systems. The system was able to actuate a servomotor to lock or unlock the door from a short distance away by just pressing a button on a smartphone. The status of the door has been integrated in the application as a toggle button to make the system more complete. Indeed, we did manage to develop a Bluetooth connection (sending a receiving data packets) between the smartphone and the HC-05 via the use of an Arduino UNO microcontroller. According to the user's smartphone MAC address, access is either granted or denied. Users can be added from within the application by the first user of the app: "the master". The passcode system did well too, by locking or unlocking the door according to the passcode provided by the user. The results of the access decision was indicated via a green or orange LED on the board.

REFERENCES

[1] Featherontheroad, (5 May 2018 à 00:34), Bluetoothhttps://fr.wikipedia.org/wiki/Bluetooth

[2] Amith Shah, (September 07, 2016), HC-05 Bluetooth Module (Master/Slave) https://www.rhydolabz.com/wireless-bluetooth-ble-c-130_132/hc05-bluetooth-module-masterslave-p-1169.html

[3] Microcontroller, (19 May 2018 at 17:20), https://en.wikipedia.org/wiki/Microcontroller

[4] Arduino UNO https://datasheet.octopart.com/A000066-Arduino-datasheet-38879526.pdf

[5] Servomotor 13 may 2018, 17:14 https://en.wikipedia.org/wiki/Servomotor

[6] Hitec HS-325HB - Standard Ball Bearing Servo December 8, 2010https://servodatabase.com/servo/hitec/hs-325hb

[7] 4x4 matrix membrane keypad (#27899) https://www.parallax.com/sites/default/files/downloads/27899-4x4-Matrix-Membrane-Keypad-v1.2.pdf

[8] https://circuitdigest.com/article/16x2-lcd-display-module-pinout-datasheet

[9] JunezRiyaz(Oct. 17, 2017) how to connect I²C LCD display to Arduino UNO http://www.instructables.com/id/How-to-Connect-I2C-Lcd-Display-to-Arduino-Uno/

[10] SHENZHEN EONE ELECTRONICS CO.,LTD, Specification for LCD Module 1602A-1 (V1.2), https://www.openhacks.com/uploadsproductos/eone-1602a1.pdf

[11] Android, (3 May 2018, at 8:55),https://en.wikipedia.org/wiki/Android

[12] Meet Android studio, (8 May 2018) https://developer.android.com/studio/intro/

[13] https://en.wikipedia.org/wiki/Artificial_neural_network

[14] Dr. Randal S. Olsan *Python machine learning: unlock deeper insights into machine learning with this vital guide to cutting edge predictive analytics*, pp 381, 383.

[15] Jonpatterns, (13:29, 2 May 2018), https://en.wikipedia.org/wiki/Arduino#Software

[16] Dawn Griffiths & David Griffiths, *Head first Android Development: A brain-friendly guide*, pp 169-176

[17] ViewPager, (April 17, 2018) https://developer.android.com/ reference/ android /support/v4/view/ViewPager

[18] Add a floating action button 8 may 2018 https://developer.android.com/guide/topics/ui/floating-action-button

[19] Observer pattern, (16 May 2018 at 13:10),https://en.wikipedia.org/wiki/Observer_pattern.

[20] Antonio Gulli, Sujit Pal, *Deep learning with Keras: Implement neural networks with Keras on Theano and Tensorflow.*

[21] Bluetooth overview April 24 2018 https://developer.android.com/guide/topics/connectivity/bluetooth

ISSN 1737-9334

Load Control Emulation for Smart Metering in Smart Grids

F. Z. DEKHANDJI*, N. ALILI and R. LABADI
Laboratory signals and systems, Institute of Electrical and Electronic Engineering, University M'hamed Bougara of Boumerdes, Boumerdes-ALGERIA
**fzdekhandji@yahoo.fr*

Abstract_ In this work, an illustration of smart home prototype is implemented and simulated. Appliances are powered by the grid during daytime and a Photovoltaic panel stored power during the night or in case of an electricity outage. The consumed power from both sources is sensed and further processed for cumulative energy, cost calculations and bill establishment using LABVIEW software. The framework consists of four houses with four different appliances each, power is distributed to the four houses either from the grid or from a backup source provided by a PV generator. The simulator predicts different power consumption profiles for the sake of peak-demand reduction through a load control process. A manual and an automatic load control is tested on the designed system as an application on smart metering load control.

Keywords*: Smart Grids, Smart Meters, Home Load Control, LABVIEW*

1. INTRODUCTION

For a century, utility companies have used conventional power grid system to provide electricity, the traditional grid is facing numerous challenges including lack of techniques to automatically monitor the grid system and transfer useful data, besides with the ever increase in energy demand (In 2030, energy consumption is expected to increase by 50% and 40% in the US and Europe respectively and to triple in China and India [1]), and the reduction of fossil fuels, which pollute the environment, finding new non-polluting energy resources and enhancing energy efficiency have become priority of many nations in the 21st century.

Smart Grid (SG), also called intelligent grid or future grid, is a modern improvement of the existing traditional power grid that will revolutionize the way electricity is produced, delivered and consumed. SG is a network that consists of many systems and subsystems built on an advanced cluster of distributed generation units, renewable energies, energy storage, equipment, and circuits for generating, transmitting, transforming, and distributing energy, it is designed to provide cost-effective, reliable and efficient supply system, and to create a real-time bidirectional communication means and information exchange between the consumer and the grid operator of electric power. One of the keys component of the SG is the Smart Meter (SM), that can be used for reducing peak demand and adapting flexible demand to fluctuating generations [2]. This device enables two-way communication between suppliers and consumers in real time. Moreover, it has the ability to remotely control electrical devices to manage loads and demands [3].

Recently, the number of electricity consumers is increasing in a great extent that handling and maintaining the power as per the growing requirements became such a hard task [4]. It is expected that 60% of all energy consumption will be converted and used as electricity. Therefore; it is a demand that production, distribution and use of electrical energy are done as efficient as possible. Further the recent challenges with nuclear power plants are arguing to find more sustainable energy generation solutions. Of many options, two major technologies will play important roles to solve parts of those future challenges. One is to change the electrical power production from conventional, fossil based energy sources to renewable energy sources; the other is to use high efficient power electronics in power generation, transmission, distribution and end-user application [5].

Distributed Power Generation (DG) is emerging a new paradigm to produce on-site highly reliable and good quality electrical power. The concept is particularly interesting when different kinds of energy resources are available, such as photovoltaic (PV) panels, fuel cells (FC's) or wind turbines. The DG of different kinds of energy systems allow the integration of renewable and nonconventional energy resources. Hence, the DG is becoming a part of strategic plans for most countries to address current challenges associated with energy management [6].

The authors in [7] state that the 21's century requirements cannot be achieved using the current grid and the modernization of the traditional grid is mandatory. The authors describe both the traditional and smart power grid. They define the current grid, also called the traditional grid, as a federal system where there is only one-way flow of electric power, from supplier, transmission, and distribution up to the consumers.

Smart grid studies and researches have mostly focused on conventional interconnected grid systems, works performed concerning the integration of renewable energies in smart grid are classified according to the research characteristics as follows: giving the concept of smart grid as well as pros and cons, technology adoption, optimal allocation of renewable energy in smart grid system, pricing and forecasting, and challenges resulting from the renewable energy integration [8].

[9] and [10] discussed smart grid applications and its potential study in the future by presenting the advantages and disadvantages of smart grid for renewable energy distributed generation pointing that the share of renewable energies requires coordinated efforts and standardized communication and certified products in order to ensure security, safety and reliability in a diversified future grid infrastructure.

[11], [12] and [13] consider the factors which can impact renewable energy investment decisions whether they are economic, technical, social political factors and obstacles.

The maintenance of the power is also important as the human operator goes to the consumer's house and produces the bill as per the meter reading, however if the consumer is not available, the billing process will be pending and the human operator needs to revisit. This process tends to be a laborious task and requires much time, human and material resources [4].

In [4] a wireless data communication based smart meter has been designed and implemented automatic metering and billing system where the amount of the consumed electric energy is displayed continuously on an LCD using Zigbee as a mean of data communication between the user and the controlling base. The system is developed to send a short message service (SMS) about the cost of the consumed energy along with the due date, and also to detect and control the power theft by identifying authorized and unauthorized users. As there is no human intervention, in the entire design and process, there is no chance of human error and corruption.

In [14] smart meter is designed and developed in LABVIEW for domestic/industrial consumers, the prototype accounts for electricity consumption, power quality, generates monthly electrical bill along with incentives provided and penalties levied for power quality and moreover establishes communication between the consumer and the utility.

From the beginning of 2010, the national legislature requires the installation of smart meters in new and refurbished buildings. Because the Germany government follows a policy driven by customer demand smart metering service investment is very small, there are only about 15 out of 800 utilities offering smart metering products in the early 2010 and only the customers with high consumption are likely to install the smart meter and benefit from it [16].

Smart grid implementation encourages end-users to actively take part in the grid operation and make them behave as real actors of the entire electricity production and distribution system [17]. Demand of electricity is increasing day by day, the demand and supply should be continuously balanced to avoid supply interruption. The overall load connected to the grid is in reality the sum of many individual working devices load profiles it is commonly variable and not stable in nature. The power demand fluctuates considerably over time [18] , resulting in a rapid increase of power consumption that stands up as the main cause of grid disruption and black-outs [17]. Power plants are designed to meet the peak demand resulting in an increase in the cost of generation. Hence, an effective solution for this problem is Demand Side Management (DSM) that reduces the peak demand and brings immediate benefits to the utility and the customers [19].

[20] proposed a green HEMS based on energy comparison. The feedback on energy consumption to energy users was used to reduce total energy use. This HEM system figures out the efficiency of a home appliance as compared to the others by displaying energy usage information of individual appliances. So it is necessary to collect the energy usage data of home appliances in this system.

2. SMART METERİNG EMULATİON

The idea behind the implementation is to design a Smart Meter that can measure the power consumed by different loads fed by the main source (grid) during the day, and by a backup source (battery) during the night. Emergency circuitry is also integrated in case of electricity outage. Data required for power calculations is collected by mean of an NI-Data acquisition card. Power consumed by the loads from either sources is displayed in LABVIEW simulator and stored for billing establishment.

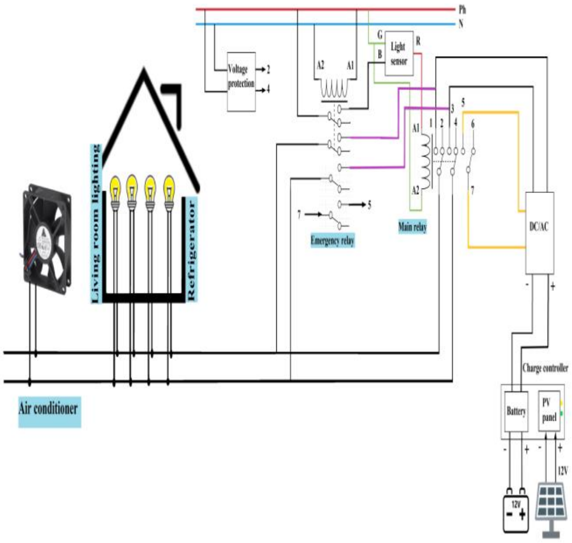

Figure 1 The overall designed circuit diagram.

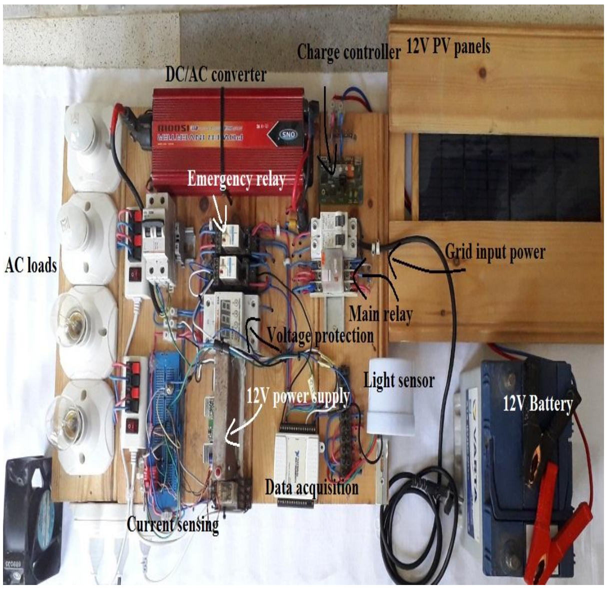

Figure 2 System Hardware.

2.1. LABVIEW Data Acquisition And Power Calculation

The DAQ is configured to acquire an analogue voltage input, the input is split into two voltage inputs; one coming from the grid (AI0) and the other coming from the PV (AI1) with respect to the ground, the RMS values are calculated for each voltage input. The current for each case is simply calculated based on Ohm's law where Rm represents the 250 Ω resistor, Vm is the voltage drop to be measured across the resistor, Ip and Is correspond to the primary and the secondary currents respectively ;

$$Vm = RmIs \qquad (1)$$

$$Is = \frac{Vm}{Rm} \qquad (2)$$

The Primary current is calculated based on the new current ratio;

$$Is = \frac{1}{480}Ip \qquad (3)$$

$$Ip = 480Is \qquad (4)$$

Power is defined as in **(Equation 1.6)**

$$P = IrmsVrmscos\theta \qquad (5)$$

Where I and V are the instantaneous values of the current and voltage and θ is the phase angle between the voltage and the current. Because the loads are considered to be resistive loads, the voltage and the current are in phase and the appropriate power is simply calculated by multiplying the RMS value of each current by the output voltage across the loads that is constant and equal to 230V.

$$P = VIp \qquad (6)$$

$$P = 480VIs \qquad (7)$$

$$P = \frac{480VVm}{Rm} \qquad (8)$$

Substituting for $V = 230V, and\ Rm = 250\Omega$;

$$P = 442Vm \qquad (9)$$

2.2 Simulation results

The designed house consists of 3 appliances; air conditioner, living room lighting and a refrigerator (Fig. 3). Power ratings of each appliance and its real power consumed measured throughout this application are stated in Table 1.

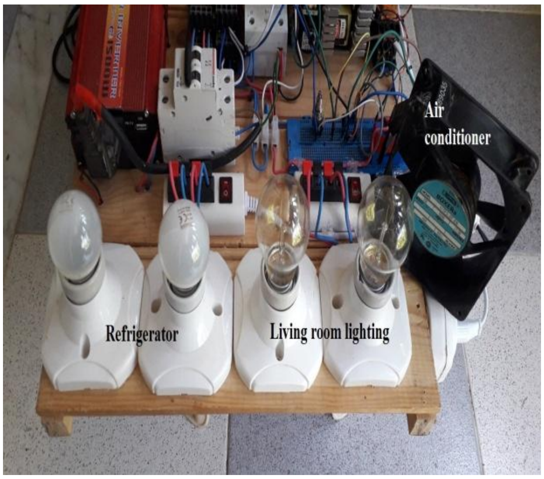

Figure 3 House appliances.

Table 1 Appliances specifications and power ratings.

Load	**Equivalent component**	**Power rating**	**Measured power**
Living room lighting	2 light bulbs	2×40 W	 Consumed power (W) 69.9
Refrigerator	2 light bulbs	2×40 W	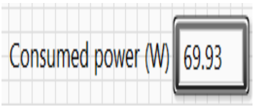 Consumed power (W) 69.93
Air conditioner	Fan	20.7W	 Consumed power (W) 22.45

2.3. Power measurements and recording

Figures down below represent a random power consumption scenario, the front panel displays the measured and the calculated parameters in case where the house is fed from the grid (Fig. 4) and in case where it is fed from the PV (Fig. 5), including, the secondary current Is calculated from (**Equation 3),** the primary current Ip obtained from (**Equation 4)** and finally the consumed power that could be concluded from (**Equation 7)**. The front panel also displays the actual current and the power plots.

ISSN 1737-9334

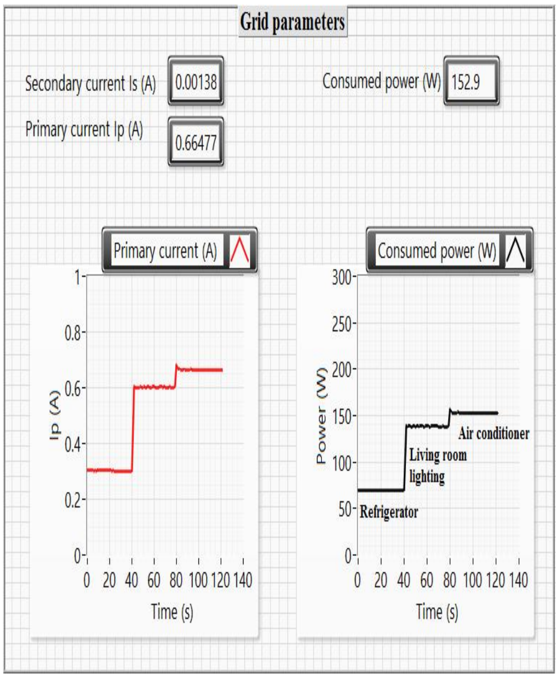

Grid parameters

Secondary current Is (A) 0.00138

Primary current Ip (A) 0.66477

Consumed power (W) 152.9

Fig. 4 Smart meter grid parameters front panel.

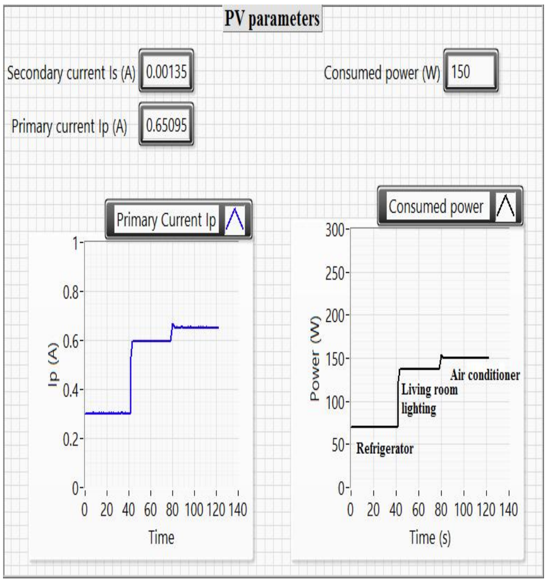

PV parameters

Secondary current Is (A) 0.00135

Primary current Ip (A) 0.65095

Consumed power (W) 150

Fig. 5 Smart meter PV parameters front panel.

Power consumed from different and random loads combinations is recorded each one second for one hour (3600s) from the grid, and for another hour from the energy stored in the battery.

3. Load control

3.1. Home Energy Management Systems

Home Energy Management Systems (HEMS) for residential customers are of recent important development especially in the smart home application where interaction between users with their home appliances will be formed, thereby the devices can be operated and programmed interactively either directly or remotely. Therefore, these appliances can operate automatically, multi functionally and efficiently, HEMS application is developed not only to manage energy use in households but also to conduct the management of energy supply, either from the provider of electrical energy or the own-generated one such as alternative energy sources through solar or wind power plant.
The HEMS configuration consists of household loads that are divided into scheduled and unscheduled loads, energy storage, alternative energy sources, connections to grid, electric cars and HEMS control systems which is supported by communication technology and smart meter [3].

3.2. Types of customer loads

Customer loads can be classified into two types: the first type is the shiftable load that can be scheduled at different time periods of the day, for example; the washing machine and the dishwasher. Such appliances should be able to receive a signal (either by wire or by wireless connections) and to contain automatic switches that can turn them on and off. The second type is the non-shiftable load that has to be operated during specific times of the day to meet the requirements such as the lighting system. Therefore, in the peak-hour, the customer can schedule their shiftable appliances to mitigate the extra load from the grid. According to these load types, a scheduling techniques need to shift the load as much as they can to enable customers to manage their energy bills and utility company to balance consumption levels [57].

3.3. Types of load control

In the smart grid loads may be controlled either by the supplier side or by the end user side.
Controlling of end-use loads can be carried out:

- **Automatically**: In response to a signal sent by a load control program operator linked to a particular event including high energy prices or network constraints.
- **Manually**: By the end user in response to an event (the initiator of the switching requires information about the event) [56].

3.4. Simulation and setup analysis

A smart metering residential load control method is designed and simulated in LABVIEW software, the framework consists of four houses with four different appliances each, power is distributed to the four houses either from the grid with a total amount of 100KW and from a backup source emitting from a PV generator with a total amount of 100KW.
Depending on the four houses total consumption, three distinct situations may occur;

- The total consumption of houses is less than the power provided from the grid, the grid power satisfies the power demand and no control procedure is considered.
- The total consumption of houses exceeds the power amount supplied from the grid but less than the power supplied from the backup, in this case, the deficiency is restored from the backup till the power demand is satisfied.

- The worst case occurs when the total consumption exceeds both power amounts supplied from the grid and from the backup, this is the case of a peak demand, the quest for power demand satisfaction implies an application of a load control procedure. Some appliances must be turned OFF, this is done by first selecting the house with largest power consumption and then switching OFF its appliance that is consuming the largest amounts of power amongst the four appliances.

The result of the three cases can be viewed in the figure **(Fig. 6)**.

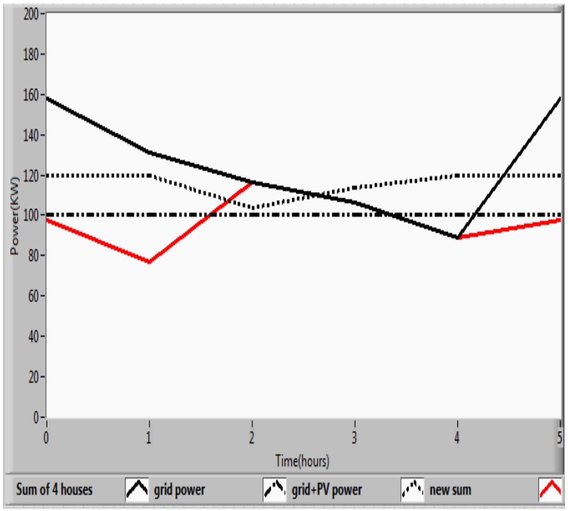

Fig. 6 Overall power consumption plots.

3.5. Interpretation of results

Three situations can be deduced from the graph simulation represented in **(Fig. 6)**: the overall power consumption of four houses with respect to time, each case is discussed separately and illustrated by its appropriate LABVIEW front panel.

4. CONCLUSION

Smart grid merges both digital technologies and long transmission networks to manage energy consumption, as well as to open up new processes for energy production and distribution. In this work, a house was designed and powered the grid and from solar energy stored in a battery, instantaneous power consumption was recorded in LABVIEW software where the required data were acquired by a DAQ card.

This work focused on describing strategies for decreasing the load demand and power consumption costs, the active role of the customer in the SG is better defined and clarified. A simulation in LABVIEW software and a hardware application are performed to demonstrate the smart metering services in decreasing the pressure on the local electricity grid by taking power from RES and also managing customer energy use and save money by controlling the loads consumption. The simulation part is performed to visualize some peak demand mitigation techniques whereas the hardware part is an application to demonstrate an automatic and a manual load control technique performed on a house in case of an increase in power demand.

REFERENCES

[1] V. Environnement, “Smart grids,” *Sci. Chron. Mag.*, vol. 18, pp. 1–7, 2010.

[2] N. Li, L. Chen, and S. H. Low, “Optimal demand response based on utility maximization in power networks,” in *2011 IEEE power and energy society general meeting*, 2011, pp. 1–8.

[3] X. Fang, S. Misra, G. Xue, and D. Yang, “Smart Grid — The New and Improved Power Grid: A Survey,” *IEEE Commun. Surv. Tutor.*, vol. 14, no. 4, pp. 944–980, 2012.

[4] V. Preethi and G. Harish, “Design and implementation of smart energy meter,” in *2016 International Conference on Inventive Computation Technologies (ICICT)*, 2016, vol. 1, pp. 1–5.

[5] M. P. Kaźmierkowski, R. Krishnan, and F. Blaabjerg, Eds., *Control in power electronics: selected problems*. Amsterdam ; New York: Academic Press, 2002.

[6] J. Guerrero *et al.*, “Distributed Generation: Toward a New Energy Paradigm,” *IEEE Ind. Electron. Mag.*, vol. 4, no. 1, pp. 52–64, Mar. 2010.

[7] A. A. Cecilia and K. Sudarsanan, “A survey on smart grid,” in *2016 International Conference on Emerging Trends in Engineering, Technology and Science (ICETETS)*, 2016, pp. 1–7.

[8] N. Phuangpornpitak and S. Tia, “Opportunities and Challenges of Integrating Renewable Energy in Smart Grid System,” *Energy Procedia*, vol. 34, pp. 282–290, 2013.

[9] W. Koykul, “Current status and action plan of utility sector on smart grid and smart community in Thailand,” in *Thailand-Japan Workshop on Smart Community in Thailand: Provincial Electricity Authority, Thailand*, 2011.

[10] A. Gaviano, K. Weber, and C. Dirmeier, “Challenges and Integration of PV and Wind Energy Facilities from a Smart Grid Point of View,” *Energy Procedia*, vol. 25, pp. 118–125, 2012.

[11] J. Reston Filho, C. Affonso, and R. Oliveira, “Pricing analysis in the Brazilian energy market: A decision tree approach,” in *2009 IEEE Bucharest PowerTech*, 2009, pp. 1–6.

[12] A. Kian and A. Keyhani, “Stochastic price modeling of electricity in deregulated energy markets,” in *Proceedings of the 34th Annual Hawaii International Conference on System Sciences*, 2001, p. 7–pp.

[13] I. Iskin, T. Daim, G. Kayakutlu, and M. Altuntas, “Exploring renewable energy pricing with analytic network process — Comparing a developed and a developing economy,” *Energy Econ.*, vol. 34, no. 4, pp. 882–891, Jul. 2012.

[14] A. Bhimte, R. K. Mathew, and S. Kumaravel, “Development of smart energy meter in LabVIEW for power distribution systems,” in *2015 Annual IEEE India Conference (INDICON)*, 2015, pp. 1–6.

[15] S. Renner *et al.*, “European smart metering landscape report,” *Imprint*, vol. 2, pp. 1–168, 2011.

[16] Jixuan Zheng, D. W. Gao, and Li Lin, “Smart Meters in Smart Grid: An Overview,” 2013, pp. 57–64.

[17] R. Miceli, “Energy Management and Smart Grids,” *Energies*, vol. 6, no. 4, pp. 2262–2290, Apr. 2013.

[18] P. Palensky and D. Dietrich, “Demand Side Management: Demand Response, Intelligent Energy Systems, and Smart Loads,” *IEEE Trans. Ind. Inform.*, vol. 7, no. 3, pp. 381–388, Aug. 2011.

[19] P. Palensky and D. Dietrich, “Demand Side Management: Demand Response, Intelligent Energy Systems, and Smart Loads,” *IEEE Trans. Ind. Inform.*, vol. 7, no. 3, pp. 381–388, Aug. 2011.

[20] J. Han, C.-S. Choi, W.-K. Park, and I. Lee, “Green home energy management system through comparison of energy usage between the same kinds of home appliances,” in *2011 IEEE 15th International Symposium on Consumer Electronics (ISCE)*, 2011, pp. 1–4.

[21] Jixuan Zheng, D. W. Gao, and Li Lin, “Smart Meters in Smart Grid: An Overview,” in *2013 IEEE Green Technologies Conference (GreenTech)*, Denver, CO, 2013, pp. 57–64.

[22] S. M. Amin and B. F. Wollenberg, “Toward a smart grid: power delivery for the 21st century,” *IEEE Power Energy Mag.*, vol. 3, no. 5, pp. 34–41, 2005.

[23] N. Jenkins, C. Long, and J. Wu, “An Overview of the Smart Grid in Great Britain,” *Engineering*, vol. 1, no. 4, pp. 413–421, Dec. 2015.

[24] Y. Kabalci, “A survey on smart metering and smart grid communication,” *Renew. Sustain. Energy Rev.*, vol. 57, pp. 302–318, May 2016.

[25] D. M. Souran, H. H. Safa, B. G. Moghadam, M. Ghasempour, and P. T. Heravi, “Smart Grid Technology in Power Systems,” in *Soft Computing Applications*, vol. 357, V. E. Balas, L. C. Jain, and B. Kovačević, Eds. Cham: Springer International Publishing, 2016, pp. 1367–1381.

[26] N. Phuangpornpitak and S. Tia, “Opportunities and Challenges of Integrating Renewable Energy in Smart Grid System,” *Energy Procedia*, vol. 34, pp. 282–290, 2013.

[27] J. A. Momoh, *Smart grid: fundamentals of design and analysis*. Hoboken, N.J: Wiley, 2012.

[28] A. Gaviano, K. Weber, and C. Dirmeier, “Challenges and Integration of PV and Wind Energy Facilities from a Smart Grid Point of View,” *Energy Procedia*, vol. 25, pp. 118–125, 2012.

MIMO System Performance Investigation Using an M-ary PAM Modulation Technique Under Rayleigh Fading Channel

Amira Mohamed Tornish
College of Electronic Technology,
Communication Engineering
Department
Tripoli, Libya
E-mail amira.tornish.94@gmail.com

Amer R. Zerek
Zawia University, Faculty of
Engineering/ EE Department,
Zawia, – Libya,
E-mail anas_94z@yahoo.co.uk

Nsreen Hawisa
University of Zawia, Faculty of
Engineering
/ EE Engineering Department
Zawia, Libya
^{3}E-mail hawisansreen@gmail.com

Abstract— **An M-ary pulse modulation technique is widely used in communication area, such as for transmission of data or information over wires and wireless communication channels , and so on. One of most important M-ary pulse modulation schemes is M- ary Pulse Amplitude Modulation (M- ary PAM) which is very important part of the implementation of modern wireless communications systems .**

The main task of this work is to investigate, implement and simulate the 4, 8 and 16- PAM using Matlab with Simulink V. 2017b over Rayleigh communication channel using multi input – multi output (MIMO) system. That MIMO system include multi antenna diversity 2x3, where the number of transmitter antenna is two and three receiver antenna.
The Bit Error Rate (BER) performance is obtained after M- ary PAM (MPAM) system simulated. The obtained results illustrated that as the level of PAM modulation increases, the BER increase at the same E_b/N_0 values. This means that, the lower level value corresponds to the better the performance. while the worse is as the level of the PAM modulation increases. Also obtained constellation diagrams , before and after the Rayleigh communication channel are confirm the BER achieved results.

Keywords— wireless communication, M-ary – PAM, Modulation and MIMO

I. INTRODUCATION

During the earlier stages, the electronic communication industry has undergone some remarkable technological changes. Traditional communication systems that use conventional analog modulation techniques are gradually being replaced with more contemporary digital communication techniques. That digital communication techniques offer several outstanding advantages over analog communication techniques, such as: noise immunity, ease of processing, ease of multiplexing, viability of regenerative repeaters, that is no weakness and attenuation along the path …etc. Despite a general trend towards digital communications, analog communication systems remain widely used, especially in audio and video broadcasting. [1, 2].

Now days wireless communication applications demand high speed data transmissions [3]. This is made possible by binary and multilevel modulation schemes These schemes of modulation have been proposed but there is a tradeoff between data rate and incompatibility of the three basic parameters as phase, frequency and time between the transmitter and receiver These digital modulation schemes include basic schemes such as M-ary Phase Shift keying (MPSK) M-ary Pulse Amplitude Modulation (MPAM) and M-ary quadrature amplitude modulation. That MPAM is the main goal of this paper and will be clarify in the next sections.

II. MULTI INPUT MULYI OUTPUY SYSTEM

Multiple iInput, Multiple Output (MIMO) is an antenna technology for wireless communications in which many antennas are used at both the Transmitter(Tx) and the Receiver (Rx) sides. That system uses mth antennas at transmitter (m_T) and nth antennas at receiver (n_R) i.e ($m_T \times n_R$) and there is a communication channel between each of the transmit and receive antennas. [4]

In general MIMO system is used to get better overall throughput of the wireless link. But there are other types of the MIMO system such as Multi Input Single Output (MISO), Single Input Multi Output (SIMO) and Single Input Single Output (SISO) channels. Although the MIMO channels offer a several advantages over their systems such as minimize fading effects, it offers high quality of service with increased spectral efficiency and data rates, It helps in achieving reduction in bit error rate and The higher data rate can be achieved … etc.

In addition to these advantages MIMO system suffering from some drawbacks such as higher cost, it is higher requirements of resource and hardware complexity and increasing power requirements of hardware resources while the battery gets drain very fast due to processing of complex and computationally … etc. [4, 5].

ISSN 1737-9334

In this paper a MIMO system considered to be two transmit antennas (m_t) and three receive antennas (n_r) i.e (2×3) as shown in figure 1

.

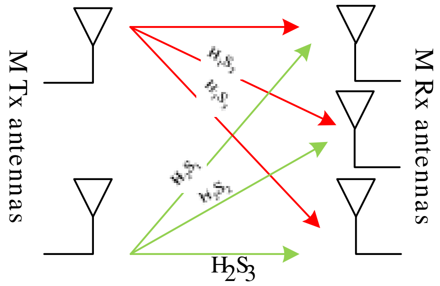

Fig. 1 MIMO channel with Two transmit and Three receive antennas

A MIMO channel shown in figure 1 can be represented as:

On the 1st receive antenna ,the received signal is

$$R_1 = H_{11}S_1 + H_{12}S_2 + N_1 \qquad (1)$$

On the 2nd receive antenna, the received signal i

$$R_2 = H_{21}S_1 + H_{22}S_2 + N_2 \qquad (2)$$

On the 3rd receive antenna, the received signal is

$$R_3 = H_{31}S_1 + H_{32}S_2 + N_3 \qquad (3)$$

Where

The received symbol on the first , second and third are $R_1, R_2,$ and R_3 antennas respectively .

H_{11} is the communication channel between the 1st transmit antenna to 1st receive antenna

H_{12}. is the communication channel between the 2nd transmit antenna to 1st receive antenna

H_{21}. is the communication channel between the 1st transmit antenna to 2nd receive antenna

H_{22} is the communication channel between the 2st transmit antenna to 2nd receive antenna .

H_{31} is the communication channel between the 1st transmit antenna to 3rd receive antenna.

H_{32} is the communication channel between the 2nd transmit antenna to 3rd receive antenna.

The transmitted symbols N_1, N_2 and N_3 are the noise on the 1st, 2nd, and 3rd receive antennas, S_1 and S_2 respectively.

Equation (1) to (3) can be represented in matrix form as follows:

$$\begin{bmatrix} R_1 \\ R_2 \\ R_3 \end{bmatrix} = \begin{bmatrix} H_{11} & H_{12} \\ H_{21} & H_{22} \\ H_{31} & H_{32} \end{bmatrix} . \begin{bmatrix} S_1 \\ S_2 \end{bmatrix} + \begin{bmatrix} N_1 \\ N_2 \end{bmatrix} \qquad (4)$$

Then received vector can be expressed mathamtically as follows

$$R = H.S + N \qquad (5)$$

Where

R = received symbols, H= channel symbols, S = transmitted symbols and N = noise symbols

Therefore

Received signal vector = $\begin{bmatrix} R_1 \\ R_2 \\ R_3 \end{bmatrix}$, Channel matrix = $\begin{bmatrix} H_{11} & H_{12} \\ H_{21} & H_{22} \\ H_{31} & H_{32} \end{bmatrix}$

Transmitted signal vector = $\begin{bmatrix} S_1 \\ S_2 \end{bmatrix}$ and

Noise signal vector = $\begin{bmatrix} N_1 \\ N_2 \end{bmatrix}$

III COMMUNICATION CHANNELS

Communication channel is a media where the information transfer between the transmitters and receivers. That media is classified in two schemes such as a physical media and free space media . The physical media which is called a guided media e.g coaxial cable, optical fiber …. etc and the free space media is called unguided media e.g free space.

The free space channel include two main schemes channel is an Additive White Gaussian Noise (AWGN) and fading channels . The fading channels has two main types such as Rayleigh and Rician channels. Only the Rayleigh channel is described briefly in the following section. [3, 5].

IV RAYLEIGH FADING CHANNEL

The Rayleigh channel is one of the fading channel scheme and that channel is known as a Non-Line of Sight (NLOS) channel normally in wireless communication systems , the envelope of the carrier signal is Rayleigh distributed; and that distribution is caused by multipath with Doppler effect or without . In the multipath case, when the main signal needs to be transmitted becomes weaker, such as in the case of NLOS, the received signal is the include of several components that are reflected from the adjacent obstacles trees , building, … etc . In this type of channel , there are several other paths by which the signal may arrive at the receiver side . When the signals arrive at the receiver, the overall signal is a combination of all the signals that have reached the receiver through the available of large number different paths.

In that scheme of fading channels include the combines of both Line Of Sight (LOS) and NLOS transmission components and because of that a number of reflections that happens to the signal could have a positive factor and performance of the communication system performance. [5].

ISSN 1737-9334

V M – ARY PAM MODULATION TECHNIQUE

In a Pulse Amplitude Modulation (PAM), the message signal which represented the sequences of bit are modulated with carrier signals having different amplitudes. When transmit symbols having only two levels of different amplitudes, it is called a binary PAM (BPAM) . While when transmit symbols having more than two levels of different amplitude s it is known as M-ary PAM (MPAM).[6, 7].

The mathematical formula of M-ary PAM modulated signal is given by

$$v_i(t) = A_i\ g(t)\cos(\omega_c t) \qquad (6)$$

Where

$A_i = 2i-1-M$, for i=1,2,…..M and g(t) train of pulses

and **M** is the possible amplitude levels , $M = 2^k$ and k=1, 2, 3…….

While Probability of error is a function of the average energy per bit (E_{bav}) to noise power density (N_0) ratio . So referring to ref [7] the probability of error for M–ary PAM is given by

$$p(e) = \frac{2(M-1)}{M} Q\left(\sqrt{\frac{(6\log_2 M)E_{bav}}{(M^2-1)N_0}}\right) \qquad (7)$$

Where

E_{bav} the average bit energy and

N_o is noise power density

In this paper BER performances and constellation diagrams of 4, 8 and 16 - PAM modulation are analysis and investigate over Rayleigh fading channel.

VI. SIMULATION of an M-ARY PULSE AMPLITUDE MODULATION USING SIMULINK

An M-ary PAM system for M=4, 8 and 16 is implemented using Simulink shown in figure 2. That implementation model consists of three main parts such as transmitter, communication Rayleigh (non line of sight) channel and the receiver. These parts include the following elements.

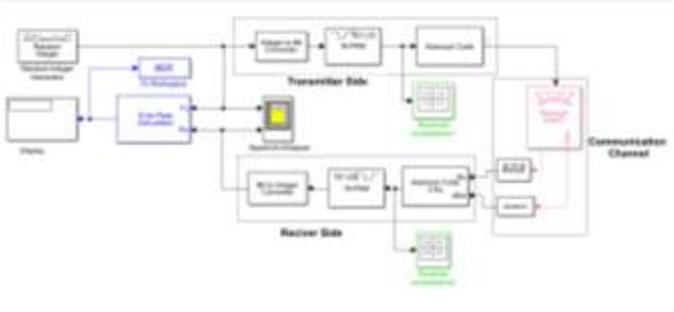

Fig. 2 Transceiver of M- ary PAM Over Rayleigh Channel

A) Transmitter Side

- T The Random Integer Generator block generates uniformly distributed random integers in the rang of [0, M-1], where M is the **set size** defined in the dialog box and is equal 2^n , where n is an integer number i.e n=1, 3, 3, ….etc.
- The Mary -PAM Modulator Baseband block modulates using the M-ary Pulse Amplitude Modulation method. The output is a baseband representation of the modulated signal. The **M-ary number** parameter, M, is the number of possible output symbols that can immediately follow a given output symbol
- The Integer to Bit Converter block charts each integer or fixed-point value in the input vector to a group of bits in the output vector.
- output symbols that can immediately follow a given output symbol

B) Communication Channel

- The AWGN Channel block is the The AWGN Channel block models a noisy channel by adding white Gaussian noise to the modulated signal.
- The orthogonal space-time block code (OSTBC) Encoder block(Alamouti) encode) an input symbol sequence using space-time OSTBC. The block charts the input symbols block-wise and concatenates the output codeword matrices in the time domain.
- The multi-input/multi-output (MIMO) Fading Channel block filters an input signal using a MIMO multipath fading channel. This block models both Rayleigh fading and utilizes the Kronecker model for modeling the spatial correlation between the links.
- The Squeeze block eliminates singleton dimensions from its multidimensional input signal. A singleton dimension is any dimension whose size is one. This squeeze block operates only on signals whose number of dimensions is greater than two.
- The OSTBC Combiner block (Almaouti Code 3Rx) combines the input signal from all of the receive antennas and the channel approximation signal to take out the soft information of the symbols that were encoded using an OSTBC. The input channel estimate can not be fixed during each codeword block transmission and the combining algorithm uses only the estimate for the first symbol period per codeword block. A symbol demodulator would follow the combiner block in a MIMO communications system.

C) Receiver Side

- The M-PAM Demodulator Baseband block demodulates a signal that was modulated using the M-ary Pulse Amplitude Modulation method. The input is a baseband representation of the modulated signal. The input and output for this block are discrete-time signals. This block accepts a scalar-valued or column vector input signal.

- ➢ The Bit to Integer Converter block charts groups of bits in the input vector to integers in the output vector. M defines how many bits are charted for each output integer.

❖ Measurement Equipments

- ➢ The Two Constellation Diagram blocks plots the constellation diagrams of the M-ary PAM modulated and demodulated signals
- ➢ The Error Rate Calculation block it compares input data from a transmitter side with input data from a receiver side . This block is used to calculate the error rate (BER) as a running statistic, by dividing the total number of unequal pairs of data elements by the total number of input data elements from one source.
- ➢ The To Workspace block inputs a signal and writes the signal data to a workspace. During the running of the simulation model , the block writes data to an internal buffer. When the simulation is completed, that data is written to the workspace.
- ➢ Display The Spectrum Analyzer block, refers as scope to displays the power spectra density of signals.
- ➢ The Integer to Bit Converter block charts each integer or fixed-point value in the input vector to a group of bits in the output vector.
- ➢ output symbols that can immediately follow a given output symbol
- ➢ The Constellation Diagram block plots the constellation diagrams of the M-ary PAM modulated signal.

VII SIMULATION RESULT

After construct and setting the simulation model parameters of both transmitter and receiver M- ary PAM which is illustrated in figure 2 for two transmit and three receive antennas (2x3 antennas) , over Rayleigh channel. I The 4, 8 and 16 – PAM modulation are investigated from point of view BER performance and the constellation diagrams over Rican channel.

A) Bit Error Rate Performance

Figure 3 is shown the relationship between the BER and E_b/N_o Performance of 4, 8 and 16-PAM system over Rayleigh channel respectively .

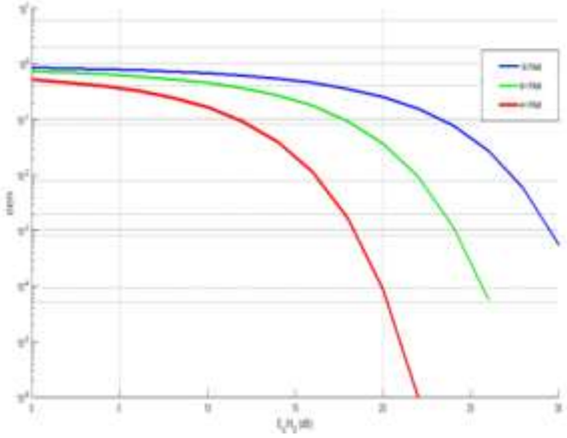

Fig. 3. Bit Error Rate vs. E_b/N_o Performance of 4, 8 and 16 - PAM Over Rayleigh Channel

The plot in figure3 which is represented BER vs. E_b/N_o performance under various levels of PAM modulation i.e 4, 8 and 16 examining when considering the effect represented by Rayleigh channel. It is fairly clear that as the level of M- ary PAM increases the BER increases i.e a more signal energy is required to get a better BER.

B) Constellation Diagrams of an M- ary PAM Modulations

When the E_b/N_o is chosen to equal 15dB constellation diagrams of the random uniform distributed and the demodulated signals of 4, 8 and 16 - PAM Over Rayleigh channel are obtained as shown in figure 4

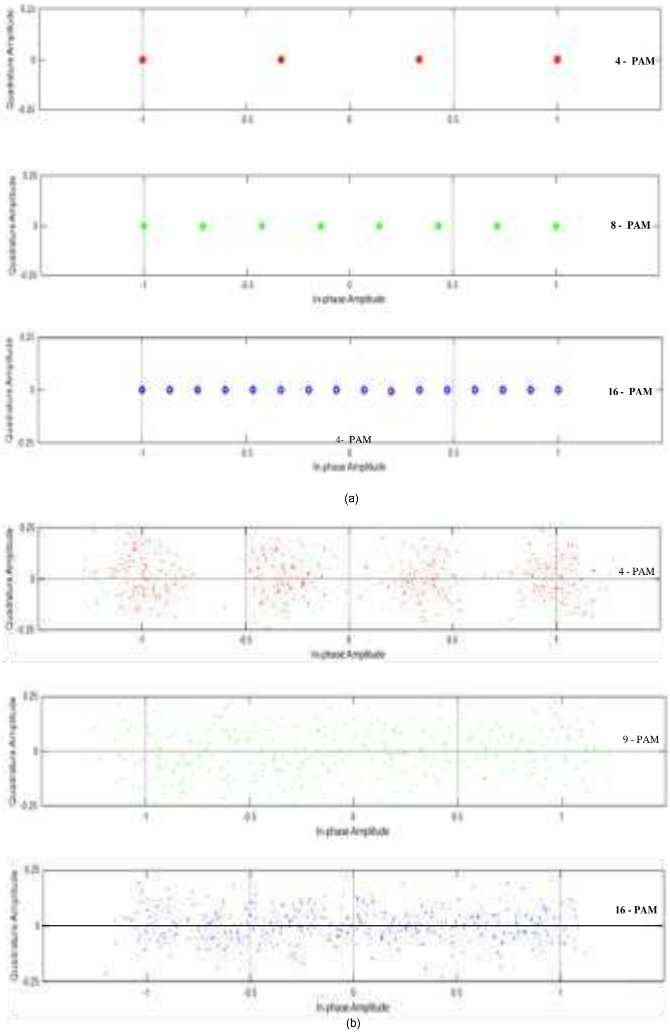

(a)

(b)

Fig. 4 Constellation Diagrams After and Before of 4, 8 and 16 –PAM MODEM

The result represented in figure 4 is emphasize the constellation diagrams of 4 , 8 and 16 –PAM respectively over the Rayleigh channel, before and after that channel i.e at the modulator output and demodulator input respectively . That constellation diagrams confirm the BER obtained results

VIII CONCLUSION

In this work the obtained simulation results represented the BER performance and constellation diagrams respectively under various levels of PAM modulation i.e 4, 8 and 16 –PAM over Rayleigh communication channel. It observes that it was quite clear that as the level increases the BER increases i.e a more signal energy is required to get a better BER performances.

Therefore the best value for BER is for 4-PAM modulation over Rayleigh channel as seen in the achieved results. Also the obtained constellation diagrams of 4, 8 and 16 –PAM respectively over the Rayleigh communication channel, before and after it are confirm the BER achieved results.

REFERNCES

[1] Simon Haykin, “Communication Systems”, 4th Ed, John Wiley & Sons, 201.

[2] Carlson, A. Bruce. Communication system. Tata McGraw-Hill Education, 2010.

[3] Du, Ke-Lin, and Madisetti NS Swamy. Wireless communication systems: from RF subsystems to 4G enabling technologies. Cambridge University Press, 2010

[4] .J.Paulraj, D.A.Gore, R.U.Nabar, H.Bölcskei, An overview of MIMO communications- A key to gigabit wireless, IEEE proceedings, vol.92, pp 198-218, Feb.2004

[5] Nsreen Hawisa and Amer R. Zerek , “Modeling and Analyzing the BER and SER Performances of MIMO System using Multi Level - DPSK Modulation Technique Under Rayleigh Fading Channel”. 5Th International Conference on Automation Control Engineering & Computer Science (ACECS’18) , Hammamet-Tunisia, Dec. 19-22, 2018.

[6] Awadhesh Kumar Singh and Nar Singh , “Performance Evaluation of M-ary Digital Pulse Amplitude Signaling Scheme” , International Journal of Electronics, Electrical and Computational System (IJEECS) ISN 2348-17X, Volume 6, Isue 12, December 2017.

[7] WITS Lab, NSYSU, “ Optimum Receivers for the Additive White Gaussian Noise Channel”, Chapter 5, 2004.

SVC inverter voltage drop regulation using FACTS applied on hybrid Pv-Wind system

BEN ACHOUR Souheyla #1, BENDJEGHABA Omar #2, IFRAH Karim #3, Bourourou Fares #4

 # LREEI
Universtity of Boumerdes
Boumerdes, Algeria
[1]so.benachour@univ-boumerdes.dz
[2]O.bendjeghaba@univ-boumerdes.dz
[3]k.ifrah@univ-boumerdes.dz
[4]f.bourourou@univ-boumerdes.dz

Abstract— **The purpose of this study is to maintain the voltage factor in the near-unity network (1pu) using a Static Variables Compensator (SVC). In order to determine the effectiveness of this device to improve the stability of a hybrid Pv-Wind system, the power flow is calculated without the existence of the SVC at first, and then the SVC is integrated. This operation is performed to make a comparison and evaluate the role of the device in the system to determine the optimal location for the integration of the SVC thus compares their contribution to the improvement of the stability. The obtained results are discussed and analysed, it is found that this device provides a considerable reduction in the voltage drop and appreciable control of the voltage at the concerned busbar.**

***Keywords*— P SS, FACTS, SVC, PSAT, Power flow, converter.**

I. INTRODUCTION

Industrialization and population growth are the primary factors for which the consumption of electrical energy is steadily increasing. Thus, to have a balance between production and consumption, it is first necessary to increase the number of power plants, lines, transformers… etc., which implies an increase in cost and environmental degradation. Consequently, it is now important to have mesh networks and work close to the stability limits to meet these new requirements [1-6]. Due to the environmental concerns, renewable energy sources such as wind or solar generation have gained the popularity in the recent years [2].

The electric power supplier is working to ensure the quality of electric power, to get to increase service continuity, now the quality criteria have evolved with the development of electronic equipment, which takes a prominent place in the production, and transport of an electrical network. It will, in the future, complete their action by implementing electronic power devices at high speed response, recently developed and known by the name FACTS (Flexible Alternative Current Transmission System) for control networks[5].

FACTS systems (Flexible Alternative Current Transmission Systems) are fast control systems networks using the resources offered by the power electronics and control microelectronics were recently studied and realized [6-9]. The recent development of FACTS devices opens up new possibilities for more efficient network operations by continuous and rapid action on the various network parameters (phase, voltage, impedance). Thus, power flows can be better controlled and better kept tensions, which will increase stability margins or tender to the thermal limits of the lines. Generally, the main role of FACTS devices is the compensation of the electric power to the inside [3-7].

•The problem of power loss, voltage drops.
•The optimization of power flow (Dispatching).
•The voltage stability.

II. STATIC VAR COMPENSATOR (SVC):

Static Var Compensator (SVC) is a parallel reactive compensation equipment with electronic power base capable of reacting in some cycles to network changes. It allows among others the connecting remote production center expenses and decreases the effects of defects or load fluctuations. The SVC controls the voltage on its terminals order the amount of reactive power is injected or absorbed in the power system [8]. When the system voltage is low, the SVC develops reactive power (SVC capacitive). When the system voltage is high, it absorbs reactive power (SVC inductive).

$$P_{G,i} - P_{D,i} = V_i \sum_{i=1}^{b} \left[V_j \left[G_{ij} \cos\left(\delta_i - \delta_j\right) + B_{ij} \sin\left(\delta_i - \delta_j\right) \right] \right] \quad (1)$$

$$Q_{G,i} - Q_{D,i} = V_i \sum_{i=1}^{b} \left[V_j \left[G_{ij} \sin\left(\delta_i - \delta_j\right) + B_{ij} \sin\left(\delta_i - \delta_j\right) \right] \right] \quad (2)$$

Where PG,i and QG,i are the active and reactive generating powers at the ith bus; PD,i and QD,i are the active and reactive of demand powers at the ith bus. Gij and Bij represent the real and imaginary components of element Y'ij of the admittance matrix.

Association of TCR devices, TSC, fixed capacity benches and harmonic filters is the hybrid compensator, better known under the name SVC (Fig. 1) [4], the first example was installed in 1979 in South Africa.

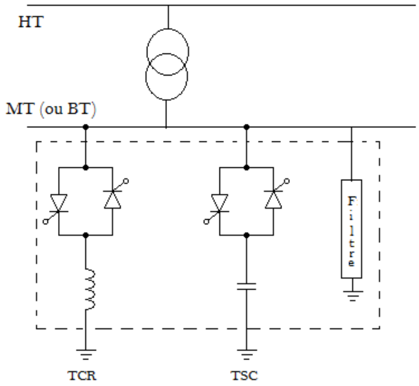

Fig. 1: SVC (Static Var Compensator).

The static characteristic is given in Fig. 2[5].

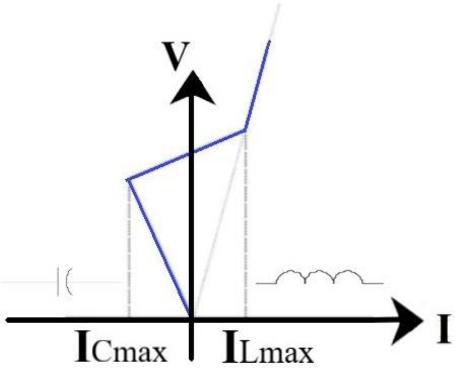

Fig. 2: characteristic of an SVC.

In this characteristic, we can distinct three areas [10]:

- An area where only the capacities are connected to the network.
- A control area where the reactive energy is a combination of the TCR and TSC.
- An area where the TCR gives its maximum energy (control stop), the capacitors are disconnected.

III. DESCRIPTION OF THE SYSTEM

This simulation is done on 14 bus system with base MVA=100 and the data [12] is taken for the standard IEEE 14 bus system. The test system is shown in Figure 4 which includes total 14 bus in which 14 bus bars, 5 generators including PV-wind generator, 11 loads, and 20 transmission lines. This simulation model is made in PSAT/MATLAB software.

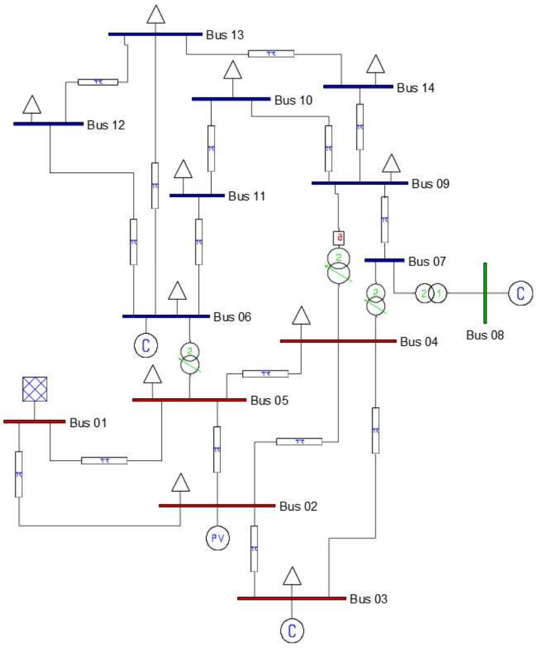

Fig. 3: 14 bus bars network.

IV. SIMULATION RESULTS

A test network of 14 bus bars (Fig. 3) has been employed in PSAT/MATLAB program to find out the performance of SVC in increasing the flow of active and reactive power.

The power flow is calculated by the conventional method (Newton-Raphson), the results are shown in table 1.

TABLE I:
Voltages and angles of 14 bus bars network

BUS BAR NUMNER	***PSAT***	
	voltage VM (pu)	***Angle (deg)***
1	1.06	0
2	1.045	-7.7717
3	1.01	-19.0201
4	0.9975	-15.125
5	1.0024	-13.0138
6	1.07	-13.0138
7	1.0349	-20.7153
8	1.09	-20.7153
9	1.0117	-23.5476
10	1.0112	-23.8017
11	1.0351	-23.4123
12	1.0461	-23.9261
13	1.0364	-23.9967
14	0.99617	-25.2386

A. *Simulation results of the system without compensation*

The calculation of the continuous power flow method (CPF) determines the amplitude of the voltages at the 14 bus bars with the increase of the load, which makes it possible to identify the sensitive bus bars (which has an inadmissible drop), Results obtain after simulation is shown in table 2 and fig. 4.

TABLE II:
Voltages and angles of 14 bus bars network without SVC

BUS BAR NUMNER	***PSAT***	
	voltage VM (pu)	***Angle (deg)***
1	1.06	0
2	1.045	-36.1848
3	1.01	-84.6673
4	0.69334	-69.6366
5	0.67636	-58.9401
6	1.07	-111.0293
7	0.79186	-95.784
8	1.09	-95.784
9	0.70174	-108.7289
10	0.72569	-111.2236
11	0.87853	-111.6237
12	0.97837	-114.8097
13	0.92969	-114.7377
14	0.68902	-119.3869

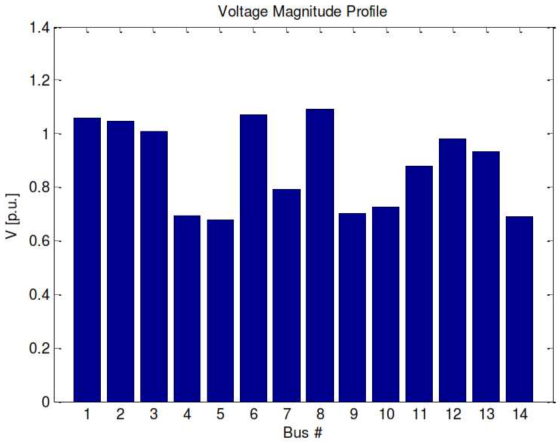

Fig. 4: voltages of 14 bus bars network without SVC.

According to the fig. 4, six bars are identified sensitive, which are bus (4), bus (5), bus (7), bus (9), bus (10), and bus (14).

The evolution of each voltage of these bus bars in function of power (P-V curve) is shown in the fig. 5; the voltage sensitivity margin corresponds to the maximum load

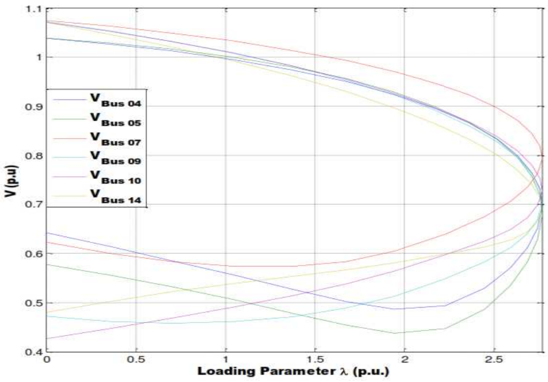

Fig. 5: P-V curves of sensitive bus bars.

From the curves P-V (fig. 5), the analyzed network has a margin of $\lambda = 2, 7699$.

B. *Simulation results of the system using Static Var Compensator (SVC)*

After having calculated the power flow in the network (14 bus bars), without the presence of the SVC element, the case of integration of a single SVC is treated (Fig. 6), the SVC is connected to the bus bar number 14.because it is the most sensitive among the bus bars affected because of the increase of the load, it present a voltage of V= 0.68902 pu.

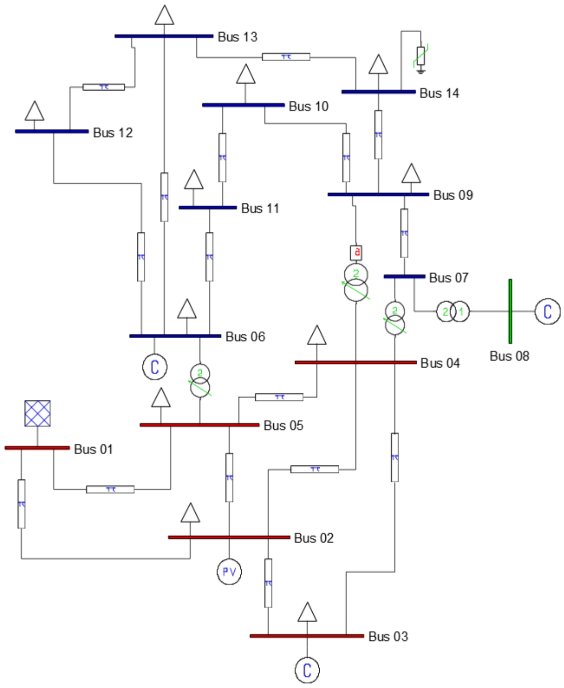

Fig. 6: Integration of a SVC at busbar n°14 in a network of 14 busbars.

The calculation of power flow have been effected with Newton-Raphson method after the SVC insertion, the results are obtained through PSAT. The table 3 illustrates these results.

TABLE III:
Voltages and angles of 14 bus bars network with SVC

BUS BAR NUMNE R	***PSAT***	
	voltage VM (pu)	***Angle (deg)***
1	1.06	0
2	1.045	-4.9999
3	1.01	-12.7822
4	1.011	-10.2416
5	1.0157	-8.7526
6	1.07	-15.1508
7	1.0462	-13.5205
8	1.09	-13.5205
9	1.0265	-15.1814
10	1.0266	-15.4582
11	1.0445	-15.4182
12	1.0509	-15.9538
13	1.0423	-15.8872
14	1.0000	-16.1481

As shown in the table 3 the integration of the SVC at the bus bar number 14 provides a considerable improvement in the voltages.

The continuous power flow (CPF) analysis in the case of the presence of an SVC gives the P-V curves shown in the fig.7.

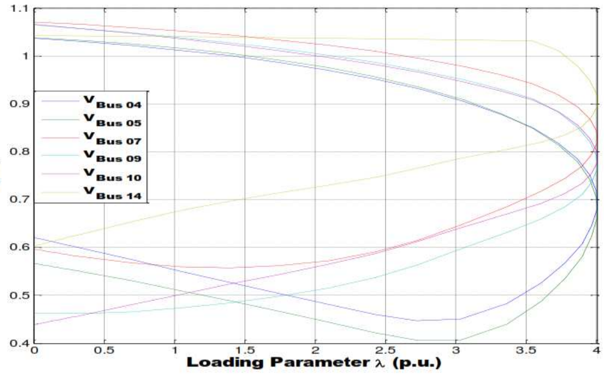

Fig. 7: P-V curves of sensitive bus bars.

It can be seen that the voltage stability margin is significantly improved with λ = 4.0017.

V. CONCLUSION

The shunt compensation is essentially intended for the adjustment of the voltage, the static compensator of the reactive power (SVC) can contribute very effectively to maintain the voltage plane in an acceptable margin (1pu). Therefore, we conclude that by connecting the SVC in the optimal location we get the best improvement in term of and stability margin the voltage.

REFERENCES

[1] MR MEFTOUHI ABDELMAK «influence des FACTS sur l'écoulement de puissance dans les réseaux d'énergie électriques »thèse de magister, département d'électrotechnique école doctorale de génie électrique (USTO), université d'Oran, 2012.

[2] G. Statistics: 'Global Wind Energy Council', April 2017. [Online]. Available: http://gwec.net/global-figures/graphs/.

[3] L. CAI, «Robust Coordinated Control of FACTS Devices in Large Power Systems » These de Doctorat, Université de Duisburg-Essen, 2004.

[4] GERALD IBE « concepts of reactive power control and voltage stability methods in power system network », university of technology Owerri Imo State, Nigeria,2013.

[5] E CATZ, non- Membre IEEE, « Evolutions techniques du système de transport et de distribution d'électricité » .Article de Emmanuelle CATZ France.

[6] Etude de l'Ecoulement de Puissance Optimal par la Méthode de Newton en Présence des Dispositifs FACTS (SVC)

[7] Ajeet Kumar Rawat, «Reactive Power Compensation in Single Phase Distribution System using SVC, STATCOM & UPFC»,EE Department KNIT Sultanpur, U.P India, 2017

[8] Mrs. Manisha patel « Reactive power compensation using STATCOM»,Mahavir Swami College of Engg. & Tech., Gujarat, India,2017

[9] Ashraf Mohamed Hemeida, «Power systems stabilization using svc and statcom»,Aswan University,Egypte,2010

[10] O. L. BEKRI, « OPTIMAL PLACEMENT OF SVC AND TCSC QDEVICES TO ENHANCE VOLTAGE STABILITY»,University Dr. Moulay Tahar, Saïda, Algeria,2010

[11] Rim BEN ALI "Design, Modeling and Simulation of Hybrid Power System (Photovoltaic-WIND)", Ecole Nationale d'Ingénieurs de Tunis, Tunisie,2016.

[12] B.U.Musa et Kalli .B. M, "Modeling and Analysis of Hybrid Solar/Wind Power System for a Small Community", Journal of Electrical and Electronics Engineering, Volume 10, Issue 1 Ver. I PP 39-45, 2015.

[13] T.ahmed et A.abd el ghani, "La commande de la puissance active et réactive d'une éolienne à génératrice synchrone," Revu des Energies Renouvlables, vol. 10, pp.327-335 ,2010.

Reliability of the APF in Wind Power Conversion Chain Network Using FLC Regulator

F. BOUROUROU[#1], S.A. TADJER[#2], I. HABI[#3], K. IFRAH[#4]

[#] *Département d'Automatisation des Procèdes et Electrification, Université M'Hamed Bougara de Boumerdes*
55 avenue de l'indépendance,35000, Boumerdes, LREEI, Algérie
[1]`f.bourourou@univ-boumerdes.dz`
[2]`s.tadjer@univ-boumerdes.dz`
[3]`i.habi@univ-boumerdes.dz`

***Abstract*-- This paper focus on regulation of the parallel active power filter (APF) Dc Voltage bus by judicious choice of rule bases and intervals for each selected fuzzy variable of suitable fuzzy logic controller. A direct application to the APF capacitor voltage regulation with their simulation, by MATLAB, applied to wind power conversion chain network is presented in the case of a non-linear variable load, after modeling, to show the effectiveness of this kind of regulators on electrical power quality and improve the reliability of the APF on wind power system. All system is simuled under Matlab Simulink; Results are discuted and analyzed to show the APF reliability on harmonic minimization of wind chain and network.**

***Index Terms*— APF, Wind, inverter, Harmonic, FLC.**

1. INTRODUCTION

The classical adjustment of the systems relies mainly on the sizing of the adjustment elements from the modeling of the overall system, but it turns out that this does not always easy to do this. It is here that the main advantage of fuzzy logic regulation resides, in fact this type of technique does not need to establish any model of the system [1-3]. A direct application to the APF capacitor voltage regulation with their simulation, by MATLAB, applied to wind power conversion chain network is presented in the case of a non-linear variable load conditions, after modeling, to show the effectiveness of this kind of regulators on electrical power quality and improve the reliability of the APF on wind power system harmonic reducing.

Where after wind chain modeling and PMSM output voltage regulation using PI controller we will present the mains knowledge of the proposed APF and the FLC controller, in the last we will present the simulation results under Matlab Simulink of each parts of the studied system described on the next step.

2. DESCRIPTION OF THE STUDIED SYSTEM

Our study presents the architecture "structure" of regulating the voltage delivered by a PMSM driven by a wind turbine via gear box controlled by a PI regulator [4], this after we present the model of each part of the conversion chain and the results of wind variation influence on the stability of PMSM output voltage amplitude, Wind profile is modeled as a fractional scalar evolves over time [5, 6]. PMSM supply a nonlinear load from the rectifier installed on the output of the conversion chain via a controlled power inverter. To see the influence of the FLC regulator on the quality of the filtering we have use a 3x3rules fuzzy regulator implanted in the control part of the APF [1,2,7], where the membership functions of the input and the output variables are shown in figure1.Simulation Bloc is presented by "fig 1".

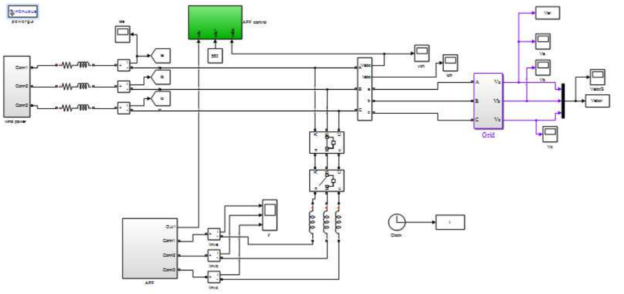

Fig. 1. Simulation Bloc of the proposed system.

3. MATHEMATIC MODELING & SIMULATION

fig.2 present an overall scheme which describe the various essential parts dedicated to the conversion of the wind power into electrical energy based on permanent magnet synchronous machine mechanically coupled with a wind turbine via a reduction gearbox, the latter is driven by a wind profile that will be modeled and simuled under Matlab Simulink Software.

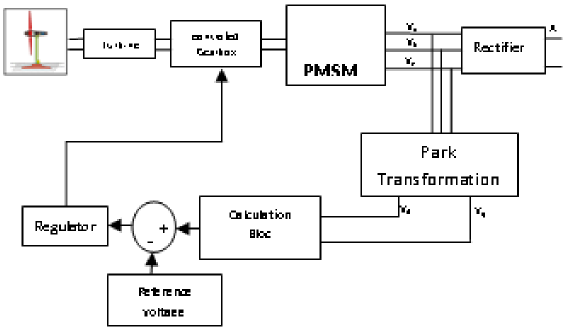

Fig. 2. wind power conversion chain PI closed loop regulator.

Where, Wind speed can be modeled as a fractional scalar evolves over time as in “(1)”

$$v_v = f(t) \tag{1}$$

Wind speed can be represented as a function of harmonics as in (2).

$$v_v(t) = A + \sum_{n=1}^{i} a_n \sin(b_n\, w_v t) \tag{2}$$

Equation “(3)” represent an uncertain wind profile evolve around a known medial value

$$v_v = 9 + 0,2\sin(0,10477t) + 2\sin(0,2665t) + \sin(1,2930t) + 0,2\sin(3,6645t) \tag{3}$$

uncertain wind profile is presented on “fig.3”

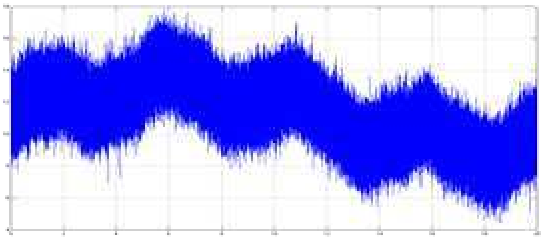

Fig. 3. Uncertain wind profile.

Where the PMSM voltage output befor PI regulation is shown on “fig. 4”

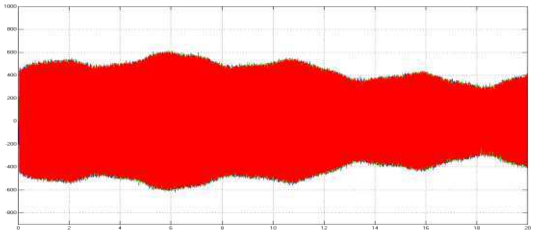

Fig. 4. PMSM output voltage (open loop)..

After closed loop PI controller installation output voltage was stable as shown on “fig. 5”

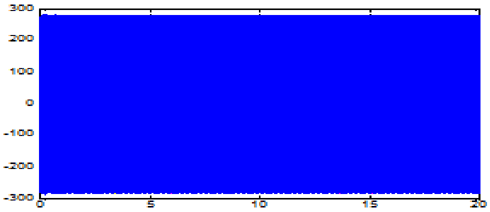

Fig. 5. PMSM output voltage (PI closed loop)..

After that we have a wind power converted to a stable tri-phases voltage by the PMSM and the PI controller loop; we will use the rectifier presented on “fig.6” modeled and implanted under Matlab Simulink to coupling the PMSM to the network via a power inverter

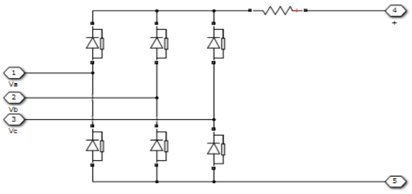

Fig. 6. Network coupling rectifier.

Presented by the simulation bloc “fig.7” after mathematic modeling on dq frame presented in (4), (5) below

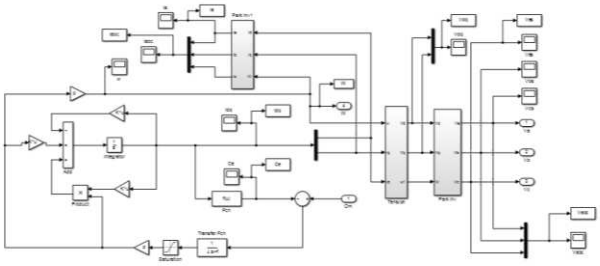

Fig. 7. PMSM simulation Bloc under Matlab.

$$v_d = R_s i_d + L\frac{d}{dt} i_d + w_r L_q i_q \tag{4}$$

$$v_q = R_s i_q + L_q \frac{d}{dt} i_q + w_r (L_d i_d + \Phi_f) \tag{5}$$

Where the simulation bloc of the studied network is shown in “fig.8”

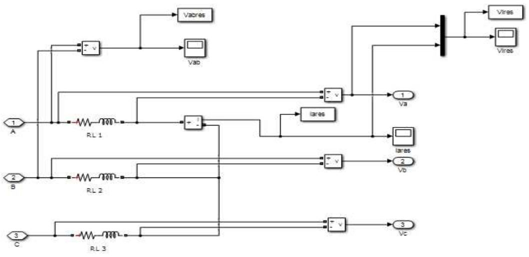

Fig. 8. Network Simulation Bloc.

network load current shown on “fig.9” show clearly the presence of The 5,7 and 11 harmonic due to the presence of a nonlinear loads on the network

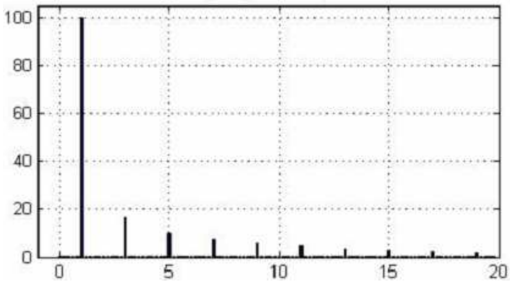

Fig. 9. Network Current Harmonic specter before filtering [4].

For the minimization of the undesired influence of harmonic on network we have propose to integrate an APF controlled by a PI controller in the first time then by a more efficiency and modern controller the FLC [7], [9], [10] as shown on “fig.1”

The FLC based on the principle summarized on “fig.10”

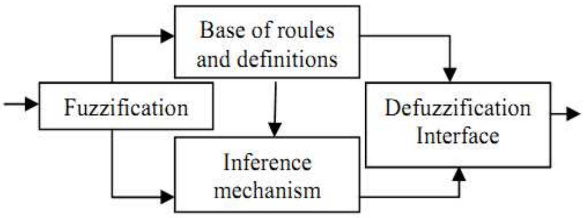

Fig. 10. Fuzzy Logic Controller general structure.

Where the chosen member sheep functions for error *e(t)*, error variation *de(t)* and control output *u(t)* are shown on “fig.11”

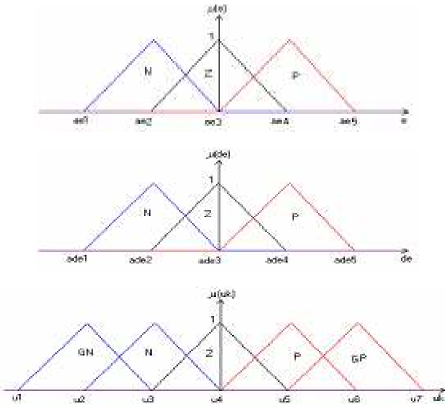

Fig. 11. FLC member sheep functions.

Simulation results shown that the installation of the APF on the network helps on harmonic minimization as improve the harmonic specter of “fig.12”

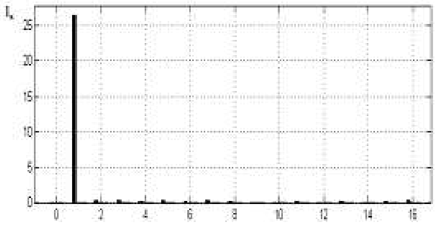

Fig. 12. Harmonic specter with APF use FLC

This let network current, shown on “fig.13”, be more near to the sinusoidal wave and the THD value decrease.

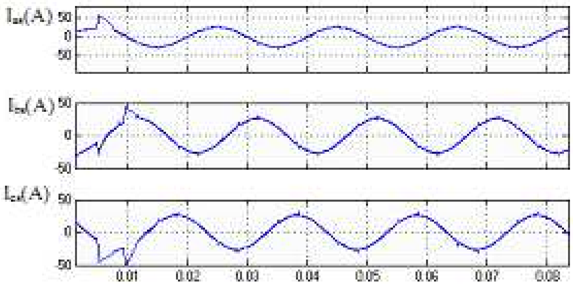

Fig. 13. Network Current after APF installation.

The APF current is shown on “fig.14” below

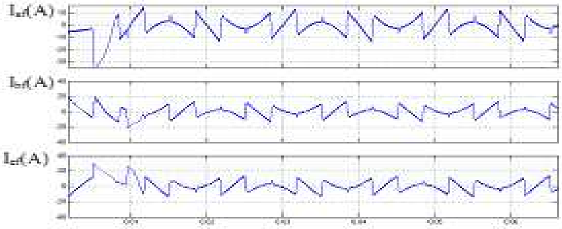

Fig. 14. APF injected Current.

So, APF installation on network has decrease the harmonic presence and this make the wind conversion chain more reliable and the regulation system working well as if the THD is more important.

The Dc voltage of APF capacitor is stabilized by de PI regulator first, as shown on “fig.15”,

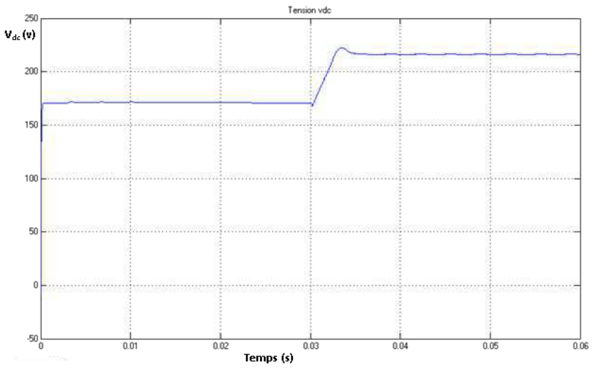

Fig. 15. APF Capacitor DC voltage regulation with PI.

then by FLC as shown on “fig.16

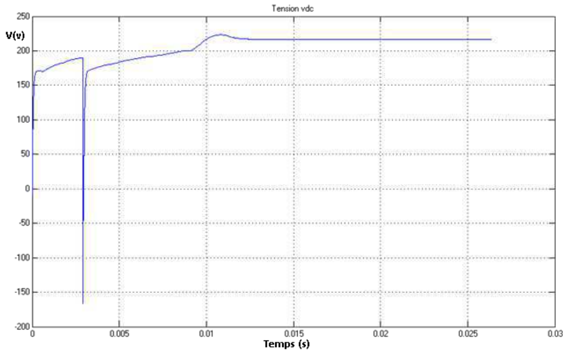

Fig. 16. APF Capacitor DC voltage regulation with FLC.

ISSN 1737-9334

We can see clearly that response time and depasement in case of FLC regulator is less then that with PI controller.

CONCLUSION

In this work we have present a wind conversion chain model oriented to the simulation, that's output voltage has been regulated by a PI controller then connected to the network via a rectifier connected to an inverter supply nonlinear loads, nonlinear loads harmonic has been decries by the use of an APF controlled by a FLC, the APF installation on the network has decrease the THD of the network current.

In the last we hope applied more intelligent techniques to the studied system to have more suitable results in other works applied on laboratory.

ACKNOWLEDGMENT

Bay this work I would send acknowledge to LREEI laboratory director, Prf Nadji Bouchra, and to my thesis director, Prf Habi Idir.

REFERENCES

[1] GHADBANE Ismail, "Etude Et Réalisation D'un Filtre Actif Parallèle En Utilisant Différentes Stratégies De Contrôle", Thèse Doctorat en sciences, Electrotechnique, Université Mohamed Khider – Biskra, 2016.

[2] Tadjer Sid Ahmeda, , Habi Idir,, El Ganaoui Mohamedb, Angel Scipioni, "Direct components extraction of voltage in photovoltaic active filter connected in a perturbed electrical network (based on robust PLL algorithm)", International Conference on Technologies and Materials for Renewable Energy, Environment and Sustainability, TMREES15; science direct Energy Procedia74 (2015) 966 – 972, 2015.

[3] L. Zelloumaa, B. Rabhib, S. Saadc, A. Benaissad, M. F. Benkhorise "Fuzzy logic controller of five levels active power filter", Energy Procedia 74 (2015) 1015 – 1025, elsevier 2015.

[4] Laid zellouma, Boualaga rabhi, Abdelbasset krama, Amar benaissa, m.f. Benkhoris,"simulation and real time implementation of three phase four wire shunt active power filter based on sliding mode controller", Rev. Roum. Sci. Techn.– Électrotechn. et Énerg, Vol. 63, 1, pp. 77–82, Bucarest, 2018.

[5] Khechiba kamel, , Zellouma Laid, Kouzou abdallah, Hafaifa Ahmed, Khiter Anissa, "Comparison of Control Strategies for Shunt Active Power Filters in Three-Phase Three-Wire Systems", The 3rd International Conference on Power Electronics and their Applications ICPEA 2017, 16-17 September 2017, Djelfa, Algeria

[6] BELHAOUCHET NOURI, "Fonctionnement à Fréquence de Commutation Constante des Convertisseurs de Puissance en Utilisant des Techniques de Commande Avancées Application : Amélioration de la Qualité de l'Energie", Thèse Doctorat en sciences, Electrotechnique, Université FERHAT ABBAS – SETIF, 2011.

[7] Ahmed Abdalrhman, Abdalhalim Zekry, and Ahmed Alshazly. "Simulation and Implementation of Grid-connected Inverters". International Journal of Computer Applications, VOL. 60,NO. 4, PP 41-49, December 2012.

[8] Han-Xiong Li and H.B.Gatland, "New methodology for designing a fuzzy logic controller", IEEE transactions on systems, man, and cybernetics, Vol.25, No. 3, March 1995.

[9] A. Mirecki,'Etude Comparative de Chaine de Conversion d'energie Dédiées à une Eolienne de petite puissance', Thèse de Doctorat, Institut polytechnique de Toulouse, Avril 2005.

[10] ChuenChien Lee, "Fuzzy logic in control systems: Fuzzy logic controller-Part I", IEEE transactions on systems, man, and cybernetics, Vol.20, No. 2, March / April 1990.

[11] ChuenChien Lee, "Fuzzy logic in control systems: Fuzzy logic controller-Part II", IEEE transactions on systems, man, and cybernetics, Vol.20, No. 2, March / April 1990.

[12] Y.Soufi et T.Bahi et M.F Harkat et M.Mohamedi, "Optimisation De La Conversion De L'énergie Eolienne," Revu des Sciences Fondamentales et Appliquées, vol. 2, pp. 201–210, April 2010.

[13] H.faida et J.Saadi et M.Khaider et S.El Alami et M.Monkadel, "Etude et analyse des données du vent en vue de dimensionner un système de production d'énergie éolienne cas d'un site au nord du maroc," Revu des Energies Renouvelables, vol. 13, pp.477–483, 2010.

[14] H.chennoufi et L.lamri et L.ahmed et K.abdemalek , "Contrôle d'une génératrice synchrone à aimant permanant dédiée à la conversion de l'énergie éolienne par la commande directe du couple," Revu des Energies Renouvelable, pp. 115–124, 2010.

[15] M.T. Benchouia, I. Ghadbane, A. Golea, K. Srairi, M.E.H. Benbouzid, "Implementation of adaptive fuzzy logic and PI controllers to regulate the DC bus voltage of shunt active power filter", Applied Soft Computing, 28, pp. 125–131,2015.

[16] Math Works, 2001, What is SIMULINK, the Math Works, Inc. M.

[17] F. Chevrie, F. Guély, "Logique Flou" Extrait du Cahier Technique Schneider n° 191, mars 1998.

[18] Michel Etique, "Régulation automatique", Yverdon-les-bains, octobre 2004.

[19] SBA. Abdelbaki, "Commande en temps réel d'un filtre actif de puissance utilisant la technique par logique floue", thèse de magistère, spécialité automatique, Université Ferhat Abbas- Sétif, Algerie, 2005.

[20] T.Etienne, "contribution à la commande de l'éolienne a mada en permettant l'amélioration de la qualité de l'onde du réseau électrique, ", mémoire présenté à l'école de technologie supérieure université québec,2009.

Simulation of the Stator and Rotor Winding Temperature of the Induction Machine for Continuous Service -Service Type S1 - Operation for Different Frequency

Hacene MELLAH[#1], Kamel Eddine HEMSAS[*2], Rachid TALEB[#3]

[#] *Department of Electrical Engineering, LGEER Laboratory, Faculty of Technology, University of Chlef, Algeria*
[*] *Department of Electrical Engineering, LAS Laboratory, Faculty of Technology, Ferhat Abbas Sétif 1 University, Algeria*
[1] `has.mel@gmail.com`
[2] `hemsas.kamel@gmail.com`
[3] `ras.taleb@gmail.com`

Abstract— **The temperature of electrical machines is one of the main factors limiting their performance. This temperature must respect the limits imposed by design and must not exceed them. Therefore, in order to be able to predict the temperature rise in the machines, thermal models are used. These allow on the one hand to thermally modeling the machines for monitoring, on the other hand to improve their design. This model must respect the complexity of the thermal phenomena by being able to take into account certain modifications on the design. This model must also consider the types of service of the machine, whether continuous, intermittent, and temporary or other types of service. In this paper, we deal with simulation of service type s1 - continuous service for different frequency of an induction motor. The main goal of this study is to prove the influence of the constant losses depend to the frequency to the stator and rotor winding temperature, the simulation results demonstrate to effect of the frequency to the temperature.**

Keywords—- **Thermal Model, Winding Temperature, Induction Motor**

I. INTRODUCTION

Nowadays, the asynchronous machine is used more and more in the industrial domain. Indeed, appreciated for its standardization, its great robustness and its low costs of purchase and maintenance. For several years, we have noticed the widening of the scientific and manufacturer works concerning the drive of these machines [1]. The research of the electromechanical devices more and more flexible supported the appearance of the new particularly powerful systems. These systems generally rest on the association of an electronic device, allowing the control of the global system, and a rotating machine ensuring electromechanical conversion [1-3]. However, the increase in the specific powers and the use of novel control modes induce the harmonics of time [2] with frequencies beyond the audible aria, even with square wave voltages [1], the adaptation of the machines to these new applications generates an important internal heating. A rigorous study of the thermal behaviour of the electric machines is increasingly necessary [2]. Many authors describe the use of sensor as solution to the thermal problems of the induction machine [3] like infrared sensor [4, 5], thermocouple [5-9]. On the other hand, the infrared sensor gives a surface temperature measurement so the measurement is not accurate [3], and the thermocouple can require some machining for a correct placement, but it has the merit to be able to provide internal temperatures in exiguous places of the machine [3]. The problem of obtaining the rotors thermal information gene the sensor measurement procedure to be successful, however some solutions in the specialized literature can be cited, an optical link between the stator and the rotor proposed in [5-12]. Michalski et all in [5] propose an industrial rotary transformer, using a rings and brushes, a high frequency or infrared modules, all these methods are discussed in [3]. Some authors to avoid the problems of temperature measurement in electrical machines; proposes the use of the estimator and observer as Kalman [13-15], Luenberger [16] or based on artificial neural network [17, 18].

Zhao *et al* in [19] proposes an online rotor temperature estimation method of induction machine based on the noninvasive measurements of current and potential sensors.

Moreno et al. study the effect of frequency on the stator and rotor winding temperature but with their model [20]. In this paper, we use the model created by Al-Tayie et all in [15] to illustrate these effects.

II. LOSS IN ELECTRICAL MACHINES

Many authors [21-23] deal with the electrical machines loss model and their dependence on frequency and temperature.

Dong *et al.* in initial study use the time-step FEM to compute the winding ac losses in the end and slot winding at different speeds as represented in Fig. 1 [21]. In fact, the additional loss at ac input in the slot winding increases with frequency much faster than that in the end-winding, according to the amplification effect of the core on the leakage magnetic field, to simplify the study assume that the conductors are uniformly distributed in the slot.

ISSN 1737-9334

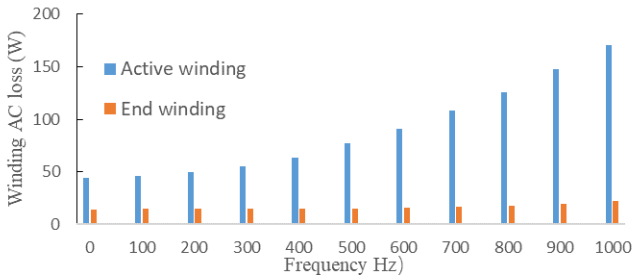

Fig. 1 Winding loss at different frequencies. Current amplitude: Im=6Arms [21].

Dong *et al.* [21] propose a fast and accurate analytical model to compute iron loss of inverter-fed induction machine, the advantage of this approach is able to takes account of the influence of the output voltage harmonics from the inverter on the iron loss of the motor based on the piecewise variable coefficients method. In addition, the proposed method incorporates slot harmonic component's influence on iron loss [21].

Xue *et al.* [22] study and proves by experiment that both the hysteresis and eddy current losses of non-oriented Si-steel laminations is a dependent on temperature.

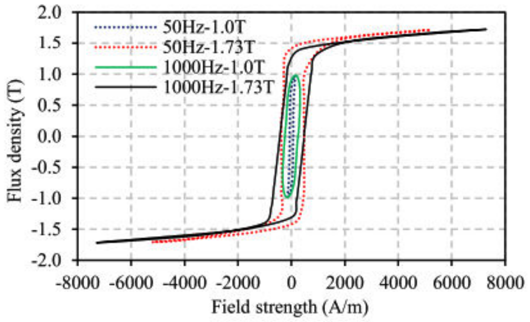

Fig. 2 Measured B–H loops at 40 °C when frequency is 50 and 1000 Hz [22]

Fig. 2 shows the measured B–H loops at 40 °C for two value of frequency 50 and 1000 Hz. We can see clearly that the B–H curves is distorted when the flux density is high due to the saturation at both 50 and 1000 Hz. The shape of B–H curves, which represents the iron losses in a time period, is frequency and flux density dependent [22].

Fig. 3 shows the comparison of the predicted iron loss by the model with the measured iron loss at different lamination temperatures. The modeled is able to accurately predict the iron loss at different flux densities and different frequencies when the lamination temperature remains 40 °C. However, the iron loss could vary significantly when the temperature increases from 40 °C to 100 °C, as shown in Fig. 3. However, the predicted iron loss cannot reflect this variation. Therefore, the prediction accuracies of this existing model can be significantly degraded when the temperature changes. The measured iron loss results show that both the hysteresis and eddy current losses vary linearly with temperature between 40 °C to 100 °C, a typical temperature range of electrical machines [23].

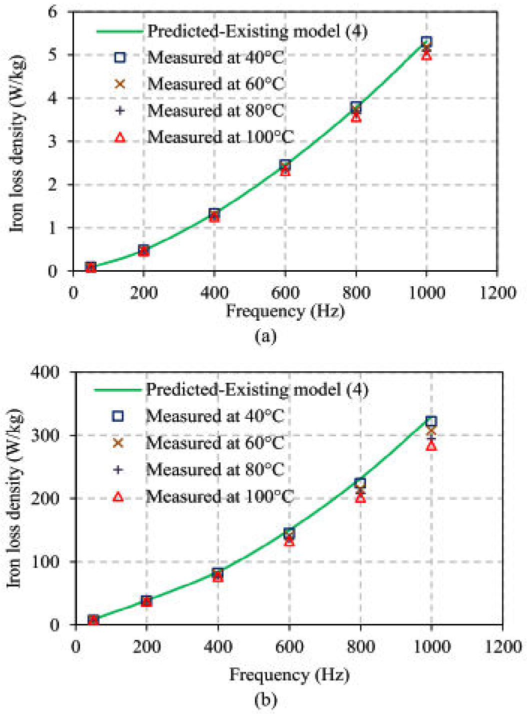

Fig. 3 Measured iron loss and predicted iron loss of existing model (4). (a) Bm =0.2 T. (b) Bm=1.73 T [23].

Xue *et al.* in [23] interested on the iron loss prediction for electrical machines fed by low switching frequency inverter, as results he summarize here results that the PWM influence on the iron loss on the electrical machines can be significantly increase, especially when the switching frequency is low.

III. A REVIEW OF THERMAL MOLDING METHODS

In the specialized literature, we find several thermal model of induction motors; we can summarize this model by three types.

A. *Simple Modeling*

We find many simple approaches in the literature in order to give bonds between the stator temperature and the rotor temperature. Beguenane *et al.* [24, 25] propose a model based on the electrical rotor resistance identification, which is unfortunately unable to identify the stator resistance; however, these articles propose two thermal approaches to bind two resistances of the electric model:

(1) The first method based on the EDF (Électricité De France) experiment. It considers that the rotor has a temperature higher of 10 °C than that the stator temperature;

(2) The second method based on work of Kubota [26]. It gives a simple relation of proportionality between two resistances calibrated on the face values of the maker badge. We find the proportionality method in other paper like [27]. On the other hand, later works were realized on EDF model

ISSN 1737-9334

and put a flat as for its validity for all the operating processes, especially NEMA design D machines with 8-13% slip [28].

B. Fine Modelling

It is based on the use of the finite element method with a detailed model geometric and mechanics. This makes it possible to obtain a complete cartography of the machine temperatures (Fig. 4). These results are very interesting since they make it possible to give an idea of the places where the temperature becomes critical according to the operations and answer the problems of the hot points [2, 3, 12].

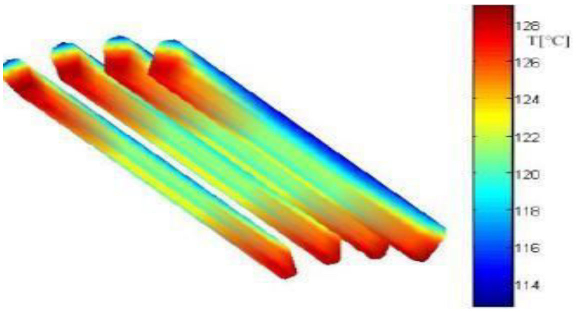

(a). Steady state stator winding temperature

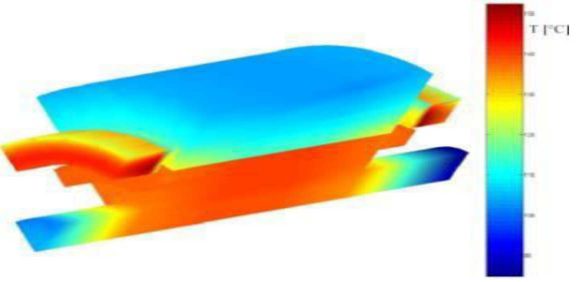

(b) Thermal cartography portion

Fig. 4 Thermal cartography portion of an induction machine, obtained by finite elements [12].

C. Electrical Equivalent Supply Networks (NODAL Method)

Those generally model the whole of the machine with nodes of temperature associated each material and divides the machine homogeneous region [26, 27]. The identification of this model is thus carried out either by finite elements, or by a great number of points of temperature measurement within the machine. These models are generally very detailed (Fig. 5) and thus too complex for our application in real time [26].

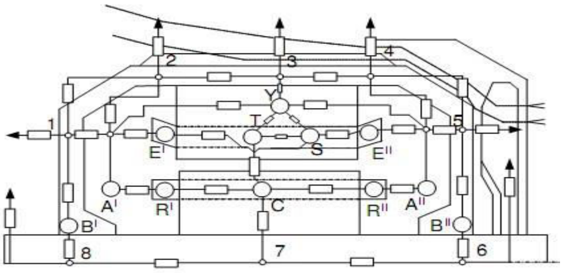

Fig. 5 Equivalent thermal models of the induction machine [4].

D. Simplified Models

Other researchers sought to simplify the models by gathering the losses in subsets and by approximating the temperature in an unspecified point with a simple exponential answer that one can simply represent by a resistance and a heat capacity (Fig. 6) [7, 17].

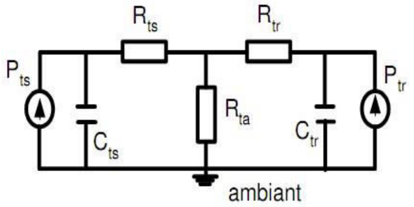

Fig. 6 Thermal model of the induction machine [7].

IV. THERMAL MODEL OF INDUCTION MOTOR

A variable-state model of the induction motor is required for the EKF algorithm. The twin-axis stator reference frame [15] is used to model the motor's electrical behavior, because physical measurements are made in this reference frame; the well-known linear relationship between resistance and temperature must be taken into account for the stator and rotor resistance.

$$R_s(\theta_s) = R_{s0}(1+\alpha_s\theta_s)$$
$$R_r(\theta_r) = R_{r0}(1+\alpha_r\theta_r) \qquad (1)$$

Where: R_{s0}, R_{r0} stator and rotor resistance at the ambient temperature, **α_s** and **α_r** their thermal coefficients. In the electrical equation of IM model, we replace the fixed resistance Rs and R_r by an adaptive resistance Rs(θs) and Rr(θr), the electrical model is as fellow [15]:

$$\delta\frac{di_{ds}}{dt} = -R_s(\theta_s)L_2\, i_{ds} + L_m^2\,\omega_r\, i_{qs} + R_r(\theta_r)\,L_m\, i_{dr}$$
$$+L_2\,L_m\;\omega_r\, i_{qr} + L_2\,V_{ds} \qquad (2)$$

$$\delta\frac{di_{qs}}{dt} = -L_m^2\omega_r\, i_{ds} - R_s(\theta_s)L_2\, i_{qs} - L_2L_m\omega_r\, i_{dr}$$
$$+R_r(\theta_r)L_m\omega_r\, i_{qr} + L_2V_{qs} \qquad (3)$$

$$\delta\frac{di_{dr}}{dt} = \quad R_s(\theta_s)L_m\, i_{ds} - L_1L_m\,\omega_r\, i_{qs}$$
$$-R_r(\theta_r)L_1 i_{dr} - L_1\,L_2\;\;\omega_r\;\, i_{qr} + L_2V_{qs} \qquad (4)$$

$$\delta\frac{di_{qr}}{dt} = -L_1L_m\omega_r\, i_{ds} - R_s(\theta_s)L_2\, i_{qs}$$
$$-\,L_1L_2\omega_r\, i_{dr} + R_r(\theta_r)L_1\, i_{qr} + L_m\,V_{qs} \qquad (5)$$

Where : $\delta = L_1L_2 - L_m^2$, L_1 and L_2 stator and rotor self-inductances.

The mechanical behavior is as fellow:

$$T = b\,\omega_r + j\,p\,\omega_r + T_L \qquad (6)$$

However, the electromagnetic torque T can represented as a function of the stator and rotor current:

$$T = pL_m(i_{qs}i_{dr} - i_{ds}i_{qr}) \tag{7}$$

By equality of these two preceding equations, the speed equation is:

$$\frac{d\omega_r}{dt} = \frac{pL_m}{j}(i_{qs}i_{dr} - i_{ds}i_{qr}) - \frac{b}{j}\omega_r + \frac{T_L}{j} \tag{8}$$

The thermal model is derived by considering the power dissipation, heat transfer and rate of temperature rise in the stator and rotor. The stator power losses include contributions from copper losses and frequency- dependent iron losses [15].

$$pL_s = (i_{qs}i_{dr} - i_{ds}i_{qr})R_s(\theta_s) + k_{ir}\,\omega_r \tag{9}$$

Where: k_{ir} is it constant of iron loss. The rotor power losses are dominated by the copper loss contribution if the motor is operated at a low value of slip so:

$$pL_r = (i_{dr}^2 - i_{qr}^2)R_r(\theta_r) \tag{10}$$

Where: H_s, H_r are the stator and the rotor heat capacity respectively. A simple representation of the assumed heat flow is given in Fig. 7.

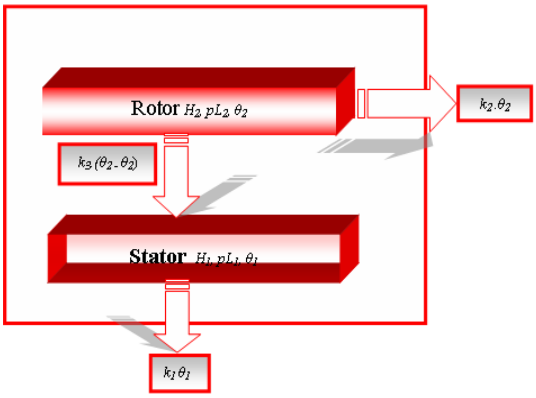

Fig. 7 Thermal model structure

Heat flow from the rotor is either directly to the cooling air with heat transfer coefficient k_2, or across the air gap to the stator with heat transfer coefficient k_3 [15].

$$pL_r = k_2\theta_r + H_r p\theta_r + k_3(\theta_r - \theta_s) \tag{11}$$

Heat flow from the stator is directly to the cooling air, with heat transfer coefficient k1[15]:

$$pL_s = k_1\theta_s + H_s p\theta_s - k_3(\theta_r - \theta_s) \tag{12}$$

For an induction motor with a shaft mounted cooling fan, the heat transfer coefficients are dependent on the rotor speed. This dependence has been modeled approximately by a set of linear relationships:

$$k_1 = k_{10}(1 + k_{1\omega}\omega_r) \tag{13}$$

$$k_2 = k_{20}(1 + k_{2\omega}\omega_r) \tag{14}$$

$$k_3 = k_{30}(1 + k_{3\omega}\omega_r) \tag{15}$$

Where: k_{10}, k_{20} and k_{30} thermal power transfer coefficients at the zero speed. k_{1w}, k_{2w} and k_{3w} variation of thermal power transfer with speed. Substitution into equations15 and 16 in the equations 13,14,17,18 and 19, and rearranging yields the thermal state equations for the stator and for the rotor [15]:

$$p\theta_s = \frac{R_s(\theta_s)}{H_s}(i_{ds}^2 + i_{qs}^2) + \frac{k_{ir}}{H_s}\omega_r^2 - \frac{k_{10}(1 + k_{1\omega}\omega_r)}{H_s}\theta_s + \frac{k_{30}(1 + k_{3\omega}\omega_r)}{H_s}(\theta_s - \theta_r) \tag{16}$$

$$p\theta_r = \frac{R_r(\theta_r)}{H_r}(i_{dr}^2 + i_{qr}^2) - \frac{k_{20}(1 + k_{2\omega}\omega_r)}{H_r}\theta_r + \frac{k_{30}(1 + k_{3\omega}\omega_r)}{H_r}(\theta_s - \theta_r) \tag{17}$$

The whole of preceding equations (6) a (9), (12), (20), and (21) us the model of following state:

$$p\delta i_{qr} = -L_1L_m\omega_r i_{ds} - R_s(\theta_s)L_2 i_{qs} - L_1L_2\omega_r i_{dr} + R_r(\theta_r)L_1 i_{qr} + L_m V_{qs} \tag{18}$$

$$p\delta i_{ds} = -R_s(\theta_s)L_2 i_{ds} + L_m^2\omega_r i_{qs} + R_r(\theta_r)L_m i_{dr} + L_2L_m\,\omega_r i_{qr} + L_2V_{ds} \tag{19}$$

$$p\delta i_{dr} = R_s(\theta_s)L_m i_{ds} - L_1L_m\omega_r i_{qs} - R_r(\theta_r)L_1 i_{dr} - L_1L_2\,\omega_r i_{qr} + L_2V_{qs} \tag{20}$$

$$p\delta i_{qs} = -L_m^2\omega_r i_{ds} - R_s(\theta_s)L_2 i_{qs} - L_2L_m\omega_r i_{dr} + R_r(\theta_r)L_m\omega_r i_{qr} + L_2V_{qs} \tag{21}$$

$$p\omega_r = p_nL_m(i_{qs}i_{dr} - i_{ds}i_{qr}) - \frac{b}{j}\omega_r + \frac{T_L}{j} \tag{22}$$

$$p\theta_s = \frac{R_s(\theta_s)}{H_s}(i_{ds}^2 + i_{qs}^2) + \frac{k_{ir}}{H_s}\omega_r^2 - \frac{k_{10}(1 + k_{1\omega}\omega_r)}{H_s}\theta_s + \frac{k_{30}(1 + k_{3\omega}\omega_r)}{H_s}(\theta_s - \theta_r) \tag{23}$$

$$p\theta_r = \frac{R_r(\theta_r)}{H_r}(i_{dr}^2 + i_{qr}^2) - \frac{k_{20}(1 + k_{2\omega}\omega_r)}{H_r}\theta_r + \frac{k_{30}(1 + k_{3\omega}\omega_r)}{H_r}(\theta_s - \theta_r) \tag{24}$$

This model has been tested and validated for several of operation of the induction motor, for more information the interested reader is invited to see [15].

ISSN 1737-9334

V. SIMULATION RESULTS

The main purpose of this simulation is to consider the influence of constant losses (hysteresis and eddy current) due to the frequency, the simulation results are illustrated in Figures 8 and 9. We note that the stator and rotor temperature at 60Hz is greater than the 50Hz.

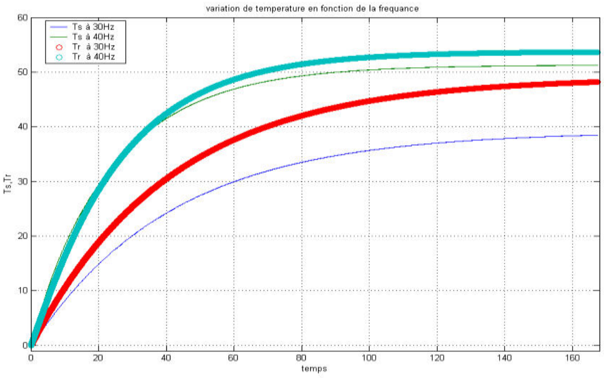

Fig. 8 stator and rotor temperature at 40 and 30 Hz

The stator and rotor temperature at 40Hz is greater than that at 30Hz.

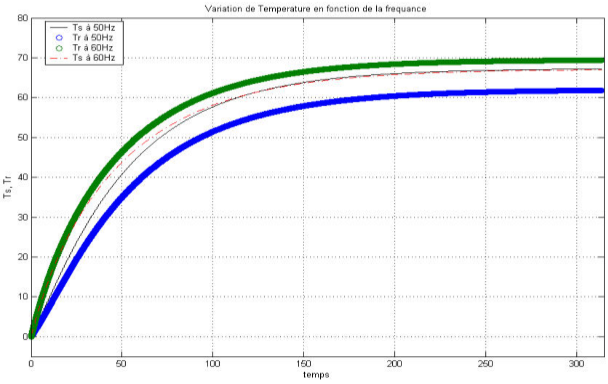

Fig. 9 stator and rotor temperature at -0 and 50 Hz

VI. CONCLUSION

In this paper, we presented a thermal model of a squirrel cage induction motor. This model is based on the theory of power dissipation, heat transfer and the rate of temperature increase in the rotor and stator, taking into account the effect of speed on the exchange. We summarize our results as that the temperature increase with the increasing of the frequency, this increasing is justified since the iron losses is a frequency depend and these losses transformed to heat.

ACKNOWLEDGEMENTS

This work was supported in part by Electrical Engineering Department, Department of Electrical Engineering, University of Chlef, UHBC, Algeria and in other part by Algerian ministry of research and High education.“

REFERENCE

[1] J. P. Bellomo, T. Lebey, F. Peltier and J. M. Oraison, “Conséquences des nouvelles formes de commande sur les matériaux de l'isolation statorique,” Journal de Physique III, vol. 7, pp. 993–1008, 1997.

[2] R. Glises, G. Hostache, and J. M. Kauffmann, “Simulation du comportement thermique en régime permanent d'un moteur asynchrone à refroidissement extérieur. Etude par éléments finis,” Journal de Physique III, vol. 4, pp. 1723–1735, 1994.

[3] H. Mellah, “Estimation des Grandeurs Intrinsèques d’une Machine Asynchrone,” 2018.

[4] E. Foulon, “Surveillance thermique de la machine asynchrone,” PhD thesis, Université de Nantes, 2005.

[5] L. Michalski, K. Eckersdorf, J. Kucharski and J. McGhee, Temperature Measurement, John Wiley & Sons, New York. 2002.

[6] H. Yahoui, and G. Grellet, “Measurement of physical signals in the rotating part of an electrical machine by means of optical fibre transmission, Measurement,” vol. 20, pp. 143–148, 1997.

[7] K. D. Hurst and T. G. Habetler, “A thermal monitoring and parameter tuning scheme for induction machines,” In IAS'97. Conference Record of the 1997 IEEE Industry Applications Conference Thirty-Second IAS Annual Meeting, vol. 1, pp. 136–142, 1997.

[8] M. Wegmuller, J. P. von der Weid, P. Oberson, and N. Gisin, “High resolution fiber distributed measurements with coherent OFDR,” in Proc. ECOC’00, 2000, paper 11.3.4, p. 109.

[9] E. Chauveau, E. H. Zaim, D. Trichet and J. Fouladgar, “A statistical approach of temperature calculation in electrical machines, IEEE T MAGN.,” vol. 36, pp. 1826–1829, 2000.

[10] S. B. Lee and T. G. Habetler, “An online stator winding resistance estimation technique for temperature monitoring of line-connected induction machines,” IEEE T IND APPL., vol. 39, pp. 685–694, 2003.

[11] Z. Lazarevic, R. Radosavljevic and P. Osmokrovic, “A novel approach for temperature estimation in squirrel-cage induction motor without sensors,” IEEE T INSTRUM MEAS.,” vol. 48, pp. 753–757, 1999.

[12] E. Chauveau, “Contribution au calcul électromagnétique et thermique des machines électriques - Application à l’étude de l’influence des harmoniques sur l’échauffement des moteurs asynchrones,” PhD thesis, Université de Nantes, 2001.

[13] H. Mellah and K.E. Hemsas, “The use of EKF to estimate the transient thermal behaviour of induction motor drive,” Journal of Electrical Engineering, vol. 1, pp. 40–47, 2013.

[14] E. Foulon, C. Forgez and L. Loron, “Resistances estimation with an extended Kalman filter in the objective of real-time thermal monitoring of the induction machine,” IET Electric Power Applications, vol. 1, pp. 549–556, 2007.

[15] J. K. Al-Tayie and P. P. Acarnley, “Estimation of speed, stator temperature and rotor temperature in cage induction motor drive using the extended Kalman filter algorithm,” IEE Proceedings-Electric Power Applications, vol. 144, pp. 301–309, 1997.

[16] H. Nestler and P. K. Sattler, “On-line-estimation of temperatures in electrical machines by an observer,” Electric machines and power systems, vol. 21, pp. 39–50, 1993.

[17] H. Mellah, K. E. Hemsas, R. Taleb and C. Cecati, “Estimation of speed, armature temperature, and resistance in brushed DC machines using a CFNN based on BFGS BP,” Turk J Elec Eng & Comp Sci., vol. 26, pp. 3181–3191, 2018.

[18] H. Mellah, K. E. Hemsas and R. Taleb, “Intelligent Sensor Based Bayesian Neural Network for Combined Parameters and States Estimation of a Brushed DC Motor,” International Journal of Advanced Computer Science and Applications-IJACSA, vol. 7, pp. 2530–235, 2016.

[19] H. Zhao, H. H. Eldeeb, J. Wang, Y. Zhan, G. Xu and O. A. Mohammed, “Online estimation of rotor temperature in induction motors based on parameter identification,” 2019 IEEE Energy Conversion Congress and Exposition (ECCE), Baltimore, MD, USA, pp. 1629-1634, 29 Sept.-3 Oct. 2019

[20] J. F. Moreno, F. P. Hidalgo and M. D. Martinez, “Realisation of tests to determine the parameters of the thermal model of an induction machine,” IEE Proceedings-Electric Power Applications, vol. 148, pp. 393–397, 2001.

[21] T. Dong, X. Zhang, F. Zhou, and B. Zhao, "Correction of winding peak temperature detection in high frequency automotive electric machines," IEEE T Industrial Electronics, 2019.

[22] S. Xue, J. Feng, S. Guo, J. Peng, W. Q. Chu and Z. Q. Zhu, "A new iron loss model for temperature dependencies of hysteresis and eddy current losses in electrical machines," IEEE T MAGN., vol. 54, pp. 1-10, 2018.

[23] S. Xue, J. Feng, S. Guo, Z. Chen, J. Peng, W. Q. Chu and Z. Q. Zhu, "Iron loss model for electrical machine fed by low switching frequency inverter," IEEE T MAGN., vol. 53, pp. 1-4, 2017.

[24] R. Beguenane and M. E. H. Benbouzid, "Induction motors thermal monitoring by means of rotor resistance identification," IEEE T ENERGY CONVER., vol. 14, pp. 566–570, 1999.

[25] R. Beguenane and M. E. H. Benbouzid, "Induction motors thermal monitoring by means of rotor resistance identification," In 1997 IEEE International Electric Machines and Drives Conference Record, pp. TD2–4, 1997.

[26] H. Kubota, D. Yoshihara and K. Matsuse, "Rotor resistance adaptation for sensorless vector controlled induction machines," IEEJ Transactions on Industry Applications, vol. 117, pp. 940–945, 1997.

[27] S. B. Lee, T. G. Habetler, R. G. Harley and D. J. Gritter, "Stator and rotor resistance estimation technique for conductor temperature monitoring," In 35th IAS Annual Meeting and World Conference on Industrial Applications of Electrical Energy, pp. 381–387, 2000.

[28] M. S. N. Sdid and M. E. H. Benbouzid, "HG diagram based rotor parameters identification for induction motors thermal monitoring," IEEE T ENERGY CONVER., vol. 15, pp. 14–18; 2000.

[29] H. Mellah, K. E. Hemsas, A. Zorig and H. Radjeai, "Modélisation et surveillance thermique d'une machine asynchrone on prend on compte les effets no Linière," In International Conference on Power Electronics and Electrical Drives, ICPEED, 2010.

[30] A. T. Abdullah and A. M. Ali, "Thermal analysis of a three-phase induction motor based on motor-CAD, flux2D, and matlab," Indonesian Journal of Electrical Engineering and Computer Sciencem, vol. 15, pp. 46-53, 2019.

M. Schoning, E. Lange and K. Hameyer, "Development and validation of a fast thermal finite element solver," In 2008 18th International Conference on Electrical Machines, pp. 1–5, 2008.

[31] D. Sarkar, P. K. Mukherjee and S. K. Sen, "Use of 3-dimensional finite elements for computation of temperature distribution in the stator of an induction motor," In IEE Proceedings B, vol. 138, pp. 75–86, 1991.

[32] A. Boglietti, A. Cavagnino, D. Staton, M. Shanel, M. Mueller and C. Mejuto, "Evolution and modern approaches for thermal analysis of electrical machines," IEEE T IND ELECTRON, vol. 56, pp. 871–882, 2009.

A Robust Nonlinear Controller for a DFIG System

Ahmed Benzouaoui*[1], Mohamed Fayçal Khelfi[2], Zoubir Ahmed-Foitih[3], Houari Khouidmi[1], Boubaker Bessedik[1]

[1]*Electronics Department, Hassiba Benbouali University of Chlef, Algeria*

[2]*Laboratory of Research in Industrial Computing and Networks, University of Oran 1 Ahmed Ben Bella, Algeria*

[3]*Laboratory of Power Systems, Solar Energy and Automation, University of Sciences and Technology of Oran, Algeria*

*`a.benzouaoui@univ-chlef.dz`

Abstract—**There are many types of controllers reported in the literature for powers doubly fed induction generators (DFIGs). Conventional vector control structures have some disadvantages such as mediocre dynamic performances, parameter tuning complications and reduced robustness. In order to avoid these disadvantages, several approaches were proposed, among them, the sliding mode control. This controller has unfortunately a large chattering on the active and reactive powers developed by stator of the DFIG used in a variable speed wind turbine system. To enhance its performances, a robust non-linear control strategy algorithm based on second order sliding mode with smooth function is presented. The efficiency of this novel topology of control is observed in the results of simulation and especially in chattering-free behaviour, response to a mechanical speed variation and robustness against machine parameters variations.**

Keywords—**Chattering, doubly fed induction generator, five-level inverter, second order sliding mode, wind energy.**

I. INTRODUCTION

In generation of power the wind energy can be considered as the most promising form of renewable energy source. Several national programs and market incentives are held by many countries for promotion wind energy. Advancement in wind generation technology has occurred remarkably during last three decade due increase in rotor size and introduction advanced power electronics to allow variation in speed [1].

Nowadays, the variable speed wind turbine system (WTS) based on DFIG is the most common in onshore wind farms [2]. The principal advantage of the DFIG is that the rotor side converter (RSC) is only sized for 30% of rated power compared to other generators used in variable speed WTSs. Consequently, the cost of the converter becomes lesser [3].

Usually, the DFIG is supplied by two-level PWM inverters. Though, in recent time the multilevel inverters have been more popular because they can result an output voltage waveform with a large number of steps with low harmonic distortion [4-5]. Their higher levels are synthesized from voltage sources with lower levels as a result of that they can help to reduce the stress on switching devices. Due to that it is suitable for application in large and medium induction machine drives. Therefore, in this research, a five-level PWM inverter is selected for the DFIG drive. Many studies have been undertaken with various control diagrams of DFIG. Most of these control diagrams are typically based on vector control notion with conventional PI controllers which were proposed by Pena and al. in [6]. Grid faults appear like unbalanced voltages [7-8] and voltage dips [9] can be sorted by these similar conventional controllers. [10-11] shows that glimmer issues can be sorted by appropriate control techniques.

Many of these studies demonstrate that stator reactive power control can be easily adapted various problems. Recently, the sliding mode control (SMC) technique has been commonly adapted for robust control of nonlinear systems [12-13]. Sliding mode control is based on the theory of variable structure systems (VSS). In last two decades, it has led to huge amount of research on control systems. In addition of a discontinuous control signal across the sliding surface it gets robust control and satisfies the sliding condition. Nonetheless, in this type of control a crucial disadvantage is that it has the chattering phenomenon caused by the discontinuous control action.

In this paper, we present a novel strategy of control of the DFIG which is supplied by multi-level PWM inverters. This strategy of control is based on the sliding mode controller in order to exploit its advantages in terms of robustness. To tackle the problem of the chattering phenomenon, we have adjusted the order of the sliding mode controller.

The rest of this research is organised as follows. First, we present the system modelling. In Section 3, the details of the SMC technique and its applications to the DFIG control are shown. Section 4 is dedicated to the control of the DFIG by SOSMC strategy. The performances of the proposed topology of control with discussions of the results are provided in section 5. Finally, a conclusion is given.

II. SYSTEM MODELLING

The overall structure of the power system including DFIG model, wind turbine and FOC control for power DFIG control based wind turbine is shown on Figure 1.

A. Wind turbine model

In order to have a horizontal axis wind turbine, the mechanical power captured from the wind is:

$$P_t = \frac{1}{2} C_P(\lambda, \beta) R^2 \rho\, v^3 \qquad (1)$$

Where the power coefficient is CP which is a function of both tip speed ratio λ and β (deg) is the blade pitch angle, the radius of the turbine is R (m), ρ is the air density (kg/m3) and

ISSN 1737-9334

v is the wind speed (m/s). According to [14] a non-linear function is being approximated used by the Cp equation.

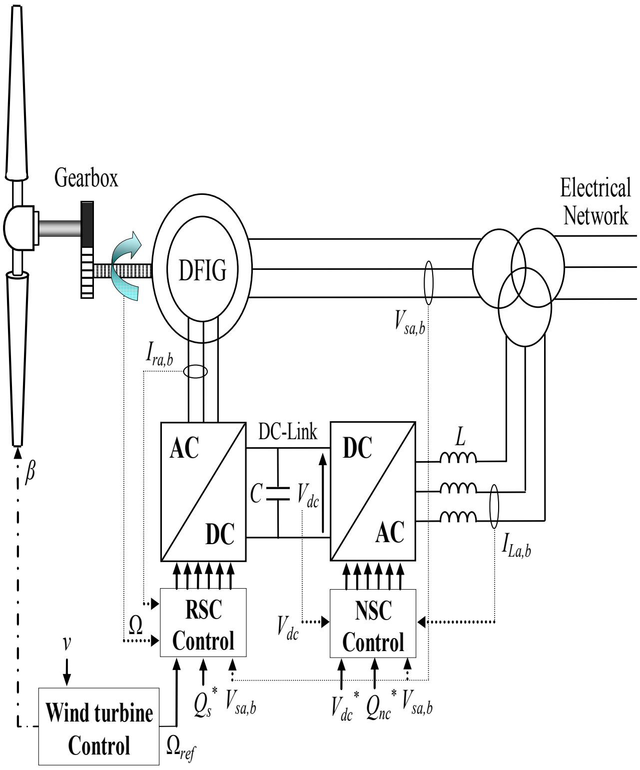

Fig. 1 Overall structure of the power system

$$C_P = (0.5-0.167)(\beta-2)\sin\left[\frac{\pi(\lambda+0.1)}{18.5-0.3(\beta-2)}\right]-0.0018(\lambda-3)(\beta-2) \tag{2}$$

$$\lambda = \frac{\Omega_t R}{v} \tag{3}$$

Where Ωt is the angular velocity of wind turbine.

B. PWM control strategy

In this work, the triangulo-sinusoidal strategy is developed using four carriers. This strategy uses the property that the three-phase five-level inverter is equivalent to four two-level inverters in series [15]. The amplitude modulation index m_a and the frequency ratio m_f characterize this strategy:

$$\begin{cases} m_a = \dfrac{A_m}{A_c} \\ m_f = \dfrac{f_c}{f_m} \end{cases} \tag{4}$$

Simulation tests are carried out for mf = 15 and ma=0.8 to verify the effectiveness of this strategy.

C. Doubly fed induction generator modeling

The following equations show the general electrical state model of the induction machine obtained using Park transformation [16]:

$$\begin{cases} V_{ds} = R_s I_{ds} + \dfrac{d}{dt}\psi_{ds} - \omega_s \psi_{qs} \\ V_{qs} = R_s I_{qs} + \dfrac{d}{dt}\psi_{qs} + \omega_s \psi_{ds} \\ V_{dr} = R_r I_{dr} + \dfrac{d}{dt}\psi_{dr} - \omega_r \psi_{qr} \\ V_{qr} = R_r I_{qr} + \dfrac{d}{dt}\psi_{qr} + \omega_r \psi_{dr} \end{cases}, \quad \begin{cases} \psi_{ds} = L_s I_{ds} + M I_{dr} \\ \psi_{qs} = L_s I_{qs} + M I_{qr} \\ \psi_{dr} = L_r I_{dr} + M I_{ds} \\ \psi_{qr} = L_r I_{qr} + M I_{qs} \end{cases} \tag{5}$$

The following relation links the stator and rotor angular velocities:

$$\omega_s = \omega + \omega_r \tag{6}$$

The mechanical equation that completes this electrical model is given as:

$$C_{em} = p\frac{M}{L_s}(\psi_{qs} I_{dr} - \psi_{ds} I_{qr}) \tag{7}$$

With:

V_{ds}, V_{qs}, V_{dr}, V_{qr}	Two-phase stator and rotor voltages,
I_{ds}, I_{qs}, I_{dr}, I_{qr}	Two-phase stator and rotor currents,
ψ_{ds}, ψ_{qs}, ψ_{dr}, ψ_{qr}	Two-phase stator and rotor fluxes,
R_s, R_r	Per phase stator and rotor resistances,
M	Mutual inductance,
L_s, L_r	Per phase stator and rotor inductances,
ω	Rotor mechanical pulsation,
ω_r, ω_s	Stator and rotor currents pulsations.

D. Doubly fed induction generator modeling

Carrying out an independent control of active and reactive powers by orientation of the stator flux facilitate the control of the production of electricity by the wind turbine.

The stator flux can be considered constant since it is directly connected to the grid, and if the voltage dropped in the stator resistance it will be neglected. This study simplifies: the voltage equations, flux equations, currents equations and stator active and reactive powers equations.

If the stator flux is linked to the d-axis of the frame we have:

$$\psi_{ds} = \psi_s \quad \text{and} \quad \psi_{qs} = 0 \tag{8}$$

The electromagnetic torque is:

$$C_{em} = -p\frac{M}{L_s} I_{qr} \psi_{ds} \tag{9}$$

The following rotor flux equations are obtained by substituting equation (9) in equation (7):

$$\begin{cases} \psi_s = L_s I_{ds} + M I_{dr} \\ 0 = L_s I_{qs} + M I_{qr} \end{cases} \tag{10}$$

The stator voltage equations are reduced to:

$$\begin{cases} V_{ds} = 0 \\ V_{qs} = \omega_s \psi_s \end{cases} \tag{11}$$

If the electrical supply network is stable, having for simple voltage Vs that led to a stator flux ψs constant with the equation (10) the electromagnetic torque only depends on the q-axis rotor current component.

The stator and rotor currents can be established with equation (11):

$$\begin{cases} I_{ds} = -\dfrac{M}{L_s} I_{dr} + \dfrac{\psi_s}{L_s} \\ I_{qs} = -\dfrac{M}{L_s} I_{qr} \end{cases} \tag{12}$$

The stator active and reactive powers are:

$$\begin{cases} P_s = V_{ds} I_{ds} + V_{qs} I_{qs} \\ Q_s = V_{qs} I_{ds} - V_{ds} I_{qs} \end{cases} \tag{13}$$

The stator active and reactive power, the rotor fluxes and voltages can be written versus rotor currents by using Equations (5), (8), (11) and (13) as:

$$\begin{cases} P_s = \dfrac{\omega_s \psi_s M}{L_s} I_{qr} \\ Q_s = -\dfrac{\omega_s \psi_s M}{L_s} I_{dr} + \dfrac{\omega_s \psi_s{}^2}{L_s} \end{cases} \tag{14}$$

$$\begin{cases} \psi_{dr} = (L_r - \dfrac{M^2}{L_s}) I_{dr} + \dfrac{M\psi_s}{L_s} \\ \psi_{qr} = (L_r - \dfrac{M^2}{L_s}) I_{qr} \end{cases} \tag{15}$$

$$\begin{cases} V_{dr} = R_r I_{dr} - g\omega_s (L_r - \dfrac{M^2}{L_s}) I_{qr} \\ V_{qr} = R_r I_{qr} + g\omega_s (L_r - \dfrac{M^2}{L_s}) I_{dr} + g\omega_s \dfrac{M\psi_s}{L_s} \end{cases} \tag{16}$$

In steady state, the second derivative terms of the two equations (17) are nil. We can thus write:

$$\begin{cases} V_{dr} = R_r I_{dr} - g\omega_s (L_r - \dfrac{M^2}{L_s}) I_{qr} \\ V_{qr} = R_r I_{qr} + g\omega_s (L_r - \dfrac{M^2}{L_s}) I_{dr} + g\omega_s \dfrac{M\psi_s}{L_s} \end{cases} \tag{17}$$

$g\omega_s \dfrac{M\psi_s}{L_s} \cong 0$ because of their small influence. These terms can be compensated by an adequate synthesis of the regulators in the control loops.

III. SLIDING MODE CONTROL

The sliding mode technique is obtained from variable structure control to resolve the disadvantages of designs of nonlinear control systems. The sliding mode is a technique to adjust feedback by previously defining a surface and the system will be forced to that surface, then the behaviour of the system slides to the desired equilibrium point [17].

The objective of the control is to drive the error to a "switching surface". When the system is in "sliding mode", the system behaviour is not affected by any modelling uncertainties and/or disturbances.

The design of the control system will be demonstrated for a nonlinear system presented in the canonical form [11]:

$$\dot{x} = f(x,t) + B(x,t)U(x,t) \tag{18}$$

where x Rn, U Rm and ran(B(x,t)) = m.

The goal of control is to keep the system motion on the manifold S, which is defined as:

$$S = \{x : e(x, t) = 0\} \tag{19}$$

$$e = x^d - x \tag{20}$$

here e is the tracking error vector, xd is the desired state, x is the state vector. The control input U has to guarantee that the motion of the system described in (18) is restricted to belong to the manifold S in the state space. The sliding mode control should be chosen such that the candidate Lyapunov function satisfies the Lyapunov stability criteria:

$$\vartheta = \frac{1}{2} S(x)^2, \tag{21}$$

$$\dot{\vartheta} = S(x)\dot{S}(x). \tag{22}$$

This can be assured for:

$$\dot{\vartheta} = -\eta |S(x)| \tag{23}$$

η is strictly positive. Essentially, equation (21) states that the squared "distance" to the surface, measured by $e(x)^2$, decreases along all system trajectories.

Therefore (21), (22) satisfy the Lyapunov condition. With selected Lyapunov function the stability of the whole control system is guaranteed. The control function will satisfy reaching conditions in the following form:

$$U^{com} = U^{eq} + U^{n} \tag{24}$$

here U^{com} is the control vector, U^{eq} is the equivalent control vector, Un is the correction factor and must be calculated so that the stability conditions for the selected control are satisfied.

$$U^n = K\,\mathrm{sat}(S(x)) \tag{25}$$

where sat(S(x)) is the proposed saturation function, K is the controller gain.

In this paper, we propose the "*Slotine"* method [15]:

$$S(X) = \left(\frac{\mathrm{d}}{\mathrm{dt}} + \xi\right)^{n-1} e \tag{26}$$

here, e is the tracking error vector, ξ is a positive coefficient and n is the relative degree.

- **Application to the DFIG control**

We choose the error between the measured and references stator powers as sliding mode surfaces, so we can write:

$$\begin{cases} \mathrm{S_d} = P_s^* - P_\mathrm{S} \\ \mathrm{S_q} = \mathrm{Q_s^*} - \mathrm{Q_S} \end{cases} \tag{27}$$

The first order derivate of (27), gives:

$$\begin{cases} \dot{\mathrm{S}}_\mathrm{d} = \dot{\mathrm{P}}_\mathrm{s}^* - \dot{\mathrm{P}}_\mathrm{S} \\ \dot{\mathrm{S}}_\mathrm{q} = \dot{\mathrm{Q}}_\mathrm{s}^* - \dot{\mathrm{Q}}_\mathrm{S} \end{cases} \tag{28}$$

Replacing the powers in (28) by their expressions given in (14), we obtain:

$$\begin{cases} \dot{S}_d = \dot{P}_s^* - \dfrac{\omega_s \psi_s M}{L_s} \dot{I}_{qr} \\ \dot{S}_q = \dot{Q}_s^* + \dfrac{\omega_s \psi_s M}{L_s} \dot{I}_{dr} - \dfrac{\omega_s {\psi_s}^2}{L_s} \end{cases} \tag{29}$$

V_{dr} and V_{qr} will be the two components of the control vector used to constraint the system to converge to S_{dq}=0. The control vector V_{dqeq} is obtained by imposing so the equivalent control components are given by the following relation:

$$\begin{cases} \mathrm{V_{eqd}} = -\dfrac{\mathrm{L_s}\left(\mathrm{L_r} - \dfrac{\mathrm{M^2}}{\mathrm{L_s}}\right)}{\omega_\mathrm{s}\psi_\mathrm{s}\mathrm{M}} \dot{\mathrm{Q}}_\mathrm{s}^* + \mathrm{R_r I_{dr}} - \left(\mathrm{L_r} - \dfrac{\mathrm{M^2}}{\mathrm{L_s}}\right) g\omega_\mathrm{s}\mathrm{I_{qr}} + \dfrac{\left(\mathrm{L_r} - \dfrac{\mathrm{M^2}}{\mathrm{L_s}}\right)\psi_\mathrm{s}}{\mathrm{M}} \\ \mathrm{V_{eqq}} = \dfrac{\mathrm{L_s}}{\omega_\mathrm{s}\psi_\mathrm{s}\mathrm{M}} \dot{\mathrm{P}}_\mathrm{s}^* + \mathrm{R_r I_{qr}} - \left(\mathrm{L_r} - \dfrac{\mathrm{M^2}}{\mathrm{L_s}}\right) g\omega_\mathrm{s}\mathrm{I_{dr}} + \dfrac{g\omega_\mathrm{s}\psi_\mathrm{s}\mathrm{M}}{\mathrm{L_s}} \end{cases} \tag{30}$$

To obtain good performances, dynamic and commutations around the surfaces, the control vector is imposed as follows:

$$\mathrm{V_{dq}} = \mathrm{V_{eqdq}} + K \cdot \mathrm{sat}(\mathrm{S_{dq}}) \tag{31}$$

The sliding mode will exist only if the following condition is met:

$$\mathrm{S} \cdot \dot{\mathrm{S}} < 0 \tag{32}$$

IV. THE PROPOSED SECOND ORDER SLIDING MODE CONTROLLER

Sliding mode control (SMC) is a standout amongst the most fascinating nonlinear control approaches. Nevertheless, a few drawbacks arise in its practical implementation, such as chattering phenomenon and undesirable mechanical effort. To reduce the effects of these problems, second order sliding mode seems to be a very attractive solution.

This method generalizes the essential sliding mode idea by acting on the higher order time derivatives of the sliding manifold, instead of influencing the first time derivative as it is the case in SMC, therefore reducing chattering and avoiding strong mechanical efforts while preserving SMC advantages [18-19].

In order to ensure the stator active and reactive powers convergence to their references, a second order sliding mode control (SOSMC) is used. Considering the sliding mode surfaces given by (27), the following expression can be written:

$$\begin{cases} \dot{S}_d = \dot{P}_s^* - \dfrac{\omega_s \psi_s M}{L_s} \dot{I}_{qr} \\ \ddot{S}_d = Y_1(t,x) + \Lambda_1(t,x) V_{dr} \end{cases} \tag{33}$$

and

$$\begin{cases} \dot{S}_q = \dot{Q}_s^* + \dfrac{\omega_s \psi_s M}{L_s} \dot{I}_{dr} - \dfrac{\omega_s {\psi_s}^2}{L_s} \\ \ddot{S}_q = Y_2(t,x) + \Lambda_2(t,x) V_{dr} \end{cases} \tag{34}$$

where Y1(t,x), Y2(t,x), Λ1(t,x) and Λ2(t,x) are uncertain functions which satisfy:

$$\begin{cases} Y_1 > 0,\ |Y_1| > \lambda_1,\ 0 < K_{m1} < \Lambda_1 < K_{M1} \\ Y_2 > 0,\ |Y_2| > \lambda_2,\ 0 < K_{m2} < \Lambda_2 < K_{M2} \end{cases}$$

Basing on the super twisting algorithm introduced by Levant in [20], the proposed high order sliding mode controller contains two parts:

$$\mathrm{V_{dr}} = \mathrm{v_1} + \mathrm{v_2} \tag{35}$$

With:

$$\dot{v}_1 = -k_1 \, smooth\ (S_d)$$

$$v_2 = -l_1 |S_d|^\gamma \, smooth\ (S_d)$$

And

$$V_{qr} = w_1 + w_2 \tag{36}$$

With:

$$\dot{w}_1 = -k_2 smooth\ (S_q)$$

$$w_2 = -l_2 \left|S_q\right|^{\gamma} smooth\ (S_q)$$

In order to ensure the convergence of the sliding manifolds to zero in finite time, the gains can be chosen as follows [21].

$$\begin{cases} k_i > \dfrac{\lambda_i}{K_{mi}} \\ l_i^2 \geq \dfrac{4\lambda_i}{K_{mi}^2} \dfrac{K_{Mi}(k_i+\lambda_i)}{K_{mi}(k_i-\lambda_i)}; \qquad i = 1,\ 2 \\ 0 < \gamma \leq 0.5 \end{cases}$$

V. SIMULATION RESULTS AND DISCUSSIONS

For this section, a 1.5 MW generator coupled to a 398V/50Hz grid is used for simulation with the parameters shown in Table 1, the overall structure scheme is shown in Figure 2.

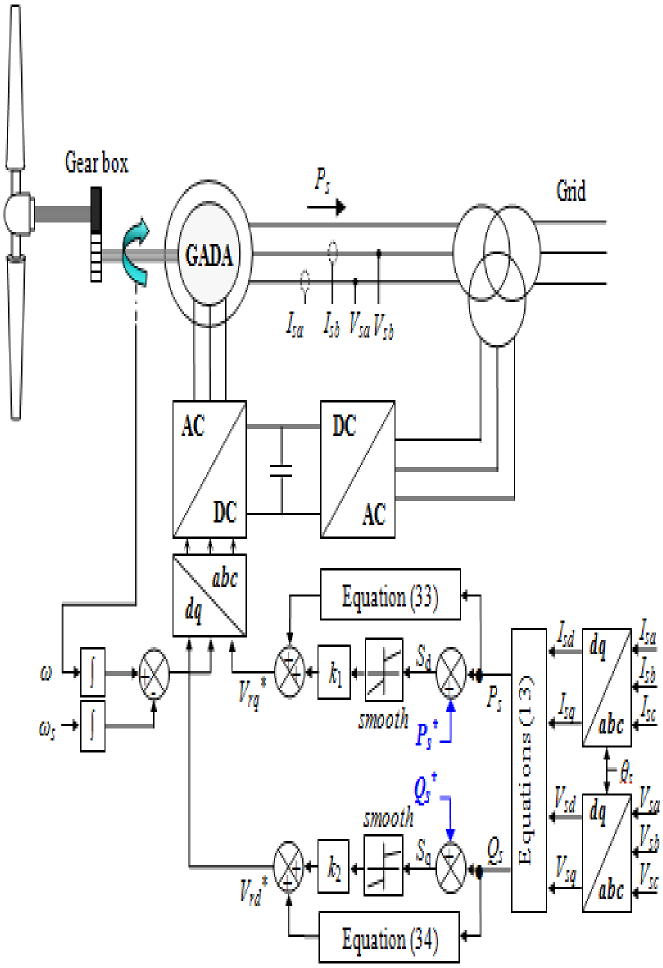

Fig. 2 Power control of the DFIG

Three categories of tests have been conducted: pursuit test, sensitivity to the speed variation and robustness against machine parameter variations to evaluate the performances of the two robust controllers: SMC and SOSMC with a DFIG supplied by a five-level inverter.

TABLE I
THE DFIG PARAMETERS [16]

Parameters	Value	IS-Unit
Nominal power	1.5	MW
Stator voltage	398/690	V
Number of pairs poles	2	
Stator resistance	0.012	Ω
Rotor resistance	0.021	Ω
Stator inductance	0.0137	H
Rotor inductance	0.0136	H
Mutual inductance	0.0135	H
Inertia	1000	Kg.m^2

A. Pursuit test

The objective of this test is the study of the two controllers' behaviour in reference tracking, while the machine's speed is considered constant and equal to its nominal value. The simulation results are presented in Figures 3 and 4. As it is shown by Figure 3, for the two controllers, the active and reactive generated powers tracks almost perfectly their references and ensures a perfect decoupling between the two axes. Therefore, it can be considered that the two types of controllers have a very good performance for this test. On the other hand, Figure 4 shows the harmonic spectrums of one phase stator current of the DFIG obtained using Fast Fourier Transform (FFT) technique for the two controllers using respectively tow level and five level power inverters. It can be clear observed that the total harmonic distortion (THD) is reduced for SOSMC (THD = 1.99%) when compared to SMC (THD = 2.09%) with a two level inverter and the THD is more and more reduced by using the five level inverters (THD = 1.87%).The amelioration between the first and the last one is 10%.

B. Speed variation test

The analysis of the influence of a speed variation of the DFIG on active and reactive powers for the two controllers was the purpose of this study. For this objective, the speed was varied from 150 rad/s to 170 rad/s at time = 0.04s. Figure 5 shows the simulation results. Also, it expresses that the speed variation produce a slight effect on the powers curves of the system with SMC controller, while the effect is almost negligible for the system with SOSMC one. It can be observed that this last has almost perfect speed disturbance rejection, actually only very small power variations can be observed (fewer than 2%). This outcome is attractive for wind energy applications to guarantee stability and quality of the generated power when the speed is varying.

C. Robustness

The machine parameters have been modified in order to test the robustness of the used controllers, the values of inductances Ls, Lr and M are divided by 2 and the values of the stator and the rotor resistances Rs and Rr are doubled. The machine is running at its nominal speed. The Figure 6 presents the results that show the parameters variations of the DFIG increase slightly the time-response of the two controllers. On the other hand, this results show that parameter variations of the DFIG presents a clear effect on the powers curves (their errors curves) and that the effect appears more significant for SMC controller than that with SOSMC one. So it can be concluded that this last is more robust than the classical SMC controller.

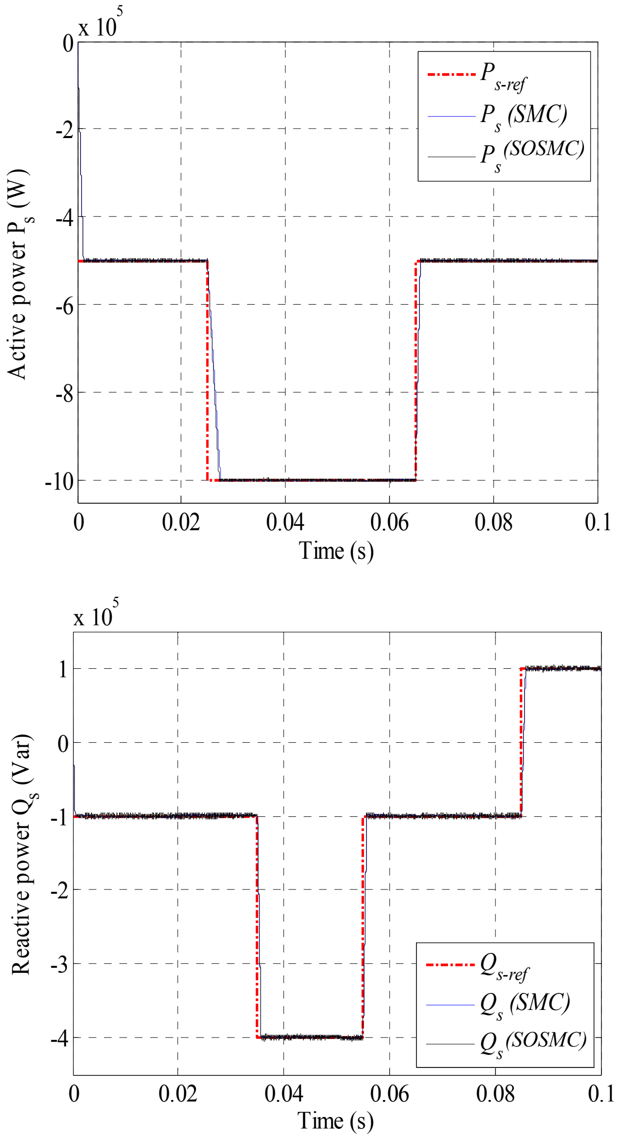

Fig. 3 References tracking test

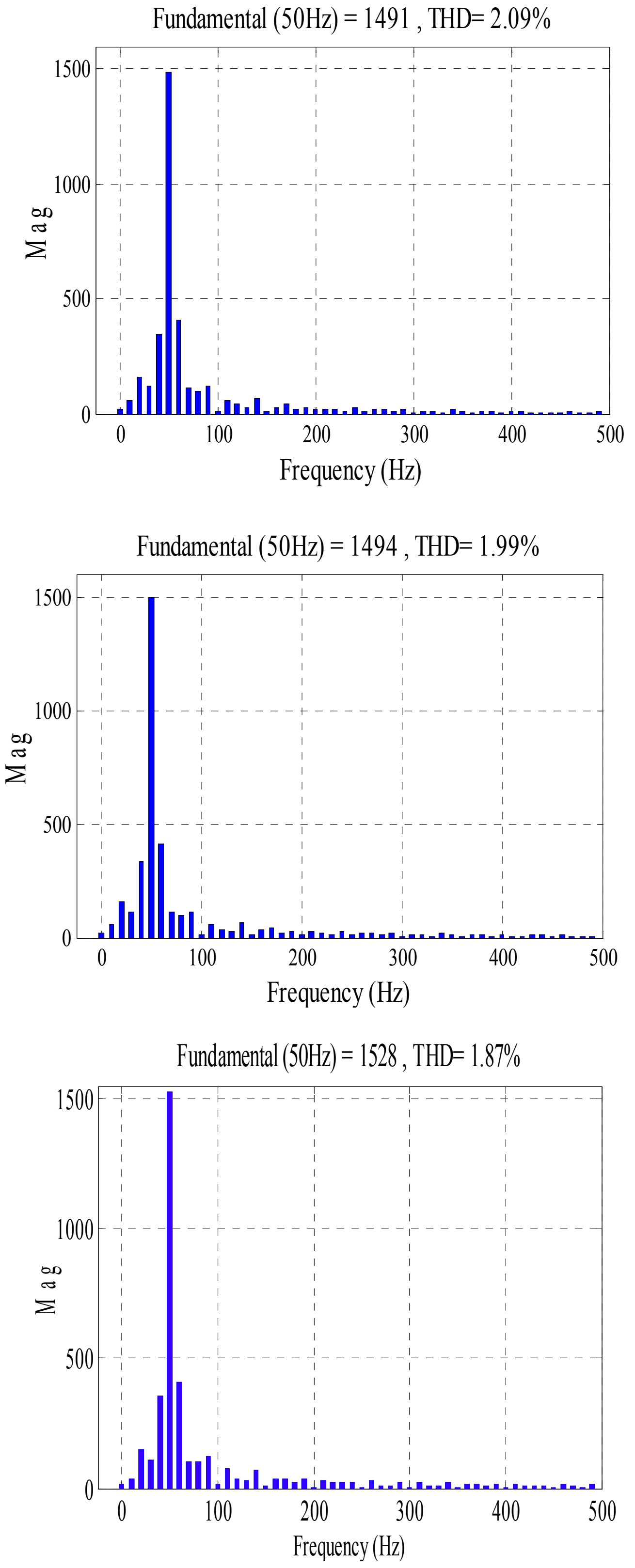

Fig. 4 Spectrum harmonic of one phase stator current. (a) for SMC controller with a two-level inverter; (b) for SOSMC controller with a two-level inverter; (c) for the SOSMC controller with a five-level inverter

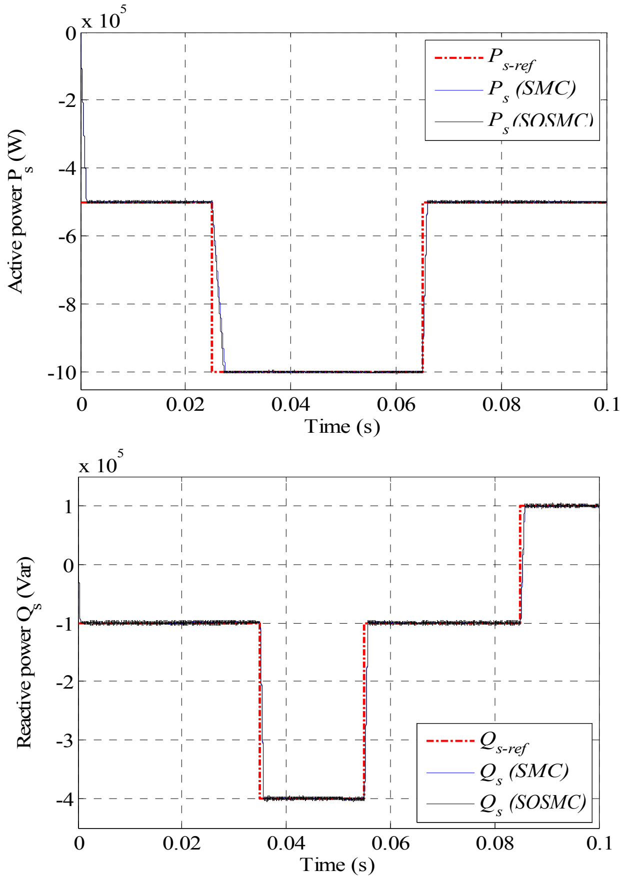

Fig. 5 Sensitivity to the speed variation

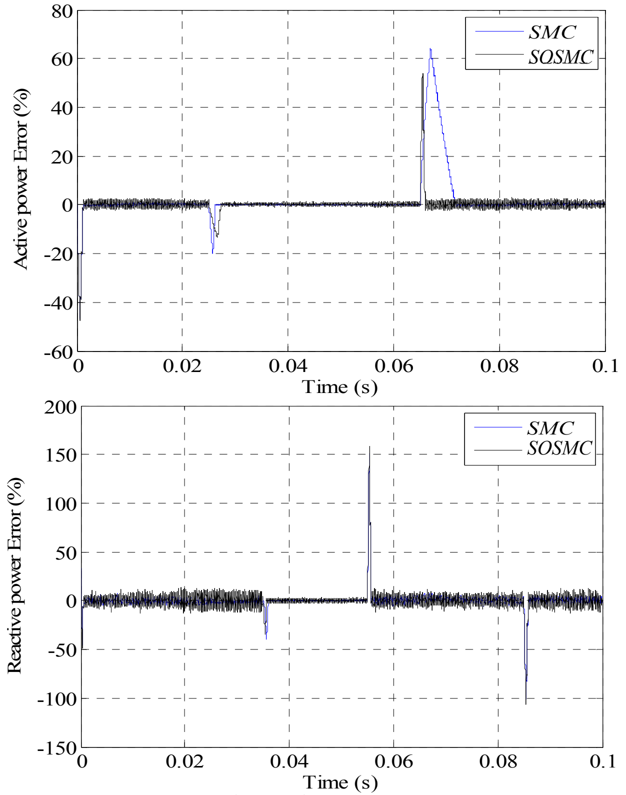

Fig. 6 Robustness test

VI. CONCLUSION

A robust control method of a DFIG connected directly to the grid by the stator and fed by a five level inverter from the rotor side has been presented in this study. In the first step, we started with a study of modelling on the five level inverter controlled by the PWM technique. In second step, we adopted a vector control strategy in order to control stator active and reactive powers exchanged between the DFIG and the grid. In a third step, two types of sliding mode controllers are synthesized and compared. In term of power reference tracking with the DFIG in ideal conditions, the two controllers ensures a perfect decoupling between the two axes (d and q). On the other hand, simulation results have confirmed that the proposed SOSMC controller is the most effective in eliminating chattering phenomenon. When the machine's speed is modified, the impact on the active and reactive powers values is slightly significant for the two controllers. A robustness test has also been investigated where the machine parameters have been modified. These changes induce some disturbances on the powers responses but with an effect almost doubled with the SMC controller than on that with SOSMC one. Basing on all these results, it can be concluded that robust control method as SOSMC can be a very attractive solution for devices using DFIG such as wind energy conversion systems.

REFERENCES

[1] O. Anaya-Lara, N. Jenkins, J. Ekanayake, P. Cartwright and M. Hughes, *Wind Energy Generation*, West Sussex, United Kingdom: John Wiley & Sons, 2009.

[2] M. Edrah, K. L. Lo and O. Anaya-Lara, "Impacts of high penetration of DFIG wind turbines on rotor angle stability of power systems", *IEEE Transactions on Sustainable Energy*, vol. 6, no. 3, pp. 759-766, 2015.

[3] T. Ahmed, K. Nishida and M. Nakaoka, "A novel stand-alone induction generator system for AC and DC power applications", in IEEE Transactions on Industry Applications, vol. 43, no. 6, pp. 1465-1474, 2007.

[4] M. R. Baiju, K. Gopakumar, K. K. Mohapatra, V. T. Somasekhar and L. Umanand, "Five-level inverter voltage-space phasor generation for an open-end winding induction motor drive", *IEE Proceedings - Electric Power Applications*, vol. 150, no. 5, pp. 531-538, 2003.

[5] N. Hatti, K. Hasegawa and H. Akagi, "A 6.6 KV transformer less motor drive using a five-level diode-clamped PWM inverter for energy savings of pumps and blowers", *IEEE Transactions on Power Electronics*, vol. 24, no. 3, pp. 796-803, 2009.

[6] R. Pena, J. C. Clare and G. M. Asher, "A doubly fed induction generator using back to back converters supplying an isolated load from a variable speed wind turbine", *IEE Proceedings - Electric Power Applications*, vol. 143, no. 5, pp. 380-387, 1996.

[7] M. A. Poller, "Doubly-fed induction machine models for stability assessment of wind farms", *IEEE Power Tech Conference Proceedings*, June 23-26; Bologna, Italy; pp. 23–26, 2003.

[8] T. Brekken and N. Mohan, "A novel doubly-fed induction wind generator control scheme for reactive power control and torque pulsation compensation under unbalanced grid voltage conditions", in *IEEE 34th Annual Power Electronics Specialist Conference,* June 15-19; Acapulco, Mexico; pp. 760-764, 2003.

[9] T. K. A. Brekken and N. Mohan, "Control of a doubly fed induction wind generator under unbalanced grid voltage conditions", *IEEE Transactions on Energy Conversion,* vol. 22, no. 1, pp. 129–135, 2007.

[10] J. Lopez, P. Sanchis, X. Roboam and L. Marroyo, "Dynamic behavior of the doubly fed induction generator during three-phase voltage dips",

IEEE Transactions on Energy Conversion, vol. 22, no. 3, pp. 709-717, 2007.

[11] T. Sun, Z. Chen and F. Blaabjerg, “Flicker study on variable speed wind turbines with doubly fed induction generators”, *IEEE Transactions on Energy Conversion*, vol. 20, no. 4, pp. 896–905, 2005.

[12] D. E. Chaouch, Z. Ahmed-Foitih and M. F. Khelfi, “A self tuning fuzzy inference sliding mode control scheme for a class of nonlinear systems”, *Journal of Vibration and Control*, vol.18, no. 10, pp. 1494–1505, 2012.

[13] M. Reddak, A. Berdai, A. Gourma, J. Boukherouaa and A. Belfiqih, “Enhanced Sliding Mode MPPT and Power Control for Wind Turbine Systems Driven DFIG (Doubly-Fed Induction Generator”, *International Review of Automatic Control*, vol. 9, no. 4, 2016.

[14] E. S. Abdin and W. Xu, “Control design and Dynamic Performance Analysis of a Wind Turbine Induction Generator Unit”, *IEEE Transactions on Energy Conversion*, vol.15, no. 1, pp.91-96, 2000.

[15] R. Guedouani, B. Fiala, E. M. Berkouk and M. S. Boucherit, “Modelling and control of three-phase PWM voltage source rectifiers five-level NPC voltage source inverter induction machine system” in *18th Mediterranean Conference on Control and Automation Congress,* June 23-25; Marrakech, Morocco, pp. 533-538, 2010.

[16] Z. Boudjema, A. Meroufel, E. Bounadja and Y. Djerriri “Nonlinear control of a doubly fed induction generator supplied by a matrix converter for wind energy conversion systems”, *Journal of Electrical Engineering*, vol. 13, no. 4, pp. 269–276, 2013.

[17] J. J. Slotine E and W. Li, *Applied Nonlinear Control*, Englewood Cliffs, New Jersey: Prentice–Hall, 1991.

[18] M. A. A. Morsy, M. Said, A. Moteleb and H. T. Dorrah, “Design and implementation of fuzzy sliding mode controller for switched reluctance motor”, in *Proceedings of the International MultiConference of Engineers and Computer Scientists,* March 19-21, Hong Kong, 2008.

[19] B. Beltran, M. H. Benbouzid and T. Ahmed-Ali, “Second-order sliding mode control of a doubly fed induction generator driven wind turbine”, *IEEE Transactions on Energy Conversion*, vol. 27, no. 2, pp. 261-269, 2012.

[20] A. Levant and L. Alelishvili, “Integral high-order sliding modes”, *IEEE Transactions on Automatic Control*, vol. 52, no. 7, pp. 1278-1282, 2012.

[21] S. Benelghali, M. E. H. Benbouzid, J. F. Charpentier, T. Ahmed-Ali and I. Munteanu, “Experimental validation of a marine current turbine simulator: Application to a PMSG-based system second-order sliding mode control”, *IEEE Transactions on Industrial Electronics,* vol. 58, no. 1, pp. 118-126, 2011.

Prefromance Evaluation of RF Noise Wavelets Reconstruction and Noise Reduction

.Hana H.Saleh[1] and Amer Ammar[2]

[1]Benghazi University, Faculty of Education- Qmins
[1]cleverageh@gmail.com
Zawia University
Zawia, – Libya,
[2]amer642002@yahoo.com

Abstract— One of the fundamental challenges affecting the performance of communication systems is the undesired impact of noise on a signal. Noise distorts the signal and originates due to several sources including, system non-linearity and noise interference from adjacent environment. Conventional communication systems use filters to cancel noise in a received signal. for instance, system bit error rate or signal to noise ratio. Hence, predicting noise in RF systems at the design stage is extremely important. Additionally, with the growing complexity of modern RF systems, a at transistor-level noise analysis for the entire system is becoming increasingly difficult. Hence accurate modelling at the component level and behavioral level simulation techniques are also becoming increasingly important. In this paper, we concentrate on developing noise simulation techniques and mathematically accurate noise models at the component level. These models will also enable behavioral level noise analysis of large RF systems.Wavelets are mathematical functions that cut up data into different frequency components, and then study each component with a resolution matched to its scale. And used to analyzing physical situations where the signal contains discontinuities and sharp spikes. By the wavelet menu in Math-lab will show that phase noise of each input signal contributes one additional white noise source that is modulated by derivatives of the steady state response. These models for autonomous and non-autonomous components of RF circuits will enable one to perform nonlinear noise simulation at the behavioural level for large RF systems. These models can also be used for behavioral level performance optimization and constraint generation for the RF components.

Keywords— wavelets, pattern detection, filters, noise and Bit Error Ratio .

I. INTRODUCTION

Based on the fact that noise and distortion are the main factors that limit the capacity of data transmission in telecommunications and that they also affect the accuracy of the results in the signal measurement systems, whereas modeling and removing noise and distortions are at the core of theoretical and practical considerations in communications and signal processing. Another important issue here is that, noise reduction and distortion removal are major problems in applications such as; cellular mobile communication, speech recognition, image processing, medical signal processing, radar, sonar, and any other application where the desired signals cannot be isolated from noise and distortion. With the explosive growth of the communication market in the past few years, mobile personal communication devices have become extremely popular. The primary design effort in this area has been to lower the cost and power dissipation of these systems. Lower power dissipation directly translates into longer battery life, which is very critical for such applications. Another area of interest is to design systems that can conform to multiple standards. This gives rise to interesting challenges in terms of designing different components in this system and the design of entire system itself. Understanding the impact of electronic devices and the underlying process technology limitations on the design of components and the overall system is an important aspect of the design process. These systems are popularly known as radio frequency (RF) or infrared (IR) systems depending on the frequency of operation. Radio frequency normally refers to the range of frequencies at which the signal is transmitted and received in such a system. Modern RF systems typically operate in 900 0MHz to 2.4 GHz frequency range. For IR systems the frequency range is much higher. Design of a complex circuit operating at such frequencies is a challenging problem. In this paper we address the problem of predicting the performance of RF systems in the presence of noise. By noise we mean any undesired signal that corrupts the signal of interest. Noise performance in such systems needs to be predicted both at the individual component level and also at the system level. In this work we address the problem of predicting noise and developing noise models at the component level which can be used in a system level noise simulation technique. We begin by discussing the architecture of a typical present day RF system and also discuss what a future RF system is predicted to look like indicate some of the challenges that are resent in designing a complex, multi-standard RF system at very high frequency ranges. We then motivate the problem of performing noise analysis in such systems, both at the component level and at the system level. Architecture of an RF Front End

ISSN 1737-9334

The block diagram of the front end of an RF system is given in Figure 1 [GM95].

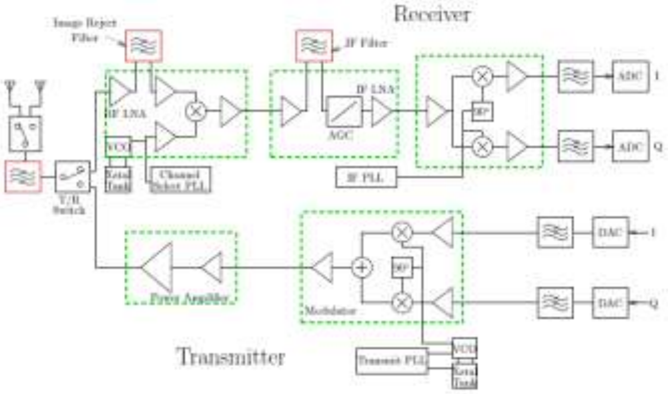

Figure 1: Block diagram of an RF transceiver front-end

The front end consists of both the transmitter and the receiver part of the RF system. An input signal from the antenna is first filtered using a band-pass filter to reject any out of band noise. This signal, which is typically very small *(few tens of microwatts to few milli-watts)* is amplified by a low noise amplifier (LNA) which typically provides a power gain of about 10dB. This also reduces the noise contribution from subsequent mixing and amplification stages of the receiver. Let the frequency of this received signal be denoted by RF . The RF signal is frequency-shifted to base band before information can be retrieved from the signal. This frequency shifting, or down conversion typically happens in more than one stage. This is due to the fact that the frequency of the received signal is of the order of few gigahertz whereas the base band signal has bandwidth of a few kilohertz which makes down conversion in one stage very expensive. Input RF signal is mixed with a large local oscillator signal of frequency f_{LO} and gets down converted to a fixed intermediate frequency signal f_{IF} where $f_{IF} = [f_{RF} - f_{LO}]$. This allows channel selection filtering and gain control at lower frequencies where high quality factor (Q) filters and variable gain amplifiers can be realized economically [1].

II. NOISE

All signals are contaminated by noise, which degrades the system performance. The noisiness of a signal is usually specified in terms of the signal-to-noise ratio, SNR = S / N where S is the signal power and N is the noise power. This parameter is generally a function of frequency. The reduction in SNR throughout a two-port network is characterized by the noise factor.

$$F = \frac{SNR_I}{SNR_o}$$

Where SNR_I and SNR_o are the input and output signal-to-noise ratios, respectively. The noise factor is often expressed in decibels. In this case, it is called the noise figure (NF) and is defined as $NF = 10\log(F)$. Since the minimum value for the noise factor is equal to one, the noise figure of an ideal noiseless network is 0 dB. ***Capacity Reduction due to Noise Factor of an RF Receiver*** A typical radio frequency (RF) receiver, including an antenna, an RF frontend and a load, is illustrated in Figure 2 [4], [5].

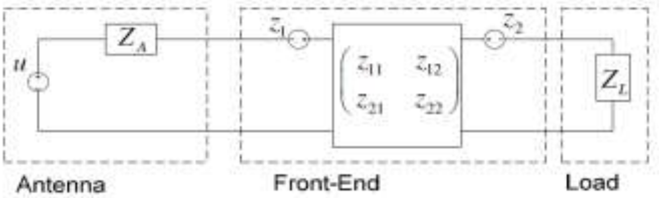

Figure. 2 A circuit model for a receiver front-end

The antenna is modelled by a Thevenin equivalent circuit with impedance $z_A = r_A + jx_A$. The front-end may include amplifiers, mixers, and filters. In this model, *u* is the antenna open-circuit voltage containing both signal and noise. It can be represented as:

$$u = hx + n_o$$

where *x* is the transmitted signal, *h* is the channel coefficient, and n_o is the thermal noise.

III. NOISE SOURCES IN RF TRANSCEIVER

In a highly integrated transceiver, switching signals from digital portions of the circuit can couple into sensitive RF circuit nodes and directly degrade the overall signal to noise ratio. This coupling can happen through power supply lines as well as substrate. However, careful design and layout techniques can minimize the effect of this coupling. By ensuring separate power supply and ground for digital and RF portions of the system, using a large bypass capacitance to remove any unwanted high frequency signals on the supply network and by making the resistance of power supply to the RF portions very low, switching noise coupled through the power supply can be minimized. Several techniques have been proposed in the literature to minimize the amount of coupling from substrate [2]. These usually involve using grounded guard rings around the sensitive RF circuits. For different substrates, different topologies of guard rings can be used to minimize the amount of signal that is coupled through the substrate [2]. Another type of noise that has a detrimental effect on the system performance is electrical noise which is intrinsic to electronic devices that make up the circuit itself. The discrete nature of charge transfer gives rise to shot noise whenever the current crosses a potential barrier. Shot noise is modelled as a zero mean stochastic process. For a general one-dimensional stochastic process X(t), the autocorrelation, as a function of two time variables *t* and τ , is given by:

$$R_{xx}(t,\tau) = \mathbb{E}\left[X(t)X(t+\tau)\right]$$

If $R_{xx}(t,\tau)$ is independent of t, the stochastic process is called wide-sense stationary. For a wide-sense stationary stochastic process, the power spectral density, i.e., power $S_{xx}(\varpi)$ in a unit frequency range at an angular frequency ϖ is given by:

$$S_{xx}(\omega) = \int_{-\infty}^{\infty} R_{xx}(\tau)\exp(-j\omega\tau)d\tau$$

The spectral density of shot noise is given by:

$$S_{xx,shot}(\omega) = 2qI_d$$

where q is the electron charge and I_d is the current. The power spectral density is constant for a very large frequency range (few tens of gigahertz) and hence can be modelled as a scaled white noise source with power spectral density.

.

IV. TRANSMITTER NOISE

Since the oscillator is a nonlinear device, the noise voltages and currents generated in an oscillator are modulating the signal produced by the oscillator. Figure 3a shows the ideal signal and the signal modulated by the noise. The noise can be classified as an AM noise, FM noise, and phase noise. Amplitude-modulated noise causes the amplitude variations of the output signal. Frequency-modulated or phase noise is indicated in Fig. 3b by the spreading of the frequency spectrum.

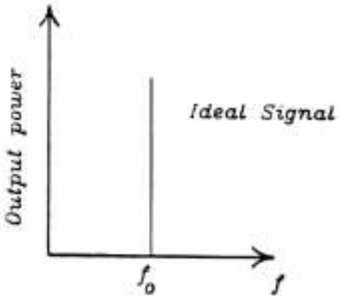

Figure 3a Ideal signal

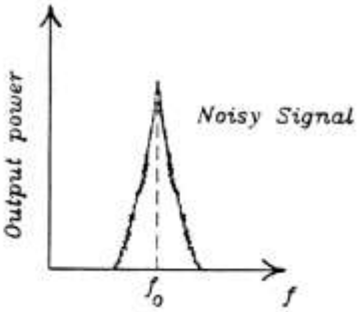

Figure 3b Ideal signal and noisy signal

A ratio of single-sideband noise power normalized in 1-Hz bandwidth to the carrier power is defined as:

$$\mathcal{L}(f_m) = \frac{\text{noise power in 1-Hz bandwidth at } f_m \text{ offset from carrier}}{\text{carrier signal power}}$$

$$= \frac{N}{C}$$

$\mathcal{L}(f_m)$ is the difference of power between the carrier at f_0 and the noise at $f_0 + f_m$. The power is plotted in the decibel scale, and the unit of $\mathcal{L}(f_m)$ is in decibels below the carrier power (dBc) per hertz. The FM noise is normally given as the number of decibels below carrier amplitude at a frequency f_m that is offset from the carrier. So Noise of the AM, FM, and phase noise. Amplitude-modulated noise is the unwanted amplitude variation of the output signal, frequency-modulated noise is the unwanted frequency variations, and phase noise is the unwanted phase variations. figure 4 shows the oscillator output power spectrum. This spectrum can be seen from the screen of a spectrum analyzer.

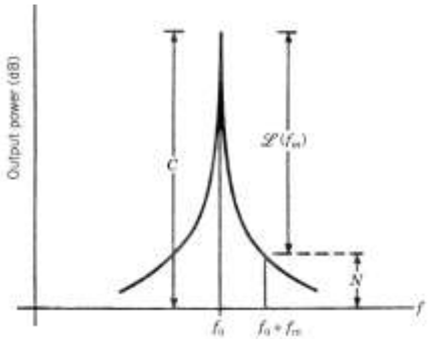

Figure 4 shows the oscillator output power spectrum

V. IMPLEMENTING AND SIMULATING of RF NOISE RECOSTRUCTION AND REDUCTION

Figure (5) shows the Mat-lab wavelet menu which consist on the tools for contrast to physical models, analytical channel models characterize the impulse response of the channel between the individual transmitting and receiving antennas in a mathematical/analytical way without explicitly accounting for wave propagation.

Fig. 5. Screen shot of Matlab wavelet menu

The four chosen noised signals red colored, the noise adapted basis **with level 2** and fixed form threshold as soft mode are described in figure 6.

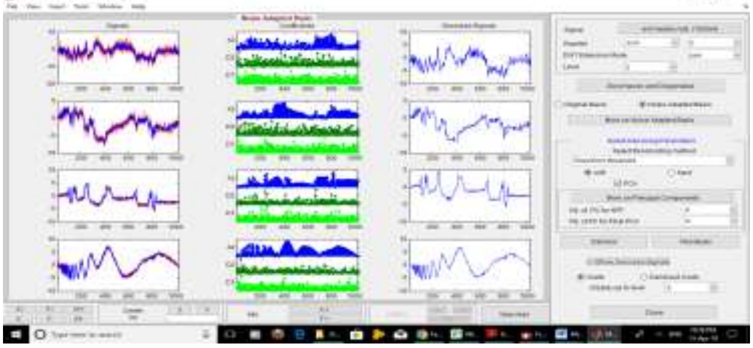

Figure . 6. De noised signals with level 2.

Among various RF impairment factors and reduction of noise is one of the major sources of performance reduction in wireless communications systems. The noise effects on general electronic systems. By modelling the performance degradation due to the noise, a clear understanding of the system and compensation techniques are provided. by providing analytical relations to model the phase noise effects, the performance can be evaluated without the requirement of conducting very time consuming simulation studies. In conjunction with component level models and system level simulation techniques for distortion and other nonidealities in the system, this effort will hopefully enable efficient design of high performance RF systems. That is why we must simulate the signals by different scenarios. Figure 7 when use **the level 6** for de noising the four signals

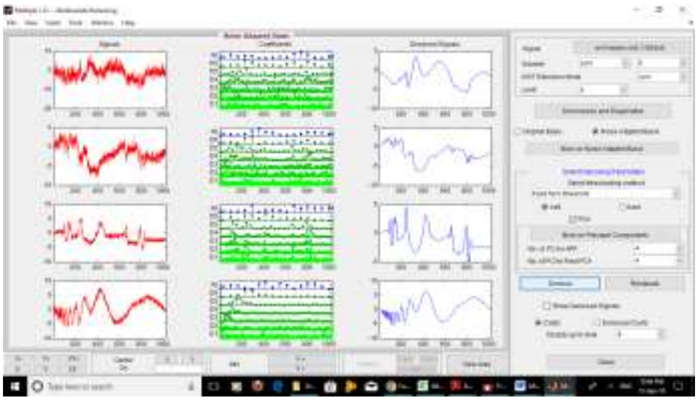

Figure 7 when use the level 6 for de noising the four signals

noise in RF circuits directly affects high level system performance such as signal to noise ratio (SNR) or the overall bit error rate (BER). Noise also affects how the system SNR degrades in presence of a large adjacent channel blocker signal. In the transmit path, it affects how much noise power the system is leaking into adjacent channels [Pat96]. In an RF circuit, noise refers to any unwanted signal coupled into the circuit as well as unwanted signals generated by the devices themselves. And the running signal is defined by:

RS= F((t-20)/8) + sqrt(2)\times F((t-40)/4) + N

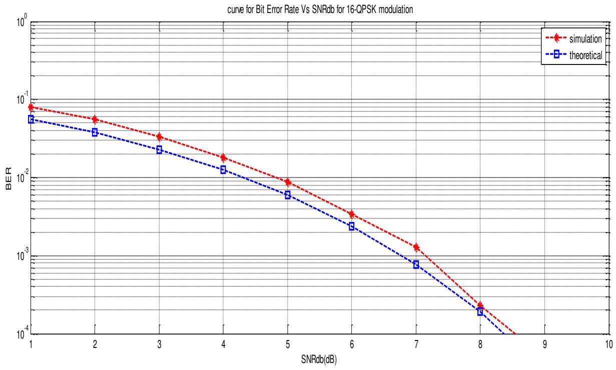

Fig. 6. Noise N added to the wave. Running Signal (RS) when QPSK = 2.

In an actual RF circuit, the signal bandwidth is limited and hence a finite number harmonics of signals are present. Hence the infinite summations in all the above expressions are truncated. We assume that harmonics corresponding to ϖ_1 are truncated to 6I and the harmonics corresponding to ϖ_2 are truncated to 6K. Hence a bi-periodic waveform z(t) in this system is given by:

$$z(t) = \sum_{i=-I}^{I} \sum_{k=-K}^{K} Z(i,k) \exp\big(\jmath(i\omega_1 + k\omega_2)t\big)$$

By this we have investigated noise analysis and modelling problem for RF circuits. We first concentrated on noise analysis of autonomous circuits and then turned our attention to noise analysis of non-autonomous circuits which are driven by oscillators which have phase noise.

VI. Conclusion

We provide a practical approach in how to conclude the lifting methods which can be used to construct pattern-adapted wavelets by addressed the noise analysis problem of nonautonomous circuits driven by a single large periodic signal which has phase noise. We discussed that since a nonautonomous circuit, along with the driving oscillator, can be viewed as a composite oscillator, the output noise process will be stationary and not cyclo-stationary, as would be predicted by classical noise analysis for such circuits. We also derived this result mathematically. by showed that the effect of input signal phase noise is to add another white noise source to the circuit noise sources which is modulated by the time derivative of the noiseless steady-state response of the circuit.so, that a more thorough understanding of how noise and other nonidealities affect the overall circuit response will be crucial in minimizing overdesign which exists in current RF design practices. Specifically for RF mobile systems, this would result in lower power and hence higher battery life. Equivalently, extra functionality can be incorporated in those parts of an RF system where lower power dissipation is not an important issue (such as base stations of RF communication systems). If the efficient 2D wavelets are associated to obtained by 1D wavelet filters and many possible patterns cannot be well approximated by such wavelets. The another problem to solve is that, up to now, we start with a pattern given a priori and separately but for many applications such motifs are noisy or have to be taken from some experimental signals.

References

[1] Keng L Fong and Robert G Meyer. Monolithic RF active mixer design. IEEE Transactions on Circuits and Systems{II: Analog and Digital Signal Processing, 46(3):231{239, March 1999.
[2] Ranjit Gharpurey. Modeling and analysis of substrate coupling in integrated circuits. PhD thesis, University of California at Berkeley, 1996.
[3] Hector Mesa1, Adapted Wavelets for Pattern Detection. University of La Habana, Faculty of Mathematics and Computer Sciences, 10400 La Habana, Cuba
[4] Greshman, A., Sidiropoulos, N.D.: Space Time Processing for MIMO Communications. John Wiley & Sons (2005)
[5] Proakis, J.G., Salehi, M.: Digital Communications, 5th edn. McGraw-Hill, New York (2008)

[6] A. K. Verma , Neema Verma : A Comparative Performance Analysis of Wavelets in Denoising of Speech Signals (2012)
[7] Ladan Ebadi,Shattri Mansor,Helmi Shafri, Ravshan Ashurov ,: A review of applying second-generation WAVELETS FOR NOISE REMOVAL FROM REMOTE SENSING DATA (2013)
[8] Selma ÖZAYDIN, Iman Khalil ALAK/ GU J Sci,: Speech Enhancement using Maximal Overlap Discrete Wavelet Transform *Part A, 5(4):159-171 (2018)*
[9] adnab quadri : A Review of Noise Cancellation Techniques for Cognitive Radio (2018)

The Impact of Device to Device Communication on Operators and the Cellular Network

Abdussalam Masaud Mohamed Ammar
Faculty of Electronic Technology
Slm2010ly@gmail.com

Amira Youssef Mohammad Ellafi
Faculty of Electronic Technology
Amoor85ly@yahoo.com

Amer R. Zerek
Zawia University, Faculty of Engineering
EE Department,
Zawia, – Libya
anas_az94@yahoo.co.uk

***Abstract* - A permanent need to increase the network capacity in order to provide the growing demands of the subscribers has led to the evolution of cellular communication networks, the number of devices is expected to radically increase in next few years, with an estimation of more than 50 billion connected devices by 2020. This large number of connections are expected to be various in nature, demanding higher data rates, lesser delays, enhanced system capacity and superior throughput. The available spectrum resources are limited and need to be flexibly used by the mobile network operators (MNOs) to be suitable with the rising demands. One of the evolving solutions were presented lately was Device To Device (D2D) communication , Various D2D solutions have been proposed, which include inband and outband D2D transmission modes. This paper discusses the main characteristics of D2D communication including its usage scenarios, architecture, technical features, and areas of active research.**

Index Terms* – *D2D , 3GPP , QoS, eNB , LTE .

I. INTRODUCTION

Today the number of handy smart devices is dramatically increasing, with a growing demand for higher data rate applications. Also to cover the needs of the next generation applications, the present data rates need a refinement. The fifth generation (5G) networks are expected and will have to meet these rising demands. A dedicated technology of the next generation networks (NGNs) is Device-to-Device (D2D) communication, which is expected to play a remarkable role in the approaching era of wireless communication. The benefits of D2D communication did not gain much importance in the previous generations of wireless communication, but in 5G networks, it is expected to be a main part. The rising trends [1] prepare a way for this emerging technology.

With the introduction of device-to-device (D2D) communication, direct transmission between devices is possible. This is expected to improve the reliability of the link between the devices, enhance spectral efficiency and system capacity [2], with reduced latency within the networks at the same time, manufacturers of the smart devices and wireless service providers had starting introducing Long Term Evolution (LTE) and 4th generation (4G) capable products (Smartphones, Tabs, Modems, etc.).

So the network capacity is increasingly limited and for mobile operators the biggest challenge in future will be the huge demand for spectrum which is will be more costly. For these reasons the mobile operators are working presently hard to improve the infrastructure and provide the bandwidth according to the users demand with less expansive.

D2D is a new paradigm in cellular networks It allows user equipment's (UEs) in close proximity to communicate using a direct link rather than having their radio signal travel all the way through the base station (BS) or the core network. One of its main benefits is the ultra-low latency in communication due to a shorter signal traversal path as will as a power saving within the network, which is not possible in case of traditional cellular communication.

Various short-range wireless technologies like Bluetooth, Wi-Fi Direct and LTE Direct ,defined by the Third Generation Partnership Project (3GPP) [3], can be used to enable D2D communication. They differ mostly in the data rates, distance between 1-hop devices, device discovery mechanisms and typical applications. It promises improvement in energy efficiency, throughput and delay. It has the potential to effectively offload traffic from the network core. Hence, it is a very flexible technique of communication, within the cellular networks.

Also in spite of the numerous benefits offered by device-to-device (D2D) communication, a number of concerns are involved with its implementation. When sharing the same resources, interference between the cellular users and D2D users' needs to be controlled.

For this, numerous interference management algorithms have been proposed in literature. Other concerns include peer discovery and mode selection, power control for the devices, radio resource allocation and security of the communication.

Figure 1. Shows the next generation network scenario, supporting device-to-device (D2D) communication along with some general use cases.

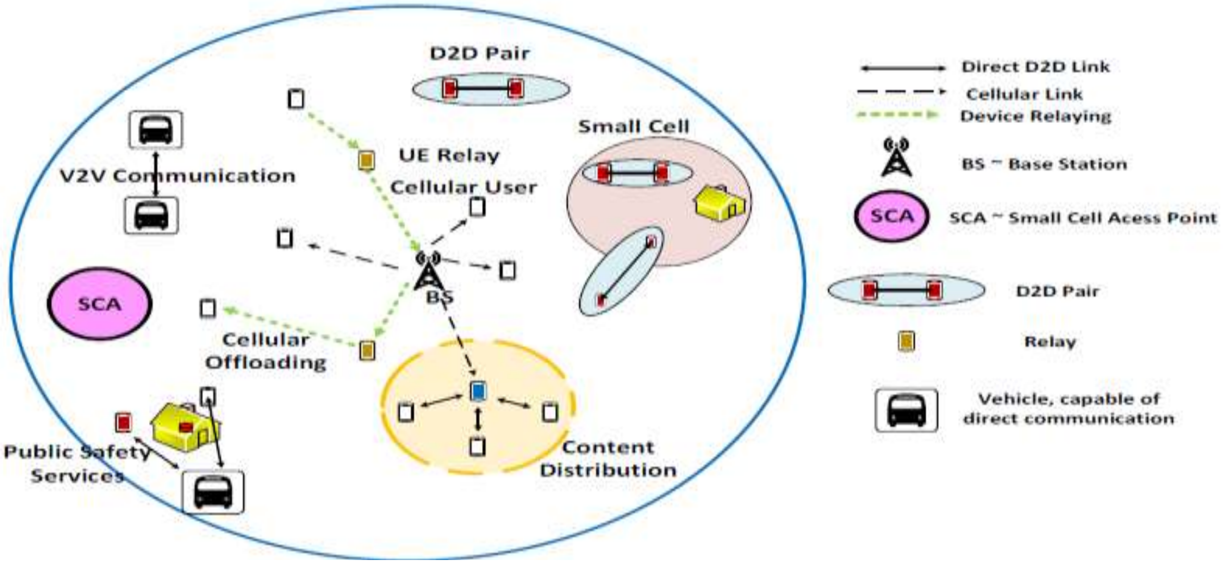

II Classification of D2D Communication

D2D communication in cellular network can be categorized as in figure 2 into both Inband D2D and Outband D2D based on the spectrum in which D2D communications occurs [4]. D2D communications is divided into two modes or categories called Inband underlay mode when the D2D communications use the cellular resources and spectrum and Inband overlay mode when cellular resources are allocated for the two D2D end devices that communicate directly.

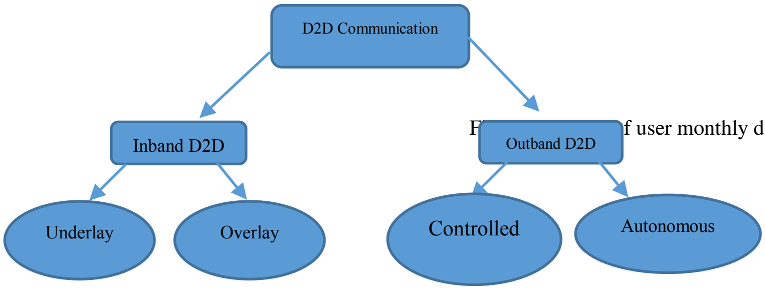

F f user monthly data rates in Petabyte [1]

Fig.2.a classification of D2D communication

High control over licensed spectrum is the key motivating factor for choosing the Inband D2D communication. In other hand, the main motivation of using Outband D2D communications is the capacity to eliminate the interference between D2D links. Furthermore, Outband D2D communications is faced with a lot of challenges in the coordination between different bands.

In this section, we provide a formal definition for each category of D2D communication and an overview to advantages and disadvantages of each D2D mode.

A. *Inband Communication.*

The cellular communication and D2D communication use the same spectrum licensed to the cellular operator. The licensed spectrum may be either divided into non-overlapping portions for D2D and cellular communication respectively (overlay) or may not be divided at all (underlay). Overlay scheme is easier to implement but underlay scheme leads to opportunistic and hence, more efficient spectrum use and more profit to operators.

The motivation for choosing inband communication is the high control over licensed spectrum.[5][6][7], Results show that QoS provisioning had a lot of requirements by the consideration of the uncontrollability of interference in the unlicensed spectrum.

To improve the spectrum efficiency the D2D inband can reuse the time and frequency resources by d2D users (i.e. Underlay) or allocating time and frequency resources occupied by D2D users (i.e. overlay) [8]. Under this, Inband communications can be divided into underlay and overlay categories.

The most disadvantage of inband D2D is the interference caused by D2D users to cellular communications .This interference can be mitigated by introducing high complexity resource allocation methods, which increase the computational overhead of the eNB of D2D users.

ISSN 1737-9334

1. *Underlay Inband D2D mode.*

In underlay inband mode, cellular and D2D communications share the same radio resources. Underlay inband can improve and enhance the performance of different targets such as spectrum efficiency, energy efficiency, and cellular coverage by the use of different techniques including diversity techniques, interference reduction, and resource allocation and by using network coding [9].

By using underlying direct D2D communications, LTE-advanced mobile network can offers several advantages such as low end-to-end latency and high spectral efficiency.

2. *Overlay Inband D2D mode.*

In this mode, cellular and D2D are given dedicated cellular resources and those cellular resources are subtracted from cellular users in order to eliminate interference for the D2D communications on cellular transmissions [10][11][12] the Base Station (BS) assisted scheduling and D2D power control was proposed in order to reduce D2D interference.

B. Outband D2D communication

D2D communication uses unlicensed spectrum (e.g., the free 2.4 GHz ISM band or 38 GHz mm Wave band) where cellular communication does not occur. It helps in eliminating the interference between D2D and cellular users although interference is still present from other electronic devices (like Bluetooth and Wi-Fi) operating in this band.

In fact, the operators can control interference when using licensed spectrum but that is infeasible for outband scheme. Outband technology is further divided into controlled and autonomous types. In the former, the radio interface for D2D communication is controlled by the cellular network while in the latter, the cellular network controls only the cellular communication leaving the control of D2D communication to the users.

On the other hand, Outband D2D may suffer from the uncontrolled nature of unlicensed spectrum. To exploit the unlicensed spectrum it is necessary to have another extra interface that implements WIFI Direct, Zig Bee or Bluetooth [13].

The coordination between two different bands for achieving Outband D2D communication has a lot of challenges because in most cases the D2D communications occur in the above mentioned extra interface [8]. Outband D2D communication can be classified into two categories or modes depend on the occurrence of the second interface.

These modes are called controlled mode when the second interface in under cellular network or autonomous when D2D control is done by users and the occurrence of the second interface is not under cellular network.

1. *D2D Outband communications: Controlled mode.*

In this category of D2D communications, all the literature propose to use the cellular network advanced management features to control D2D communication in order to improve the efficiency and reliability of D2D communications and to improve also the system performance in terms of throughput, power efficiency and multicast.

The D2D communication paradigm can be implemented on LTE infrastructure by using the Wi-Fi Direct and without making a major change in LTE protocols.

2. *D2D Outband communications: Autonomous mode*

There are very few works on this category. Autonomous D2D communication is motivated by reducing the overhead of cellular network. This category does not require any changes at the BS (eNB) and can be deployed easily.

C. Advantages and disadvantages of the different types of D2D communications.

Today, Outband communications is attracting more and more attention. With the arrival of new smartphones and new mobile devices in phone market, device will be capable to implement Outband D2D schemes. Some studies provides an overview of the advantages and disadvantages of Outband D2D communications. It is putting high hopes and are seeing it as the alternative to inband D2D communication category.

A brief look of advantages and disadvantages of Inband D2D and Outband D2D communications are given in the following table 1 and table 2:

Table 1. Advantages and disadvantages of Inband D2D communication

Advantages of Inband D2D	Disadvantages of Inband D2D
• Underlay D2D increases the spectral efficiency of cellular spectrum by exploiting the spatial diversity. • QoS management is easy by reason of entirely controlled by eNBs . • The possibility of using Inband D2D communication on any mobile equipment .	• Challenging control of interference. • No possibility for D2D and cellular simultaneous transmission. • High complication of resource allocation procedure and power control

Table 2. Advantages and disadvantages of Outband D2D communication

Advantages of Outband D2D	Disadvantages of Outband D2D
• Easier resource allocation. • Possibility of simultaneous occurrence of D2D and	• Necessary to decode and to encode packets. • D2D communication only

cellular users. • None interference between D2D and cellular subscribers. • None necessary to devote cellular resources to D2D spectrum	used by LTE and WiFi radio interfaces • Need of the efficient power management

III Technical Aspects and Challenges.

We will now discuss the various technical aspects and the corresponding challenges of D2D communication in wireless networks.

A. Synchronization

In a typical cellular network, UEs achieve time and frequency synchronization using periodic broadcasts from the BS. Devices in D2D communication can also synchronize with the same broadcasts so long as they belong to the same BS.

The situation gets complicated in the following cases:

1. UEs belong to different BSs that may not be themselves synchronized.
2. Some of the UEs are in the coverage of the network and some outside the coverage.
3. All UEs lie outside network coverage [14].

Synchronization among UEs is beneficial for D2D communication because it helps a UE to use the right time slot and frequency for discovering and communicating with its peer and thus engage in more energy-efficient communication.

B. Peer Discovery.

Looking at the demand of D2D network, there should be an efficient method for discovering peers. This means a UE should be able to discover other nearby UEs quickly and with low power consumption. From user perspective, there are two types of peer discovery techniques, restricted and open [15].

In the first case, devices cannot be discovered by the end users without their permissions. In the second case, devices can be discovered whenever they lie in the proximity of other users. From network perspective, peer discovery can be controlled lightly or tightly by the BS [15]

C. Mode Selection.

A pair of UEs that have discovered themselves are potential candidates for a D2D communication. But performance-wise, cellular communication may be more preferable if, for example, the direct channel is noisier. Mode selection is concerned with choosing the right mode – cellular or D2D – for communication between two UEs to achieve some performance objective like high spectral efficiency, low latency, or low transmit power.

Mode selection can be done by the network or by the UEs. Mode selection is generally coupled with power control. The analysis could be done using instantaneous system information (which may be difficult to acquire in practice) or statistical system information leading to decisions that are respectively optimal at a given instant or optimal in an average sense over a longer duration.

D. Resource Allocation.

After device discovery, availability of resources is important for enabling communication over the direct links. Radio resource allocation is thus important for enhancing the spectral efficiency of D2D communication, underlaying cellular communication. Resource allocation strategies in D2D communication can be centralized or distributed.

The distributed techniques improve the scalability of the D2D links. Hybrid solutions also can be provided and are an area of research. A number of different techniques are available under the literature survey. For obtaining maximum throughput, D2D communication can operate in a number of modes. These can be:

- *Silent Mode*: In this mode, the D2D devices stay silent and cannot transmit because of lack of resources. Spectrum reuse, as a result, is not possible.
- *Dedicated Mode*: In this mode, some of the available resources are dedicated for the D2D users, to be used for direct transmission.
- *Reuse Mode*: In this mode, uplink or downlink resources of the cellular users are reused by the D2D users.
- *Cellular Mode*: In this, conventional communication occurs, through the eNBs and D2D data is transmitted.

An improvement in the spectrum efficiency can be achieved by the use of reuse mode. Interference management is better with the dedicated and cellular modes. However, these two modes maybe inefficient to maximize the overall network throughput. The decision for resource sharing is made by the base station. When the D2D links and cellular links reuse the same resources, it is referred to as non-orthogonal sharing, and when they do not share the same resources, it is referred to as orthogonal sharing. Better resource utilization efficiency is achieved by non-orthogonal sharing.

E. Interference Management.

In inband communication, cellular and D2D links may interfere with each other based on how they share the frequencies. In outband communication, D2D links suffer interference from each other as well as from other devices operating in the same band [16].

Interference can be reduced if UEs transmit at lower power levels which might, however, affect the QoS at the receiver. Power control, in addition to interference mitigation, leads to energy-efficient operation which is one of the goals of next generation wireless networks. A general scenario of interference in D2D under laid cellular networks is depicted in Figure 3.

A very critical term related to interference avoidance is mode selection. Generally, distance between the D2D users and cellular users is considered for mode selection. Also, distance between cellular user and the BS is an important parameter for selection of the mode in the network, thus avoiding interference. Mode selection, resource allocation and interference minimization are closely related and often jointly optimized.

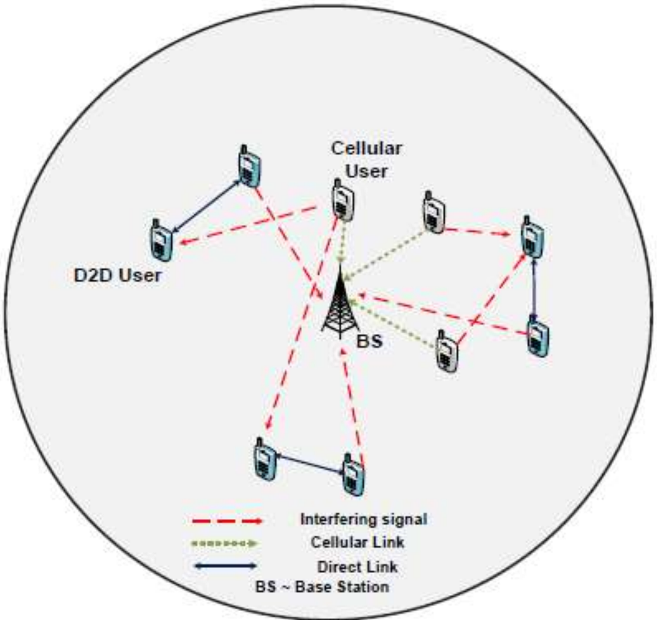

Fig.3.An interference scenario in D2D underlay cellular network

F. D2D with Mobility.

Most D2D-related research has focussed on static users while cellular networks essentially cater to mobile users. More analysis is needed to understand how the performance gains auger in dynamic scenarios (from pedestrian to vehicular speeds) and what interference handling and handover mechanisms are needed as UEs move within and across cells [17].

IV. Security and Privacy in D2D Communication.

D2D communication affords stronger anonymity and data privacy compared to conventional cellular communication since the data are not stored at a central location. However, various common attacks like eavesdropping, denial of service, man in-the-middle, node impersonification, IP spoofing, malware attack, etc. can paralyzer D2D links. Users would also like to protect their privacy, e.g., by restricting the availability of their sensitive personal data.

The 3GPP Security Workgroup (SA3) has identified six vulnerability categories for the security and privacy domain [18] as follow :

1. Physical attacks.
2. Compromised credentials.
3. Configuration attacks.
4. Protocol attacks.
5. Attacks on core networks.
6. User data and privacy attacks.

Especially for D2D, connections between proximate devices are vulnerable to security threats due to: (a) direct wireless connection, (b) mobility of end users and (c) privacy issues in social applications [19].

To make D2D communication secure, physical layer security plays a key role [90]. Incorporating security features in D2D communication, at the physical layer is beneficial

V Conclusion

In this paper, an extensive survey on device-to-device (D2D) communication has been done. This emerging technology is expected to solve the various tribulations of the mobile network operators (MNOs), efficiently satisfying all the demands of the subscribers. A complete overview about the different types of D2D communication and the supported architectures has been brought up.

A number of features can be used in conjunction with D2D communication, to enhance the functionality of cellular networks. Some challenges related to the implementation of device-to-device (D2D) communication have been brought up in this survey, and various algorithms for dealing with them have been discussed.

Architecture has been proposed in the survey, for optimal resource allocation to the D2D users underlaying cellular networks. This is important to ensure efficient communication in the existing cellular networks. Some use cases have been quoted, where D2D communication will play a crucial role. Thus, D2D communication is an integral technology of the future networks, motivating the researchers to overcome the associated challenges in order to completely take advantage of its utility.

REFERENCES

[1] D. Astely et al., “LTE Release 12 and Beyond.” IEEE Commun. Mag., vol.51, no. 7, 2013, pp. 154-60 .

[2] Chai, Yingqi, Qinghe Du, and Pinyi Ren. "Partial time-frequency resource allocation for device-to-device communications underlaying cellular networks." Communications (ICC), 2013 IEEE International Conference on. IEEE, 2013.

[3] 3GPP, 3rd generation partnership project (3GPP). Available: http://www.3gpp.org/ (Accessed 18 march 2019).

[4] Zhijian Lin • Zhibin Gao • Lianfen Huang • Chi-Yuan Chen • Han-Chieh Chao "Hybrid Architecture Performance Analysis for evice-to-Device Communication in 5G Cellular Network" © Springer Science+Business Media New York 2015.

[5] Arash Asadi ,Qing Wang, , and Vincenzo Mancuso," A Survey on Device-to-Device Communication in Cellular Networks" arXiv:1310.0720v6 [cs.GT] 29 Apr 2014.

[6] Doppler, K.; Rinne, M.P.; Janis, P.; Ribeiro, C.; Hugl, K "Device-to-Device Communications; Functional Prospects for LTE-Advanced Networks" ICC Workshops 2009.

[7] K. Akkarajitsakul, P. Phunchongharn, E. Hossain, and V. K. Bhargava, "Mode selection for energyefficient D2D communications in LTEadvanced networks: A coalitional game approach," in Proceedings of IEEE ICCS, 2012, pp. 488–492.

[8] Chithra B Das "A Study on Device To Device Communication in Wireless Mobile Network" International Journal of Modern Communication Technologies & Research (IJMCTR) ISSN: 2321- 0850, Volume-3, Issue-3, March 2015.

[9] A.Osseiran, K. Doppler, C. Ribeiro, M. Xiao, M. Skoglund, and J. Manssour, "Advances in device-todevice communications and Network coding for IMT-Advanced," ICT Mobile Summit, 2009.

[10] B. Zhou, H. Hu, S.-Q. Huang, and H.-H. Chen, "Intracluster deviceto-device relay algorithm with optimal resource utilization," IEEE Transactions on Vehicular Technology, vol. 62, no. 5, pp. 2315– 2326, Jun. 2013.

[11] J. C. Li, M. Lei, and F. Gao, "Device-to-device (D2D) communication in MU-MIMO cellular networks," in Proceedings of IEEE GLOBECOM,2012, pp. 3583–3587.

[12] G. Fodor, E. Dahlman, G. Mildh, S. Parkvall, N. Reider, G. Mikls, and Z. Turnyi, "Design aspects of network assisted device-to-device communications," IEEE Communications Magazine, vol. 50, no. 3, pp. 170–177, 2012.

[13] W. ALLIANCE, "Wi-Fi Peer-to-Peer (P2P) Specification v1. 1," WI-FI ALLIANCE SPECIFICATION, vol. 1, pp. 1–159, 2010.

[14] N. Abedini, S. Tavildar, J. Li, T. Richardson, Distributed synchronization for device-to-device communications in an lte network, IEEE Trans.Wireless Commun. 15 (2) (2016) 1547–1561.

[15] D. Feng, L. Lu, Y. Yuan-Wu, G. Li, S. Li, G. Feng, Device-to-device communications in cellular networks, IEEE Commun. Mag. 52 (4) (2014) 49–55.

[16] M. Noura, R. Nordin, A survey on interference management for device-todevice (d2d) communication and its challenges in 5G networks, J. Netw. Comput. Appl. 71 (2016) 130–150.

[17] A. Murkaz, R. Hussain, S. Hasan, M. Chung, B.-C. Seet, P. Chong,S. Shah, S. Malik, Architecture and protocols for inter-cell deviceto-device communication in 5G networks, in: Proceedings of the 14th IEEE International Conference on Pervasive Intelligence and Computing,(PICom-2016), IEEE, 2016, pp. 489–492.

[18] 3GPP, "Feasibility Study on Remote Management of USIM Application on M2M Equipment: Technical Report 33.812," 2007.

[19] M. Wang and Z. Yan, "A Survey on Security in D2D Communications, " Mobile Networks and Applications, pp. 1- 14, 2016.

ISSN 1737-9334

Comparison Study Between Mamdani and Sugeno Fuzzy Inference Systems for Speed Control of a Doubly-Fed Induction Motor

Herizi Abdelghafour [#1], Smaini Houssam Eddine[#], Mahmoudi Ridha[#], Bouguerra Abderrahmen[#], Zeghlache Samir[*2], & Rouabhi Riyadh[#]

[#]*LGE Research Laboratory, Department of Electrical Engineering, Faculty of Technology*
University of M'sila, BP 166 Ichbilia 28000, Algeria
[1]`abdelghafour.herizi@univ-msila.dz`

[*]*Laboratoire d'Analyse des Signaux et Systèmes, Department of Electronic, Faculty of Technology*
University of M'sila, BP 166 Ichbilia 28000, Algeria
[2]`samir.zeghlache@univ-msila.dz`

Abstract— **In this article we present a comparative study between the two types of fuzzy logic mamdani and sugeno applied to the doubly-fed induction motor (DFIM). The proposed command combines the flow-oriented vector control and the type 1 fuzzy logic to get a robust control. The oriented stator flux vector control is efficient because of the simplicity of design and allows natural decoupling between flows and currents. The application of this strategy is carried out using Integral Proportional Controllers (PI) which are calculated directly from the machine parameters using conventional analytical methods which need a careful calculation and a good knowledge of all machine settings. The aim of our study is to try to replace the speed control controller (PI) with a type 1 fuzzy logic controller (mamdani or sugeno). Robustness tests of the control with respect to the parametric variations of the machine will be carried out.**

Keywords— **doubly fed induction machine; vector control; stator flux oriented; PI controller; fuzzy logic; mamdani; sugeno**

I. INTRODUCTION

Nowadays, several works have been directed towards the study of the doubly-fed induction motor "DFIM": it is a three-phase asynchronous machine with a wound rotor which can be powered by two voltage sources, one to the stator and the other to the rotor [1]. Thanks to the development of power electronics equipment and the emergence of modern control technologies, the DFIM presents an ideal solution for high power and variable speed drives. The interest of such machines is that they ensure very low speed operation [2].

However, from the control point of view, this motor has properties that obscure all the assumptions of classical control theory [3-5]. It is characterized by a nonlinear dynamics, coupled, multi-variable, with variable parameters in time and with an inaccessible rotor. To this end, significant efforts have been made to develop efficient controls to control the dynamic behavior of the doubly-fed induction motor.

Various control approaches have been exploited, we can distinguish in a non-exhaustive way the vector control, the input-output linearization technique, the sliding mode control ... etc. They have been developed and applied in various fields, in particular the control of the doubly-fed induction motor.

Flux-Oriented Vector Control (FOC) was introduced in the early 1970s by F. Blaschke and Hass [6] to make a decoupling between magnetic flux and electromagnetic torque similar to that of a DC machine with separate excitation. Two types of directional flow vector control are possible, the first direct requires knowledge of the modulus and phase of the real rotor flux and the second indirect, where only the place of the rotor flux is estimated [7, 8]. This technique allows dynamic performance of good quality. However, experience has shown that this technique has a high sensitivity to parametric variations, including the variation of the rotor resistance which has a direct relationship with the flow orientation angle. As a result, several control techniques have been developed to improve performance and robustness about parametric variations. One can quote, the nonlinear control by return of state of linearization input-output, the direct command of the couple "DTC", the control by mode of sliding, the Technique of the Backstepping ... etc [9-12].

On the other hand, an important development has been recorded during the last two decades. Indeed, the appearance of new techniques, such as: fuzzy logic, neural networks, genetic algorithms and others, has formed a new discipline called artificial intelligence. Artificial intelligence techniques have not only improved the control of systems and overcome the disadvantages of conventional techniques, but also completely change the concepts used in the study and realization of control systems. The essential advantage of the techniques evoked is that they orient themselves more towards the approximation of the systems than towards the search for their precise models.

The fuzzy logic that is in full expansion has become clearly imposed because of their properties, such as: allows obtaining a law of adjustment often very effective without having to do extensive modeling. In contrast to a standard regulator or a state feedback regulator, the fuzzy logic controller does not deal with a well-defined mathematical relationship, but uses inferences with multiple rules, based on linguistic variables [13]. The fuzzy logic of being one of the most used means for improving the robustness of a control of nonlinear systems and against modeling errors and parametric drifts. These properties have been largely verified, theoretically and practically, in several works [14-16].

In the light of what has been said, we propose, in this work, an association combining fuzzy logic with flow-oriented direct vector control, this association will be exploited to set up a new robust control, based on fuzzy logic, to improve the dynamic responses of the doubly-fed induction motor.

The present work is structured as follows: Section 2 is devoted to the synthesis of the mathematical model of the doubly fed induction machine. The vector control of the DFIM will be presented in section 3 after the principle of the orientation of the stator flux which makes it possible to solve the decoupling problem. In the fourth section, we synthesize type-1 fuzzy (mamdani and sugeno) vector control law of the DFIM. Finally, robustness tests of the proposed control will be made, the simulations will be presented under Matlab / Simulink.

II. MATHEMATICAL MODELING OF DFIM

The modeling of the DFIM is described in the Park reference system. The following system of equations describes the global modeling of the machine [13, 14]:
The electrical equations:

$$\begin{cases} V_{sd} = R_s I_{sd} + \frac{d\varphi_{sd}}{dt} - \omega_s \varphi_{sq} \\ V_{sq} = R_s I_{sq} + \frac{d\varphi_{sq}}{dt} + \omega_s \varphi_{sd} \\ V_{rd} = R_r I_{rd} + \frac{d\varphi_{rd}}{dt} - (\omega_s - \omega_r)\varphi_{rq} \\ V_{rq} = R_r I_{rq} + \frac{d\varphi_{rq}}{dt} + (\omega_s - \omega_r)\varphi_{rd} \end{cases} . \tag{1}$$

The magnetic equations:

$$\begin{cases} \varphi_{sd} = L_s I_{sd} + M I_{rd} \\ \varphi_{sq} = L_s I_{sq} + M I_{rq} \\ \varphi_{rd} = L_r I_{rd} + M I_{sd} \\ \varphi_{rq} = L_r I_{rq} + M I_{sq} \end{cases} \tag{2}$$

Where:
L_s and L_r : cyclic inductances of a stator and rotor phase ;
M: maximum mutual inductance between a stator and rotor phase (the axes of the two phases coincide).

The electromagnetic torque is expressed as a function of currents and flows by:

$$C_{em} = P\frac{M}{L_s}\left(\varphi_{sq} I_{rd} - \varphi_{sd} I_{rq}\right) \tag{3}$$

With:
P: The number of pole pairs of the DFIM.

The model of the doubly-fed induction machine can be written in matrix form as follows [10, 14]:

$$\dot{X} = AX + BU \tag{4}$$

Where:
$X = [\varphi_{sd} \quad \varphi_{sq} \quad I_{rd} \quad I_{rq}]^T$, $U = [V_{sd} \quad V_{sq} \quad V_{rd} \quad V_{rq}]^T$

$$[A] = \begin{bmatrix} -\frac{1}{T_s} & \omega_s & \frac{M}{T_s} & 0 \\ -\omega_s & -\frac{1}{T_s} & 0 & \frac{M}{T_s} \\ \alpha & -\beta\omega & -\delta & (\omega_s - \omega) \\ \beta\omega & \alpha & -(\omega_s - \omega) & -\delta \end{bmatrix} ;$$

$$[B] = \begin{bmatrix} 1 & 0 & 0 & 0 \\ 0 & 1 & 0 & 0 \\ -\frac{M}{\sigma L_s L_r} & 0 & \frac{1}{\sigma L_r} & 0 \\ 0 & -\frac{M}{\sigma L_s L_r} & 0 & \frac{1}{\sigma L_r} \end{bmatrix}$$

With:
$\sigma = 1 - \frac{M^2}{L_r L_s}$; $T_r = \frac{L_r}{R_r}$; $T_s = \frac{L_s}{R_s}$; $\alpha = \frac{M}{\sigma L_r L_s T_s}$; $\beta = \frac{M}{\sigma L_r L_s}$; $\delta = \frac{1}{\sigma}\left(\frac{1}{T_r} + \frac{M^2}{L_s T_s L_r}\right)$.

The mechanical equation is of the following form:

$$J\frac{d\Omega}{dt} = C_{em} - C_r - f\Omega \tag{5}$$

With:
C_{em} and C_r : the electromagnetic torque and the resisting torque (the mechanical load) ;
f and J : coefficient of friction and moment of inertia of the rotor shaft.

III. THE VECTOR CONTROL OF DFIM

The dynamic behavior of the doubly fed induction machine is never satisfactory with a scalar command. That is why we will be interested in a control that is better adapted to dynamic regimes: the vector control with stator-oriented flow that ensures the control of the torque and the regulation of the flow in transient regime.

The control by orientation the flux, consists in aligning the stator flux along the axis d of the rotating reference [10, 15]. On therefore has: $\varphi_{sd} = \varphi_s$ and consequently $\varphi_{sq} = 0$.

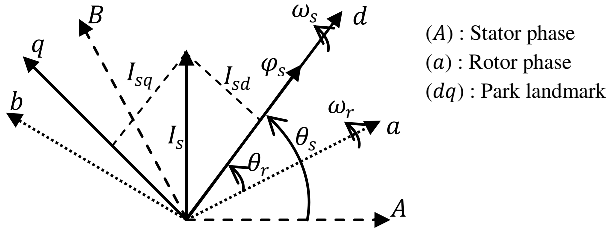

Fig. 1 Stator flux orientation on the d axis.

The electromagnetic torque of equation (3) is then written:

$$C_{em} = -P\frac{M}{L_s}\varphi_{sd} I_{rq} \tag{6}$$

And the equation (2) of the flows becomes:

$$\begin{cases} \varphi_{sd} = L_s I_{sd} + M I_{rd} \\ 0 = L_s I_{sq} + M I_{rq} \end{cases} \tag{7}$$

If one takes the stator current in the axis of null, $I_{sd} = 0$, realistic hypothesis for the machines of high power, the current and the tension in this axis are then in phase $V_s = V_{sq}$ and $I_s = I_{sq}$, the equations of the stator currents of the machine are reduced to:

$$\begin{cases} I_{rd} = \frac{\varphi_s}{M} \\ I_{rq} = -\frac{L_s}{PM\varphi_s} C_{em} \end{cases} \tag{8}$$

With the assumption of constant stator flux, we obtain the electric equations in the form:

$$\begin{cases} V_{sd} = R_s I_{sd} \\ V_{sq} = R_s I_{sq} + \omega_s \varphi_{sd} \\ V_{rd} = R_r I_{rd} - (\omega_s - \omega_r)\varphi_{rq} \\ V_{rq} = R_r I_{rq} + (\omega_s - \omega_r)\varphi_{rd} \end{cases} \tag{9}$$

The model of the doubly-fed induction machine is written:

$$\begin{cases} \frac{d\varphi_{sd}}{dt} = \frac{M}{T_s} I_{rd} - \frac{1}{T_s}\varphi_{sd} + V_{sd} \\ \frac{d\varphi_{sq}}{dt} = \frac{M}{T_s} I_{rq} - \omega_s \varphi_{sd} + V_{sq} \\ \frac{dI_{rd}}{dt} = -\delta I_{rd} + (\omega_s - \omega) I_{rq} + \alpha\varphi_{sd} - \frac{M}{\sigma L_s L_r} V_{sd} + \frac{1}{\sigma L_r} V_{rd} \\ \frac{dI_{rq}}{dt} = -(\omega_s - \omega) I_{rd} - \delta I_{rq} + \beta\omega\varphi_{sd} - \frac{M}{\sigma L_s L_r} V_{sq} + \frac{1}{\sigma L_r} V_{rq} \end{cases} \tag{10}$$

The mechanical equation is written:

$$\frac{d\Omega}{dt} = -\frac{1}{J}\left(P\frac{M}{L_s}\varphi_{sd} I_{rq} + f\Omega + C_r\right) \tag{11}$$

IV. FUZZY LOGIC CONTROLLER

A fuzzy system (were established in 1965 by Professor Lotfi Zadeh [16]) can be seen as an expert system operating from a knowledge representation based on set theory. A fuzzy system is composed of a database that counts all the information we have about the process which allows us to define the membership functions and fuzzy rules of this fuzzy system, a rule base Fuzzy which is an IF-THEN rule collection, a singleton digital-symbolic or fuzzification interface and a symbolic-numeric interface or defuzzification by the weighted center method which amounts to a weighted sum of the centers of the sets inferred blur multiplied by the corresponding degrees of belonging [17, 18].

$$y = \sum_{j=1}^{M} w_j b_j / \sum_{j=1}^{M} w_j \tag{12}$$

With:

w_j is the degree of activation of the j^{th} fuzzy rule.

$b_{j,i}$ $i = 1,2,\dots n$ are the coefficients of the j^{th} linear consequence.

y^i the numerical output of the j^{th} fuzzy rule or $j \in [1, M]$.

M: the total number of inference rules.

A. Principle of a fuzzy control

The structure of a fuzzy control, shown in figure 2, can be broken down into three large modules.

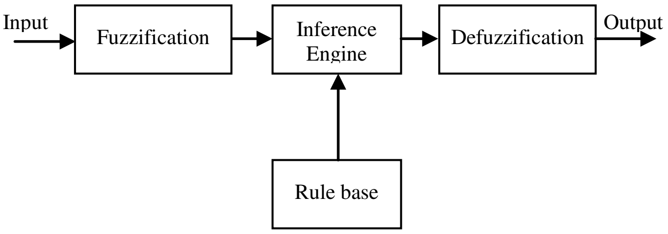

Fig. 2 General structure of a fuzzy control.

The first of these modules deals with the inputs of the system: it is fuzzification. It allows associating with each of the real inputs, through membership functions, a degree of membership for each of the fuzzy subsets defined on the whole speech.

The second module consists of the inference engine and the rule base. This one consists of rules of the type: "If ..., Then ..." and will make it possible to pass degrees of belonging of the quantities of entries to the degrees of belonging to the fuzzy subsets of the size of command. The inference engine, it will allow to generate a conclusion from the entries and active rules. It then calculates the degrees of membership of the fuzzy subsets corresponding to the control of the system.

Finally, the last module, the defuzzification interface, will make it possible to transform the degrees of belonging of the fuzzy command subassemblies into digital quantity. This is the inverse transformation of the fuzzification module.

From this structure, different types of fuzzy correctors will then be able to be defined. The following section presents more specifically the structure that we used during our work.

B. Fuzzy PI controller

Figure 3 shows the general structure of a non-adaptive gain PI type fuzzy controller. To make a PI type corrector, simply integrate the fuzzy motor output as shown in figure 3. Noting y the output of the PI type fuzzy controller.

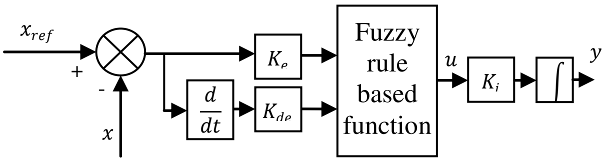

Fig. 3. Fuzzy PI controller.

The fuzzy controller is basically an input/ output static non-linear mapping, the controller action can be written in the form [10]:

$$u = k_e . e + k_{de} . \frac{d}{dt} e \tag{13}$$

The Fuzzy-PI output is:

$$y = \int k_i . u \tag{14}$$

Where:

k_e is the gain of error, k_{de} is the gain of derivative error, k_i is the integral factor, u is the fuzzy output.

C. Knowledge base proposed

For mamdani fuzzy inference systems : Fig. 4 show the triangle-shaped membership functions of error e and derivative of error ė. The fuzzy sets are designated by the labels: NB (Negative Big), NM (Negative Medium), NS (Negative Small), ZE (Zero), PS (Positive Small), PM (Positive Medium), PB (Positive Big). Fig 5 show the proposed membership functions for output variable.

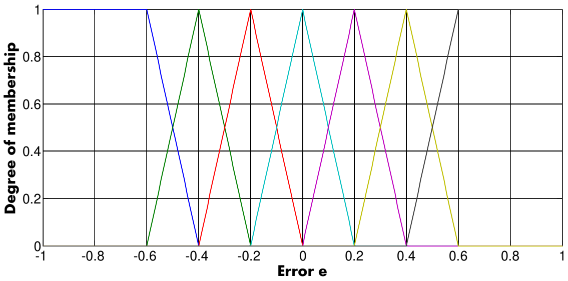

Fig. 4 Membership functions for error e and derivative of error ė.

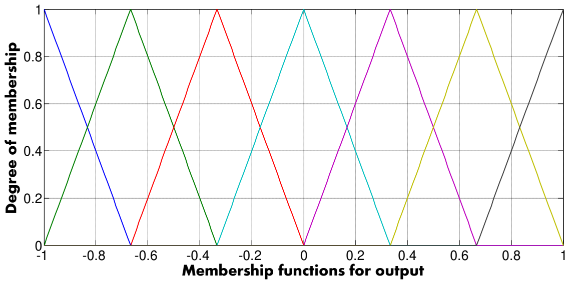

Fig. 5 Membership functions for output u.

In this paper, the triangular membership function, the max-min reasoning method, and the center of gravity defuzzification method are used, as those methods are most frequently. All the membership functions (MFs) are asymmetrical because near the origin (steady state), the signals require more precision. Seven MFs are chosen for e and ce signals and nine for output. All the MFs are symmetrical for positive and negative values of the variables.

TABLE I
LINGUISTIC RULE TABLE

Control		***e*(*t*)**						
		NB	NM	NS	ZE	PS	PM	PB
ė(t)	NB	NB	NB	NB	NB	ZE	ZE	ZE
	NM	NB	NB	NM	NM	ZE	ZE	ZE
	NS	NB	NB	NS	NS	PS	PS	PM
	ZE	NB	NM	NS	ZE	PS	PM	PB
	PS	NM	NS	NS	PS	PS	PB	PB
	PM	ZE	ZE	ZE	PM	PM	PB	PB
	PB	ZE	ZE	ZE	PB	PB	PB	PB

For sugeno fuzzy inference systems : The membership functions of the input error e and derivative error ė (same the mamdani) and the output discontinuous control are presented by Figure 6.

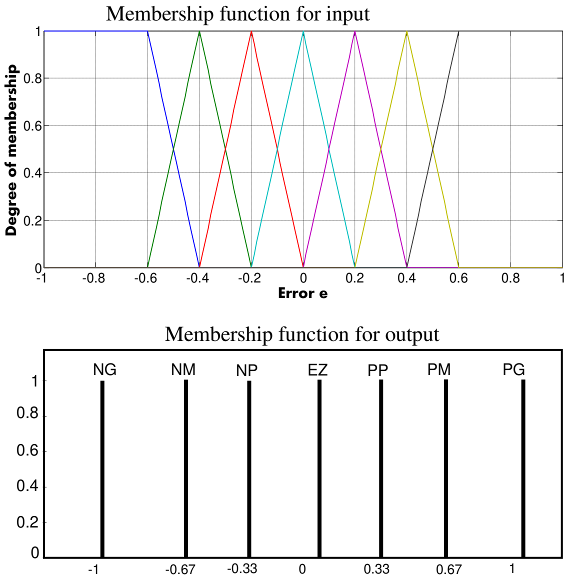

Fig. 6 Membership functions of input and output.

The Figure 7 presents the block diagram of the proposed type-1 fuzzy vector control of the DFIM. As shown in this figure, the speed loop, stator flux and quadrature rotor currents use a fuzzy logic controller.

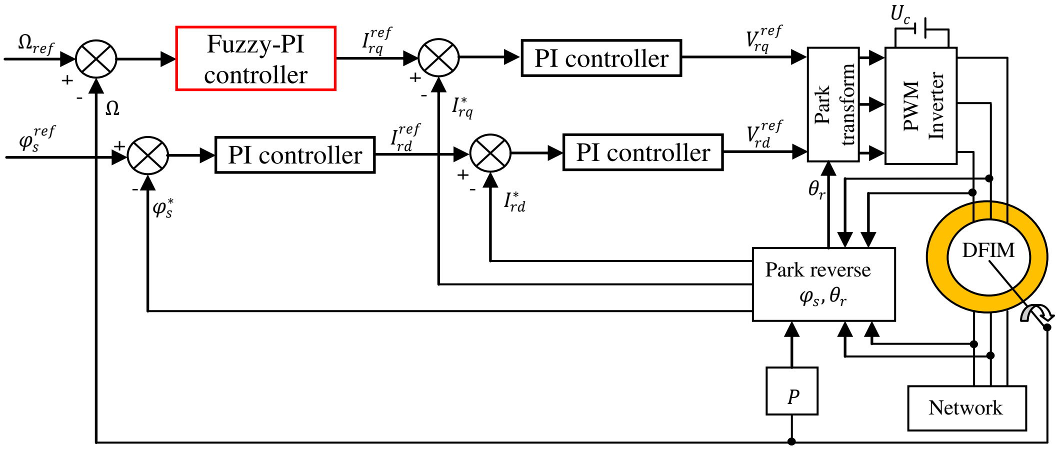

Fig. 7 Block diagram of the speed control based on fuzzy controller of the DFIM.

V. SIMULATION RESULTS

The aim of this step is to control the DFIM by the hybrid type-1 fuzzy vector of which the stator of the machine is powered directly by the three-phase network [220 / 380V, 50Hz] and the rotor is supplied with voltage through a PWM inverter. The parameters of the DFIM used in this work are given in the appendix.

The section, simulations results are presented to illustrate the performance and robustness of proposed control law when applied to the DFIM. The motor is operated at 157 (rad/s) under no load and a load disturbance torque (15 N.m) is suddenly applied at $t = 1.5s$ and eliminated at $t = 2.5s$ (-15 N.m), while the other parameters are held constant. The responses of speed, torque, stator flux and rotor current are shown in figure 8.

ISSN 1737-9334

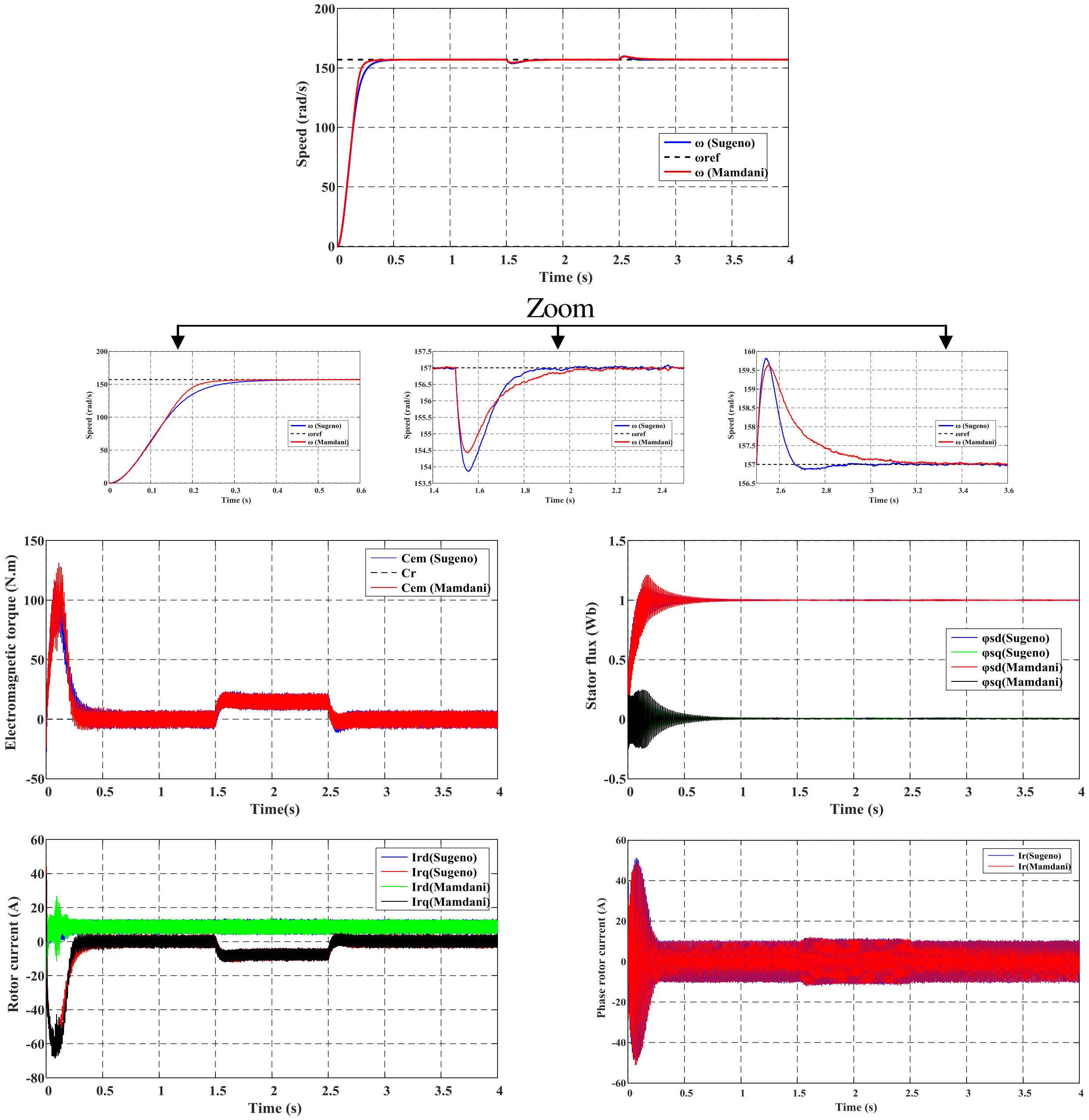

Fig. 8 Simulation results when changing the load

The machine is initially running at a nominal speed of 157 rad/s. At the instant $t = 1.5s$ the direction of rotation of the machine is reversed (-157 rad/s) and at time $t = 3s$, the machine rotates at a low speed of 50 rad/s. the load torque in this case equals 15 N.m between instants 1.5s and 3s.

The corresponding simulation results are grouped together in Figure (9), where the speed, the flux, the torque and the rotor current are presented.

We can point out the good continuation of the speed towards its new reference presenting a completely null error with a peak during the passage from one state to another. Similarly, the stator flux perfectly follows its reference value having a perfect decoupling with the torque. The flux undergoes a small variation when changing the speed.

Figure (10) shows the simulation results when rotor resistance changes by + 100% of its nominal value due to heating of the machine. The variation of R_r will be applied in the interval $t \in [1.5 - 2.5]$. The results show that the variation of the rotor resistance does not influence the speed of the machine. The flux has a slight variation of its modulus while the decoupling is still maintained. The rotor currents have a sinusoidal shape which increases with increasing resistance.

ISSN 1737-9334

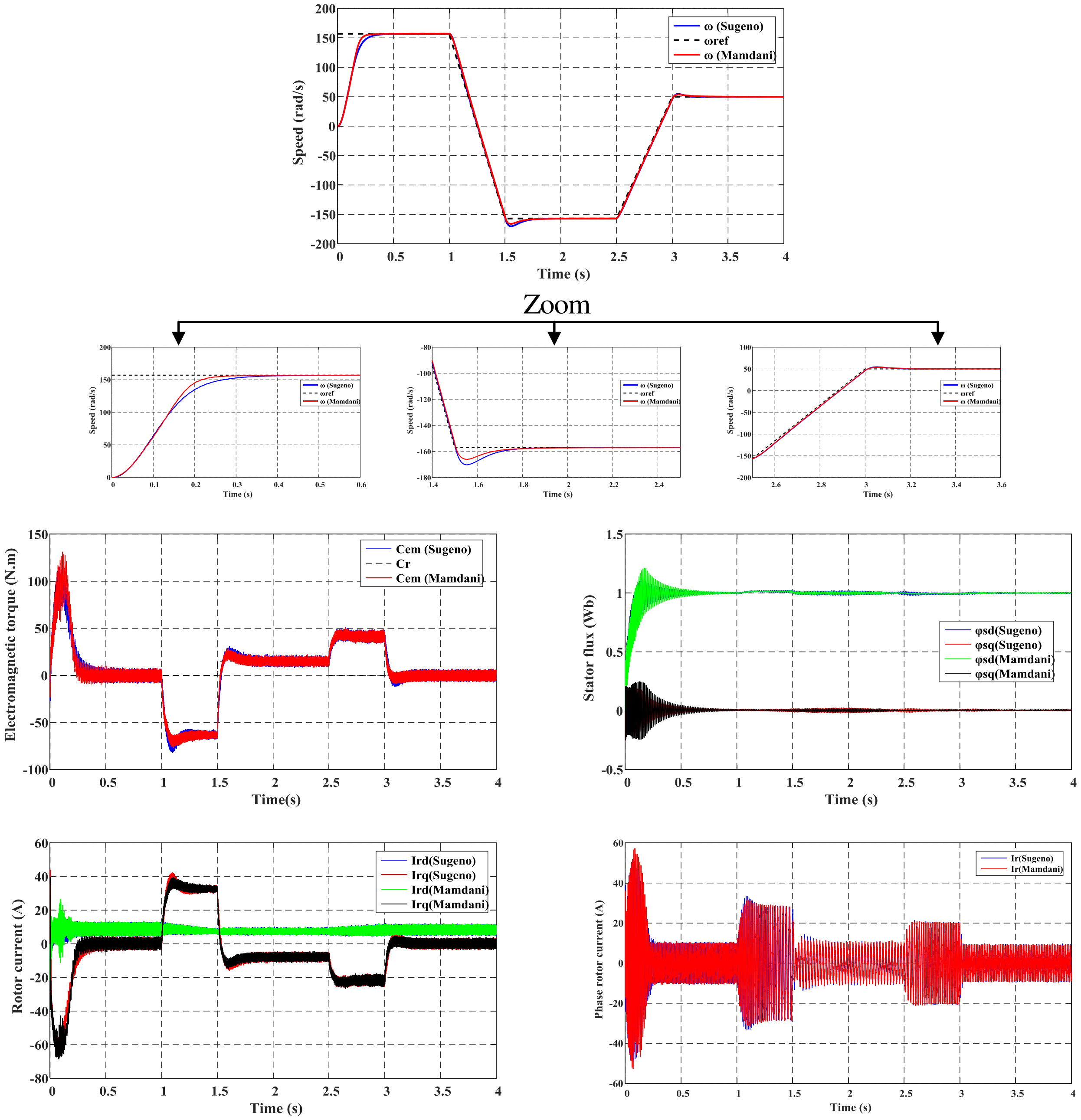

Fig. 9 Simulation results when varying the speed.

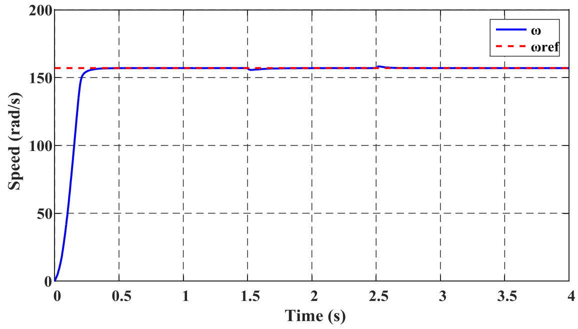

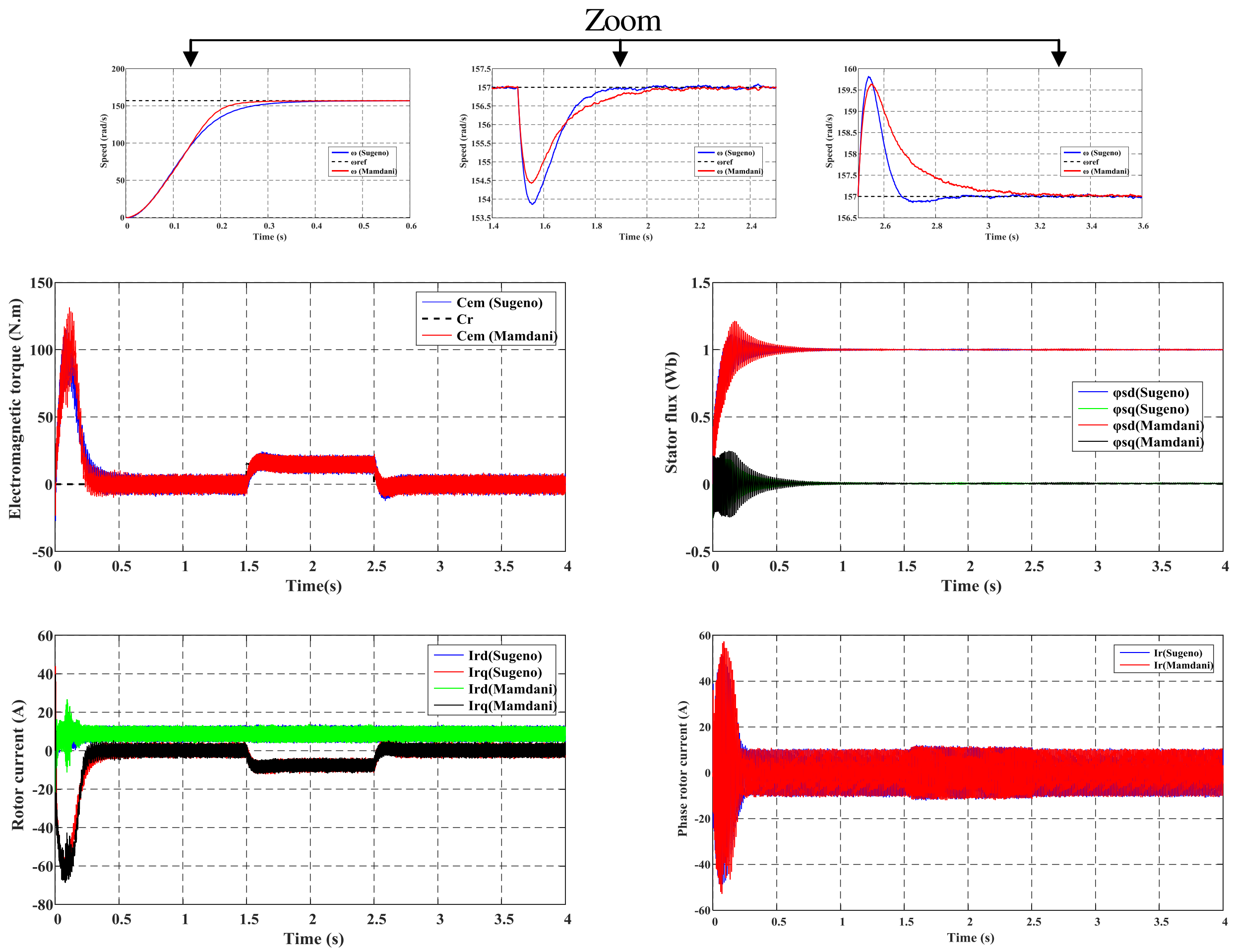

Fig. 10 Simulation results when varying the rotor resistance.

VI. DISCUSSION

The results obtained show, for the fuzzy controller used excellent performance, not only in tracking but also in regulation, with a very good monitoring of the reference speed, a static error almost zero. This results in a tracking error lower than that obtained using the PI structure, this showing the perfect fuzzy adjustment to the command.

Note also that the orientation of the stator flux is perfectly ensured, the fuzzy approach also gives better speed and time to cancel the effect. The speed also follows its reference in rotation change tests, during parametric variations we notice a superiority of fuzzy control type 1 compared to the other commands.

After these robust tests we can conclude that:

- the "Sugeno" type regulator It is very good to cancel the effect of parametric variations with respect to "mamdani" and it shows in speed. But "mamdani" has a good response time
- the variation of stator and rotor resistance do not influence the speed.
- the variation of the rotor inductance influences the speed, but also the flow orientation which is altered during the transient phases and during disturbances.
- The variation of the moment of inertia does not affect the flow orientation, and still affects the speed.

So fuzzy logic control type 1 (Sugeno or mamdani) gave good results in robust tests.

VII. CONCLUSION

In this paper, we have proposed a fuzzy logic controller for the speed control of doubly fed induction machine and performance evaluations with a direct stator flux orientation control. This approach is based on the Type-1 fuzzy logic, ie is replaced the speed controller (PI) by a type-1 fuzzy logic controller.

The obtained simulation results illustrate the good performance of the proposed method in the case of the change of load and resistance variation torque and its robustness about to parametric uncertainties.

In the futures works we propose another controls techniques such as the adaptive interval type-2 fuzzy controller of the DFIM, fusion of neural networks with fuzzy techniques and high-order sliding mode control.

APPENDIX

TABLE II
PARAMETERS OF THE DFIM [10]

Parameters	**Value**
Nominal power	$P_n = 4\,KW$
Stator voltage	$U_{sn} = 380\,V$
Rotor voltage	$U_{rn} = 220\,V$
Nominal current	$I_n = 15/8.6\,A$
Nominal mechanical speed	$\Omega_n = 1440\,rpm$
Nominal stator and rotor frequencies	$\omega_{sn} = 50\mathrm{Hz}$
Pole pair number	$P = 2$
Stator resistance	$R_s = 1.2\,\Omega$
Rotor resistance	$R_r = 1.8\,\Omega$
Stator self inductance	$L_s = 0.1554\,H$
Rotor self inductance	$L_r = 0.1568\,H$
Mutual inductance	$M = 0.15\,H$
Moment of inertia	$J = 0.2\,Kg.m^2$
Friction coefficient	$f = 0.001\,IS$

REFERENCES

[1] Hinkkanen M., "Flux estimators for speed-sensorless induction motor drives", thesis for the degree of doctor of science in technology, helsinki university of technology, finland, september 2004.

[2] Leonhard W., "Control of electrical drives", spring verlag, new york, 1990.

[3] Bodson M. and Chiasson J. "Differential-geometric methods for control of electric motor", Int. J. Robust and Nonlinear control, vol. 8, 1998, pp. 923-954.

[4] Gimènez R.B., "High performance sensorless vector control of induction motor", Thesis submitted to the university of nottingham for the degree of doctor of philosophy, december 1995.

[5] Hinkkanen M., "Flux estimators for speed-sensorless induction motor drives", thesis for the degree of doctor of science in technology, helsinki university of trchnology, finland, september 2004.

[6] Kabache N., "Amélioration des performances de la commande d'un moteur asynchrone à cage et élaboration d'un estimateur universel de ses paramètres en utilisant les réseaux de neurones artificiels", Doct. Thesis, LREEI, university of Boumerdes, Algeria, 2007.

[7] Bekakra Y. and Benattous D., "Speed and flux control for DFOC of doubly fed induction machine using sliding mode controller", Acta Electrotechnica et Informatica, vol. 10, no. 4, pp. 75-81, 2010.

[8] Allam M. and al., "Etude comparative entre la commande vectorielle directe et indirecte de la Machine Asynchrone à Double Alimentation", Journal of Advanced Research in Science and Technology, vol. 1, no. 2, pp. 88-100, 2014.

[9] Chaiba A., "Commande de la Machine Asynchrone à Double Alimentation par des Techniques de l'intelligence artificielle", Doct. Thesis, university of Batna, Algeria, 2010.

[10] Herizi A., Bouguerra A., Zeghlache S., Rouabhi R., "Backstepping control of a doubly-fed induction machine based on fuzzy controller", European Journal of Electrical Engineering, vol. 20, no. (5-6), pp. 647-657, December 2018.

[11] Bouguerra A., Zeghlache S., Loukal K. and Saigaa D., "Fault Tolerant Fuzzy Sliding Mode Controller of Brushless DC Motor (BLDC MOTOR)", the Mediterranean Journal of Measurement and Control, vol. 12, no. 2, pp. 585-597, 2016.

[12] Herizi A., Smaini H., Mahmoudi R., Bouguerra A., Zeghlache S., Rouabhi R., "Speed control of a doubly-fed induction machine using fuzzy controller", The First International Conference on Materials, Environment, Mechanical and Industrial Systems ICMEMIS'19, 29-30 June 2019, University of DJELFA, Algeria.

[13] Müller S., "Doubly fed induction generator systems", IEEE Ind. Appl. Mag., vol. 8, no. 3, pp. 26-33, May/June 2002.

[14] Rouabhi R., "Contrôle des puissances générées par un système éolien à vitesse variable basé sur une machine asynchrone double alimentée", Doct. Thesis, Dept. of Elect, university of Batna, Algeria, 2016.

[15] Ardjoun S.A., and al., "A Robust Sliding Mode Control Applied To The Double Fed Induction Machine", IU-JEEE, vol. 12, no. 1, pp. 1445-1451. 2012.

[16] Zadeh LA., "The Concept of a Linguistic Variable and its Application to Approximate Reasoning", Information Sciences, 1975; 8:199-249.

[17] Chafaa K., Ghanai M. and Benmahammed K., "Fuzzy Modeling using Kalman Filter", IET(ex IEE) Control theory and applications, vol. 1, no 1, pp. 58-64, 2007.

[18] Meunier B.B., "La logique floue et ces applications", Addison, 1995.

8 ème Conférence Internationale en Automatique & Traitement de Signal (ATS-2019)
Proceedings of Engineering and Technology PET

Hydrographic Plant Identification Based on Particle Swarm Optimization Algorithm

Marwa BEN HAJ AHMED
Electric Department
National Engineering School of Monastir
Ibn ElJazzar, 5000, Monastir, Tunisia
Email: marwa.belhajeahmed@gmail.com

Nesrine MAJDOUB
Electric Department
National Engineering School of Monastir
Ibn ElJazzar, 5000, Monastir, Tunisia
Email:majnesrine@yahoo.fr

Taoufik LADHARI
Electric Department
National Engineering School of Monastir
Ibn ElJazzar, 5000, Monastir, Tunisia
Email: taoufik.ladhari@enim.rnu.tn

Faouzi M'SAHLI
Electric Department
National Engineering School of Monastir
Ibn ElJazzar, 5000, Monastir, Tunisia
Email: faouzi.msahli@enim.rnu.tn

***Abstract*—In order to present an exact model of the three tank system, this paper proposes a meta-heuristic method based on Particle Swarm Optimization (PSO) Algorithm. This method allows us to identify the optimal parameters of this system while minimizing the quadratic error between simulated and measured outputs.**

***Index Terms*—Three tank system, system parameters, optimization, Particle Swarm Optimization**

I. INTRODUCTION

Optimization is a mathematics branch that solves problems by determining the best elements of a set according to certain predefined criteria. It has evolved since Euclid and it is presented in all fields.

In 1995, Russell Eberhart, an electrical engineer and James Kennedy, a socio-psychologist, introduced a meta-heuristic which is the particle swarm optimization (PSO) [1]. It is inspired by the social behavior of a flock of migrating birds.

This method has been successfully applied in various problems [2], [3] and [4]. Indeed, the authors Wang, Liang, Che and Sun use the particle swarm optimization algorithm to ARMA model identification [5]. Also, this technique is proposed to identify the direct and quadrature stator inductances and the stator resistance of permanent-magnet synchronous machines (PMSMs) [6]. Moreover, PSO algorithm is applied to identify the dynamic parameters of a fourth order synchronous generator non-linear model [7]. In the paper of the authors Mahdi, Tang and Wu , the particle swarm optimization algorithm is employed to identify the electrical parameters of a permanent magnet synchronous generator (PMSG) [8]. It is also used to identify the DC motor [9] and the Parameters of photovoltaic cell/module [10]. Furthermore, This method is proposed by the authors Anshory, Robandi and Wirawan to optimize the speed settings of a motor Brushless Direct current (BLDC) [11]. It is also adopted to optimize the key parameters of the dynamic pool model in the process of constructing ESN electricity load forecast model [12]. In the paper of Chouket, Abdelkafi, and Krichen, the PSO algorithm is used to optimize PI parameters controllers of wind turbine base on direct drive permanent magnet synchronous generator (DDPMSG) [13]

In our case, we will use the PS0 algorithm in order to identify the optimal parameters of the three tank system.

This paper is organized as follows:
In section 2, the description of the three tank system and its mathematical model are presented. Section 3 is devoted to the optimization method which is the particle swarm optimization algorithm. However, this method is employed in section 4 in order to identify the optimal system parameters. The results are shown in the same section. In section 5, We end this paper with a conclusion .

II. THE THREE TANK SYSTEM

A. System description

The three tank system, presented in Fig. 1, is composed of three prismatic tanks; T_1, T_2, and T_3, having the same section S_T. They are connected to each other by cylindrical pipes having the same section S_p , and by the two switching valves V_{12} and V_{23}. The system has two inputs, Q_{P_1} and Q_{P_2}, which represent the pump's flow rate, and three variables of state h_1, h_2, and h_3, which denote the water level of these tanks. They are measured via physical sensors MPX 2010 which are marketed by the company MOTOROLA. It also has four outflow valves, V_1,V_2, and V_3, which are at the bottom of each tank, and V_e which is on the right side of tank 3. The out flowing liquid is collected in a reservoir and it returns to the tanks via the two pumps P_1 and P_2.

ISSN 1737-9334

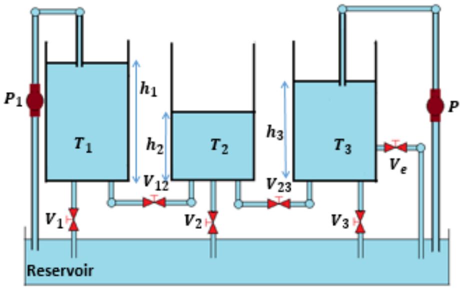

Fig. 1. The three tank system

B. The mathematical model

The mathematical model is based on Bernoulli's law for liquids [14] and [15]:

$$\frac{dV_i}{dt} = S_{T_i}\frac{dh_i}{dt} = \sum (Q_{in,i} - Q_{out,i}) \tag{1}$$

where $Q_{in,i}$ and $Q_{out,i}$ represent the inflow rate and outflow rate in tank, respectively.
So, the differential equations for the system shown above are as follows:

$$\begin{cases} \frac{dh_1}{dt} = \frac{1}{S_T}(Q_{P_1}(t) - Q_{12}(t) - Q_1(t)) \\ \frac{dh_2}{dt} = \frac{1}{S_T}(Q_{12}(t) - Q_{23}(t) - Q_2(t)) \\ \frac{dh_3}{dt} = \frac{1}{S_T}(Q_{P_2}(t) + Q_{23}(t) - Q_e(t) - Q_3(t)) \end{cases} \tag{2}$$

where:
t represents the time
$Q_{i,j}$, $i = \{1, 2\}$ and $j = \{2, 3\}$, denote the flow rate between tanks
Q_i, $i = \{1, 2, 3\}$, and Q_e represent the output flow of these three tanks
Using the Torricelli's law [16] and [17], the expressions of the flows $Q_{i,j}$ and Q_e are as follows:

$$Q_{ij}(t) = \gamma_{zi} S_p \text{sign}(h_i - h_j)\sqrt{2g|h_i - h_j|} \tag{3}$$

$$Q_e(t) = \gamma_{z3} S_p \sqrt{2gh_3} \tag{4}$$

where:
g represents the gravitational acceleration
γ_{zi} denote the outflow coefficients
The valves V_1, V_2 and V_3 are closed.
Thus, the mathematical model of the three tank system is:

$$\begin{cases} \frac{dh_1}{dt} = \frac{Q_{P_1}(t)}{S_T} - \gamma_1 \text{sign}(h_1 - h_2)\sqrt{|h_1 - h_2|} \\ \frac{dh_2}{dt} = \gamma_1 \text{sign}(h_1 - h_2)\sqrt{|h_1 - h_2|} - \\ \gamma_2 \text{sign}(h_2 - h_3)\sqrt{|h_2 - h_3|} \\ \frac{dh_3}{dt} = \frac{Q_{P_2}(t)}{S_T} + \gamma_2 \text{sign}(h_2 - h_3)\sqrt{|h_2 - h_3|} - \gamma_3\sqrt{h_3} \end{cases} \tag{5}$$

with γ_i,$i = \{1, 2, 3\}$, represent the system parameters given by :

$$\gamma_i = \frac{1}{S_T}\gamma_{zi} S_p \sqrt{2g} \tag{6}$$

After finding the mathematical model of the three tank system, a simulation test was done in order to comprehend more the dynamics of the system's different quantities and their variations over time.
in this essay, we assume that $h_1(0) = h_2(0) = h_3(0) = 90cm$ and $Q_{P_1}(0) = Q_{P_2}(0) = 0$.
The results of this essay are presented in Fig. 2, Fig. 3 and Fig. 4.

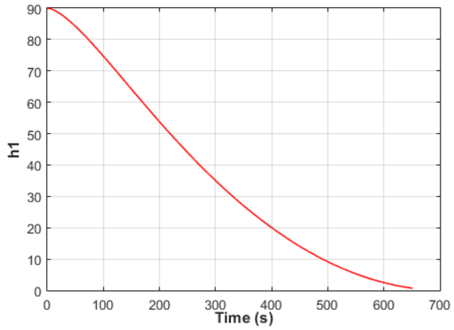

Fig. 2. Temporal evolution of level h_1

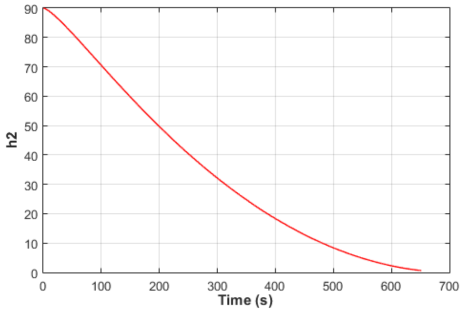

Fig. 3. Temporal evolution of level h_2

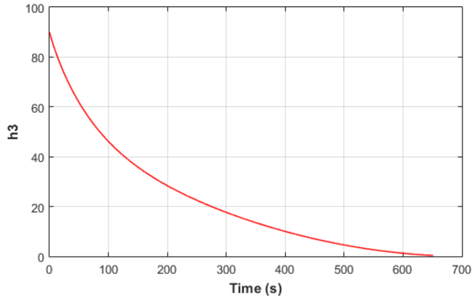

Fig. 4. Temporal evolution of level h_3

III. OPTIMIZATION METHOD: PARTICLE SWARM OPTIMIZATION ALGORITHM

The particle swarm optimization (PSO) ,which is an optimization technique, was proposed by Russell Eberhart, an electrical engineer and James Kennedy, a socio-psychologist in 1995.
It is strongly inspired by the gregarious relations of migratory

birds which have to travel long distances and which must therefore optimize their movements in terms expended energy. Each bird may be called a particle in a population, called a swarm, moving over a search space to achieve an objective.
So, in order to apply PSO, it is necessary to define a search space consisting of particles and an objective function to optimize. The principle of the algorithm is to move these particles to find the optimum.
Each of these particles is characterized by:

- X: its position in the search space
- V: its velocity
- P_{best}: its best position
- G_{best}: The best position of the swarm
- $f(P_{best})$: the fitness value of its best solution
- $f(G_{best})$: the fitness value of the best position of the swarm

The movement of the particle is represented by the Fig. 5

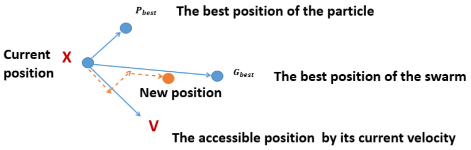

Fig. 5. The movement of the particle

The equations of the velocity and position of the particle are as follows:

$$V_{i+1}(t+1) = wV_i + c_1 r_1 (P_{besti} - X_i) + c_2 r_2 (G_{best} - X_i) \quad (7)$$

with: $V_i = V_i(t)$ and $X_i = X_i(t)$

$$X_i(t+1) = X_i(t) + V_i(t+1) \quad (8)$$

where:
t denotes the time, w is the inertia coefficient. c_1 and c_2 represent the acceleration coefficients. r_1 and r_2 are random number between 0 and 1.
The flow chart of PSO algorithm is presented in Fig. 6

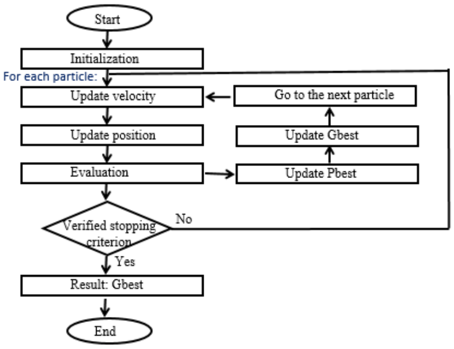

Fig. 6. PSO flow chart

with:

- Initialization:
  Initialize the parameters of PSO (number of generations, swarm size, inertia coefficient, acceleration coefficients) and the random velocities and positions of particles in the search space.
  For each particle:
  $P_{best} = X$ and if $(f(P_{best}) < f(G_{best}))$ then $G_{best} = P_{best}$ with f: objective function.
- Update velocity V_i using (7).
- Update position X_i using (8).
- Evaluation:
  if $(f(X) < f(P_{best}))$ then $(P_{best}) = X$, update (P_{best}).
  if $(f(P_{best}) < f(G_{best}))$ then $(G_{best}) = (P_{best})$, update (G_{best})

In this paper, each particle represents a parameter of the three tank system γ_i with $i = \{1, 2, 3\}$ which is characterized by a position X and velocity V.

IV. EXPERIMENTAL RESULTS

A. *Identification of three tank system*

The objective is to identify the parameters of the three tank system using the experimental measurements and the method of PSO algorithm.

To apply this technique, first we must choose the objective function which is in our case the cumulative quadratic error.

Supposing that $Q_{P_1}(t) = Q_{P_2}(t) = 0$ and using the approximation of Euler theorem, the system (5) becomes:

$$\begin{cases} h_1(k+1) = h_1(k) - \gamma_1 T_e sign(h_1 - h_2)\sqrt{|h_1 - h_2|} \\ h_2(k+1) = h_2(k) + \gamma_1 T_e sign(h_1 - h_2)\sqrt{|h_1 - h_2|} - \\ \gamma_2 T_e sign(h_2 - h_3)\sqrt{|h_2 - h_3|} \\ h_3(k+1) = h_3(k) + \gamma_2 T_e sign(h_2 - h_3)\sqrt{|h_2 - h_3|} - \\ \gamma_3 T_e \sqrt{|h_3(k)|} \end{cases} \quad (9)$$

where:
$h_1 = h_1(k)$, $h_2 = h_2(k)$, $h_3 = h_3(k)$
T_e denotes the sample period

So, the expression of the quadratic error is given by:

$$\varepsilon = \sum_{i}^{n} (Y_i - \hat{Y}_i)^2 = (Y - H\theta)^T (Y - H\theta) \quad (10)$$

where:
Y_i and $\hat{Y}_i$ are respectively the measured and the estimated responses of the system

$$Y = \begin{bmatrix} h_1(k+1) - h_1(k) \\ h_2(k+1) - h_2(k) \\ h_3(k+1) - h_3(k) \end{bmatrix} \quad (11)$$

$$\theta = \begin{bmatrix} \gamma_1 \\ \gamma_2 \\ \gamma_3 \end{bmatrix} \quad (12)$$

$$H = \begin{pmatrix} -c_1 & 0 & 0 \\ c_1 & -c_2 & 0 \\ 0 & c_2 & -c_3 \end{pmatrix} \tag{13}$$

with:
$c_1 = T_e sign(h_1(k) - h_2(k))\sqrt{|h_1(k) - h_2(k)|}$
$c_2 = T_e sign(h_2(k) - h_3(k))\sqrt{|h_2(k) - h_3(k)|}$
$c_3 = T_e\sqrt{h_3(k)}$

After determining the objective function, we choose now the parameters of the PSO algorithm which are mentioned in Table I:

TABLE I
PSO PARAMETERS

Parameter	***Value***
Population size	50
Number of generations	10
Inertia coefficient	0.99
Personal Acceleration coefficient	2
Social Acceleration coefficient	2

B. Results

In order to identify the optimal parameters of the system, we did 10 runs . Thus, these parameters are mentioned in Table II:

TABLE II
ESTIMATED PARAMETERS

	γ_1	γ_2	γ_3
Run1	0.0995	0.0818	0.0966
Run2	0.0966	0.0804	0.0995
Run3	0.0993	0.0823	0.0964
Run4	0.0986	0.0811	0.0954
Run5	0.0998	0.0809	0.0995
Run6	0.0987	0.0858	0.0995
Run7	0.0988	0.0810	0.0983
Run8	0.0971	0.0830	0.0987
Run9	0.0995	0.0850	0.0985
Run10	0.0987	0.0859	0.09971
Mean	0.09866	0.08272	0.09821

The best value of each parameter of our system is the mean of those found by the 10 runs. Then, γ_1 = 0.09866, γ_2 =0.08272 and γ_3 =0.09821

In order to test the validity of the parameters found by the PSO algorithm, the idea is to compare between simulated and measured outputs.
The results of simulated and measured outputs are shown in Fig. 7, Fig. 8 and Fig. 9.

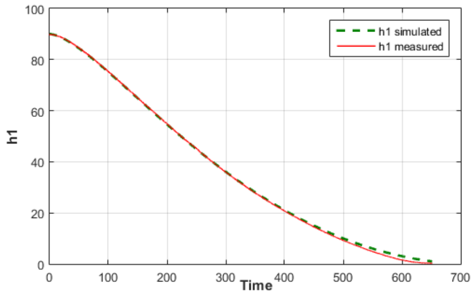

Fig. 7. Measured and simulated output h_1

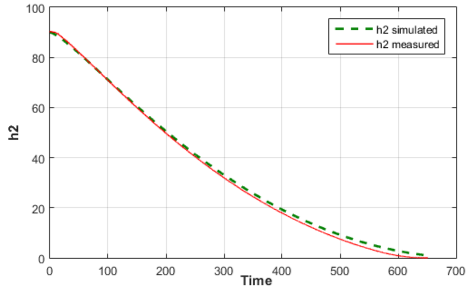

Fig. 8. Measured and simulated output h_2

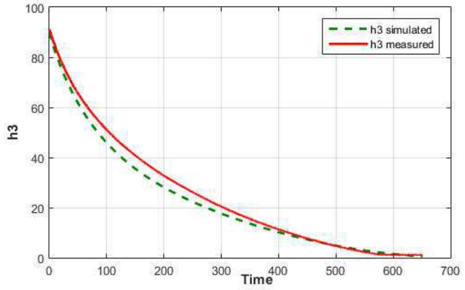

Fig. 9. Measured and simulated output h_3

Each figure contains two curves. The red one presents the measured outputs and the green curve presents the simulated outputs .
According to the two figures Fig. 7 and Fig. 8, we see that the simulated and measured outputs are coincident with a very low error at the end of the simulation time.
The Fig.9 shows that the curve of the simulated output h_3 follows the shape of the measured output curve with a high error at the start of the simulation time. Then they become coincident at the end of the simulation time.
The quadratic error is equal to 0.0243.
So, these results showed us the performances and the advantages of the PSO algorithm.

V. CONCLUSION

In this paper, an optimization method based on the PSO algorithm is proposed in order to determine the optimal parameters of the three tank system.
This method can easily be adapted to the identification prob-

ISSN 1737-9334

lem guarantees an optimal accuracy.

Therefore, it can be concluded that the PSO had a better performance and more effectiveness .

This work can be enhanced by using of other optimization techniques in order to reduce more the quadratic error between simulated and measured outputs.

As continuity, the optimal control problem for this system will be interesting.

REFERENCES

[1] Eberhart,R.C., and Kennedy, J., ”A new optimizer using particle swarm theory.” Proceeding of the Sixth International Symposium on Micro Machine and Human Science, Nagoya, Japan, 1995, pp. 39−43.
[2] Wu, J.−Y. (2012). Hybrid Artificial Immune Algorithm and Particle Swarm Optimization for Solving Unconstrained Global Optimization Problems. 2012 International Symposium on Computer, Consumer and Control.
[3] Ding, W., and Fang, W. (2018). Target Tracking by Sequential Random Draft Particle Swarm Optimization Algorithm. 2018 IEEE International Smart Cities Conference (ISC2).
[4] Agarwal, S., and Vasan, A. (2016). Computational Strategy for Structural Analysis, Design, and Optimization of Trusses Using Genetic Algorithm and Particle Swarm Optimization. 2016 IEEE 6th International Conference on Advanced Computing (IACC).
[5] Wang, J., Liang, J., Che, J., and Sun, D. (2008). ARMA Model identification using Particle Swarm Optimization Algorithm. 2008 International Conference on Computer Science and Information Technology.
[6] Sandre−Hernandez, O., Morales-Caporal, R., Rangel-Magdaleno, J., Peregrina-Barreto, H., and Hernandez−Perez, J. N. (2015). Parameter Identification of PMSMs Using Experimental Measurements and a PSO Algorithm. IEEE Transactions on Instrumentation and Measurement, 64(8), 2146−2154.
[7] Khereshki, N. I., Choolabi, E. F., and Shahalami, S. H. (2017). Identification of dynamic parameters of a fourth−order Synchronous generator nonlinear model using Particle Swarm Optimization algorithm. 2017 Iranian Conference on Electrical Engineering (ICEE).
[8] Mahdi, A. J., Tang, W. H. and Wu,Q. H. (2010). Parameter Identification of a PMSG Using a PSO Algorithm Based on Experimental Tests. 2010 1st International Conference on Energy, Power and Control (EPC−IQ), College of Engineering, University of Basrah,Basrah, Iraq
[9] Farid, A. M., and Barakati, S. M. (2014). DC Motor neuro-fuzzy controller using PSO identification. 2014 22nd Iranian Conference on Electrical Engineering (ICEE).
[10] Dali, A., Bouharchouche, A., and Diaf, S. (2015). Parameter identification of photovoltaic cell/module using genetic algorithm (GA) and particle swarm optimization (PSO). 2015 3rd International Conference on Control, Engineering and Information Technology (CEIT)
[11] Anshory, I., Robandi, I., and Wirawan. (2016). Monitoring and optimization of speed settings for Brushless Direct Current (BLDC) using Particle Swarm Optimization (PSO). 2016 IEEE Region 10 Symposium (TENSYMP).
[12] Wei, L., and Haitian, L. (2017). Electrical Load Forecasting Using Echo State Network and Optimizing by PSO Algorithm. 2017 10th International Conference on Intelligent Computation Technology and Automation (ICICTA).
[13] Chouket, M., Abdelkafi, A. and Krichen, L. (2018). Wind turbine PI controllers optimization using PSO algorithm. 2018 15th International Multi-Conference on Systems, Signals and Devices (SSD)
[14] Amor, M., Ladhari, T., Hadj Said, S., and M’Sahli, F. On−line Continuous−Discrete Time Observer For Three−Tank System. (2018) 15th International Multi-Conference on Systems, Signals and Devices (SSD)
[15] Joseph, C., George, V. I., and Venkateswaran, P. R. (2011). Hybrid modeling and discrete controller design of three-tank benchmark system. 2011 2nd International Conference on Instrumentation Control and Automation.
[16] Join, C., Sira−Ramirez, H., and Fliess, M. (2005). Control of an uncertain three tank system via on line parameter identification and fault detection. IFAC Proceedings Volumes, 38(1), 251−256.
[17] Duro, N., Dormido, R., Vargas, H., Dormido−Canto, S., S, J., Farias, G., Dormido, S. (2008). An Integrated Virtual and Remote Control Lab: The Three Tank System as a Case Study. Computing in Science and Engineering, 10(4), 50−59.

A Comparison between Path Loss Models for Vehicle-to-Vehicle Communication

Hanene ZORMATI
ENISO
NOCCS laboratory
University of Sousse
zormati.hanen@hotmail.fr,

Jalel CHEBIL,
ISTLS
NOCCS laboratory
University of Sousse
chebil8@hotmail.com,

Jamel BEL HADJ TAHAR
ENISO
NOCCS laboratory
University of Sousse
belhadjtahar.jamel@gmail.com,

Abstract— **Characterizing the channel for vehicle-to-vehicle communication system in the 5.9 GHz frequency band has been of great interest within the increasingly growing of the field of intelligent transportation systems. Path loss models can give different results when they are used in different environment other than in which they were designed. In this paper basic empirical propagation path loss models are presented and compared with measurement results taken in Valencia, Spain.**

Keywords—Empirical, vehicle-to-vehicle communication, Path loss, Propagation model

I. INTRODUCTION

Recently vehicle–to-vehicle (V2V) has received a lot of attention as a part of the future of Intelligent Transportation System (ITS) [1] especially in terms of allowing exchange of information between cars, road safety and reduction of accidents.

In order to study propagation in the V2V environment, it is necessary to characterize the channel [1][2]. The strength of the received signal can change significantly, depending on the environment (such as weather conditions) and objects around transceivers (buildings, trees, human bodies…) and especially in the presence of channel dispersion caused by multi-path propagation [3].

The path loss propagation models have been an active area of research in recent years. Path loss is unwanted signal strength reductions that signal suffers when propagating from transmitter to receiver. The losses present in a signal take place during propagation from base station to receiver.

The remainder of this paper is organized as follows: section II considers basic empirical path loss models for V2V communication and their equations. Measurement scenario is described in section III. In section IV a comparison between simulated path loss models and measurements is provided, and section V concludes the paper

II. EMPIRICAL PATH LOSS MODELS

Actually it is difficult to set a path loss model available for all scenarios for V2V communication, thus in practice most studies use empirical models which are developed basing on measurements done in various environments , in this section we present most used theoretical models.

A. Free space model

It resides in an ideal propagation in which waves travel from transmitting source and propagating with no degradation, in an unobstructed communication path [4]. The received power depends only on the transmitted power, the antenna gain and the distance between the sender and the receiver [5][6],

$$P_r(d) = \frac{P_t G_t G_r \lambda^2}{(4\pi)^2 d^2 L} \qquad (1)$$

Where P_t is the transmitted power, G_t and G_r are the gains of the transmitter and receiver antenna gains and λ is the wavelength, L is the system loss and d is the separation distance between transmitter and receiver.

B. Hata model

According to Hata model the path loss in an urban area at a distance d is [6]:

$$PL_{50} = 69.55 + 26.16\log_{10}(f) - 13.82\log_{10}(h_t)$$
$$-a(h_r) + (44.9 - 6.55\log_{10}(h_t))\log_{10}(d) \qquad (2)$$

Where f is the carrier frequency, ht is the height of the transmitting antenna, h_r is the height of the receiving antenna, and $a(h_r)$ is a correction factor for the mobile antenna height based on the size of coverage area.

C. Cost 231

This model is widely used for predicting path loss in mobile wireless system, its simplicity and the availability of correction factors let it be widely used for path loss prediction. The basic equation for path loss in dB for this model is [6][7]

$$PL = 16.3 + 33.9\log_{10}(f) - 13.82\log_{10}(h_t) - ah_m$$
$$+(44.9 - 6.55\log_{10}(h_t))\log_{10}(d) + c_m \qquad (3)$$

Where,

f is the frequency in MHz,

d is the distance between transmitter and receiver antennas in km, h_t is the transmitter antenna height above ground level in meters, c_m is defined as 0 dB for suburban or open environments and 3 dB for urban environments, ah_m is constant which values depend on the environment(urban, suburban or rural).

D. ECC 33 model

The ECC 33 path loss model, which is developed by Electronic Communication Committee (ECC), is extrapolated from original measurements by Okumura and modified its assumptions so that it more closely represents a fixed wireless access (FWA) system. The path loss model is defined as [6],

$$PL = Af_s + Ab_m - G_t - G_r \qquad (4)$$

Where,

Af_s is free space attenuation,

Ab_m is basic median path loss,

G_t is the gain factor of transmitter

G_r is the gain factor of receiver antenna.

$$Af_s = 92.4 + 20\log(d) + 20\log(f) \tag{5}$$

$$Ab_m = 20.41 + 9.83\log(d) + 7.894\log(f) + 9.56\left(\log(f)\right)^2 \tag{6}$$

$$G_t = \log(\frac{h_r}{200})\left[13.98 + 5.8(\log(d))^2\right] \tag{7}$$

$$G_r = \left[42.57 + 13.7\log(f)\right]\left[\log(h_r) - 0.585\right] \tag{8}$$

E. Two ray model

The two ray path loss model considers the direct path in addition to a reflected one via the ground [4]. This model is widely used in literature to model the LoS channel in V2X. The path loss according to the two ray model is given by [8]:

$$PL = 20log_{10}(\frac{4\pi}{\lambda}) - 20\log_{10}\left|\frac{e^{-jkd_{Los}}}{d_{Los}} + \Gamma(\theta)\frac{e^{-jkd_{ground}}}{d_{ground}}\right| \tag{9}$$

Where

$k = \frac{2\pi}{\lambda}$ is the wave number

$d_{Los} = \sqrt{d^2 + (h_t - h_r)^2}$ and $d_{ground} = \sqrt{d^2 + (h_t + h_r)^2}$ are the propagation distances

$\theta = \tan^{-1}\left(\frac{h_t + h_r}{d}\right)$ is the reflection angle

$\Gamma(\theta) = \frac{\varepsilon_r \sin(\theta) + \sqrt{\varepsilon_r - \cos^2(\theta)}}{\varepsilon_r \sin(\theta) - \sqrt{\varepsilon_r - \cos^2(\theta)}}$ is the ground reflection coefficient

ε_r is the permittivity of the ground

F. Log distance model

Theoretical and measurement based propagation models indicate that average received signal power decreases logarithmically with distance in radio channels. The expression for path loss in this model is:

$$PL(dB) = PL(d_0) + 10n\log(\frac{d}{d_0}) \tag{10}$$

Where n is path loss exponent d is the between transceivers d_0 is the reference distance

G. SUI model

The proposed standards for the frequency bands below 11 GHz contain the channel models developed by Stanford University, namely the SUI models. The basic path loss equation with correction factors is presented as follows [6][7]:

$$PL = A + 10\gamma\log_{10}\left(\frac{d}{d_0}\right) + X_f + X_h + s \tag{11}$$

Where

$$A = 20\log_{10}\left(\frac{4\pi d_0}{\lambda}\right) \tag{12}$$

$$\gamma = a - bh_b + \frac{c}{h_b} \tag{13}$$

$$X_f = 6\log_{10}\left(\frac{h_r}{2000}\right) \tag{14}$$

$$X_h = -h\log_{10}\left(\frac{h_r}{2000}\right) \tag{15}$$

a, b, c and h are constants and depend according to the environment, *γ* is the path loss exponent, *f* is in MHz and h_r is the antenna height of the receiver. The SUI model is used to predict the path loss in all three environments, namely rural suburban and urban.

H. Okumura model

This is a widely used model for signal prediction in an urban area; the model is expressed as [7]

$$PL = L_f + Amu(f,d) - G(h_t) - G(h_r) - G_{area} \tag{16}$$

Where,

$$G(h_t) = 20\log_{10}\left(\frac{h_t}{200}\right) \tag{17}$$

$$G(h_r) = a\log_{10}\left(\frac{h_r}{200}\right) \tag{18}$$

PL is the 50th percentile (i.e., median) value of propagation path loss,

L_f is the free-space propagation loss,

Amu is the median attenuation relative to free space,

$G(h_t)$ is the base station antenna height gain factor,

$G(h_r)$ is the mobile antenna height gain factor, and

G_{area} is the gain due to the type of environment.

a is constant that depend on the height of antenna receiver

Okumura's model is completely based on measured data and there is no analysis to justify it. All extrapolations to these curves for other conditions are highly subjective. Yet it is considered the simplest and best in terms of accuracy in path loss prediction for cellular systems in a cluttered environment. It has become a standard in Japan.

III. METODOLOGY

Measurement results have been taken from [9] scenarios which have been performed in an urban area at 5.9 GHz frequency, with two scenarios: scenario 1 is with high traffic density, and scenario 2 is with low traffic density (figure 1).

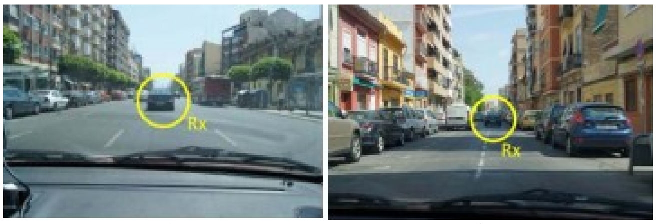

(a) (b)

Fig. 1 Views of the measurement scenarios from the Tx vehicle: (a) scenario 1, (b) scenario 2[9]

Scenario 1 corresponds to a large avenue of the urban area of the city of Valencia, Spain, characterized by high road traffic density, a one-way avenue including a lane of parked cars on both sides and the sidewalks, and ends at the port. The total length of the measured route was about 2773 m. Fig. 1(a) shows a view from the transmitter (Tx) vehicle of this scenario.

Scenario 2: This environment corresponds to an urban area of Valencia characterized by low road traffic and one or two lanes of one-way travel direction. The street includes a lane of parked cars on both sides and the sidewalks. The total length of the measured route was about 1410 m. Fig.2b shows a view from the Tx vehicle of this scenario, for both scenarios the speed limit is 50 km/h.

The vehicles involved in the measurements campaign were a Renault Clio as Tx and a Peugeot 406 as receiver (Rx) as it is shown in figure 2. The monopoles antennas were mounted in the roof-center of the vehicles, respectively with the heights 1.41 m and 1.43 m.

The two vehicles were equipped with a Global Positioning System (GPS) which were controlled by two laptops

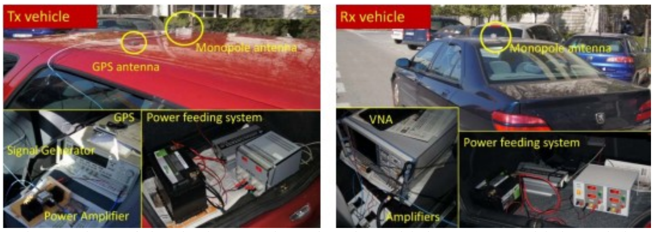

Fig. 2 View of the devices on-board at the vehicles: (a)Tx vehicle and (b) Rx vehicle [9].

The measurements were taken between 11:00 a.m. and 12:30 p.m., with the Tx and Rx vehicles in the same direction and in real driving and traffic conditions, predominating the blockage of the line-of-sight (LOS) due to the vehicles between the Tx and Rx link.

IV. COMPARISON BETWEEN SIMULATED PATH LOSS MODELS AND MEASUREMENTS

After obtaining measurements data taken in the area of Valencia, Spain, we have calculated the mean value of path loss and compared it to different simulated empirical path loss models using Matlab software and we have got the results presented in figure 3.

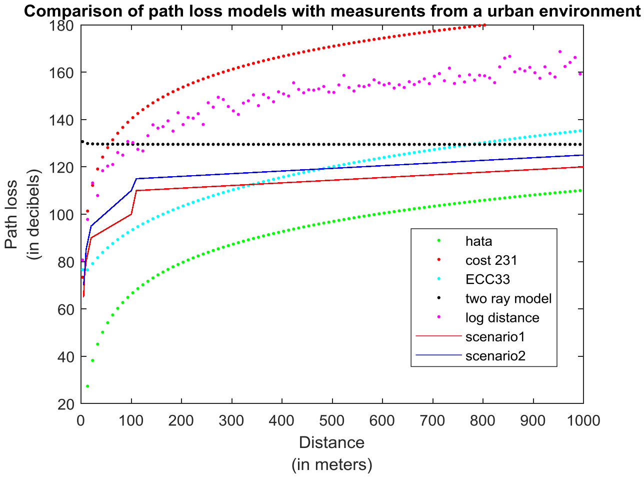

Fig.3 Comparison of path loss models with measurents from an urban environment

According to this simulation ECC33 model is giving the best results in this urban area, in fact it presents the nearest curve shape in comparison to measurements done for both scenarios.

V. CONCLUSION

In this paper we have presented basic empirical path loss models for V2V communication in an urban area using MATLAB Software and obtained results were compared with the measurement data taken in two environments in the city of Valencia, Spain with different traffic densities, Results show that ECC33 is giving the nearest results compared to other models which is true for this case and not for all scenarios and environments, thus we need to develop a new path loss model applicable for all scenarios.

REFERENCES

[1] Sun-Kuk Noh, Phil-jung Kim, Jung-Hyun Yoon," Doppler Effect on V2I Path Loss and V2V Channel Models", ICTC 2016

[2] Yi Yuan, Cheng-Xiang Wang, Xiang Cheng, Bo Ai, David I. Laurenson, Novel 3D Geometry-Based Stochastic Models for Non-Isotropic MIMO Vehicle-to-Vehicle Channels, IEEE transactions on wireless communications, vol. 13, no. 1, january 2014

[3] Jessen Narrainen, "Performance evaluation of vehicle radiofrequency communication systems: contribution to the modelling approach", PhD thesis, INSA Rennes,March 2017.

[4] Vaishali d. khairnar, Ketan Kotecha, "Propagation Models for V2V Communication in Vehicular ad-hoc Networks", Journal of Theoretical and Applied Information Technology, 31st March 2014. Vol. 61 No.3

[5] Lei Zhang,"channel measurement and modeling in complex environments", PhD thesis from the school of telecommunications systems and engineering technical university of Madrid, September 2016

[6] S.Dhar, R.Bera, R.B. Giri, S.Anand, D.Nath, S.Kumar, An Overview of V2V Communication Channel Modeling, International Symposium on Devices MEMS, Intelligent Systems & Communication (ISDMISC) 2011, Proceedings published by International Journal of Computer Applications (IJCA)

[7] Purnima K. Sharma, R.K.Singh," Comparative Analysis of Propagation Path loss Models with Field Measured Data", International Journal of Engineering Science and Technology, Vol. 2(6), 2010, 2008-2013

[8] Billy Kihei, John A. Copeland, Yusun Chang," Improved 5.9GHz V2V Short Range Path Loss Model", 2015 IEEE 12th International Conference on Mobile Ad Hoc and Sensor Systems

[9] Herman Fernández, Lorenzo Rubio, Juan Reig, Vicent M. Rodrigo-Peñarrocha, Alejandro Valero," Path loss modeling for vehicular system performance and communication protocols evaluation", International Journal of Mobile Networks and Applications, 18(6):755-765, doi:10.1007/s11036-013-0463-x, 2013.

Noise Performances in Image Processing

Fareda A. Elmaryami
Zawia University
Faculty of Engineering
M.sc Student in EE. Department
faredaalmarem90@gmail.com

Ali Almouri
Zawia University
Faculty of Engineering
EE. Department
Zawia, Libya
1

***Abstract*— In signal processing field the word noise is always recurrence, and it means unwanted signals that can prevent, distort, or change the meaning of a message or video and comes from miscellaneous of sources, whether it is thermal, electrical or otherwise. Electronics noise can refer to the electronic signal corresponding to acoustic noise in an audio system or the electronic signal corresponding to the visual noise commonly seen as snow on deteriorating television or video image, one of the electronic noise is periodic noise which arises in an image usually from electrical or electromechanical interference during image capture. This is the only type of spatially dependent noise.**

This noise can be reduced in spatial domain or frequency domain, where noise reduction means the operation of removing noise from a signal, these techniques are conceptually very akinesia regardless of the signal being processed, however a priori knowledge of a properties of an expected signal can mean the applications of these techniques vary greatly depending on the type of signal.

Keywords—***Image, Noise, Filter and Spectral Density***

I. INTRODUCATION

In electrical engineering and computer science, image processing is one form of signal processing for which the input is an image, such as photographs or frames of video; the output of image processing can be either an image or a set of characteristics or parameters related to the image. Most image-processing techniques involve treating the image as a two-dimensional signal and applying standard signal-processing techniques to it.

Therefore an image may be defined as a two-dimensional function, f(x,y), where x and y are spatial (plane) coordinates, and the amplitude of f at any pair of coordinates (x, y) is called the intensity or gray level of the image at that point, when x, y, and the intensity values of f are all finite, discrete quantities, it mimes image that is a digital image. The field of digital image processing refers to processing digital images by means of a digital computer. It observes that a digital image is com-posed of a finite number of elements, each of which has a particular location and value. These elements are called picture elements, image elements, pixel, pixel is the term used most widely to denote the elements of a digital image. [1]

II. TYPES OF THE NOISE IN IMAGE

There are several types of the noise affecting the images such as White noise, Quantization noise and Impulse noise……etc. In this work it will describe briefly in the following subsection, the White noise, Quantization noise and Impulse noise, as follows:

A . White Noise

White noise is a random signal with a flat power spectral density. Also a White Noise can be defined in another way, as a signal contains equal power within a fixed bandwidth at any center frequency, as shown in figure 1 , White noise is called white light in which the power spectral density of the light is distributed over the visible band in such as eye's three color receptors are approximately equally stimulated.

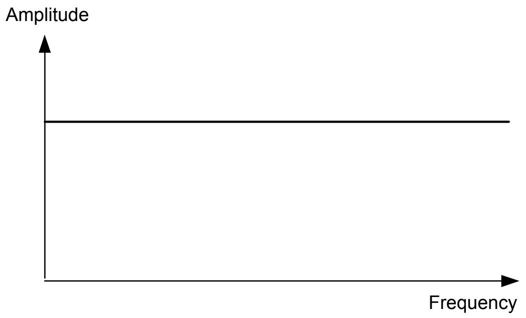

Fig. 1.Spectral Density of White Noise

Although, some noise sources generate frequencies spread everywhere of the spectrum. When the noise level is equal at all frequencies the noise is named as White noise, White noise is considered just as white light contains all frequencies equally. In practice, no noise is truly white due to if it was its total power would be infinite, just in the case of stellar radiation this is approximately true because it contains frequencies from very long wavelength radio right through x-rays. The bandwidth of real noise is finite, but it is still called White if it is the same level throughout the frequency range of

ISSN 1737-9334

concern, which for Digital Subscriber Line (xDSL) and telephony is from a few hundred Hz to MHz. [1, 2 , 3]

For example [6]: If an original image, $f(x,y)$in corrupted with White Noise, $\eta(x,y)$ it given that: the degraded image= original image+ White Noise, i.e.:

$$g(x,y) = f(x,y) + \eta(x,y) \qquad (1)$$

Where:

$g(x,y)$: is the degraded image.

$f(x,y)$: is the original image.

$\eta(x,y)$: is the Noise.

x and y are spatial (plane) coordinates.

B. Quantization Noise:

When converting from an analog signal to a digital signal, error can't be avoided. An analog signal is continuous, with ideally infinite accuracy, while the digital signal's accuracy is dependent on the quantization resolution, or number of bits of the analog to digital transformer. The difference between the actual analog value and approximated digital value due to the "rounding" that occurs while is called transformation quantization error. Therefore, Quantization noise is a noise error presented by quantization in the analogue to digital conversion (ADC), as shown in figure 2.

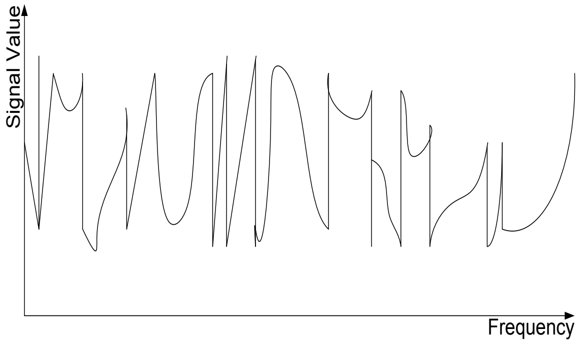

Fig. 2 Power Spectral Density of Quantization Noise.

This quantization error is inescapable during procurator because of the limitations of the ADC, but should not be growing during data preparation while converting the image to another data type. During any change of color depth (bits per pixel) round-off errors usually occur that can affect the information very much. [2] Which can be defined as:

Quantization Noise = output – input.

$$e_r = x_d - x_n \qquad (2)$$

C. Impulse Noise:

Impulse noise is a special type of interference. Which it is consists of short high energy bursts of wideband noise. In other words, Impulse noise: isolated bad pixels. In a binary image this wherewithal that some black pixels become white and some white pixels become black. This noise is named salt and pepper noise. [2, 3]

The specification of the impulse is that the amplitude is to higher, and the duration is too short, instead being an absolute power measurement, as shown in figure 3

Fig.3 Power Spectral Density of Impulse Noise.

Sometimes the noise generated from digital or even analog image transmission system is impulsive in nature, which can be defined in the following equation:

$$g(x,y) = (1-\rho)f(x,y) + \rho.i(x,y) \qquad (3)$$

Where:

$i(x,y)$: Is the impulsive noise.

ρ Is a binary parameter that assumes the values of either 0 or 1.

The impulse noise may be easily detected from the noisy image due to of the contrast anomalies.

Impulse noise does not affect some systems services such as xDSL, as much as baseband services, because of error emendation, but it however a signification impact on lines and should be measured as part of a review the overall noise. [1,2].

III MODELING OF NOISE IN AN IMAGE

Quite often an image gets corrupted by noise, which may arise in the practicability of acquiring the image, or during its transmission. Depending on the nature of the noise, such as White type of noise .There are many approaches towards redaction noise from an image. The nature of the noise is firstly inherent to the imaging procedure. The general model of such systems consists of a detector and a recorder. The imaging procedure including corruption by noise can be represented mathematically by:

$$v(x,y) = g[u(x,y)] + \eta(x,y) \qquad (4)$$

$$g[u(x,y)] = \iint h(x,y;x',y')u(x',y')dx'dy' \qquad (5)$$

$$\eta(x,y) = f[g(u(x,y))]\eta_1(x,y) + \eta_2(x,y) \qquad (6)$$

Where:

$u(x,y)$: Represents the object also called the original image.

$v(x,y)$: Is the observed image.

$h(x,y;x',y')$: Represents the impulse response of the image acquiring process.

$f(\ )$ and $g(\ )$: are generally nonlinear and represent the properties of detector or recording mechanisms.

$\eta(x,y)$: Represents the White noise.

In general the noise model $\eta(x,y)$ is apply in many cases. For example, in photographic systems the noise in the electron beam current is often modeled by the following equations:

$$\eta(x,y) = \sqrt{g(x,y)}\eta_1(x,y)\eta_2(x,y) \qquad (7)$$

Where:

$g(\ )$: is the detector model.

η_1 and η_2: are zero mean, white noise fields.

The detector function can, for example, back the illumination at the point (x,y).

The signal dependent expression arises from the random deposition of silver grain on the film due to exposure and the term $\eta_2(x,y)$ represents White wideband thermal noise. In case of films $\eta_2(x,y)$ is not usually present.

A different type of noise in the coherent imaging of objects is called speckle noise, e.g. when a photograph is digitized by using optical scanners, speckle noise can occur due to the roughness.

Of the paper surface is much of the order of the long wavelength of the light used for scanning. Speckle noise can be modeled by the following equations:

$$v(x,y) = u(x,y)s(x,y) + \eta(x,y) \qquad (8)$$

Where: the speckle noise intensity is given by $s(x,y)$ and $\eta(x,y)$ is a White Gaussian noise.

IV IMAGE RESTORATION

The purpose of image restoration is to compensate for defects which degrade an image. Degradation comes in many forms such as motion blur, noise, and camera miss focus. In cases like motion blur, it is possible to come up with a very good estimate of the actual blurring function and the blur to restore the original image. In cases where the image is corrupted by noise, the best way may hope to do is to compensate for the degradation it caused. In this work, it will introduce and implement some of the methods used in the image processing world to restore images. Although the general block diagram method to image restoration consists the low pass filter, h and additive noise, η as shown in figure 4.

1.

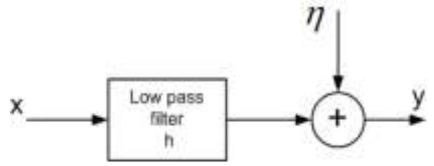

Fig. 4 General Degradation Method.

Where: y is the corrupted image obtained by passing the original image x through a low pass filter (blurring function) h and adding noise to it [4].

In this work it will describe only two methods: such as inverse filtering and wiener filter in the following subsections.

A. Restoration of Blurred Image:

Blurring is a powerful process used in image processing, figure 5 represented the original and blurred image techniques, and it involves calculating weighted averages of areas of pixels in a source image for each pixel of the final blurred image. As general rule, blur is a form of bandwidth minimize of an ideal image owing to the incomplete image formation operation. It can be resulting by relative motion between the camera and the original scene, or by an optical system that is out of focus.

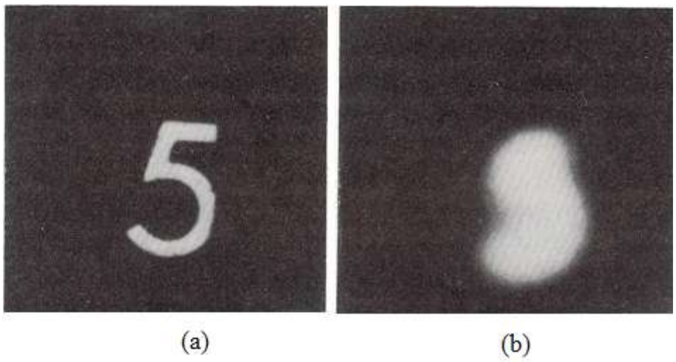

Fig. 5 Restoration of Blurred Image:

(a). Original Image.
(b). Blurred Image.

The main basic of image restoration principle is as follows: If a given an image f(x,y), wounded with a blurring function h(x,y), with added noise n(x,y), the main task is to reconstruct the original image from the noisy image. In the frequency domain, as described in the following formula [5]:

$$G(u,v) = F(u,v).H(u,v) + N(u,v) \qquad (9)$$

Where:

$G(u,v)$: is the Fourier transform of the input image g(u,v).

$F(u,v)$: is the Fourier transform of the original image f(u,v) .

$H(u,v)$: is the Fourier transform of the blur mechanism ***h*.**

Copyright - 2019
ISSN 1737-9334

$N(u,v)$ is the Fourier transform of the noise additive to the image.

From equalization (9) the ratio at the input image in frequency domain to the blur mechanism in frequency domain is given by:

$$F(u,v) = \frac{G(u,v)}{H(u,v)} \qquad (10)$$

If substitute the value of $G(u,v)$ given by equalization (10) it gets:

$$F(u,v) = 1 + \frac{N(u,v)}{H(u,v)} \qquad (11)$$

From the equation (11) it observes that the original image cannot be restored due to the random noise function $N(u,v)$is unidentified. Moreover, if the degradation function $H(u,v)$ has very small or zero values, the ratio $\frac{N(u,v)}{H(u,v)}$ would be very large or infinite and the estimate going to $F(u,v)$ would be controlled by this factor. This problem can be get rid to by limiting the analysis to the frequencies near the origin *H(0,0)* as it represents the average value of h(x,y) and it is normally the highest value of $H(u,v)$.

However, blurring mechanism is mainly a filter, and thus $H(u,v)$ is large at low frequencies and it decreases at high frequencies. The power spectrum of noise is more or less integrated. The power spectrum of the image will be in any event large a t low frequencies and decreases at high-frequency. Subsequently at low frequencies $\frac{N(u,v)}{H(u,v)}$ is low and $F(u,v)$ is much larger than $\frac{N(u,v)}{H(u,v)}$. [5]

B. Inverse Filtering:

Inverse filtering approach toward image restoration assumes that the degradation of the image is caused by a linear function h(u ,v).The additive noise is assumed to be independent of the image signal .Thus the degradation can be expressed in the Fourier domain mathematically as previous equation (9).

Therefore equation (9) can be write as:

$$F(u,v) = G(u,v)H^{-1}(u,v) - N(u,v)H^{-1}(u,v) \quad (12)$$

From the equation (12) it is evident that the original image cannot be restored in case the nature of the random noise function is unknown. In case there is no additive noise $N(u,v)$the inverse filtering performs very well.

If however, the noise $N(u,v)$ is present, then its influence becomes significant at higher frequency(u,v), where the magnitude of $H(u,v)$ becomes quite low. The effect of noise in such cases influences the result of restoration. If however, it restricts the restoration to a small neighborhood region around the origin of(u,v), the $H(u,v)$ is usually large in this neighborhood and thus the restoration results are moderately acceptable [7].

C. Wiener Filter:

Wiener filter is a kind of discrete time linear FIR filter. This type of filter has been widely used in many applications such as reconstruction of one-dimensional signals and two-dimensional images. Although Wiener filter is sensitive to noise, yet it can be used for good restoration of the original image. The elegance of Wiener filter lies in the fact that it incorporates the prior knowledge about the noise embedded in the signal and also the spectral density of the object being imaged. As a result, Wiener filter gives a better and improved restoration of original signal since it takes care of the noise process involved in the filtering. The discrete version of the Wiener filter is a straightforward extension to the continuous Wiener filter [6, 7].

Wiener filters are category of optimum linear filters which involve linear estimation of a required signal sequence from another related sequence.

In the statistical approach to the solution of the linear filtering problem, we assume the availability of specific statistical parameters, e.g. mean and correlation functions of the helpful signal and unwanted additive noise. The problem is to design a linear filter with the noisy data as input and the requirement of minimizing the effect of the noise at the filter output per to some statistical criterion.

A helpful approach to the Wiener filter-optimization problem is to minimize the mean-square value of the error signal that is defined as the variance between some desired response and the actual filter output. For fixed inputs, the resulting solution is commonly known as the Weiner filter.

The Weiner filter is inadequate for dealing with cases in which non-stationary of the signal and/or noise is intrinsic to the problem. In such cases, the optimum filter has to be assumed a time-varying form.

A Wiener Filter has some advantages such: begins to exploit signal, controls output error, straightforward to design, in addition to that it Suffers to from some draw baks: results often too blurred, spatially invariant.[7]

V CONCLUSION

In this work it in investigate and study the noise performance in image processing. That performance include the main types of noise in an image, modeling of noise in an image and image restoration. Finally Investigation of an image enhancement and restoration techniques have been covered in this paper.

References

[1] Uwe M., ’’Digital Signal Processing With Field Programmable Gate Arrays ‘‘ Springer Berlin Heidelberg New York, 2007, Third Edition.

{2] John C., ’’The Image Processing Handbook ‘‘Taylor & Francis Group, LLC, 20075th Ed.

[3]Rafal C. and Richard E., ”Digital Image Processing“ Addison-Wesley Publishing Company, 1992.

[4] Robert J., ”Digital Image Processing And Computer Vision“ John wiley and sons, Inc, 1989.

[5] Tinku A., and Ajoy K., ”Image Processing Principles and Applications“ John wiley and sons, Inc, 2005.

[6] Jan T., ”Digital Image Processing“ Prentice Hall, Inc, 1993.

[7] Steven W., ”The Scientist and Engineer’s Guide To Digital Signal Processing“ California Technical Publishing, 1999, Second Edition.

Study and Test Performance of the Zigbee Wireless technology in Some Network Models by Using OPNET Software

(1)Mariam Aboajela Msaad, (2) Almoatasem Aboaisha , (3)Ahmed Eshoul
(1) Tripoli Unversity -Faculty of Information Technology “network Department
Tripoli, Libya, meemee_02@yahoo.com
(2) Tripoli Unversity -Faculty of Information Technology “network Department
Tripoli, Libya
(3) Tripoli Unversity -Faculty of Information Technology “network Department
Tripoli, Libya

Abstract— **ZigBee Wireless Technology is the leading global standard for implementing low-cost, Low-data-rate, short-range wireless networks with extended battery life. The ZigBee standard provides network, security, and application support services operating on top of the IEEE 802.15.4 Medium Access Control (MAC) and Physical Layer (PHY) wireless standard. It employs a suite of technologies to enable scalable, self-organizing, and self-healing networks that can manage various data traffic patterns, The low cost allows the technology to be widely deployed in wireless control and monitoring applications, the low power-usage allows longer life with smaller batteries, and the mesh networking provides high reliability and larger range. ZigBee has been developed to meet the growing demand for capable wireless networking between numerous low power devices.**

In this paper , we will try to give a complete picture about ZigBee technology including the structure of this technology, the layers where this technology works referred to the OSI model, how this technology works, the main components that use to create a ZigBee network, The objective of this simulation is to establish tree topology network by; using an OPNET Modeller 14.5 program, and to investigate the performance of the network model, and see the effect on data when we change the time of transmission and finally we will investigate the performance of some network models that employ IEEE 802.15.4 protocol using different scenarios.

Keywords— **ZigBee; formatting; MAC; PHY; IEEE; OPNET**

I. INTRODUCTION

The cellular network was a natural extension of the wired telephony network that became pervasive. As the need for mobility and the cost of laying new wires increased, the motivation for a personal connection independent of location to that network also increased. Coverage of large area is provided through (1-2km) cells that cooperate with their neighbors to create a seemingly seamless network.[1]

During the mid-1980s, it turned out that an even smaller coverage area is needed for higher user densities and the emergent data traffic. The IEEE 802.11 working group for WLANs is formed to create a wireless local area network standard.

*

Whereas IEEE 802.11 was concerned with features such as Ethernet matching speed, long range(100m), complexity to handle seamless roaming, message forwarding, and data throughput of 2-11Mbps, WPANs are focused on a space around a person or object that typically extends up to 10 min all directions. The focus of WPANs is low-cost, low power, short range and very small size.[1]

The IEEE 802.15 working group is formed to create WPAN standard. This group has currently defined three classes of WPANs that are differentiated by data rate, battery drain and quality of service (QoS). The low rate WPANs (IEEE802.15.4/LR-WPAN) is intended to serve a set of industrial, residential and medical applications with very low power consumption and cost requirement not considered by the above WPANs and with relaxed needs for data rate and QoS. The low data rate enables the LR-WPAN to consume very little power.[3].

II. ZIGBEE TECNOLGY

ZigBee is expected to provide low cost and low power connectivity for equipment that needs battery life as long as several months to several years but does not require data transfer rates as high as those enabled by Bluetooth. In addition, ZigBee can be implemented in mesh networks larger than that is possible with Bluetooth.

ZigBee compliant wireless devices are expected to transmit 10-75 meters, depending on the RF environment and the power output consumption required for a given application, and will operate in the unlicensed RF worldwide (2.4GHz global, 915MHz Americas or 868 MHz Europe). The data rate is 250kbps at 2.4GHz, 40kbps at 915MHz and 20kbps at 868MHz.[2]

IEEE and ZigBee Alliance have been working closely to specify the entire protocol stack. IEEE 802.15.4 focuses on the specification of the lower two layers of the protocol (physical and data link layer). On the other hand, ZigBee Alliance aims to provide the upper layers of the protocol stack (from network to the application layer) for interoperable data networking, security services and a range of wireless home and building control solutions, provide interoperability compliance testing, marketing of the standard, advanced engineering for the evolution of the standard. This will assure consumers to buy products from different manufacturers with confidence that the products will work together.

IEEE 802.15.4 is now detailing the specification of PHY and MAC by offering building blocks for different types of networking known as ”star, mesh, and cluster tree”. Network routing schemes are designed to ensure power conservation, and low latency through guaranteed timeslots. A unique feature of ZigBee network layer is communication redundancy eliminating ”single point of failure” in mesh networks. Key features of PHY include energy and link quality detection, clear channel assessment for improved coexistence with other wireless networks.

III. OPNET

The OPNET Modeler gives the facility of the graphical user interface in which the users can model and simulate their networks. For developing different communication structures and implementing different scenarios’, different hierarchal layers are present in the environment of the modeling. Users can build a detailed model according to the requirement needed to do the analysis of the system. The systems are designed in the object oriented way, on compilation of the model its produces a discrete event simulation in the C language. After performing the simulation, the results are analyzed with the different statistics related to the performance provided by the OPNET [12].

The primary goal of this project is to use the OPNET Modeler14.5, simulation tool to study the protocol of interest, ZigBee. In order to achieve this goal, we will simulate several simple ZigBee WPAN networks while altering certain parameters using OPNET Modeller 14.5.

The objective of this simulation is to establish tree topology network by using an OPNET Modeller 14.5 program, and to investigate the performance of the network model, and see the effect on data when we change the time of transmission. Appendix B shows the steps used to create this network.

The program offers several parameters, which by right clicking to any node can change. Samples of these parameters are illustrated in Figure (1)

Figure.1 Editing Attributes for the ZigBee Network Set-up

IV. ZIGBEE PARAMETERS

There are three types of ZigBee parameters: MAC parameters, physical layer parameters and network parameters (NOTE: The network properties are available only for change in Coordinator).

A. *MAC Parameters*

I. ACK Mechanism

This attribute defines ACK related behavior for the MAC. Figure 2 illustrates this parameter.

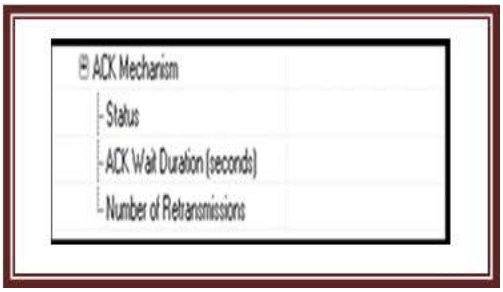

Figure 2 ACK Mechanism parameters

- Status: This attribute tells whether the ACKs are enabled for this node's transmission or not.
- ACK Wait Duration (seconds): This is the duration for which the MAC will wait to receive ACK for a given transmission. If the ACK did not receive during this duration, the MAC will retransmit.
- Number of Retransmissions: Number of times a packet retransmitted before it is marked as failed.

  CSMA-CA Parameter: This set defines the parameters for the CSMA-CA implementation of the 802.15.4 MAC. Figure 3 illustrates CSMA-CA Parameters

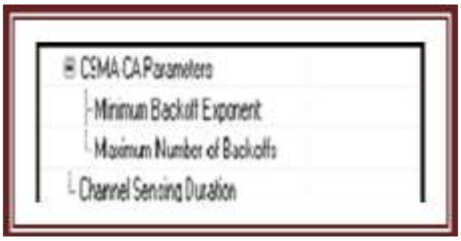

- ⊟ CSMA-CA Parameters
  - Minimum Backoff Exponent
  - Maximum Number of Backoffs
- Channel Sensing Duration

Figure 3 CSMA-CA Parameters.

- ❖ **Minimum Back off Exponent**: The minimum value of the back off exponent in the CSMA-CA algorithm. Note that if this value is set to zero collision avoidance disabled during the first iteration of the algorithm.
- ❖ **Maximum Number of Back offs**: The maximum number of back offs the CSMA-CA algorithm will attempt before declaring a channel access failure.
- ❖ **Channel Sensing Duration**: This is the duration for which each channel will be scanned for beacons after the beacon request is sent out.

If 'Auto-Compute' was specified, the node will automatically determine the channel sensing duration based on the data rate of the channel being scanned [12].

B. Physical Layer Parameter

The Physical Layer Parameters were illustrated in Figure 4

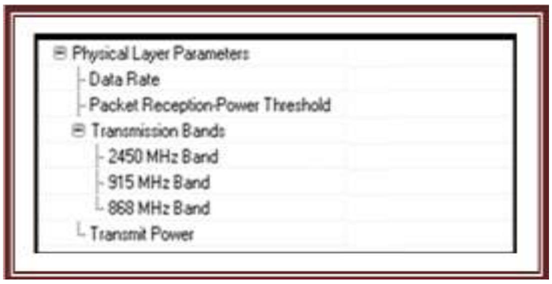

- ⊟ Physical Layer Parameters
  - Data Rate
  - Packet Reception-Power Threshold
  - ⊟ Transmission Bands
    - 2450 MHz Band
    - 915 MHz Band
    - 868 MHz Band
  - Transmit Power

Figure 4 Physical Layer Parameters

I. **Data Rate:** Specifies the data rate that will be used by the MAC for the transmission of the data frames via physical layer. "Auto Calculate" will determine the data rate based on the transmission band the channel that is belongs to it. For example if the channel is in the 2450 MHz band, the data rate will be auto selected to be 250000 bps.

II. **Packet Reception – Power Threshold: Defines** the received power threshold (receiver sensitivity) value of the radio receiver in dBm for arriving WPAN packets.

III. **Transmission Bands: Specifies** the transmission bands the device may use. A ZigBee device may choose a channel in any of the bands that are enabled 868 or 915 or 2450MHz

IV. **Transmit Power: This** attribute specifies the transmission power allocated to packets transmitted through the channel , [12].

C. Network Parameter: Specifies

The type of network (star/tree/mesh) that the coordinator will form.

D. PAN (Personal Area Network) ID

Allows the user to specify the PAN ID of the node. A coordinator will form a network with that PAN ID. A router or end device will attempt to join a network with that PAN ID. A coordinator with PAN ID set to 'Auto Assigned' will choose an arbitrary PAN ID. A router or end device with PAN ID set to 'Auto Assigned' will join any network, regardless of its PAN ID.

F. Applications Traffic

Figure 5 specifies the application traffic parameter setting.

- ⊟ Application Traffic
  - Destination
  - Packet Interarrival Time
  - Packet Size
  - Start Time
  - Stop Time

Figure 5 Application traffic

I. **Destination: Name** of the traffic destination node. The following special symbolic values can be specified :
   - ❖ "Random"-The node will choose a random destination node within its own PAN.
   - ❖ "All Nodes" - The node will broadcast traffic to all nodes in its PAN.
   - ❖ "All Coordinators and Routers" - The node will broadcast traffic to all Coordinators and Routers in its PAN.
   - ❖ "Parent" - The node will always send traffic to its parent node. If this specified on a Coordinator, the traffic had dropped.
   - ❖ "No Traffic" - The node will not send application traffic.

II. **Packet size**: Specifies the distribution name and arguments to be used for generating random outcomes for packet size.

III. **Start Time: Specifies** the distribution name and arguments to be used for generating random application traffic start time.

IV. **Stop Time: Specifies** the stop time for application traffic.

V. ENTITIES OF THE NETWORK

We have selected different network elements and configure it according to the requirement of our scenario. The following are the entities which we have selected from the Object Palette Tree in the OPNET Modeler.

- ❖ Coordinator.
- ❖ Router.
- ❖ End Device.

All these network entities are configured according to the requirements of this scenario. This scenario is explained in the following sections.

VI. SIMULATION OF TREE TOPOLOGY NETWORK

A network model of tree topology is built to cover the area which required from End Devices at least one coordinator is needed. Also choose routers that needed to establish the connection the network of the nodes to relay messages from node to other nodes.

as shown in figure 6 We want to investigate the performance of ZigBee network in tree topology, which consists of :

- one coordinator,
- two routers,
- five fixed end devices,

We noticed the ZigBee model in OPNET has some limitations and unfinished features; one of these limitations is connecting only up to two End Device per router [12].

Four different scenarios used to test and analyze the ZigBee performance using tree topology.

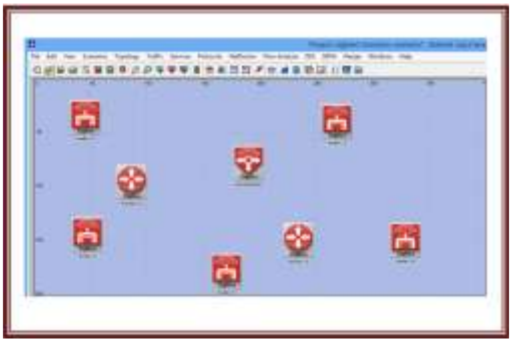

Figure 6 Tree topology of ZigBee network model

A. *General Assumptions for all scenarios:*

The main parameters in our simulation (for all scenarios) are indicated in Table 1.

Table 1 Simulations parameters.

Parameters
Transmission Band
Transmit Power
Packet Reception-Power Threshold
Data Rate
ACK Wait Duration
Number of Retransmission
CSMA-CA
Channel Sensing Duration

*B. **Scenario 1***

This scenario is general and simple case to observe the behavior of a ZigBee network in OPNET model. The settings of application traffic for this scenario are indicated in table.2, and all nodes are fixed in the network.

Table.2: Application traffic parameter setting

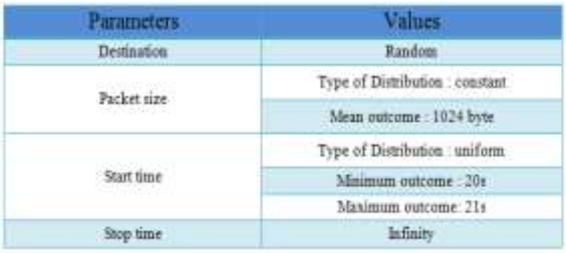

Parameters	Values
Destination	Random
Packet size	Type of Distribution : constant
	Mean outcome : 1024 byte
Start time	Type of Distribution : uniform
	Minimum outcome : 20s
	Maximum outcome: 21s
Stop time	Infinity

In this scenario the transmission times for all devices are same, they start at 20sec, and all nodes don’t stop transmission throughout the simulation time. And observe the effects on the (throughput, end-to-end delay, media access delay).

I. Simulation Results:

When we run the program and insert a period of time (a period of time for the simulation is set at 900 seconds). The program calculates all the required results and presented graphically. Figure 7 illustrates the traffic paths from the Coordinator to End Devices through the Routers.

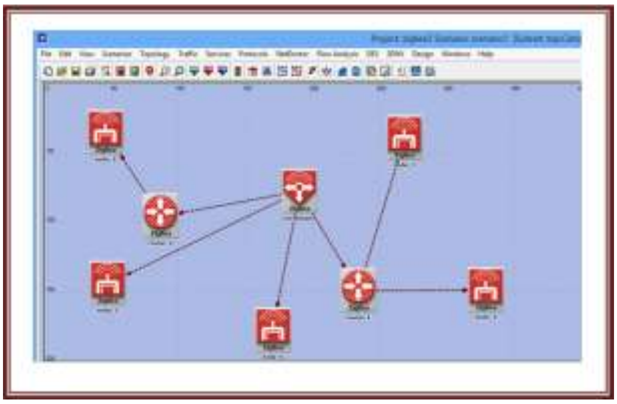

II. Figure 7 Tree topology of ZigBee network model during simulation

ZigBee performs route discovery to determine the optimal path for messages to take to its destination. The end devices will be sending data with a constant bit rate to the coordinator by first sending to the router, and then allowing the router to relay the message to the destination. Alternatively, sending directly from end devices to coordinator.

Figure 7 shows that the routers in the tested model are receiving traffic from all neighboring devices initially. And notice that the End Device 1 and End Device 6 sends data directly to the Coordinator and End Device 2 send

ISSN 1737-9334

data through the Router2, and both End Devices 4 and End devices 3 sending data through the Router1

- Throughput:

In Figure 8, we can see that the throughput starts to increase after 10 seconds, and after 45 seconds, the throughput is almost constant on a maximum value (17160bps) throughout the simulation time for Throughput of global ZigBee network.

The throughput defined as total data traffic in bits/sec successfully received and forwarded to the higher layer by the 802.15.4 MAC. Figure 8 shows the throughput of global ZigBee network; we can notice that the throughput is almost constant on a maximum value (17,160 bps) throughout the simulation time.

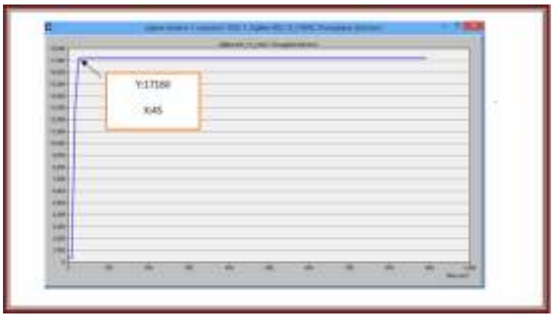

Figure 8 Throughput of global ZigBee network model

- End -To - End Delay :

The end-to-end delay represents the total delay between creation and reception of application packets generated by the node.

Figure 9 shows the average end-to-end (ETE) delay of traffic from the end devices to coordinator, and we can see that data traffic much less delay at End device 1, because it is connected directly to the coordinator without router.

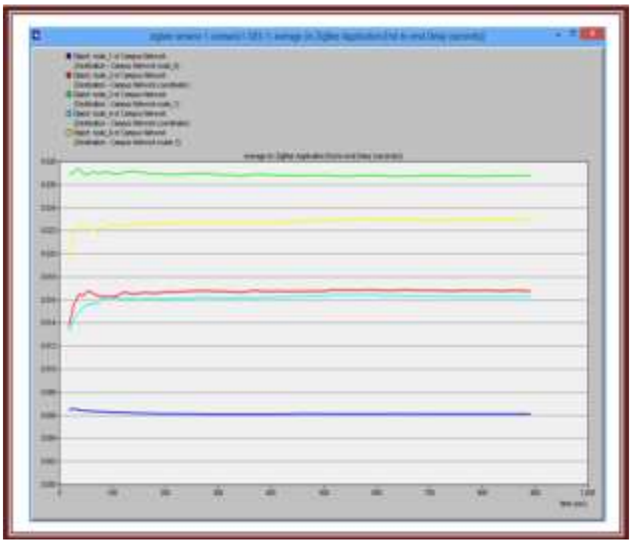

Figure 9 End -To - End Delay from each end device to coordinator (average)

- Media access delay

This represents the total of queuing and contention delays of the data frames transmitted by the 802.15.4 MAC. For each frame, this delay is calculated as the duration from the time when it is inserted into the transmission queue, which is arrival time for higher layer data packets and creation time for all other frames types, until the time when the frame is sent to the physical layer for the first time [12].

Figure 10 shows average Media access delay for each end device, we observe that the access delays for all end devices are nearly with same value and reach a maximum value of (0.13 sec) in the first (10 sec) in the simulation time. As we can see from Figure 10 about (0.1 sec) is spent from each node at the beginning which represent channel sense duration.

After the first 10 sec the delay until stable around (0.006 sec) at throughout the simulation time. (Note: The values for average Access Delay are nearly the same for each end device. And this makes the colors mixture together).

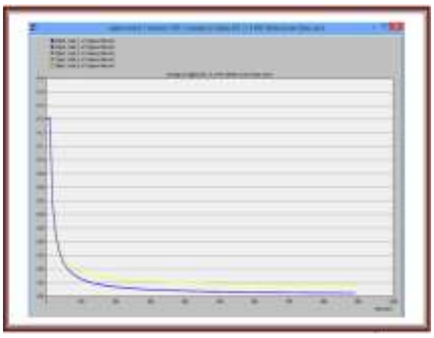

Figure.10 Media Access Delay for each end device (average)

C. Scenario 2

In this scenario, we will stop sending data after a period of time from the time of simulation in one of the End Devices, and will observe the effects on the network; we make the End Devices1to stop the transmission after (400seconds).

We can stop the transmission of any device by changing the stop time as indicated before in figure 11, from infinite to 400 second. The settings of application traffic are indicated in table .3.

Table.3 Application traffic parameter setting

Parameters	Values
Destination	Random
Packet size	Type of Distribution : constant
	Mean outcome : 1024 byte
Start time	Type of Distribution : uniform
	Minimum outcome : 20s
	Maximum outcome: 21s
Stop time	400s

- ❖ Throughput

The Throughput performance of the network model taking into consideration two scenarios is isullrated in Figure 11. We observe that when sending of data from end device 1 is stopped at 400 sec for scenario 2, the throughput is decreased from the (17100 bps) to (16000 bps), the difference is about (1100 bps) which is equivalent to the throughput of End Device 1 for scenario 1.

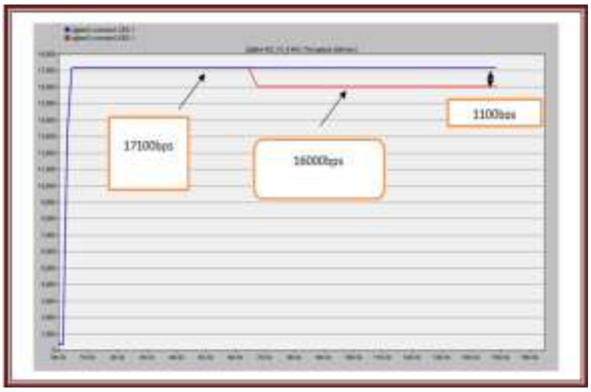

Figure.11 Throughput of global network for scenario 1 and 2**.**

- ❖ Media Access Delay

Figure 12 shows the performance of the network model, taking into consideration the Media Access Delay for end device 1 for both scenario 1 and scenario 2. We observe that both scenarios here equal value of access delay up to 400 sec, but when end device 1 stopped transmission data in scenario 2 only scenario 1 access delay remains while the access delay for scenario 2 is not calculated, because not necessary for channel sense if there is no data for send.

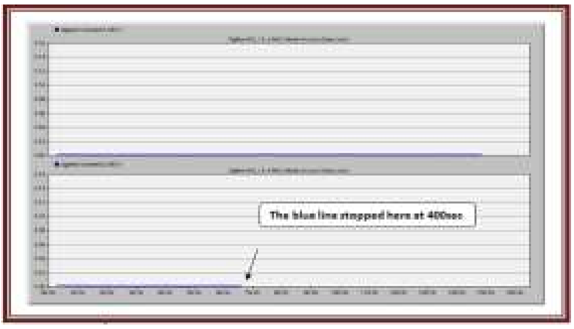

Figure 12 Media Access Delay of end device 1 for scenario 1 and 2

D. Scenario 3

In this scenario, we will change the start and stop times of the transmitter of End Device1, where we change the starting time for the beginning of data transmission of End device 1 at 300 seconds. This means that it will start transmission after all end devices, and will stop after a time of less than the time of the end of the simulation, and in this scenario we will put the stop time to be 600 seconds. And settings of application traffic for this scenario are indicated in Table 4.

Table 4 Application traffic parameter setting

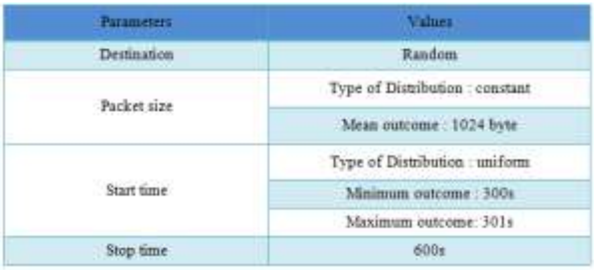

Parameters	Values
Destination	Random
Packet size	Type of Distribution : constant
	Mean outcome : 1024 byte
Start time	Type of Distribution : uniform
	Minimum outcome : 300s
	Maximum outcome: 301s
Stop time	600s

- ❖ Scenario Results:
- ❖ Throughput:

The Throughput performance of the Router 1 for both scenarios 1 and 3 is shown in figure 13. We observe that when end device 1 without sending any data, the Throughput of Router 1 will be less than for scenario 1 about (1144bps). In addition, when start to send data at 300 sec; we observe increase the Throughput until arrive to (2288bps). This value was in the first scenario.

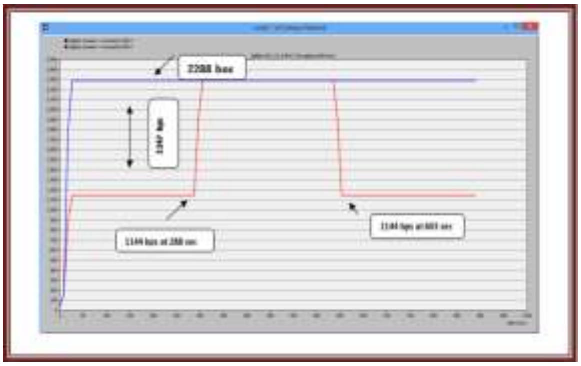

Figure 13 Throughput of Router 2 for scenario 1 and 3.

- ❖ Media Access Delay

Figure 14 shows the Media Access Delay of End Device 1 for both scenario 1 and 3. We observe there is no delay where there is no any send data in scenario 3 (blue line). But after 300 sec (when start of send data).

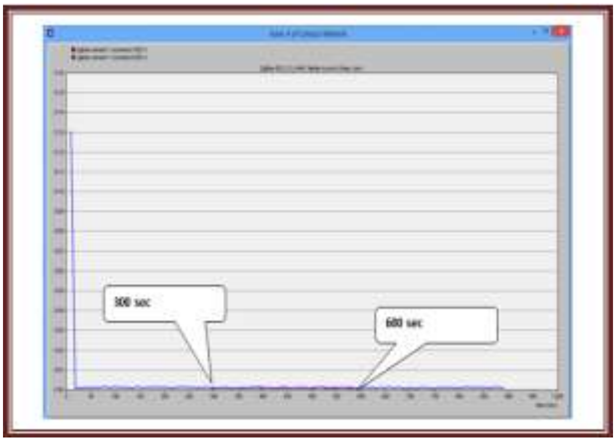

Figure 14 Media Access Delay of End Device 1 for both scenario 1 and 3

VII CONCLUSION

Referring to the main task of this paper it conclude that The incomplete implementation of the beaconing2 capability ("Note: Beacon Enabled mode is not currently supported. This attribute is a placeholder"). Lacking, is support for slotted CSMA/CA mode and contention – free operation mode. This seemed to prevent the devices from having "fair" use of the resource by scheduling the end devices to gain access to the channel.

One of the difficulties at the early stages of this project was the lack of mention in the range capability of ZigBee. Since the OPNET ZigBee model was incomplete we expected an earlier version of ZigBee with specified range of ~100meters. However, the OPNET ZigBee model was capable of handling ranges beyond 1200meters at default settings for transmission power and reception power. This initially caused the end devices to skip over the routers and communicate directly with the coordinators. Through simplified scenarios with an assortment of variations, we were able to better understand the results in reasonable time compared to having complex scenarios and results, then having to spend a lot of the project time trying to make sense of things.

With the data collected from the four scenarios a few observations and conclusions noted: The throughput is depend on the the number of the end devices and the time distribution and for result of that when we use a position distribution we get the maximum throughput The media access delay depends on the sending data from the end devices to their destination because if there is no data to send the access delay will be zero, and the reason for that belong to the queuing theory.End device that is not in the network has a higher end-to-end delay than those that are inside the network.

REFERENCES

[1] J. Gutierrez, et al, "Low-*Rate Wireless Personal Area Networks,*" IEEE Press, 2007.

[2] Shahin Farahani, "***ZigBee Wireless Networks and Transceivers***", UK, 2008, Oxford OX2 8DP.

[3] IEEE 802.15.4: Wireless Medium Access Control (MAC) and Physical Layer (PHY) Specifications for Low-Rate Wireless Personal Area Networks (WPANs), Sept. 2006.

[4] Castro Jose Manuel Tome, "Design of low-cost ZigBee modules", 3/07/06.

[5] Open Systems Interconnection Basic Reference Model: The Basic Model, ISO/IEC7498-1:1994.

[6] European Radio communications Committee (ERC)/CEPT Report 98, available at www.learnZigBee.com.

[7] The OSI Model: Understanding the Seven Layers of Computer Networks by Paul Simoneau, 2004.

[8] ZigBee Specification 053474r17, Jan. 2008; available from www.zigbee.org

[9] IEEE 802.11: Wireless LAN Medium Access Control (MAC) and Physical Layer (PHY) Specifications, 2005.

[10] D. M. Dobkin, "RF *Engineering for Wireless Networks,*" Elsevier Science, 2005.

[11] H. LABIOD , H. AFIFI, C. DE SANTIS, "WI-FI TM , BLUETOOTH TM , ZIGBEE TM AND WIMAX TM ", © 2007 Springer, Published by Springer, P.O. Box 17, 3300 AA Dordrecht, The Netherlands.

[12]http://www.opnet.com/support/des_model_library/umts.html [Accessed: March. 25.2010, 5:00 PM].

[13] Austen Chan, Brian Cheung, Wing Kit Lee,"ENSC427:ZigBeeTransmission Analysis in Tree Topology", Spring 2009, http://www.sfu.ca/~kyc1

Implementation Network Management Solution Using PRTG and Solar Winds Tools

(1)Mariam Aboajela Msaad, (2) Mohamed Fathi Almograbi , (3)Anas Moftah Alshoukri
(1) Tripoli Unversity -Faculty of Information Technology “network Department
Tripoli, Libya, meemee_02@yahoo.com
(2) Tripoli Unversity -Faculty of Information Technology “network Department
Tripoli, Libya
(3) Tripoli Unversity -Faculty of Information Technology “network Department
Tripoli, Libya

Abstract— **Successful companies know that network management is crucial for the proper support and maintenance of network infrastructure. When it comes to managing a large-scale or highly complex network, you’ll need a powerful network management system that will meet your challenging business needs. There are several programs suggested different types of solutions.**

PRTG and SolarWinds are an excellent solution, since they have many features that help the network engineer, administrator or technician to easily control, manage and monitor the devices comprehensively. Moreover, PRTG and SolarWinds can integrate with monitoring and management protocols such as SNMP and NetFlow to provide an excellent integrated unified management solution.

That being said, PRTG and SolarWinds will facilitate the management of network devices throughout performing configuration, Security, Fault, Performance and Accounting management which will increase productivity, Quality, Revenue and lower the cost.

Keywords— **SolarWinds; PRTG ; SNMP ; NetFlow ; IEEE;**

I. INTRODUCTION

The earliest computer networks were simple, consisting mainly of one or more mainframes connected to a few peripherals. Since the number of network resources was quite small, managing such networks was relatively simple and ad hoc techniques were sufficient. In comparison, today’s networks are considerably more complex and in addition, network complexity is constantly increasing. Network complexity arises mainly from two aspects: The large number of devices and the diversity of devices on the network. Typical networks may consist of hundreds or thousands of devices. It is quite common for organizations to have networks with one PC per individual. Besides, today’s networks are typically composed of a variety of devices such as PCs, workstations, file servers, printers, routers, hubs, firewalls. Each device on network could be manufactured by a different vendor and as a result, even the characteristics of similar devices could be widely dissimilar. Because of the increased network complexity, there is a need to use automated tools to perform network management. Here in this project, such issues will be addressed by implementing SolarWinds Network Performance Monitor (NPM) as well as Paessler Router Traffic Grapher (PRTG) management tool.

II. NETWORK MANAGEMENT

Network management refers to the activities, methods, procedures, and tools that pertain to the operation, administration, maintenance, and provisioning of networked systems.

Sometimes a distinction is made among the management of the networks themselves, the management of the end systems that are connected to networks, and the management of (networked) applications running on the systems connected to the networks. This distinction separates the terms network management, systems management, and application management. In addition, networks, systems, and application might all be involved in providing a service. Management of the service is therefore often distinguished as well and subsumed under the term service management.[1]

III. NETWORK MANAGEMENT APPROACHES

a) SNMP-Based:

Current network management systems use a set of solutions. The Simple Network Management Protocol (SNMP) is one of these solutions, which allows the exchange of management information between a network manager and the agents. SNMP is a widely common used protocol for fixed network management (monitoring and configuration). SNMP-Based approach focuses on developing a lightweight management protocol for MANETs that is compatible with SNMP protocol.[2]

b) Policy-Based:

Traditional approaches to network management focus on individual devices and often rely upon proven technologies, such as the SNMP protocol. However, it can

ISSN 1737-9334

be quite a time-consuming resource if the number of managed nodes is great. Policy-based network management (PBNM) simplifies the complex management tasks of large scale systems, since policies monitor the network and automatically enforce appropriate actions in the system. However, policies specify the conditions that should be satisfied before executing management operations for any desired goals.

c) Self-managing based:

The self-managing approach allows systems to manage themselves by given high-level objectives from administrators. This approach is based on autonomic computing paradigm that has been proposed by IBM in 2001. IBM has defined four general properties a system should have to constitute self-management: self-configuring, self-optimizing, self-healing, self-protecting.[2]

IV. NETWORK MANAGEMENT SYSTEM (NMS)

A Network Management System is an application or set of applications that lets network administrators manage a network's independent components inside a bigger network management framework. NMS may be used to monitor both software and hardware components in a network. It usually records data from a network's remote points to carry out central reporting to a system administrator.[3]
Network Management System includes but not limited to the following:

1-PRTG.
2-Solarwinds.

1- Paessler Router Traffic Grapher (PRTG)

PRTG is a network-monitoring tool that assures the availability of network components and measures traffic and use. PRTG Network Monitor includes more than 150 sensor types for all common network services, including Hyper Text Transfer Protocol (HTTP), Simple Mail Transfer Protocol / Post Office Protocol 3 (SMTP/POP3) (Email), File Transfer Protocol (FTP).[4]

2- SolarWinds Network Performance Monitor:

SolarWinds Network Performance Monitor (NPM) makes it easy to quickly detect, diagnose, and resolve performance issues before outages occur. This affordable, easy-to-use agentless software delivers real-time views and dashboards that enable you to visually track and monitor network performance at a glance. Plus, using dynamic network topology maps and automated network discovery, you can deploy and keep up with your evolving network. [5]

V. Management Protocols

Network management includes the complete range of protocols used to configure, monitor, and manage a network. Will be a detailed discussion about the management protocols that are of importance in this paper such as SNMP, NetFlow and Syslog.

A. Simple Network Management Protocol

SNMP is a standard TCP/IP protocol for network management. Network administrators use SNMP to monitor and map network availability, performance, and error rates. System management software uses SNMP to allow administrators to remotely monitor and manage thousands of systems on a network, often by presenting the data gathered from monitored devices in a snapshot or dashboard view. [6]

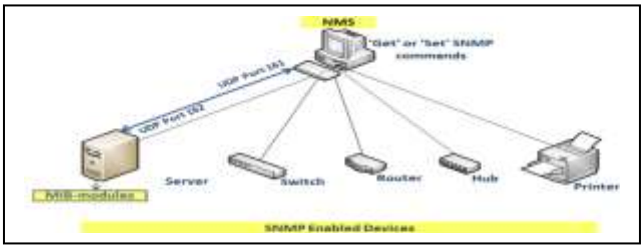

Figure 1 SNMP Enabled Devices

B. NetFlow Protocol

NetFlow is a Cisco IOS application that provides statistics on packets flowing through the routing devices in the network. It's emerging as a primary network accounting and security technology.
NetFlow Identifies packet flows for both ingress and egress IP packet. It does not involve any connection setup protocol, ether between routers or any other networking device or in station.

NetFlow does not require any change externally—either to the packet themselves or to any networking device. NetFlow is completely transparent to existing network, including end station and application software and network devices like Local Area Network (LAN) switches.[7]

C. Syslog Protocol

This protocol provides a transport to allow a device to send event notification messages across IP networks to event message collectors, also known as syslog servers. The protocol is simply designed to transport these event messages from the generating device to the collector. The collector doesn't send back an acknowledgment of the receipt of the messages.

Syslog uses the User Datagram Protocol (UDP), port 514, for communication. Being a connectionless protocol, UDP does not provide acknowledgments. Additionally, at the application layer, syslog servers do not send acknowledgments back to the sender for receipt of syslog messages. [8]

Following figure is a sample syslog message generated by a Cisco IOS device

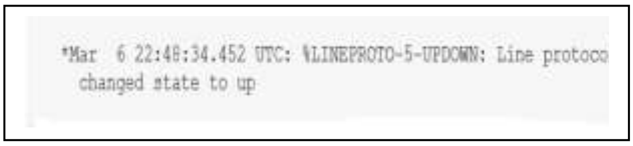

```
*Mar  6 22:48:34.452 UTC: %LINEPROTO-5-UPDOWN: Line protoco
  changed state to up
```

Figure 2 Syslog Message

➤ ***Additional Protocols:***

In this section there will be an overview about protocols used in our paper to ensure connectivity, increase network efficiency and availability.

- *Command Line Interfaces*

A Command Line Interface (CLI) enables users to interact with and operate software (including operating systems) via a text-based interface. There are several very convenient tools for CLI based network management: Secure Shell (SSH) and Telnet.[9]

- *Telnet*

Telnet is mostly intended for text-based login to computers but can also be used for communication between automated processes. Because many of the application protocols on the Internet are text based (request and reply), Telnet applications can be used to communicate with many servers. Examples of such protocols are Simple Mail Transfer Protocol (SMTP), Post Office Protocol version 3 (POP3), and Internet Message Access Protocol (IMAP) for email; Hypertext Transfer Protocol (HTTP) for web access; and Network News Transfer Protocol (NNTP) for Usenet access. [9]

- *Secure Shell*

SSH is a protocol for secure connections with computers/devices over the Internet. It is a secure substitute for Telnet as all traffic is encrypted. SSH has two versions, named SSH version 1 (SSH-1) and SSH version 2 (SSH-2), with the latter being the improved version. When initiating a secure connection, a packet encrypted with a 128-bit key is sent from the client to an SSH server. After the connection is established each data segment is encrypted using encryption algorithms, such as Rivest, Shamir, Adleman (RSA), Data Encryption Standard (DES), Triple DES (3DES), International Data Encryption Algorithm (IDEA), and Blowfish, among others. [9]

- *Hot Standby Router Protocol (HSRP)*

HSRP is Cisco's standard method of providing high network availability by providing first-hop redundancy for IP hosts on an IEEE 802 LAN configured with a default gateway IP address. HSRP routes IP traffic without relying on the availability of any single router. It enables a set of router interfaces to work together to present the appearance of a single virtual router or default gateway to the hosts on a LAN.[9] One of the routers is selected to be the active router and another to be the standby router, which assumes control of the group MAC address and IP address should the designated active router fail. HSRP provides high network availability by providing redundancy for IP traffic from hosts on networks. [9]

- *Link Aggregation Control Protocol (LACP)*

The LACP is defined in IEEE 802.3ad and enables Cisco switches to manage Ethernet channels between switches that conform to the IEEE 802.3ad protocol. LACP facilitates the automatic creation of Ether Channels by exchanging LACP packets between Ethernet ports. By using LACP, the switch or switch stack learns the identity of partners capable of supporting LACP and the capabilities of each port. It then dynamically groups similarly configured port s into a single logical link (channel or aggregate port). [10]

VI. SIMULATION OF TOPOLOGY NETWORK

VI.I Devices and Software

This section gives an overview of each device and software used in this paper, such as EVE Network Emulator, Operating Systems, routers, switches images used herein.

➤ *The Emulated Virtual Environment (EVE-NG)*

EVE-NG (or UNetLab) is a clientless network emulator that provides a user interface via a browser. Users may create network nodes from a library of templates, connect them together, and configure them. Advanced users or administrators may add software images to the library and build custom templates to support almost any network scenario. EVE-NG Benefits is Learning, Design, Efficiency and Flexibility. [11]

➤ *VMware Workstation:*

VMware pioneered x86-based virtualization in 1998 and continues to be the innovator in that market, providing the fundamental virtualization technology for all leading x86based hardware suppliers. The company offers a variety of software-based partitioning approaches, utilizing both hosted (Workstation and VMware Server) and hypervisor (ESX Server) architectures.

➤ *Devices Images Used in the Emulator*

1- Cisco 7200 VXR Series Router
2- Layer 2 Switch Image
3- Layer 3 Switches Image

➤ *Operating Systems*

1- Windows Server 2012 R2
2- Windows Server 2016
3- Windows 7

VI.II Practical Lab

- ***Project Topology***

The devices in this project were connected as shown in this topology diagram

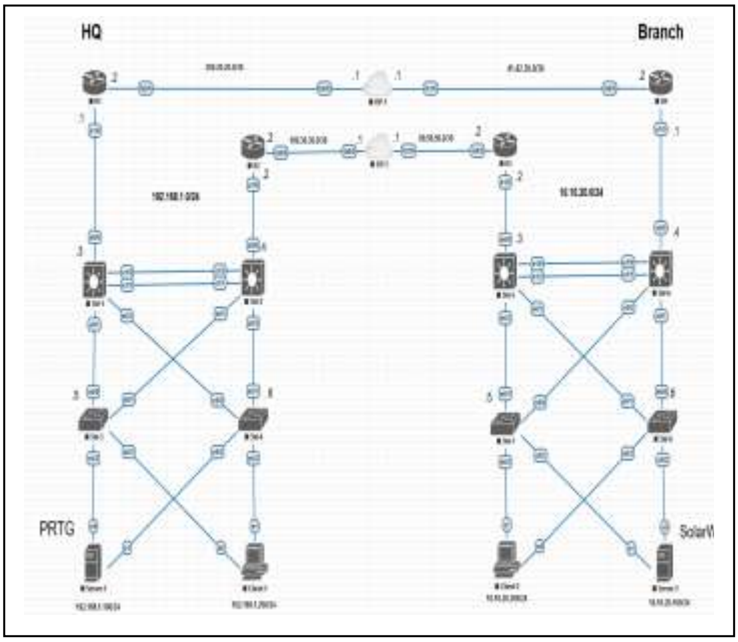

Figure 3 Topology Diagram

A. *Addressing Tables for the Proposal Topology*

Table [1] Addresses Table for HQ Site:

Device	Interface	IP address	Subnet Mask	Connected to
R1	Fa0/0 e1/0	200.20.20.2 192.168.1.1	255.255.255.0 255.255.255.0	SW-1
R2	Fa0/0 e1/0	100.30.30.2 192.168.1.2	255.255.255.0 255.255.255.0	SW-2
SW-1	e0/0 e1/0 e1/1 e0/1 e0/2	N/A		R1, SW-2, SW-3, SW-4
SW-2	e0/0 e1/0 e1/1 e0/1 e0/2	N/A		R2, SW-1, SW-3, SW-4
SW-3	e0/0 e0/1 e0/2 e0/3	N/A		SW-1, SW-2, SW-4, Server-1, Client-1
SW-4	e0/0 e0/1 e0/2 e0/3	N/A		SW-1, SW-2, SW-3, Client-1
Server-1	NIC-1 NIC-2	192.168.1.100	255.255.255.0	SW-3, SW-4
Client-1	NIC-1 NIC-2	192.168.1.200	255.255.255.0	SW-3, SW-4

Table [2] Addresses Table for Branch Site

Device	Interface	IP address	Subnet Mask	Connected to
R3	Fa0/0 e1/0	80.50.50.2 10.10.20.2	255.255.255.0 255.255.255.0	SW-5
R4	Fa0/0 e1/0	41.42.30.2 10.10.20.1	255.255.255.0 255.255.255.0	SW-6
SW-5	e0/0 e1/0 e1/1 e0/1 e0/2	N/A		R3, SW-6, SW-7, SW-8
SW-6	e0/0 e1/0 e1/1 e0/1 e0/2	N/A		R4, SW-5, SW-7, SW-8
SW-7	e0/0 e0/1 e0/2 e0/3	N/A		SW-5, SW-6, Server2, Client-2
SW-8	e0/0 e0/1 e0/2 e0/3	N/A		SW-5, SW-6, Server2, Client-2
Server-2	NIC-1 NIC-2	10.10.20.100	255.255.255.0	SW-7, SW-8
Client-2	NIC-1 NIC-2	10.10.20.200	255.255.255.0	SW-7, SW-8

- *Tasks and Configuration:*

This section shows only the configuration of the devices on HQ site, which is similar to Branch site, also the installation of PRTG on HQ site and SolarWinds NPM on Branch site.

Step 1: R1 Basic Configuration

The basic configuration of R1 is hostname, username, password, and the configuration of OSPF protocol.

ISSN 1737-9334

```
router>enable
router#configure terminal
router(config)#service password-encryption
router(config)#hostname R1
R1(config)#username Admin privilege 15 secret cisco
R1(config)#no ip domain lookup
R1(config)#interface FastEthernet0/0
R1(config-if)#description ** Connects To ISP-1 **
R1(config-if)#ip address 200.20.20.2 255.255.255.252
R1(config-if)#no shutdown
R1(config-if)#exit
R1(config)#interface FastEthernet1/0
R1(config-if)#description ** Connects To SW-1 **
R1(config-if)#ip address 192.168.1.1 255.255.255.0
R1(config-if)#no shutdown
R1(config-if)#exit
R1(config)#router ospf 1
R1(config-router)#network 192.168.1.0 0.0.0.255 area 0
```

Figure 4 R1 Basic Configuration

Step2: Configure Console, Remote Access, Time and Date on R1:

```
R1(config)#line con 0
R1(config-line)#logging synchronous
R1(config-line)#exec-timeout 0 0
R1(config-line)#login local
R1(config-line)#exit
R1(config)#line vty 0 4
R1(config-line)#logging synchronous
R1(config-line)#exec-timeout 0 0
R1(config-line)#transport input all
R1(config-line)#login local
R1(config-line)#exit
R1(config)#clock timezone LIBYA +2
R1(config)#ntp master
R1(config)#exit
R1#clock set 03:01:00 9 JUN 2018
```

Figure 5 Configure Console, Remote Access, Time and Date on R1

Step 3: Configure SNMP, NetFlow and Syslog:

SNMP, Syslog and NetFlow configuration were performed on R1 to configure Community String for PRTG and to enable SNMP traps.

```
R1(config)#snmp-server community PRTG rw
R1(config)#snmp-server community SOLARWINDS rw
R1(config)#snmp-server host 192.168.1.100 version 2c PRTG
R1(config)#snmp-server host 10.10.20.100 version 2c SOLARWINDS
R1(config)#snmp-server enable traps
R1(config)#logging on
R1(config)#logging host 192.168.1.100
R1(config)#logging host 10.10.20.100
R1(config)#interface Ethernet1/0
R1(config-if)#ip flow ingress
R1(config-if)#ip flow egress
R1(config-if)#exit
R1(config)#ip flow-export version 9
R1(config)#ip flow-export destination 192.168.1.100 999
R1(config)#ip flow-export destination 10.10.20.100 666
R1(config)#exit
R1#show ip flow export
R1#copy running-config startup-config
```

Figure 6 Configure SNMP, Syslog and NetFlow on (R1)

Step 4: Configure Hot Standby Redundancy Protocol (HSRP)

HSRP Configuration on HQ Site was performed on R1 with higher priority than R2, so R1 will act like a Primary Router.

```
R1(config)#interface FastEthernet1/0
R1(config-if)#standby version 2
R1(config-if)#standby 1 priority 150
R1(config-if)#standby 1 ip 192.168.1.254
R1(config-if)#standby 1 preempt
R1(config)#exit
R1#copy running-config startup-config
```

Figure 7 Configure HSRP on R1

Step 5: Configure Hot Standby Redundancy Protocol (HSRP) on R2

HSRP Configuration was performed on R2 with the default priority which is lower than R1, so R2 will act like a Standby Router.

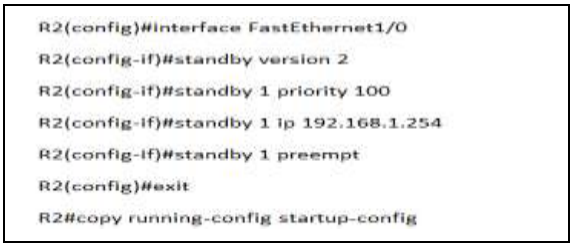

```
R2(config)#interface FastEthernet1/0
R2(config-if)#standby version 2
R2(config-if)#standby 1 priority 100
R2(config-if)#standby 1 ip 192.168.1.254
R2(config-if)#standby 1 preempt
R2(config)#exit
R2#copy running-config startup-config
```

Figure 8 Configure HSRP on (R2)

Step 6: Configure Link Aggregation Control Protocol (LACP) on SW-1.

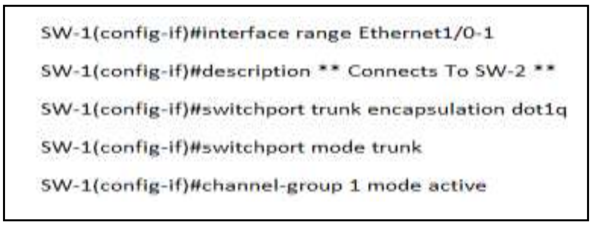

```
SW-1(config-if)#interface range Ethernet1/0-1
SW-1(config-if)#description ** Connects To SW-2 **
SW-1(config-if)#switchport trunk encapsulation dot1q
SW-1(config-if)#switchport mode trunk
SW-1(config-if)#channel-group 1 mode active
```

Figure 9 Configure Link Aggregation Control Protocol (LACP) on SW-1

Step 7: Configure SNMP and Syslog.

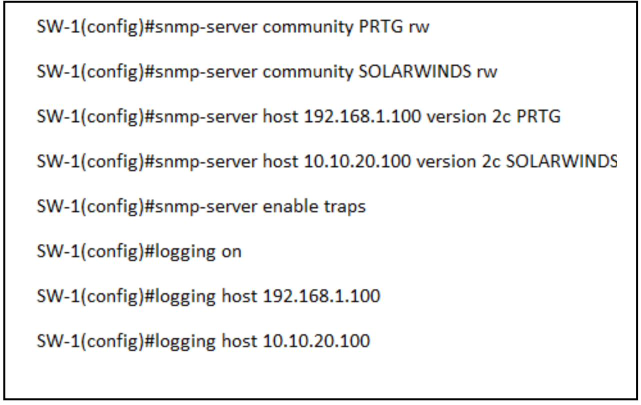

```
SW-1(config)#snmp-server community PRTG rw
SW-1(config)#snmp-server community SOLARWINDS rw
SW-1(config)#snmp-server host 192.168.1.100 version 2c PRTG
SW-1(config)#snmp-server host 10.10.20.100 version 2c SOLARWINDS
SW-1(config)#snmp-server enable traps
SW-1(config)#logging on
SW-1(config)#logging host 192.168.1.100
SW-1(config)#logging host 10.10.20.100
```

Figure 10 Configure SNMP and Syslog

- *Configure PRTG and SolarWinds NPM*

Figure 11 PRTG Home Page

Figure 12 SNMP Trap Receiver

- Show Alarms

The Alarm for Ping Sensor Status on (SW-3).

Figure 13 Sensor Alarm

The following figure shows an overview of NetFlow Sensor, (Top Talkers, Top Connection, Top Protocols), as well as the traffic types and total traffic used.

Figure 14 NetFlow Sensor

You can change the view as shown in figure (14) which shows the status of each device, in this case all devices were up in green color.

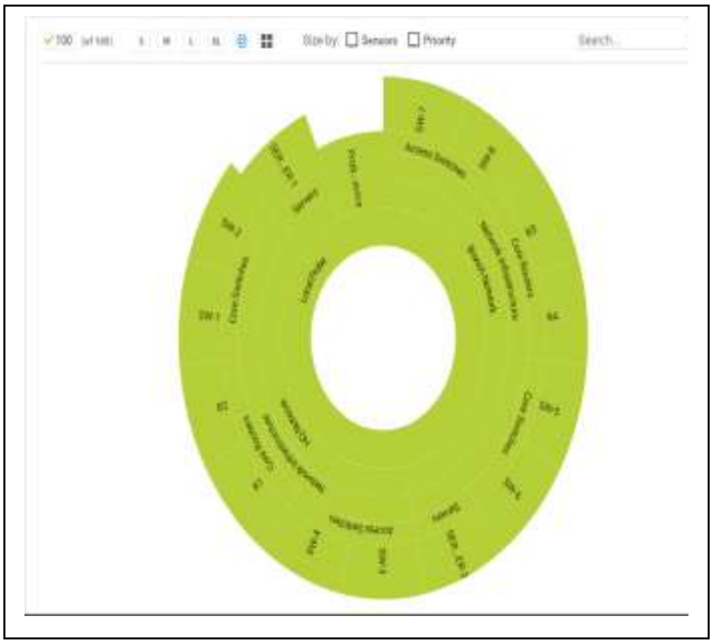

Figure 15 Devices View PRTG

- ➢ Run and Copy Reports.

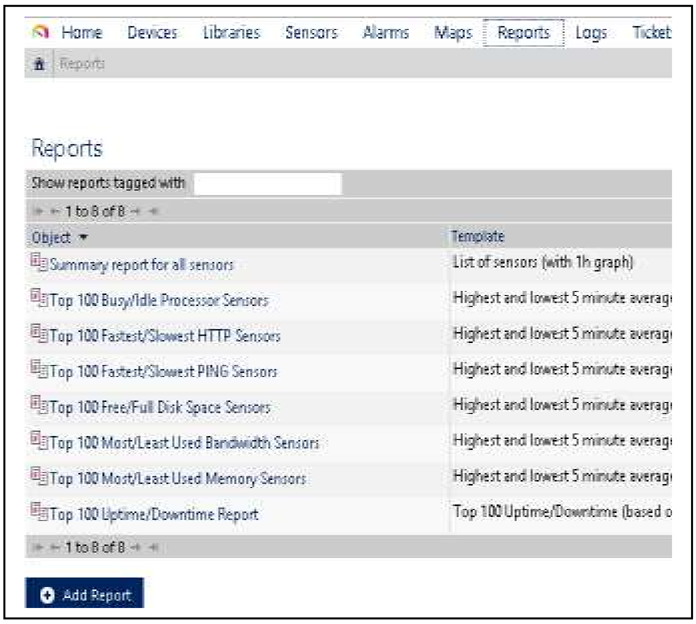

Reports

Object	Template
Summary report for all sensors	List of sensors (with 1h graph)
Top 100 Busy/Idle Processor Sensors	Highest and lowest 5 minute averag
Top 100 Fastest/Slowest HTTP Sensors	Highest and lowest 5 minute averag
Top 100 Fastest/Slowest PING Sensors	Highest and lowest 5 minute averag
Top 100 Free/Full Disk Space Sensors	Highest and lowest 5 minute averag
Top 100 Most/Least Used Bandwidth Sensors	Highest and lowest 5 minute averag
Top 100 Most/Least Used Memory Sensors	Highest and lowest 5 minute averag
Top 100 Uptime/Downtime Report	Top 100 Uptime/Downtime (based o

Figure 16 Open Summary Reports

- ➢ View Logs

The log entries are viewed in the appearing page as shown in the following figure

Log Entries

Date Time	Parent	Type
7/3/2018 3:54:00 PM	SW-4	SNMP Traffic 64bi
7/3/2018 3:53:55 PM	SW-4	SNMP Traffic 64bi
7/3/2018 3:53:50 PM	SW-4	SNMP Traffic 64bi
7/3/2018 3:50:32 PM	None	Notification
7/3/2018 3:48:32 PM	None	Notification
7/3/2018 3:48:32 PM	None	Group
7/3/2018 3:48:32 PM	SW-3	Ping
7/3/2018 3:46:00 PM	SW-4	NetFlow V9
7/3/2018 3:44:21 PM	Probe Device	System Health
7/3/2018 3:43:43 PM	SW-4	SNMP Traffic 64bi
7/3/2018 3:43:43 PM	SW-4	SNMP Traffic 64bi
7/3/2018 3:43:33 PM	SW-4	SNMP Traffic 64bi
7/3/2018 3:43:28 PM	SW-4	SNMP Traffic 64bi
7/3/2018 3:43:21 PM	Probe Device	System Health

Figure 17 View Logs 1

- *SolarWinds NPM Customization and Results*

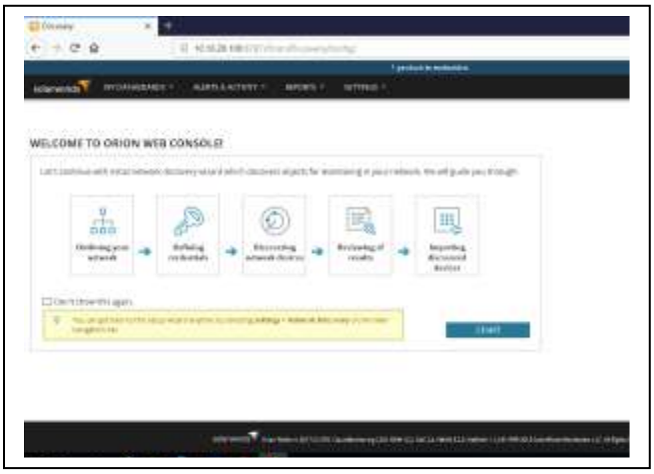

WELCOME TO ORION WEB CONSOLE!

Figure 18 Initial Network Discovery

- **Showing Results:**

The following figures shows some of the NetFlow protocol results:

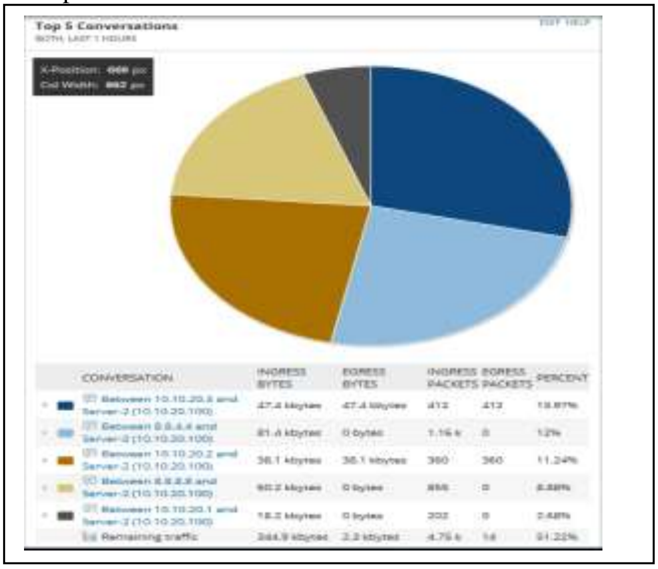

Top 5 Conversations
BOTH, LAST 1 HOURS

	CONVERSATION	INGRESS BYTES	EGRESS BYTES	INGRESS PACKETS	EGRESS PACKETS	PERCENT
■	Between 10.10.20.3 and Server-2 (10.10.20.100)	47.4 kbytes	47.4 kbytes	413	413	13.87%
■	Between 8.8.4.4 and Server-2 (10.10.20.100)	81.4 kbytes	0 bytes	1.16 k	0	12%
■	Between 10.10.20.2 and Server-2 (10.10.20.100)	38.1 kbytes	38.1 kbytes	360	360	11.24%
■	Between 8.8.8.8 and Server-2 (10.10.20.100)	60.2 kbytes	0 bytes	855	0	8.88%
■	Between 10.10.20.1 and Server-2 (10.10.20.100)	18.2 kbytes	0 bytes	202	0	2.68%
	Remaining traffic	344.9 kbytes	2.2 kbytes	4.75 k	14	51.22%

Figure 19 NetFlow Top 5 Conversation

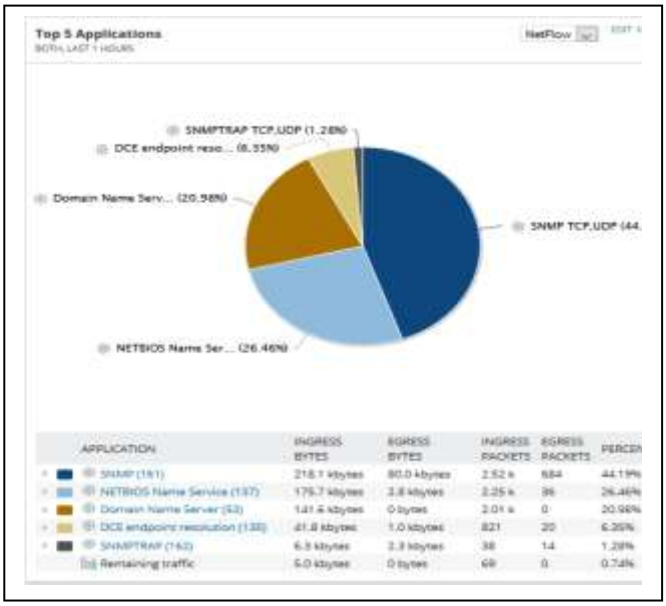

APPLICATION	INGRESS BYTES	EGRESS BYTES	INGRESS PACKETS	EGRESS PACKETS	PERCEN
SNMP (161)	218.1 kbytes	80.0 kbytes	2.52 k	684	44.19%
NETBIOS Name Service (137)	175.7 kbytes	2.8 kbytes	2.25 k	36	26.46%
Domain Name Server (53)	141.6 kbytes	0 bytes	2.01 k	0	20.98%
DCE endpoint resolution (135)	41.8 kbytes	1.0 kbytes	821	20	6.35%
SNMPTRAP (162)	6.3 kbytes	2.3 kbytes	38	14	1.28%
Remaining traffic	5.0 kbytes	0 bytes	69	0	0.74%

Figure 20 NetFlow Top 5 Applications

VII CONCLUSION

This paper was aimed to implement a network management solution in order to illustrate the important and the need for network management.

For these purposes, the paper first discussed the concept of network management, the need for network management; listed the approaches of network management and some other details about network management.

Then it explored how to do the familiar management tasks in SolarWinds. Was looked at the major areas including inventory and elements management, configuration management, fault management, and performance management.

This paper it tested other network management tool (PRTG) to help us gain familiarity with corresponding features in SolarWinds.

It explained the concept, issues, and current capabilities in network management with Simple Network Management Protocol (SNMP). We compared and contrasted the functionality of SNMP v1, v2c, and v3.

In the paper NetFlow for application visibility are covered, also Syslog Protocol and its Importance to track and monitor.

Other protocols were used in this project to increase overall network performance and availability such as Link Aggregation Control Protocol (LACP) and Hot Standby Router Protocol (HSRP).

REFERENCES

[1] Danny Lev, "*White Paper The importance of network management in reducing costs, increasing value in digital signage systems*", November 2010.

[2] Sebastian Abeck, Adrian Farrel, "*Network Management Know It All*" © 2009 by Elsevier Inc.

[3]www.searchnetworking.techtarget.com/definition/network-management-system Accessed at 6 May 2018 5:45 PM.

[4] www.paessler.com/prtg Accessed at 25 May 2018 10:22 AM.

[5] www.solarwinds.com/network-performance-monitor

[6] "*A Guide to Understanding SNMP*", © 2013, by SolarWinds Worldwide, LLC.

[7] "*NetFlow Services Solutions Guide*", © 2007 by Cisco Systems, Inc.

[8] www.ciscopress.com/articles/article.asp?p=426638 Accessed at 2 June 2018 7:58 PM

[9] "*Using the Cisco IOS Command-Line Interface*", © 2014 by Cisco Systems, Inc.

[10] "*Link Aggregation Control Protocol (LACP) (802.3ad) for Gigabit Interfaces*", © 2007 by Cisco Systems, Inc.

[11] **http://www.eve-ng.net/** Accessed at 30 June 2018 5:34 PM

Data Collection, Analysis and Trajectory Determination of A Quadrotor Using Ardu IMU and MATLAB

O Maklouf [#1], *Fateh Alej* [#2], *A. Eljubrani* [#3]
Faculty of Engineering. Aeronautical Engineering Department. University of Tripoli, Libya.
[1]othman@uot.edu.ly, [2]falej@afriqiyah.aero & [3]eljubrani@yahoo.com

***Abstract*—** Quadrotors are very interesting. Among the UAVs, these vehicles can play an important role in many civilian and military applications. Quadrotors are also commonly known as drones. Indeed, the quadrotor is a small vehicle with four propellers placed around a main body. The main body includes power source, sensors and control hardware. The four rotors are used to controlling the vehicle. The rotational speeds of the four rotors are independent. It is possible to control the pitch, roll and yaw attitude of the vehicle. Then, its displacement is produced by the total thrust of the four rotors whose direction varies according to the attitude of the quadrotor. The vehicle motion can thus be controlled Due to their self-reliance, inertial navigation systems (INS) are extremely well-suited to the field of unmanned systems, widely used on quadrotor. This paper aims to identify the motion of an unmanned aerial vehicle using a low cost inertial navigation system. An electronic circuit that consists of inertial measurement unit (IMU) with data logger and battery was designed. An implementation of the design was achieved and built on an off the shelf low cost quadrotor. The navigation system was tested and several experiments were conducted in an open field environment. Inflight measurements were collected and description of the flight data was Made. These collected data were then post processing using MATLAB and Simulink to estimate the trajectory of the quadrotor.

***Keywords*—** Keywords— UAV, IMU, INS, Drones, Quadrotor.

I. INTRODUCTION

INS is based on the implementation of Newton's laws of motion using the sensor measurements of force and rate. It is limited in accuracy by the quality of these sensor measurements.

It is a self-contained system navigation technique in which measurements provided by accelerometers and gyroscopes are used to track the position and orientation of an object relative to a known starting point, orientation and velocity. IMU typically contain three orthogonal rate-gyroscopes and three orthogonal accelerometers, measuring angular velocity and linear acceleration respectively. By processing signals from these devices it is possible to track the position and orientation of a device . Inertial navigation is used in a wide range of applications including the navigation of aircraft, tactical and strategic missiles, spacecraft, submarines and ships. Recent advances in the construction of MEMS devices have made it possible to manufacture low cost and light INS[1].

II. INERTIAL SYSTEM CONFIGURATIONS

INS nearly fall into one of the two categories outlined in the following sections. The difference between the two categories is the frame of reference in which the rate-gyroscopes and accelerometers operate.

A. Stable Platform Systems

In stable platform type systems the inertial sensors are mounted on a platform which is isolated from any external rotational motion. In other words the platform is held in alignment with the global frame. This is achieved by mounting the platform using gimbals (frames) which allow the platform freedom in all three axes, as shown in Fig. 1. The platform mounted gyroscopes detect any platform rotations. These signals are fed back to torque motors which rotate the gimbals in order to cancel out such rotations, hence keeping the platform aligned with the global frame. [1]

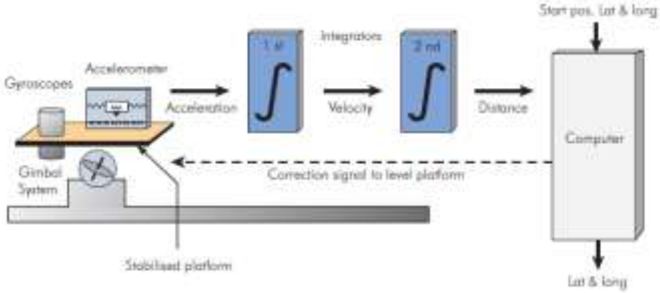

Fig, 1 A stable platform INS.

B. Strapdown Systems

In strapdown systems the inertial sensors are mounted rigidly onto the device, therefore output quantities measured in the body frame rather than the global frame. To keep track of orientation the signals from the rate gyroscopes are 'integrated'. To track position the three accelerometer signals are resolved into global coordinates using the known orientation, as determined by the integration of the gyro signals. Fig. 2 shows the Strapdown inertial navigation algorithm.

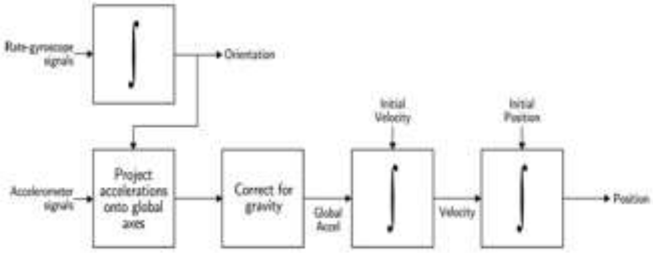

Fig, 2 Strapdown inertial navigation algorithm.[2]

Strapdown systems have reduced mechanical complexity and tend to be physically smaller than stable platform systems. These benefits are achieved at the cost of increased computational complexity. As the cost of computation has

ISSN 1737-9334

decreased strapdown systems have become the dominant type of INS [2].

I. INERTIAL SENSORS

This section introduces the main inertial sensors, this will include the accelerometer and the rate-gyroscope, inertial sensors measuring linear acceleration and angular velocity respectively.

C. Accelerometer

This sensor can be modelled as a weight hanging in spring . A tension sensor is connected to the spring and must be very strong to prevent oscillations. The accelerometer have a direction of sensitivity as shown in Fig. 3. when the force is acting on the "spring " this will create a tension that can be measured .

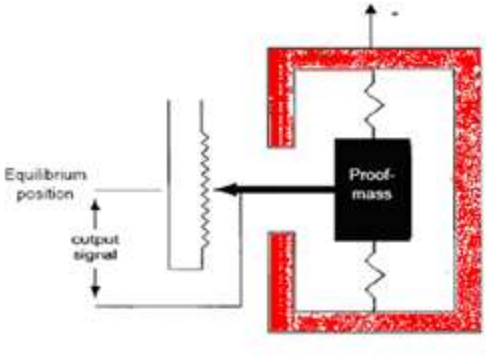

Fig. 3 Accelerometer.

D. Gyroscope

The standard old gyro is a rotating disc with a very high rotating speed as in Fig. 4 , it will try to keep the direction of the rotating vector, if the direction will changes there will be a momentum applied to the mount axis. With some sensors at the mounting points it is possible to measure the force and or the stress of the material. It is possible to keep track of angles. the angular rate gyro of today use vibrating piezoelectric ceramic transducer .[3]

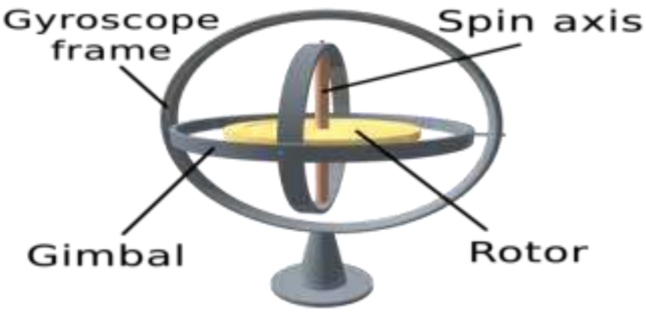

Fig. 4 Gyroscope.

E. MEMES Inertial Sensors

Micro-Electro-Mechanical Systems (MEMS) is the integration of mechanical elements, sensors, actuators, and electronics on a common silicon substrate through micro fabrication technology[1]. MEMES accelerometer modelled as a proof mass suspended from two sides with flexible coils. When the platform is accelerated, the displacement of the mass is measured by a differential capacitance as shown in Fig. 5.

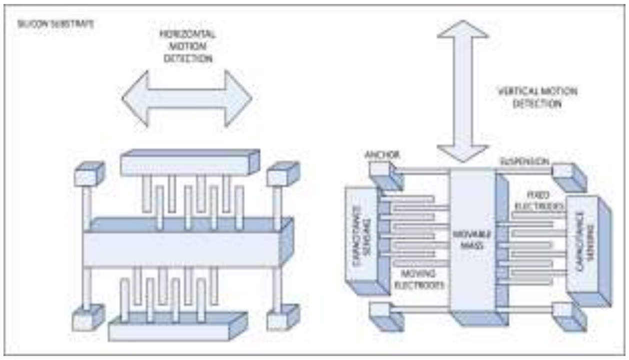

Fig. 5 working principle of an ADXL MEMS-capacitive accelerometer.[3]

A MEMS gyroscope was initially made practical and producible by System Donner Inertial (SDI). Today, SDI is a large manufacturer of MEMS gyroscopes. At present MEMS sensors cannot match the accuracy of optical devices, however they are expected to do so in the future.[3]

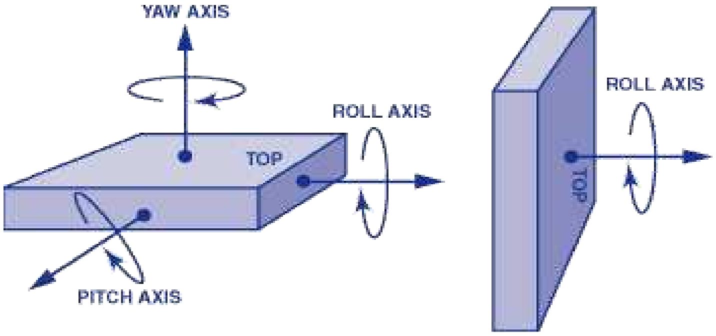

Fig. 6 MEMS gyroscopes [3]

F. Inertial Sensors characteristics

In order to ensure the appropriateness of an INS for a specific application, the application's performance requirements have to be fulfilled. The overall performance of an inertial navigation sensor is determined through accumulating the performances of individual inertial sensors involved in the system. This can be achieved in turn by quantifying the parameters or characteristics describing the performance of each particular inertial sensor through a series of lab tests. The most important among those characteristics are: bias, scale factor, output stability, thermal sensitivity, magnetic sensitivity, and centrifuge, shock survivability, effect of vibrations, as well as ageing and storage [3].

II. INS MECHANIZATION

INS mechanization is the process of determining the navigation states (position, velocity and attitude) from the raw inertial measurements through solving the differential equations describing the system motion. Mechanization is usually expressed by a set of differential equations and typically performed in the local level frame defined by the local east, north and ellipsoid normal. The local level frame is often selected as the navigation frame [4].

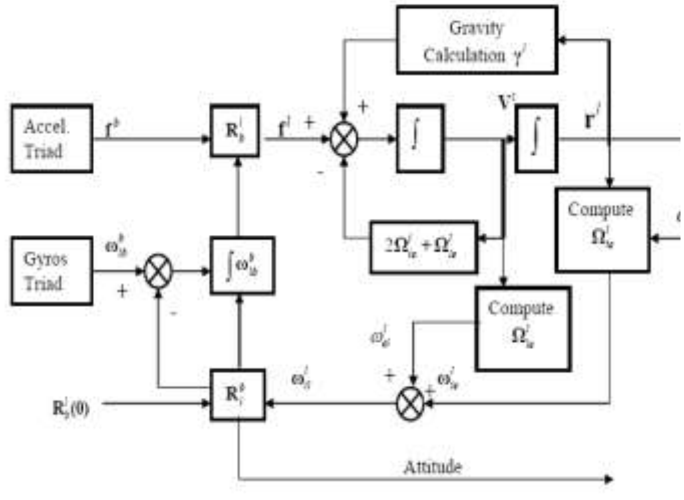

Fig.7 Local Level Mechanization Equations Block Diagram.

As given in Equation 1 the IMU measurements include three angular rate components provided by the gyroscopes and denoted by the 3x1 vector ω_{ib}^b as well as three linear acceleration components provided by the accelerometers and denoted by the 3x1 vector f^b. This means that the angular velocities ω_{ib}^b of the body frame are measured with respect to the inertial frame Fig.7 shows the Local Level Frame Mechanization Equations[4].

$$\begin{pmatrix} \dot{r}^l \\ \dot{V}^l \\ \dot{R}_b^l \end{pmatrix} = \begin{pmatrix} D^{-1}V^l \\ R_b^l f_b - \left(2\Omega_{ie}^l + \Omega_{el}^l\right) \; V^l + g^l \\ R_b^l\left(\Omega_{ib}^b - \Omega_{il}^b\right) \end{pmatrix} \tag{1}$$

Where

V^l is the velocity vector in the local level frame (v_{east}, v_{north}, v_{up}),

R_b^l is the transformation matrix from body to local frame as a function of attitude components,

g^l is the gravity vector in the local level frame,

$\Omega_{ib}^b \Omega_{il}^b$, are the skew-symmetric matrices of the angular velocity vectors $\omega_{il}^b \omega_{ib}^b$ respectively, and

D^{-1} is a 3x3 matrix whose non zero elements are functions of the user's latitude **φ** and ellipsoidal height (**h**).

The solution and numerical implementation of the above differential equation are discussed in more detail in several references [5].

III. COORDINATE FRAMES

The INS typically requires transformations between four coordinate systems, which are defined in Fig. 8. These definitions follow from [4].

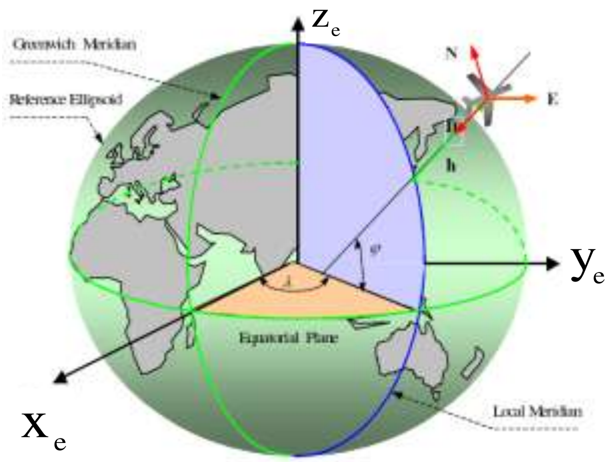

Fig. 8 ECEF and LLF Frame [6]

IV. ELECTRONIC CIRCUIT DESIGN

This section describes the design and implementation of the instrument that was built on board for a Quadrotor UAV, and presents the experiments performed for the Quadrotor UAV at the field environment. The flight data are collected and then analysed.

A. *Design Requirements*

The embedded electronics architecture is designed based on the following requirements:

- Both the rotational and translational motions of the UAV in space shall be detected and recorded
- Rotational and translational motion shall be sampled and recorded at a rate that provide sufficient data for post-flight analysis.
- The physical dimensions of the embedded electronic shall be as minimal to be built on board of a UAV and its weight shall be negligible compared to the weight of the UAV.

B. *Circuit Components*

The following electronics devices and sensors shown in Fig, 9 are used to design the electronic circuit:

- DIYDrones ArduIMU+ V3.
- The Open Log Data Logger.
- Spark Fun FTDI.

The ArduIMU+ V3 is the DIYDrones smart IMU. MPU-6000 MEMS 3-axis gyro and accelerometer as well the 3-axis I2C magnetometer HMC-5883L. With the GPS port and on-board Atmega328 microprocessor, the ArduIMU+ V3 is a tiny but powerful orientation solution. This device is suitable for any application from rockets to simple movement detection[7]. The Open Log Data Logger shown in Fig. 8 is a simple to use, open source solution for logging serial data. The Open Log provides a simple serial interface to log data from a project to a micro SD card[8].

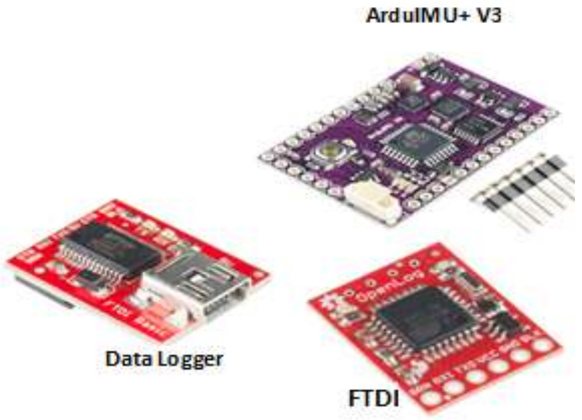

Fig.9 circuit components

The FT232R is a USB to serial UART interface. it is used for programming the ArduIMU+ V3 and The Open Log Data Logger previously described. [9].

C. Design of Instrumentation

The Ardu IMU V3 module is capable of estimating the orientation and velocities of the UAV. The microcontroller is programmed to sample the accelerometers and gyroscopes at about 40 Hz. The FTDI is used for programming the ArduIMU+ V3.

Finally, the designed flight data acquisition circuit contains data logger module and Ardu IMU V3 are connected together via serial communication lines. A small battery with a small plug power are connected to the IMU to provide power to all connected sensors as illustrated in Fig. 10.

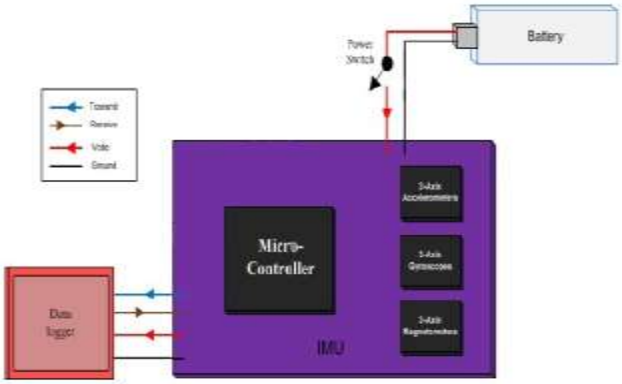

Fig. 10 Architectural block diagram of the embedded electronics.

D. Circuit implementation

In order to determine the orientation of the quadrotor UAV, we read data from the ArduIMU. The ArduIMU is a collection of sensors and is typically comprised of at least a three-axis accelerometer and a 3-axis gyroscope and sometimes can employ magnetometers, barometers, and other sensors to supplement these. The electronic circuit consists of an ArduIMU, a data logger and a battery with its power plug.

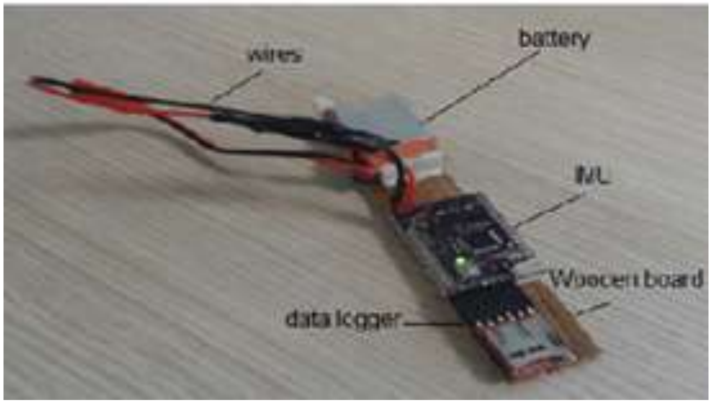

Fig. 11 Implementation of the electronic circuit

The electronic pieces was connected to each other with wires. After that, the instrumentation was set on a piece of wood using double side sticky tape. The location of the instrumentation was in front of the wooden board as shown in Fig. 11. Sensor characteristics is provided in Table 1.

TABLE 1
: SENSOR CHARACTERISTICS AND OTHER EQUIPMENT.

Sensor	Dimension	Weigh	Type
IMU	83.1*25.4*1.5	3.2	DIYDronesArduIMUv3
DATA LOGGER	19 15 4	1.8	Spark fun open log
BATTERY		11g	E-flit LiPo

E. On board System

To maintain the UAV balance, the system is placed at the bottom of the quadrotor board as illustrated in Fig. 12.

Fig. 12 Installation of the instrumentation on the quadrotor

V. FIELD TESTS AND FLIGHT DATA COLLECTION

The experiments were performed in outdoor field environment under a fine weather condition. The instrumented Drone was set up on a solid platform to ensure its stability before flying it Fig. 13. Then the instrument was powered to start recording the movement of the UAV.

Fig. 13 Setting up the quadrotor on a solid platform for collecting flight data.

After that, the UAV was prepared for take-off flown using remote controller for several seconds. Once the UAV landed on the ground, the collected flight data was transferred from the on board data logger to be stored on a portable computer. The experiments were performed for several manoeuvres attempted with random speed and orientation.

A. *Field Test 1*

Closely looking to Figs (14 and 15), all acceleration and angular velocity components x .y. z experienced a slight change from 0 to 25 seconds. This indicates that the UAV was in flight but in a low altitude with slow motion. After that, the UAV was in flight for 70 seconds which recorded in a noticeable change in all acceleration and angular velocity components x .y. z. Last phase, the UAV landed on the ground.

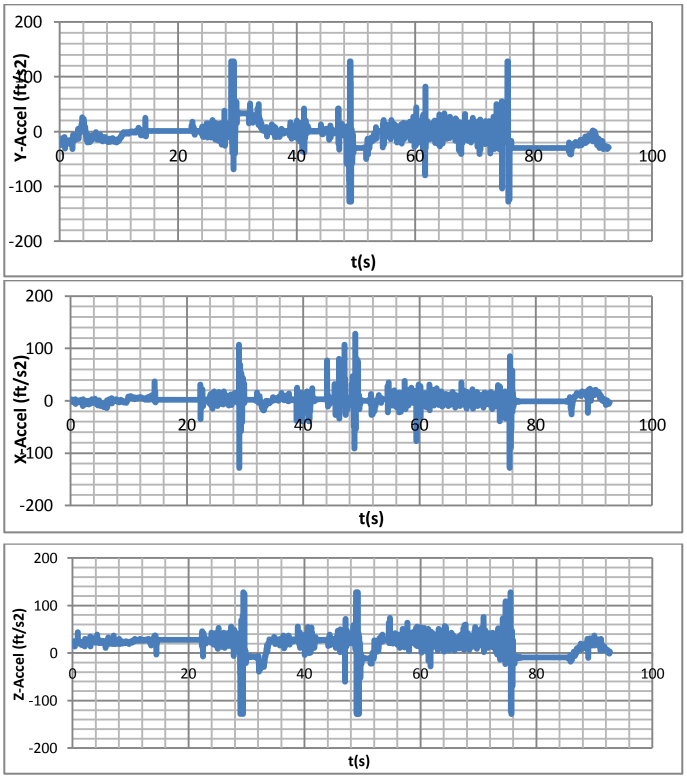

Fig. 14 Measurements of the acceleration components of the accelerometers of fight test 1.

B. *Field Test 2*

Revealing to Figs (16 and 17), the changing of the acceleration values of y axis and gyroscope values of z axis were more noticeable than the other axes from 0 to 35 seconds. These changes indicate that the UAV moving in y direction with spin around z axis. After that, the UAV was on the ground for 7 seconds which can be noticed that all records show no change. In phase 24 to 118 seconds, there was a noticeable change in all axes of accelerometer and gyroscope which implies that the UAV was in flight situation. In final phase, the UAV rested on the ground.

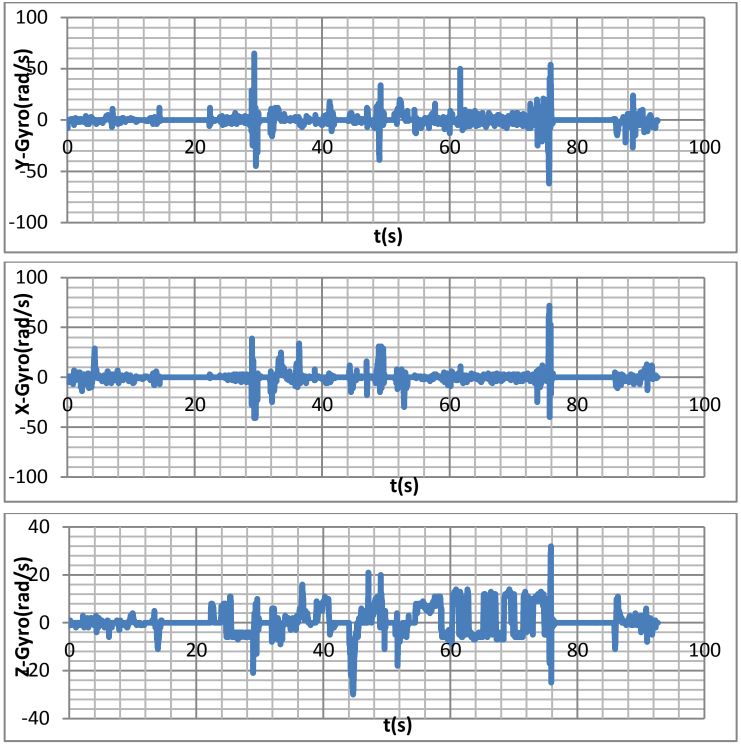

Fig. 15 Measurements of the angular velocity components of the gyroscopes of the fight test 1..

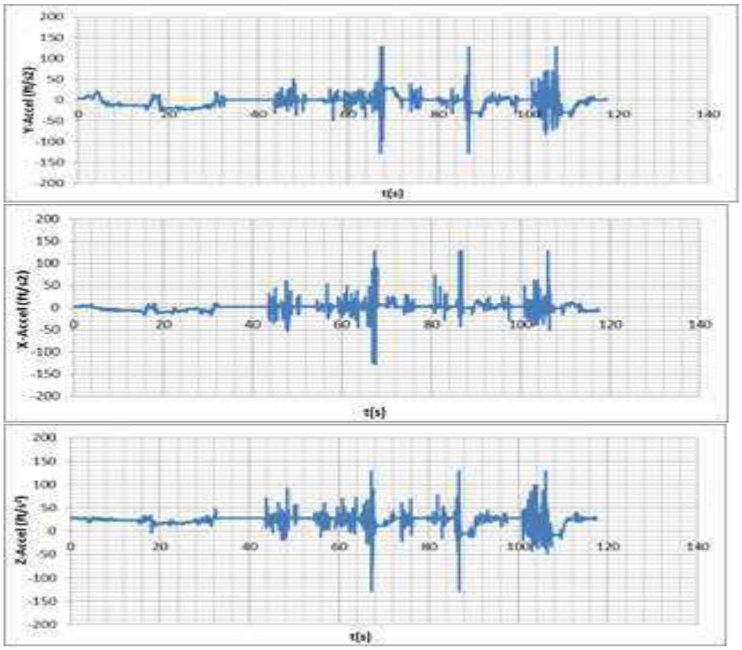

Fig. 16 Measurements of the Acceleration components of the accelerometer of the fight test 2.

C. Field Test 3

The collected flight data as depicted in Figs (18 and 19), There is a short oscillation of angular velocity components can be observed for the first 12 seconds which means that the UAV spinning on the ground. Then, there was no change in all acceleration and angular velocity components for all axes which indicates that the UAV was on the ground. After that, the UAV was in flight from 25 to 65 seconds which can be seen in the change in all acceleration and angular velocity components for x, y and z axes. In final phase, the UAV was on the ground as it appears in the dramatic decrease in all acceleration and angular velocity components for all axes to remain then steady.

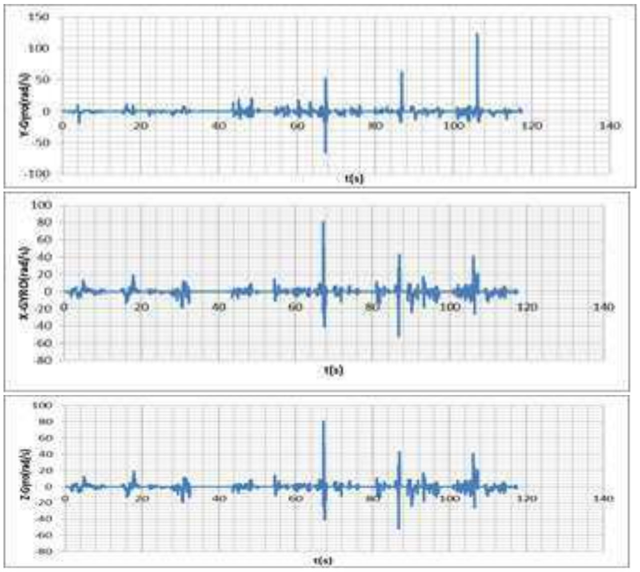

Fig. 17 Measurements of the angular velocity components of the gyroscopes of the fight test 2.

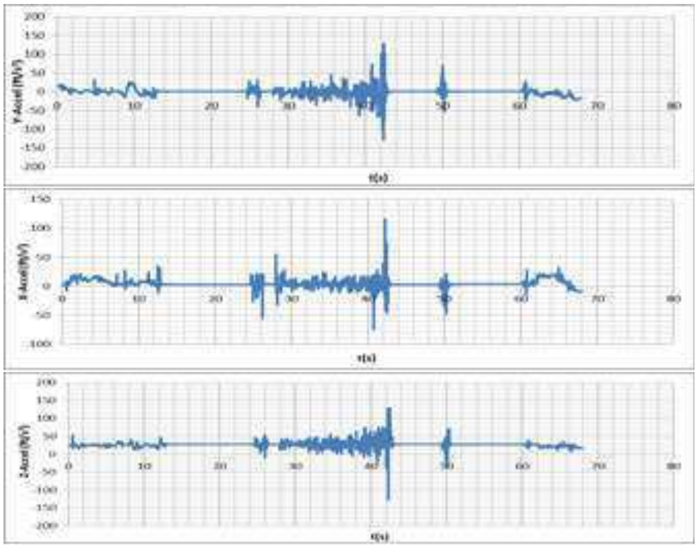

Fig. 18 Measurements of the acceleration components of the accelerometer of the fight test 3

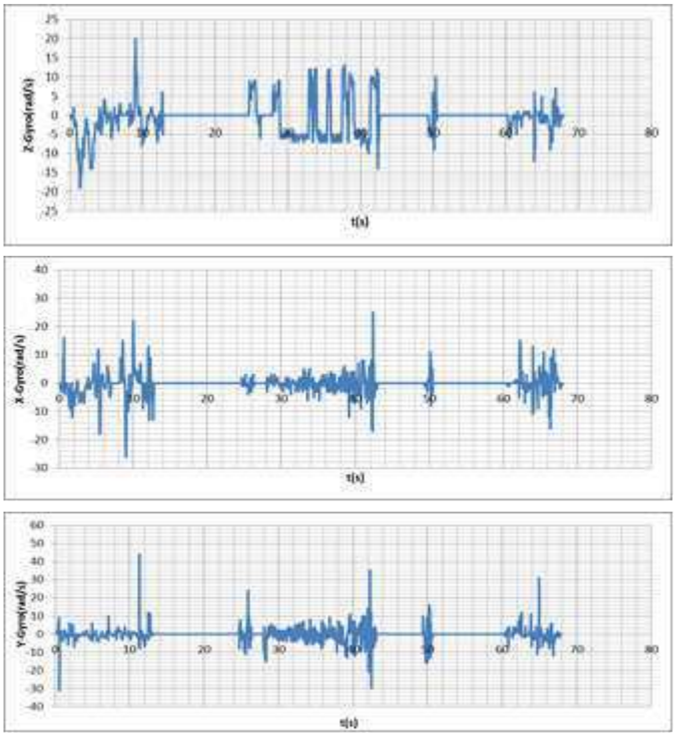

Fig.19 Measurements of the angular velocity components of the gyroscopes of the fight test 3.

VI. PROCESSING COLLECTED FLIGHT DATA USING SIMULINK

Once the UAV landed on the ground after making several tests, the collected flight data was transferred from the onboard data logger to be stored on a portable computer. After that, SMILUNK with MATLAB block diagram shown in Fig. 20 was used to estimate the UAV trajectory. The Aeronautical Simulation Blockset for MATLAB (AeroSim) [10] is used to build up the INS navigation algorithm. AeroSim blockset provides a complete set of tools for developing nonlinear 6-degree-of-freedom aircraft dynamic models. INS navigation algorithm block diagram used for analyzing the recorded flight data is shown in Fig. 21. The resultants flight trajectories for the different recording data represented in previous section are shown in Figs 22,23, and 24 Respectively.

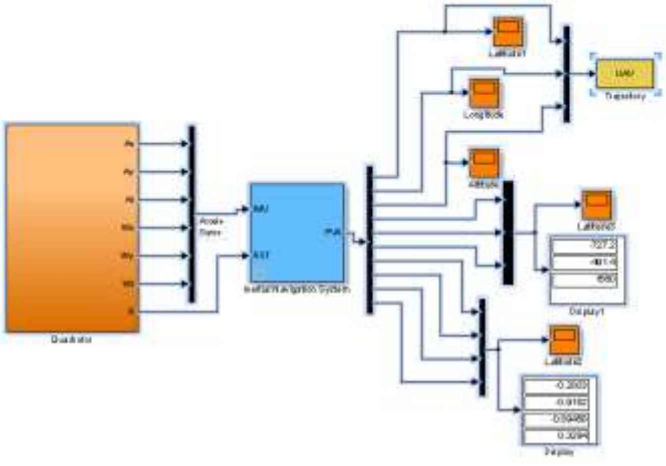

Fig.20 The SIMULINK Block Diagram Used for Analyzing The Flight Data.

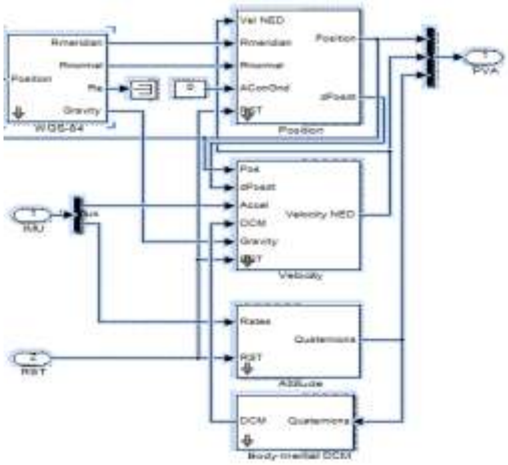

Fig.21 INS Simulink Block Diagram Navigation Algorithm Used For Processing The Recorded Flight Data.

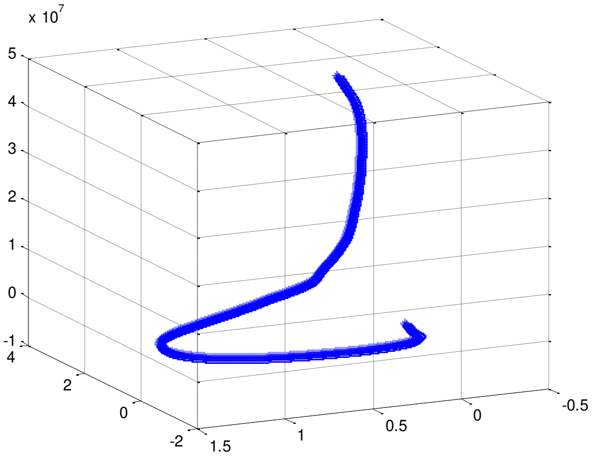

Fig.22 Trajectory of UAV Estimated After Analysing Flight Data for Test (1).

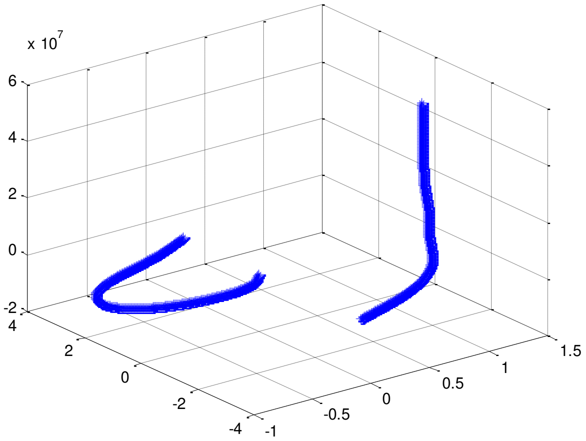

Fig.23 Trajectory of UAV Estimated After Analysing Flight Data for Test (2).

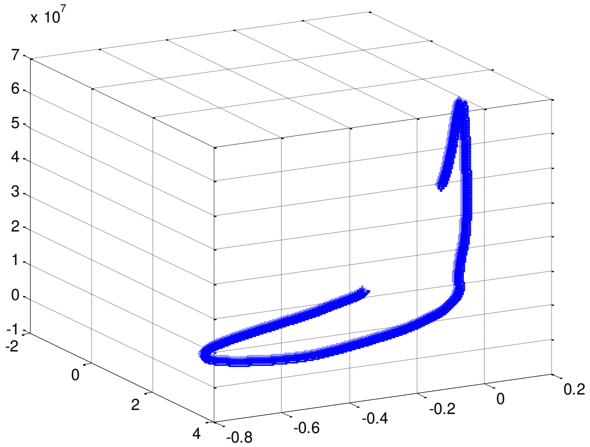

Fig.24 Trajectory of UAV Estimated After Analyzing Flight Data for Test (3).

VII. CONCLUSIONS

The paper has addressed the implementation of onboard navigation system of a low cost drone. It has been proposed that onboard sensor measurements for the UAV would provide flight data that enables to identify its motions in the field environment. It has been presented that using low cost electronic sensors to collect in flight measurements can be achieved. The electronic circuit constructed into a low cost drone is capable of sensing and logging high frequency flight data. The circuit comprised low cost sensors including 3-D gyroscopes and accelerometers. The circuit was tested on a low cost drone and successfully logged flight data. Several experiments were performed and results were analyzed then off line processed using Simulink is done in order to detect the movement and trajectory of the UAV.

REFERENCES

[1] O.J. Woodman, An Introduction to Inertial Navigation, Technical Report UCAM-CLTR- 696, ISSN 1476-2986, University of Cambridge Computer Laboratory, Aug. 2007.
[2] Rolf Christensen , Nikolaj Fogh / Inertial Navigation System / MSc thesis , Aalborg University/ June 2008 .
[3] Titterton D.H. and Weston, J.L. (1997): “Strapdown inertial navigation technology;” Peter Peregrinus Ltd., London, UK, 1997.
[4] El-Sheimy.” *Inertial techniques and INS/DGPS Integration*”. ENGO 623-Lecture Notes, the University of Calgary, Department of Geomatics Engineering, Calgary (2004).
[5] Schwarz, K.P. and Wei, M. (2000), “Inertial Geodesy and INS/GPS Integration”, partial lecture notes for ENGO 623, Department of Geomatics Engineering, The University of Calgary, Canada.
[6] Salychev, O.S. (1998), "Inertial Systems in Navigation and Geophysics", Moscow State Technical University, Bauman MSTU Press, Moscow.
[7] https://www.sparkfun.com/products/9530.Last Accessed 29 /11/ 2019
[8] https://www.sparkfun.com/products/13712 Last Accessed: 29/11/2019.
[9] https://www.sparkfun.com/products/9716 Last Accessed: 25/08/2019.
[10] Unmanned dynamics, LLC. Aerosim Blockset User’s Guide. Version1.2.

Basics and Applications of Ground Penetrating Radar as a Tool of High Resolution Cross-Sectional Images

Amira Youssef Mohammad Ellafi
Faculty of Electronic Technology
Amoor85ly@yahoo.com

Abdussalam Masaud Mohamed Ammar
Faculty of Electronic Technology
Slm2010ly@gmail.com

Amer R. Zerek
Zawia University, Faculty of Engineering
EE Department,
Zawia, – Libya
anas_az94@yahoo.co.uk

Abstract - **Ground Penetrating Radar (also referred to as GPR, Ground Probing Radar, or georadar) is a near-surface geophysical tool with a wide range of applications. Over the past 30 years, GPR has been used successfully to help in constraining problems in many fields such as archaeology, environmental site characterization, glaciology, etc. GPR is a Non Destructive Testing (NDT) method which generates an electromagnetic signal that penetrates the subsurface and measures the amplitude and the travel time of the returned signal. GPR data provides high-resolution cross-sectional images of the scanned material. Antennae of different frequencies allow for varying levels of resolution and depths of investigation. The data is very versatile and applicable across many disciplines. In many cases, however, GPR surveys have been planned or executed with little or no understanding of the physical basis by which GPR operates and is constrained. As a result, many unsuccessful GPR studies have also been presented or published over the past 30 years. This paper provide an introduction to the important variables pertinent to GPR and to explain the relevant aspects of these variables in GPR acquisition, in an attempt to provide fundamental knowledge for improving GPR usage in the future.**

Index Terms – GPR , FMCW ,CMP, Dielectric Constant.

I. INTRODUCTION

To be able to find information about the sub-surface without digging, several methods can be utilized. These are often referred to as NDT inspection methods, and are based on geophysical theory.

One method is Ground Penetrating Radar, this technique is based on the use of focused radar energy that can goes through the ground, and reflected to the system when sub-surface interfaces are encountered. To effectively do this over a large area and obtain detailed information about the ground, a 3D georadar system is often preferred.

GPR can be used to obtain information on a wide range of surfaces by emitting electromagnetic waves into the ground and receiving the electromagnetic waves that are reflected where there is a change in the electrical properties between two layers, GPR can measure and map subsurface features such as asphalt thickness, position of rebars, position of pipes, etc.

A typical GPR unit consists of a transmitting and receiving antenna, where the transmitting antenna generates an EM pulse that travels into the subsurface and then reflects off an interface or scatters off point sources (both caused by a contrast in relative permittivity). This reflected or scattered energy then travels back to the surface, where it is recorded by the receiving antenna.

The time it takes for the wave to travel down to an interface and back up to the surface is called the travel time, and it is used to determine the in situ propagation velocity of the subsurface material. The velocity (distance/travel time) for an EM wave in Earth's atmosphere at or near sea level is 0.33 m/ns. Because the relative permittivity of all earth materials is greater than the permittivity of air, the velocity of an EM wave in all earth materials will be less than the EM propagation velocity in air, typical materials range between 0.05 and 0.15m/ns [1].

II. GPR SYSTEM DESIGN PARAMETERS

Every material has electrical properties which those properties are important for knowing. Those properties are permittivity (ε), conductivity (σ) and permeability (μ). In GPR application, value of permittivity and conductivity is important while permeability is rare of concern. GPR is most useful if used in low electrical loss materials. If conductivity (σ) is zero, then GPR can be see under surface deeper. In reality, low electrical loss materials are not prevalent. Water under surface or moist material or clay rich environment makes the capability of GPR to penetrate the deeper surface is limited. Ground materials are composites from many materials. Ice and water are examples that represent a most case.

ISSN 1737-9334

Practically, the issue of low electricity losses is common. An environment that rich in groundwater or saline can made conditions where GPR signal penetration is very limited. Earth material is a combination of many other elements or components. Water and ice represent several cases where one main component exists. Simple beach sand is a mixture of soil grains, air, and dissolves in the air.

Ground grains will usually be placed 60 to 80% of the available volume. Understanding the physical nature of the mixture is a key factor in the interpretation of the GPR response. A mixture of materials that rarely shows properties proportional to the volume fraction of its constituent components. In many cases, this can make quantitative analysis impossible without additional information.

The work concept of GPR is simple. Its aim is to measure the amplitude of signal and time after excitation. The core of the GPR system is a time management unit which regulates the signal generating and detects signal echo as shown in Fig. 1. Most of GPR is works in time domain so that to synthesize time domain responses, frequency domain is used.

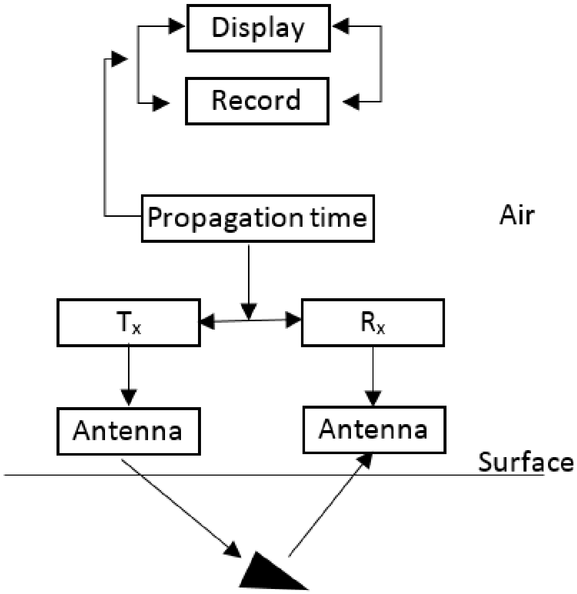

Fig. 1. Block diagram of GPR [2].

III. GPR SYSTEM DESIGN PARAMETERS

GPR systems manufacturers offer several configurations according to their system components. The system configuration directly affects the performance of the NDT assessment. In numerous applications, prior information about the structure under test and the target characteristics are known.

Different GPR applications and the main GPR limitations cited demand different types of antennas. There are several types of antennas used in GPR. For instance, some applications demand a high depth penetration with low resolution while other applications require opposite characteristics. High resolution applications require antennas with higher bandwidths which in turn results in low penetration depth of inspection.

The tradeoff between resolution and depth of penetration is defined when the antenna central frequency is chosen. On the other hand, target identification usually imposes much more strict requirements on antennas in comparison with a system for merely target detection. It is important to notice that the antenna is a system in itself with its own transfer function that can be frequency-dependent with a non-linear phase response that can be critical for an impulse GPR system. Since the main objective of GPR systems is the generation of an image, phase distortion is a serious problem. On the other hand, in frequency modulated or synthesized GPR, the requirement for linear phase response from the antenna can be relaxed. This allows the use of certain types of antennas with complex frequency response, as their effect can be corrected by system calibration if necessary [3].

Considering the foregoing, important aspects of GPR antenna design are:

i. The antenna should have a wide frequency bandwidth for better resolution. The maximum depth of investigation decreases when the electromagnetic wave frequency increases. In reality, most sub-surface radar systems operate at frequencies below 5 GHz, as the examples in Tables 1 and Table 2 shows.
ii. The antenna should have well behaved and consistent performance across the antenna's operational band, including the radiation pattern, gain, impedance matching and a requirement for low dispersion. High gain and narrow beam width are fundamental to resolve close proximity targets.

Table I. Application using Time Domain Waveform

No	Application media	Antenna type	Coupling (Air/Ground)	Bandwidth (GHz)	Ringing concern
1	Forest litter	Horn	A	0.8 to 5.2	No
2	Pavement inspection	Half Ellipse	A	0.25 to 0.75	Yes
3	Landmine detection	Bowtie	A	1.5	Yes
4	Forensic survey	Horn	A	0.27 to 0.9 MHz	No
5	Boundary layer detection	Loaded dipole	G	0.25 to 0.75	Yes

6	Metallic target behind concrete wall	Horn and vivaldi	A	1.5 to 4.5	No

Table 2. Application using Frequency Domain Waveform

No	Application media	Antenna type	Coupling (Air/Ground)	Bandwidth (GHz)
1	Pavement inspection	Aperture	A	0.2 to 3
2	Generic	Mimo	A	0.3 to 4
3	Generic	Horn	A	0.8 to 4
4	Dispersive media	Vivaldi	A	0.8 to 3
5	Generic	Bowtie	G	0.2 to 0.6
6	Solid hydraulic	Spiral, vivaldi	A	0.8 to 5.2
7	Layered media	Horn	A	0.8 to 2
8	Soil permittivity	Loaded diapole	G	0.5 to 4.5

Table 1 presents recent works for different GPR applications for time-domain systems. Time-domain systems are basically characterized by sending a pulse or impulsive waveform to the structure under test. This type of waveform has a short period of time and a large bandwidth.

As can be seen in Table 1, it is possible to use various types of antenna with this waveform. However, some types of antennas present some drawbacks when considering time-domain waveforms or the coupling to the structure under test. Planar bowtie and dipole antennas can cause late-time ringing when used for transmitting a short time pulse. Late-time ringing can blur target information in a GPR assessment. In addition, these antennas can exhibit coupling problems when used on irregular surfaces. For those applications, horn antennas are more appropriate since they can be located at some height from the structure under test [4][5][6][7][8][9].

Most of the commercial GPR systems use time-domain waveforms. However, there are developments and ongoing research into frequency-domain options. The later have some advantages over time-domain systems since they require less energy and provide more information about the target characteristics. Table II shows some recent works for several applications that use frequency-domain waveforms in the GPR system.

According to Table II frequency-domain GPR systems can be used for a variety of applications. Some applications may require better images. One important characteristic of images is the phase-dependent feature. To improve GPR images antenna arrays can be used to minimize phase problems. In addition, air or ground-coupled options can be used for different depth or resolution specifications [10][11][12][13] [14][15][16][17].

When it comes to commercial options, time-domain systems are prevalent. This is due to the fact that frequency-domain systems are relatively new compared to the time-domain option. However, since the electronics of frequency-domain systems are less expensive than the time-domain option there is a growing offering of this system in the market.

IV. Categories of GPR system.

Most of the GPR equipment is based on two categories: time or frequency-domain options. Fig. 2 shows the most relevant options considering these categories. GPR systems that shape a time-limited waveform considering changes in its amplitude are known as impulse GPR. Continuous wave (CW) GPR are based on band-limited signals. This type of GPR transmits a signal of infinite duration, as a continuous sine wave, and receives it simultaneously.

In this configuration, it could detect buried targets but it not possible to estimate range since the signals do not change. To improve detection the signal bandwidth should be widened. This can be done by using some sort of modulation.
For instance, in amplitude modulation the continuous wave can be modified with amplitudes 1 and 0 at different times during the inspection. This is called pulsed GPR. Since the transmission and reception times are well defined it is possible to associate then with the target range. However, when dealing with GPR and its applications it is desirable to have control of the power spectral density and in turn the resolution of the assessment.

Another approach to do this is adding more frequencies by increasing or decreasing the oscillation in the waveform. This configuration is called Frequency Modulated Continuous Wave (FMCW) [17]. Instead of using transmitted and received times of pulses FMCW uses the difference in frequency. This type of GPR system suffers from interference issues.

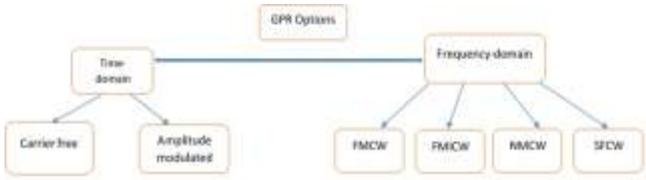

Fig .2. GPR systems options.

A different method can be employed to both CW or pulsed GPR where the transmitted frequency of tones or pulses shifts in a given interval or steps across a defined bandwidth. In this way, the signal spectrum is finite and not continuous. This technique is called Stepped Frequency Continuous Wave (SFCW). The frequency step avoids phase ambiguity by measuring the phase difference between returned signals at each frequency. In addition, the hardware associated with SFCW is simpler than that employed in FMCW. A variation of the SFCW technique involves gating the timing of the transmitter and receiver circuits.

Advantages and disadvantages of different waveforms for GPR are also dependent on operational requirements. One of the challenges when using impulse waveforms is that of producing a pulse short enough to achieve the desired bandwidth, i.e. with suitable fast rise and fall times.

The antenna should be designed to avoid ringing effects or distortion of the pulse shape. Another challenge arises if the received pulses are sampled in real time in the analogue-to-digital converter (ADC), since the ADC must operate at high enough frequencies to digitize correctly the waveforms. A common problem for active radar systems for CW is the strong backscattered signal from the air-ground interface.

This undesired signal can overshadow the reflections from actual targets, especially those with low radar cross section such as human beings, and limit the dynamic range of the receiver, which could be saturated and blocked. Although techniques have been developed to address this problem including the Frequency Modulated Interrupted Continuous Wave (FMICW) or the Noise Modulated Continuous Wave (NMCW) waveforms, which can be used as an alternative technique or combined with the existing ones.

V. THE CONCEPT OF GPR DATA PROCESSING DEVELOPMENT

This paper studying how to develop a GPR data processing, which is expected to be used freely. The development phase of GPR data processing is briefly explained in the Fig. 3.

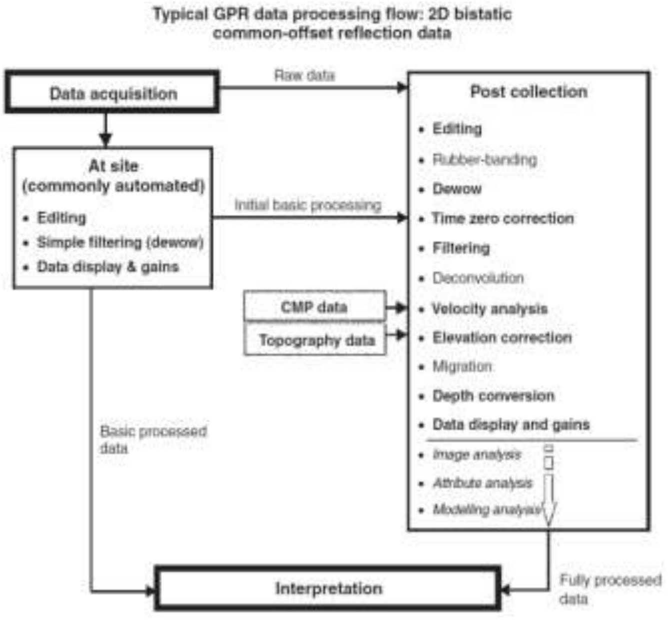

Fig. 4. GPR data processing and analysis steps [3].

the editing and rubber-banding phases are the stages of preparing survey GPR data that will be processed. Information about the frequency used, the distance between lines, the number of lines, the number of traces, the type of file used and the others are things that must be known from the beginning so that the data processing in the next step is not wrong. The dewow phase is the stage that aims to eliminate the low frequency and DC bias in the data. Wow is a noise that has a very low frequency value, this occurs due to an electronic instrument saturated by the value of large amplitude of direct waves and air waves. Dewowing is a vital step as it reduces the data to a mean zero level and, therefore, allows positive–negative colour filling to be used in the recorded traces [3]. If done with incorrectly way, the data will be decayed and the low frequency component will distort the spectrum from trace data. This incorrectly processed data will affect to the next data processing stage. If this process is done manually step by step, it is better to eliminate the DC component first and then implement the filter. The dewow concept can be seen in Fig. 4.

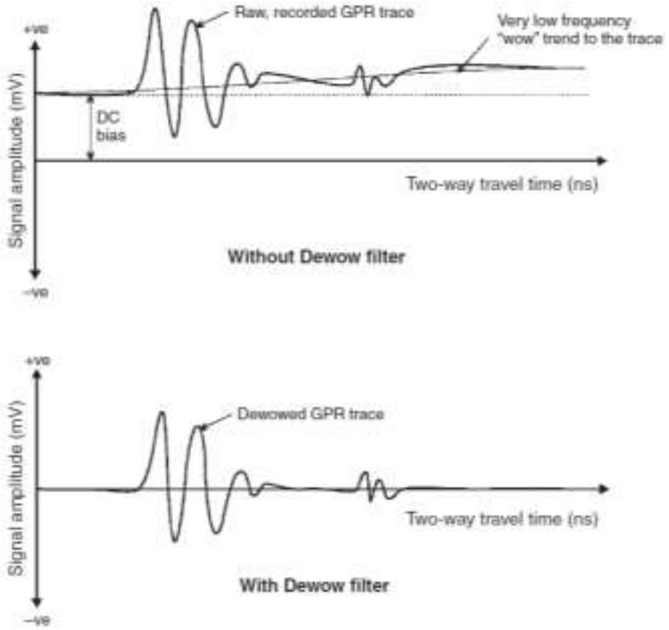

Fig. 4. Dewow concept stage for processing GPR data [3].

The next phase is time zero correction. This aimed to correct the initial time to be exactly the same with the surface of the ground. Thermal drift, electronic instability, cable length differences and variations in antenna airgap can cause 'jumps' in the air/ground wavelet first arrival time [3].

The next phase is filtering, which is done by implementing 1D and 2D filtering to improve signal to noise ratio and correcting image quality. There are many types of filters that can be applied at this phase, from simple band-pass filters to transform filters. Simple filters sometimes effective to eliminate the high frequency noise and low frequencies. And sometimes some complex filters are not needed. In general, filters can be divided into two types, which are temporal (one by one filtering the trace data) and spatial (filter for some trace data). Examples of temporal filters are simple mean, simple median, low pass, high pass and band pass. Examples of spatial filters are simple running average, average subtraction,

ISSN 1737-9334

both background removal and spatial low, high and bandpass filter.

The next stage is deconvolution. Deconvolution aims to contrast signals for increasing the resolution by compressing GPR wavelet data into a narrow band. The purpose is to remove the effect of the source wavelet from the GPR data and leave the impulse response to subsurface layers. This deconvolution process assumes that the subsurface is horizontally layered and has a uniform intra-layer velocity and the signal reflection appears an interface coherently. The next step is velocity analysis. The purpose of this velocity analysis is to analyze the speed of the GPR signal. Electromagnetic signals are propagating in a medium which depend on the characteristics of the media itself. If in the air, the velocity of electromagnetic waves is 3.108 m/s. If other than air, the velocity of the electromagnetic wave is smaller than that value. Table 3 summarizes the electromagnetic wave velocity on certain media.

Table 3: Approximate dialectical permittivity, electrical conductivity and radio wave velocities for various material

Material	Relative Permittivity	Conductivity (mS/m)	Averages Velocity (m/ns)
Fresh Water	1	0	0.3
Air	80	0.5	0.033
Sea Water	80	3000	0.01
Ice	3-4	0.01	0.16
Dry Sand	3-5	0.01	0.15
Saturated Sand	20-30	0.1-1	0.06
Limestone	4-8	0.5-2	0.12
Shales	5-15	1-100	0.09
Silts	5-30	1-100	0.07
Clays	5-40	2-1000	0.06
Granites	4-6	0.01-1	0.13
Anhydrites	3-4	0.01-1	0.13

The next step is elevation correction and migration. The purpose of this step is to correct the effects of topography and the effects of geometry survey also the effects of the spatial distribution energy. The next step is depth conversion. This step synchronizes between two-way travel time and depth. As explained in the Table I, the depth of a surface can be converted from electromagnetic wave velocity and twoway travel time.

CONCLUSION

GPR has been developed into a sophisticated technique that can provide detailed images of the near surface. As opposed to other locating techniques that are capable of detecting only metallic or conductive utilities and underground targets, GPR can locate and characterize both metallic and non-metallic subsurface features. It is completely non-intrusive, non-destructive and safe.

REFERENCES

[1] Gregory S. Baker, Thomas E. Jordan, and Jennifer Talley, “An introduction to ground penetrating radar (GPR) ” Special Paper 432, 2007.

[2] H. M. Jol, Ground Penetrating Radar Theory and Applications,Oxford: Elsevier Science, 2008.

[3] M. Biancheri-Astier, V. Ciarletti, A. Reineix, and A. Le Gall (2015), “Optimization of the Antennas of the EISS Radar Designed to Perform Deep Martian Subsurface Sounding” IEEE Transactions on Geosciences and Remote Sensing, v. 53, n. 8, pp. 4627-4637.

[4] F. André, M. Jonard, and S. Lambo (2015), “Non-Invasive Forest Litter Characterization Using Full-Wave Inversion of Microwave Radar Data”, IEEE Transactions on Geosciences and Remote Sensing, v. 53, n. 2, pp. 828-840.

[5] X. Li, YicaiJi, W. Lu, and G. Fang (2013), “Analysis of GPR Antenna System Mounted on a Vehicle”, IEEE Antennas and Wireless Propagation Letters, v. 12, pp. 575-578.

[6] I. Giannakis, A. Giannopoulos and Craig Warren (2016), “A Realistic FDTD Numerical Modeling Framework of Ground Penetrating Radar for Landmine Detection”, IEEE Journal of Selected Topics in Applied Earth Observations and Remote Sensing, v. 9, n. 1, pp. 37-51.

[7] E. R. Almeida, J. L. Porsani, I. Catapano, G. Gennarelli, and F.Soldovieri (2016), “Microwave Tomography-Enhanced GPR in Forensic Surveys: The Case Study of a Tropical Environment” IEEE Journal of Selected Topics in Applied Earth Observations and Remote Sensing, v. 9, n. 1, pp. 115-124.

[8] J. F. Höfinghoff and L. Overmeyer (2013), “Resistive Loaded Antenna for Ground Penetrating Radar Inside a Bottom Hole Assembly”, IEEE Transactions on Antennas and Propagation, v. 61, n. 12, pp. 6201-6205.

[9] L. Quanhua, Y. Wang, A. Fathy(2012), "A compact integrated 100 GS/s sampling module for UWB see through wall radar with fast refresh rate for dynamic real time imaging," In: IEEE Radio and Wireless Symposium (RWS), pp. 59-62.

[10] J. De Pue, M. Van Meirvenne and W. M. Cornelis (2016), “Accounting for Surface Refraction in Velocity Semblance Analysis With Air-Coupled GPR”, IEEE Journal of Selected Topics in Applied Earth Observations and Remote Sensing, v. 9, n. 1, pp. 60-73.

[11] Z. Zeng, J. Li, L. Huang, X. Feng, and F. Liu (2015), “Improving Target Detection Accuracy Based on Multipolarization MIMO GPR”, IEEE Transactions on Geosciences and Remote Sensing, v. 53, n. 1, pp. 15-24.

[12] A. De Coster, A. P. Tran, and S. Lambot (2016),”Fundamental Analyses on Layered Media Reconstruction Using GPR and Full-Wave Inversion in Near-Field Conditions”, IEEE Transactions on Geoscience and Remote Sensing, v. 54, n. 9, pp. 5143-5158.

[13] B. Guan, A. Ihamouten, X. Derobert, D. Guilbert, S. Lambot, and G. Villain (2016), “Near-Field Full-Waveform Inversion of Ground-Penetrating Radar Data to Monitor the Water Front in Limestone”, IEEE Journal of Selected Topics in Applied Earth Observations and Remote Sensing, v. x, n. x, pp. 1-9.

[14] M. Salucci, L. Poli, N. Anselmi, and A. Massa (2017), “Multifrequency Particle Swarm Optimization for Enhanced Multiresolution GPR Microwave Imaging”, IEEE Transactions on Geosciences and Remote Sensing, v. 53, n. 3, pp. 1305-1317.

[15] F. Jonard, L. Weihermüller, M. Schwank, K. ZaibJadoon, H. Vereecken, and S. Lam (2015), “Estimation of Hydraulic Properties of a Sandy Soil Using Ground-Based Active and Passive Microwave Remote Sensing”, IEEE Transactions on Geosciences and Remote Sensing, v. 53, n. 6, pp. 3095-3109.

[16] S. Saiti, S. K. Patra and A. Bhattacharya (2017), “A Modified Plane Wave Model for Fast and Accurate Characterization of

Layered Media”, IEEE Transactions on Microwave Theory and Techniques, v. 65, pp. 3492-3502.

[17] D. Comite, A. Galli, S. E. Lauro, E. Mattei, and E. Pettinelli (2016), “Analysis of GPR Early-Time Signal Features for the Evaluation of Soil Permittivity Through Numerical and Experimental Surveys” IEEE Journal of Selected Topics in Applied Earth Observations and Remote Sensing, v. 9, n. 1, pp. 178-187.

[18] R. Deng and Ce Liu (1999), “FM-CW radar performance in a lossy layered medium”, Journal of Applied Geophysics, Elsevier, v. 42, n. 1, pp. 23-33.

Structural Optimization of a Composite Wind Turbine Blade for Material and Blade Weight

[1]Ramadan A. Almadane, [2] Eman Alijaly Daman and [3]Amal Jamal Boukar

[1] Libyan Academy for Postgraduate Studies Tripoli – Libya
E- mail ramadanalmadani@ymail.com
[2] College of Engineering Technology-Jounzur- Libya
E- mail eman_daman@yahoo.com
[3]Tripoli University – Faculty of Education , Janzour. Physics Department
Tripoli- Libya
E- mail amal_boukar@yahoo.com

***Abstract*— In order to reduce electrical energy production costs, the size of commercial wind turbines has grown considerably during the past decade. Currently, the largest wind turbine installed gives more power. However, as the size of the wind turbine rotor increases, the structural performance, durability and dynamic stability requirements tend to become more and more challenging to meet. The two main structural performance requirements for wind turbines are sufficient flapwise bending strength to withstand highly rare extreme static and dynamic loading conditions (e.g. 50-year return-period gust or a short-term extreme operating gust), • sufficient flapwise bending stiffness to ensure that a minimal clearance is maintained between blade tip and the turbine tower at all times during wind turbine operation. To satisfy the above two extreme operating conditions, several methods have been proposed to evaluate the extreme structural performances of horizontal axis wind turbine (HAWT) blades. One of these method materials basis and weight of wind turbine blade so in this paper two different blade materials were modeled with ANSYS software and the stress ratio and tip deflection under extreme gust loads and the normal wind load are evaluated. results were shown..**

***Index Terms*—wind , blade, composite, stress, deflection**

I. INTRODUCTION

THE blade design process starts with a "best guess" compromise between aerodynamic and structural efficiency. The choice of materials and manufacturing process will also have an influence on how thin (hence aerodynamically ideal) the blade can be built, and at what cost. Therefore, the structural engineering process has a critical role in bringing all the disciplines of design and manufacture together and producing the optimum solution in terms of performance and cost. The lift force on the blade, which drives the turbine round, is distributed along the blade approximately in proportion to the local radius, i.e. there is more lift force close to the tip than there is near the hub. The reasons why this is so, and why it is desirable, are explained in the preceding work .The lift force tends to make the blade bend. If we look at a section of the blade at some point along its length, all the lift forces outboard of that point will have a cumulative effect on the tendency to bend, with those furthest away having the *greatest effect as they have the greatest leverage. The effect is called bending moment. The bending moment is greatest at the root of the blade: at this point there is more blade outboard (contributing to bending moment) than at any other point along the* blade. At the tip the bending moment drops to zero.

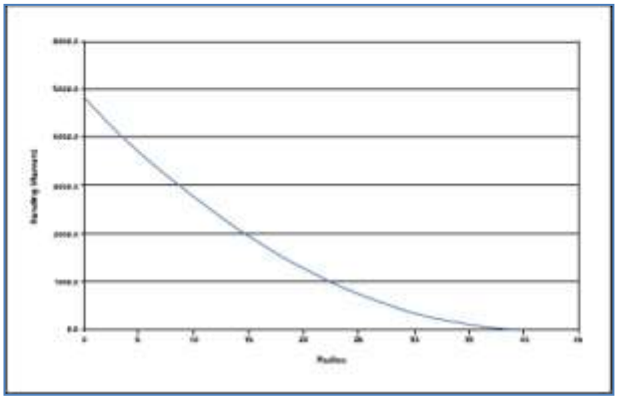

Fig.1 Bending moment against radius in a large turbine blade

So it is intuitive that the blade must be thickest, i.e. strongest, at the root and can taper in thickness towards the tip where the bending moment is less. As it happens, that suits the aerodynamics too: the blade needs a thinner section at the tip where drag is most critical and the local chord (width) of the blade is small. Also for turbines that rely on stall for power regulation in strong winds, a thin section stalls more easily so is beneficial at the tip. Closer to the root the chord is wider, but to avoid making it very wide (hence expensive) the blade needs to be thicker to generate enough lift given the lower

ISSN 1737-9334

wind speed close to the hub (thicker aero foils can generate a greater maximum lift before they stall).

Unfortunately the thickness needed to make the blade stiff and strong enough is greater than that required for aerodynamic efficiency, so a compromise must be found between structural weight (= cost) and loss of aerodynamic efficiency.

2. Governing Principle of Wind Turbine Blade

The principle behind the operation of the wind turbine for generating power from the forces of nature is a revolutionary one. The blades harness the energy from the wind by rotation depending on the wind force applied and the direction of the wind. The wind turbine blade geometry plays vital role in power generation process.

The most important part in designing a wind turbine is the blade and the choice of airfoils used at various sections of the blade. The lift generated from these airfoils causes the rotation of the blade and performance of the blade is highly depended of airfoils performance. For this research, SERI-8 wind turbine blade was selected.

The SERI-8 was originally designed by the Solar Energy Research Institute (SERI), now called the National Renewable Energy laboratory, (NREL) in 1984. The SERI-8 blade is **7.9 m** long and has a set of airfoils S806A, S806A, S807, S808 airfoils which were designed for medium size turbines rated at 20-100 kW. The airfoils closer to the tip of the blade generate higher lift due to the speed variation in the relative wind. The purpose of the airfoils at the root of blade is mainly structural, contributing to the aerodynamics performance of the blade but at a lower level. Thus the root of the blade is bigger and stronger than its tip.

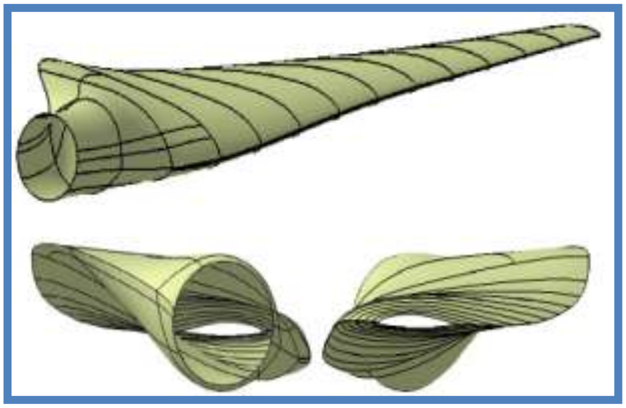

Fig.2. CATIA model of SERI-8 blade

The SERI-8 blade is shown in Fig.2. The SERI-8 blade is 7.9 m long and was divided into 13 equal sections. The twist axis is located at 30% of chord and the blade geometry. The SERI-8 has two ribs at 60 inch and 252 inch locations from the root, which were not considered in the present research. The geometry data of SERI-8 was found in Ong and Tsai [5]. The baseline design of SERI-8 blade was designed in CATIA v14.5 based on the data provided and imported into the ANSYS design modeler as shown in Fig.2.

3. Composite Material

Majority of wind turbine blades is made of fiberglass material and reinforced with polyester or epoxy resin. The materials used for SERI-8 blade design were same as that of Ong and Tsai [5]. This design consists of TRIAX and MAT as skin materials and C260 glass/epoxy as the major structural material (Table 1.). The reference fiber direction for the composite material is considered along the span direction. All sections have same number of MAT skin material layers. The ANSYS ACP composite prepost [8] was used as a preprocessor for composite layups modeling as well as for post processing to check the failure criteria. The numbers of layers of C260 material for individual sections were tagged as a parameter which would be the input as the structural design variable for the optimization process.

Table 1. SERI-8 composite materials properties

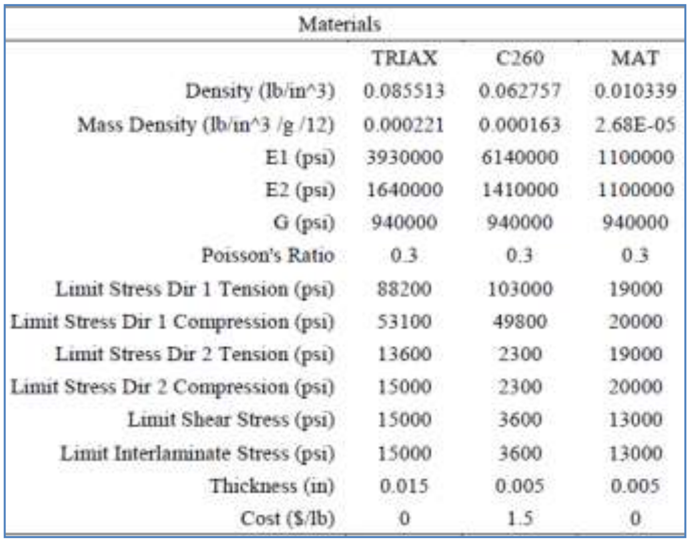

Materials			
	TRIAX	C260	MAT
Density (lb/in^3)	0.085513	0.062757	0.010339
Mass Density (lb/in^3 /g /12)	0.000221	0.000163	2.68E-05
E1 (psi)	3930000	6140000	1100000
E2 (psi)	1640000	1410000	1100000
G (psi)	940000	940000	940000
Poisson's Ratio	0.3	0.3	0.3
Limit Stress Dir 1 Tension (psi)	88200	103000	19000
Limit Stress Dir 1 Compression (psi)	53100	49800	20000
Limit Stress Dir 2 Tension (psi)	13600	2300	19000
Limit Stress Dir 2 Compression (psi)	15000	2300	20000
Limit Shear Stress (psi)	15000	3600	13000
Limit Interlaminate Stress (psi)	15000	3600	13000
Thickness (in)	0.015	0.005	0.005
Cost ($/lb)	0	1.5	0

4. Multidisciplinary Design Optimization

In this research, the cost calculation for one blade based on Ong and Tsai [5] was done. The labor cost, material cost and total cost were calculated. Assumptions were made as per Ong and Tsai's paper [5] and only major structural material C260 was used for cost estimation. Furthermore, the tooling cost was not considered in this analysis. The total labor hour for each lay-up is taken as 9.1 hours [5]. The total cost for single blade can be calculated as follows:

$$\text{Material cost} = \text{Material mass (lb)} \times \text{Material cost (\$/lb)} \tag{1}$$

$$\text{Labor cost} = \text{Total labor hours (hr)} \times \text{Labor rate (\$/hr)} \tag{2}$$

$$\text{Total cost} = \text{Material cost} + \text{Labor cost} \tag{3}$$

The total cost of the blade was calculated by defining new output parameter in ANSYS workbench [8] and mentioned as a design objective to be minimized in the optimization process.

ISSN 1737-9334

It is not possible to formulate the problem of optimum design of wind turbine blades as a single-criteria optimization task because this process requires many criteria to be taken into account. In many cases, these criteria are mutually incomparable, uncountable and sometimes even contradictory, which precludes their simultaneous optimization. The following criteria have taken into account in the process of optimal wind turbine design,

- Minimize weight of the blade
- Minimize blade total cost
- Minimize blade vibration and keep modal frequency at acceptable level
- Maximize power output
- Accomplishment of appropriate strength requirements

The mass and material cost of a blade is correlated and depends on the blade structural stiffness. If the blade design robustness is at optimal level then both the criteria can be satisfied. The optimal blade thickness for different blade section helps to satisfy these criteria. Minimization of vibration is a better way to obtain optimal design of blade structure and at the same time it contributes to keep the cost low and provide high stiffness. Hence, to minimize vibration, the natural frequency of the blade should be separated from the harmonic vibration associated with rotor resonance. Therefore, mode separation constraint was setup to examine the first three natural frequencies and is separated from each other by more than ±5% of its natural frequency.

Furthermore, to meet the strength requirements of the structure, optimization of maximum displacements of the blade at the tip would have to be carried out with a limiting constraint and permissible stress should not be exceeded. To maximize a torque and hence power, blade pitch angle and shape should be optimized. Henceforth, optimal pitch angle need to be obtained to maximize the power generated.

As explained earlier, the main objective of the present work was to develop a multidisciplinary design optimization procedure for SERI-8 blade. The blade needs to be optimized for optimal aerodynamic performance and structural robustness. The key objectives were to minimize mass and cost of the blade and maximize power output. The reference SERI-8 blade was aerodynamically optimized based on BEM theory with modified twist angle. The blade pitch angle was given as an input variable parameter to guarantee a good aerodynamic performance. The numbers of layups at different sections were tagged as a structural design variable.

The constraints in wind turbine blade design are as follows:

- Displacement of the blade cannot exceed the set value (global stability must be ensured),
- Maximum stresses generated in the blade cannot exceed permissible stresses (appropriate strength requirements for the structure), and
- Separation of natural frequencies of the blade from harmonic vibrations associated with rotor rotation.

The design constraints, variables and objectives for this case study are summarized in Table 4.5.

Table. 2. Variables, constraints and objective for the MDO process

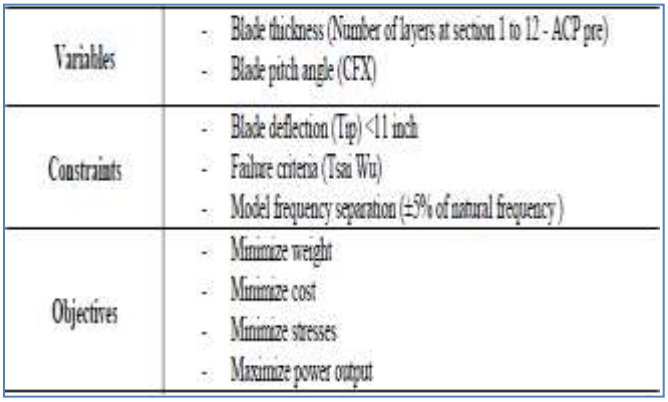

Variables	- Blade thickness (Number of layers at section 1 to 12 - ACP pre) - Blade pitch angle (CFX)
Constraints	- Blade deflection (Tip) <11 inch - Failure criteria (Tsai Wu) - Model frequency separation (±5% of natural frequency)
Objectives	- Minimize weight - Minimize cost - Minimize stresses - Maximize power output

ANSYS Workbench 14.5 [8] and design explorer module was used to carry out the multidisciplinary design optimization problem. Design exploration describes the relationship between the design variables and the performance of the blade by using Design of Experiments (DOE), combined with response surfaces and identifies the relationship between the performance of the blade and the input design variables. Once the response surface has been introduced, the optimization study needs to be defined, Central Composite Design-G optimality method was used and desired objectives and constraints were set within the specified domains.

II. RESULTS

The two comparable materials fiber glass reinforced Epoxy and carbon fiber reinforced epoxy were used in modeling for composite turbine blade with the help of ANSYS finite element software. The stress and deflection results were obtained as ;

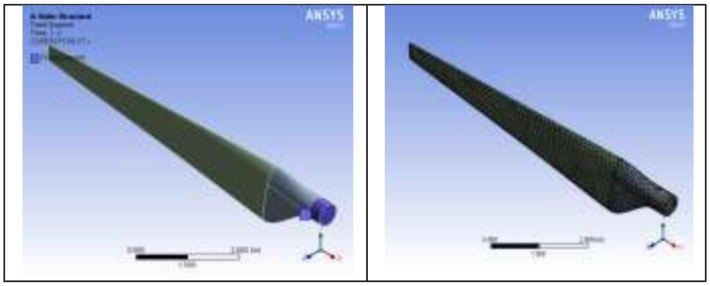

Fig.3. F.E. Model of Composite Turbine Blade

Fiber Glass - Epoxy	Fiber Carbon - Epoxy

Fig.4. Equ. Stress of Composite Turbine Blade

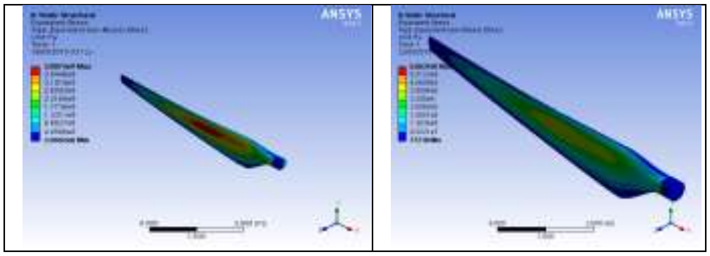

Fig.5. Equ. Strain of Composite Turbine Blade

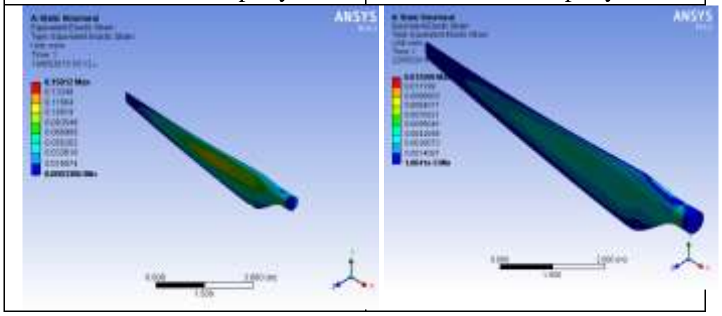
Fiber Glass - Epoxy | Fiber Carbon – Epoxy

Fig. 6. Deformation of Composite Turbine Blade

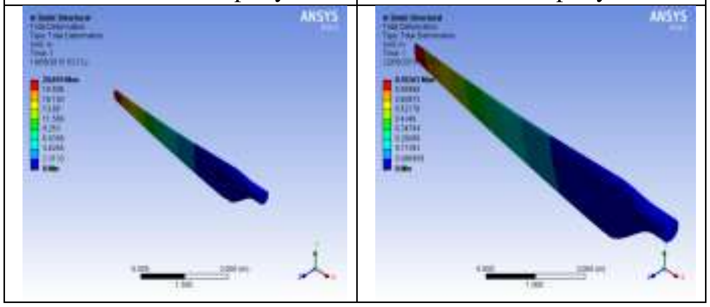
Fiber Glass - Epoxy | Fiber Carbon – Epoxy

Fig. 7. Iso stress of Composite Turbine Blade

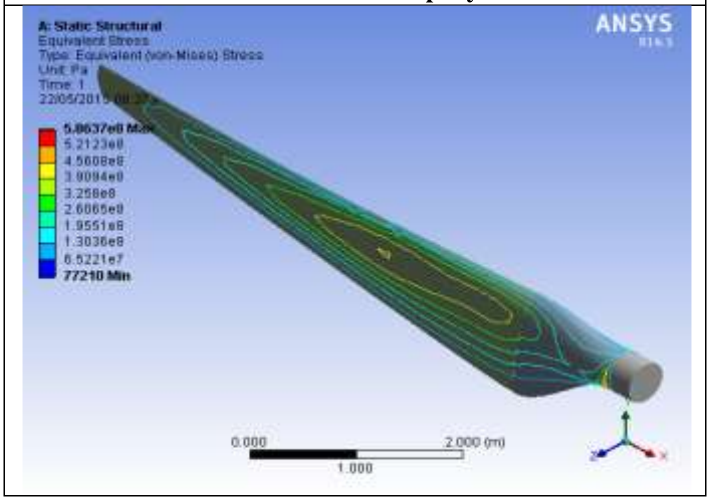
Fiber Carbon - Epoxy

III. CONCLUSION

The aerodynamic performance of the optimized wind turbine design is improved by about 4% compared to the baseline design. In addition the following were observed in the optimized design: mass reduction of 23.67%, cost reduction of 27.25%, reduction of maximum deformation of 19.98% and maximum stress reduction of 12.35%.

This complex MDO process presented here can be applied to the design of wind turbine blades to obtain a structurally optimized blade design with optimal blade thickness distribution and maximum power output without compromising its aerodynamic performance.

With respect to the different issues concerning material properties and manufacturing capabilities discussed in this paper, the following conclusions are drawn:

Material properties:

- Because of their low cost, engineering polymers have been identified as the only matrix system possible for wind turbine blade thermoplastic composite materials. Advanced thermoplastic composites based on PEI, PPS or PEEK cannot be used, due to their prohibitive cost.
- Due to their recyclable nature, thermoplastic composites will offer the possibility of full material recovery at the product end-of-life. With some engineering polymers being cheaper than conventional thermoset resin systems, blade material cost could potentially be reduced when using thermoplastic composites.
- With polymer weight, strength and stiffness being comparable to conventional thermoset resin systems, no significant reduction in static mechanical performance is to be expected when using thermoplastic composite for wind turbine blade structures. This holds true if the matrix behaves similarly hygrothermally and can ensure equivalent fiber/matrix adhesion.
- Fatigue performance of thermoplastic composites will need to be investigated before being considered for wind turbine blade structures.

REFERENCES

[1] T. E. W. E. Association, Pure Power-Wind Energy Scenarios Upto 2030, March-2008.
[2] J. Logan and M. K. Stan , "Wind Power in the United States: Technology, Economic, and Policy Issues," June 20, 2008.
[3] T. Berlin, "Qblade," [Online]. Available: http://qblade.de.to/.
[4] Dassault Systems, "CATIA," France.
[5] S. Tsai and C. H. Ong, "The Use of Carbon Fiber in Wind Turbine Blade Design: A SERI-8 Blade Example," Sandia National Labs, March 1, 2000.
[6] J. W. Lee and S. N. Gangadharan, "Multidisciplinary Design Optimization of a Hybrid Composite Wind Turbine Blade," 2011.
[7] B. Kim, K. Woojune, B. Sungyoul, P. Jaehyung and K. Manneung, "Aerodynamic Design and Performance Analysis of Multi-MW Class Wind Turbine Blade," vol. 25, no. 8, April 24, 2011.
[8] "ANSYS Workbench," 2010.
[9] D. Digraskar, "Simulations of Flow Over Wind Turbines," University of Massachusetts, Amherst, May 2010.
[10] C. E. Carcangiu, "CFD-RANS Study of Horizontal Axis Wind Turbines," January 2008.
[11] J. Tangler, B. Smith, N. Kelley and D. Jager, "Measured and

Predicated Rotor Performance for the SERI Advanced Wind Turbine Blades," February 1992.

[12] Gujicic, M.; Arakere, G.; Sellappan, V.; Vallejo, A.; Ozen, M., "Multidisciplinary Design Optimization for Glass-Fiber Epoxy-Matrix Composite 5 MW Horizontal-Axis Wind-Turbine Blades",2009.